UNIVERSITY OF Southampton

The Optical Properties of Nano-photonic Biomimetic Antireflective Structures

by

Asa Asadollahbaik

Thesis submitted for the degree of Doctor of Philosophy

in the

Faculty of Engineering and the Environment
Computational Engineering and Design

February 2012

UNIVERSITY OF SOUTHAMPTON

ABSTRACT

FACULTY OF ENGINEERING AND THE ENVIRONMENT
COMPUTATIONAL ENGINEERING AND DESIGN

PhD Thesis

The Optical Properties of Nano-photonic Biomimetic Antireflective Structures

by Asa Asadollahbaik

The field of biomimetics is vastly expanding in engineering and technology. Natural examples of successful photonic devices in nature have shown potential for engineering applications. One biomimetic example is the "moth-eye" structure known to have low reflection over a wide wavelength spectrum and incident angle, and have potential for use as anti-reflective and anti-glare surfaces. In this thesis computational and experimental studies on silicon moth-eye structures are presented, investigating their reflectance properties for use in solar cell anti-reflective coatings and anti-glare applications.

Computational studies showed that periodicity and height of protuberances in moth-eye structures are critical parameters to produce low reflectance at a desired wavelength range and allows the design of moth-eye structures for a variety of applications from the visible wavelength to the micron-scale. Computational optimisation identified a moth-eye structure of low reflectance (under 1%) in the visible wavelength spectrum, insensitive to the angle of incidence and orthogonal polarisation up to an incident angle of 40°. The azimuth orientation of moth-eye structures was found have little effect to their specular reflectance, a novel finding showing a strong potential of moth-eye structures for anti-glare applications. Moth-eye structures were found to remove the single polarisation reflectance property of silicon surfaces and be capable of introducing inverse polarisation in the visible wavelength spectrum.

Experimental studies revealed that increasing the periodicity of moth-eye structures shifts the normal incidence and specular reflectance spectrum towards higher wavelengths. Increasing the incident angle not only increases the reflectance value but also shifts the reflectance minima and maxima towards higher/lower wavelengths. The profile of the protuberances was found to affect the specular reflectance of moth-eye structures; tapered profiles reduce the reflectance more than vertical pillars. The reflectance measurements at different azimuth orientations confirmed the simulation study and showed that moth-eye structures are well suited for anti-glare applications.

A comparison between optical properties of silicon moth-eye structures and photovoltaic anti-reflective technologies showed that a moderate silicon moth-eye anti-reflective structure is successfully fabricated using nano-imprinting technique. Employing this fabrication technique to produce the silicon moth-eye structure suggested by the computational results can produce a silicon moth-eye coating of omnidirectional low reflectance over a wide bandwidth which is insensitive to azimuth orientation, making it well suited for anti-reflection and anti-glare purposes.

Contents

List of Figures

List of Tables

Declaration Of Authorship

I, *Asa Asadollahbaik*, declare that the thesis entitled *The Optical Properties of Nanophotonic Biomimetic Antireflective Structures* and the work presented in it are my own. I confirm that:

- this work was done wholly or mainly while in candidature for a research degree at this University;
- where any part of this thesis has previously been submitted for a degree or any other qualification at this University or any other institution, this has been clearly stated;
- where I have consulted the published work of others, this is always clearly attributed;
- where I have quoted from the work of others, the source is always given. With the exception of such quotations, this thesis is entirely my own work;
- I have acknowledged all main sources of help
- where the thesis is based on work done by myself jointly with others, I have made clear exactly what was done by others and what I have contributed myself;
- parts of this work have been published as: journal and conference papers and posters, and technical documentation listed in Appendix A.

Signed: ..... Date: .....

Acknowledgements

I would like to thank Dr Marc Molinari for the start of this project and his guidance during the initial stages of supervision. My greatest appreciations goes to Prof. Simon Cox for continuing my supervision and helping me during the hard times, and to Prof Darren Bagnall for suggesting this project to me and co-supervising me in the moments I was struggling. Without their support and guidance I wouldn't have been able to finish this work.

Special thanks also goes to Dr. Ken Thomas for his smile and warming words. I would like to thank Dr Stuart Boden for providing the moth-eye samples and his constant and patient help. I shall also thank Dr Martin Charlton for his help and guidance with the reflectometer experiment. I also thank Mr David Payne for his help with the reflectometer, his effort designing and setting up the integrating sphere and providing me the data. Also thank to Dr Michael Pollard for his comments, chats and helps during this work. I would also like to thank Microsoft for providing the funding for this work.

Special thanks to my "team of proof-readers": Richard Croxall and Dr Sylvia Croxall, Dr Kevin Briggs, Dr Tristan Temple, Dr Michael Pollard and Dr Stuart Boden.

I have called myself a "nomad PhD student": I have changed office four times and desk five times during my PhD. As a result, I have many friends and have learnt from each individual. I shall thank the staff and students of: Engineering Materials group, especially the residents of Eustice 3025 in 2008: Toby, Anna and Christian; Gwyneth, the beloved secretary of the group; and Prof Phillipa Read. Computational Engineering and Design group: the friendliest secretary of all Ms Ros Mizen; my old officemates Liz(Dr), Steven(Dr), Neil, JJ(Dr) and Greg. My second home and family, the Nano Research Group: Glenys and Lucia the most helpful secretaries; all students, staff and technicians in NSI for accepting me as a member of the group for two years especially Darren's group: Stuart(Dr), Tristan(Dr), Owain(Dr), David, Peter(Dr), Farrah, Mehdi, Akhtar and Steffi, and Mike. I would also like to thank the old and new admin staff of the School of Engineering Sciences especially Alessia and Julia for helping me from the day one, and Jacqui and colleagues for their help during these last days to get me on track.

No one has ever survived without friends. I need to thank those who have always given me energy, hope and warmth: Newsha for reading my long lasting emails, Sepideh for calling me "Doci", Asieh and Shirin for being there on "that day", Hatice, Pramod and Hamid for fun, support and memories and Elnaz for being there at the start. There are also those whom without them the experience of Southampton wouldn't be as it is, since names are many I would summarise as: the Iranians, PhDs of Civil engineering group and Bio group, and the Portuguese. I would also like to thank Kevin's parents, Mark and Andrea, for comforting me and giving me hope.

This paragraph is dedicated to thank those who have to be mentioned, no matter what they have done. Richard and Sylvia (Croxall) have always been there for me just like my parents. Kevin, has been very patient with me for two years and given me "that special thing" I wouldn't be able to find on my own. My brothers, have been supporting and encouraging me from the first day I left home, and the most important of all my parents who made the departure, the path, the start, the process and the end possible for me. I cannot say anything, except thank you.

To my parents; AbbasAli and Zohreh,
And my brothers; Amir and Ashkan,
For their Patience,
Support,
and Love.

Chapter 1

Introduction

1.1 Biomimetics

"Biomimetics is the extraction of good design from nature"

Prof. Andrew R Parker [69]

From the very early stages of science, nature has been an inspiration to humans, helping to solve problems in a variety of fields such as mechanics, materials science, flight engineering, architecture, and pharmacology. The use of wings to fly, invention of Velcro similar to the hooks of burrs, iridescent car paints, and waterproof clothes copying the lotus leaf are just a few examples of where humans have borrowed from nature to ease the difficulties encountered within science and technology. In a case of a difficulty or a change, nature has modified itself to adapt to the surrounding environment to its best extent.

Biomimetics is exploiting the advantage of the "nature's trial and error" procedure [67]. The eternal aim of natural existences is to survive. Thus they have made changes into their body organs to live longer and to increase the probability of mating so that they can reproduce. These changes have occurred gradually and slowly to provide efficiency in terms of time and cost. An example of such is the species of butterflies with random features which are delivering the same properties as the arranged features, however since producing random arrangement is cheaper than regular arrangements, the butterfly has preferred to choose a random arrangement [65]. Natural structures are built for special purposes, hence they have to be employed accordingly, where they operate the optimum. An example is an optical effect from the wing of species of butterflies which is optimal only from oblique incidence to be viewed by butterflies during courtship [67].

The biological structures studied at present are the result of millions of years of adaptation and refinement taken place within nature. However, it is only since 1960s[24] that

biomimetics has become a scientific discipline in which worldwide researches are performed to develop solutions for industrial and commercial problems. At the Technical University of Denmark, a group working on the "Biomimetics Project" [1], has provided resources and libraries of natural structures, and scientific methodologies for the study of biomimetics. Torben Lenau, a member of this group, believes that the stages in a biomimetic project, in which a successful biomimetic product is produced, can be formulated to five phases (Figure 1.1). The first phase is the problem definition phase where a problem in the industry is discovered and formulated. At the second phase, the correct terms are derived from the definition of the problem to be used to search for a biological structure which provides a phenomena similar to what is required by the industry. Finding the biological phenomena or mechanism is in the analysis phase whereafter the principals behind the function of the biological phenomena or mechanism is studied. The latter, principal phase, delivers inspirations and ideas to design the biomimetic structure in the design phase.

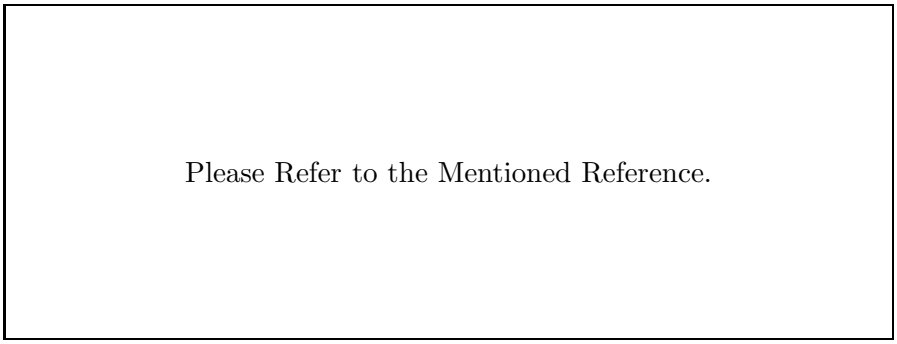

FIGURE 1.1: Flow chart of phases in biomimetic [1].

1.2 Biomimetics in Photonics Industry

One of the fields that has borrowed from nature is photonics. Lately, improvements in nano-scale fabrication and optical characterisation have helped the field of photonics utilise solutions from nature. The invention of electron microscopy has allowed observation of nano structures in organs of birds and insects, and revealed natural photonic structures. Since then, research in this field has enabled the development of several technologies inspired by nature. In the field of solar cells, the antireflectivity of cells plays an important role in reducing power loss. A nano-structure that covers the eyes of certain species of moth has great potential to reduce reflection from the top layer of solar cells [71]. There has also been the invention of iridescent car paint in which thin film nano structures copied from butterfly scales alter the reflected colour for different incident angles [67]. The most interesting example of biomimetics in the field of photonics is the recently made Mirasol displays technology from Qualcomm [3]. They have invented a method of colour production in displays where tuning the air gap between a reflective membrane and thin-film stack produces the three main visual colours of green, red and

blue. A pixel is made of many of these cells and the whole display is covered by millions of these pixels. Qualcomm has announced that its invention is inspired by the colour production process in butterfly wings.

A biomimetic structure is the optimal design of nature in an animal/plant for a specific purpose. However nature's choice of materials is limited. Within the field of the photonics industry where semiconductors are the building material, the range of the materials is wider which helps to customize nature's design to our needs. The higher refractive index of semiconductors improves the performance of the biomimetic structure. The chosen natural structure might not completely fulfil the needs of the industry and thus optimization processes are required to design a biomimetic structure which adequately fits industry's needs. Even so, the use of the biomimetic structure and "nature's billion years of experience" has saved industry huge amount of time, material and cost.

1.3 Photonic Structures in Nature

A wide variety of photonic structures have been found in the bodies of animals, and plants. A. R. Parker has performed intensive studies on a variety of such structures [66, 68]. Following his work, we hereby categorize natural photonic structures into two broad groups based on their optical performance; reflectors and non-reflectors. The reflectors group includes the micro-structured colour producing structures reminiscent of multilayer mirrors, diffraction gratings, liquid crystals, and photonic crystals. The non-reflectors group delivers other optical functionalities such as light concentration, guiding, and antireflection, and typically involves lenses, photonic crystal fibres, and zero order gratings.

1.3.1 Reflectors

The striking colours of certain species of butterflies, peacock feathers, and feathers on the neck of ducks and pigeons are all a result of photonic reflectors. These colours are different from pigment colours in which the colour is produced by the material's intrinsic absorption and reflection. Instead they are caused by variation of the structure's refractive index at the length scale of visible light, and are thus called micro-structural colours.

A multilayer structure of chitin-air material in some species of beetle produces a striking gold colour on the cuticle of the insect [64]. This colour is produced through the multiple reflections of the light wave as it passes through the multilayer structure (Figure 1.2). Multilayers have also been observed in many species of butterflies producing iridescent colours on their wings [27, 92, 42, 43, 93, 75, 64, 67]. Another example of reflectors is a grating structure on the antenna of a seed-shrimp, which is responsible for the metallic

iridescent colour of the antenna (Figure 1.3) [66]. The variety of colours observed at different angles come from the wavelength-dependent diffraction. A famous photonic crystal structure that produces striking colours is the opal-like structure in some species of weevil, which makes the insect's body blue (Figure 1.4) [70]. The blue colour of the famous morpho rhetenor butterfly also depends on a photonic crystal structure, in this case resembling the shape of a Christmas tree.

1.3.2 Non Reflectors

Non-reflector structures provide other optical behaviours to insects. Some species of a brittle star are covered with lenses that increase their photosensitivity, and trigger a change of colour between day and night (see Figure 1.5)[8, 93]. Such lenses have also been observed on the compound eye of arthropods, and help to concentrate the light into their photopigments. In some species of moth, the surface of the eyes is covered with zero order diffraction gratings, which reduce the reflection from the surface to almost zero and increase the insect's vision in low-light conditions. Similar structures have also been observed on the wings of species of moth, making the wing transparent and consequently the insect less visible to predators (Figure 1.6) [11, 93]. Similar non-reflective behaviour is observed in the black region of the wings of species of butterflies. The striking colours of the wing is surrounded by the black regions and thus appears very distinctive. It is known that the striking colours of the wing are to attract mates. However these highly absorbing structures have a complicated three dimensional shape on top and a non-reflective layer underneath to prevent backscattering at lower parts of the wing to interfere with the "ultra-black" (Figure 1.7) [72].

The current need for black or non-reflective structures in industry is spread over a wide range of applications: reproduction of jewellery gemstones, stealth applications from infra red to radio frequencies, fade-resistant paints, coating of solar cell and detector surfaces, electronic paper and high contrast ultra black displays [72].

Among the non-reflective and high-absorbing structures, the moth-eye is famous for its promising anti-reflective properties. The moth-eye structure consists of subwavelength conical or sinusoidal protuberances arranged on the surface in hexagonal lattices. Along with anti-reflectivity, hydrophobic and self-cleaning properties of moth-eyes are also studied and thus multi-purpose applications are proposed for them [82].

1.4 Objectives

This thesis presents research into moth-eye structures and their potential application for anti-reflection technologies. It builds on work carried out by Boden [15] in which silicon moth-eyes were optimised for anti-reflective coatings on solar cells and samples were

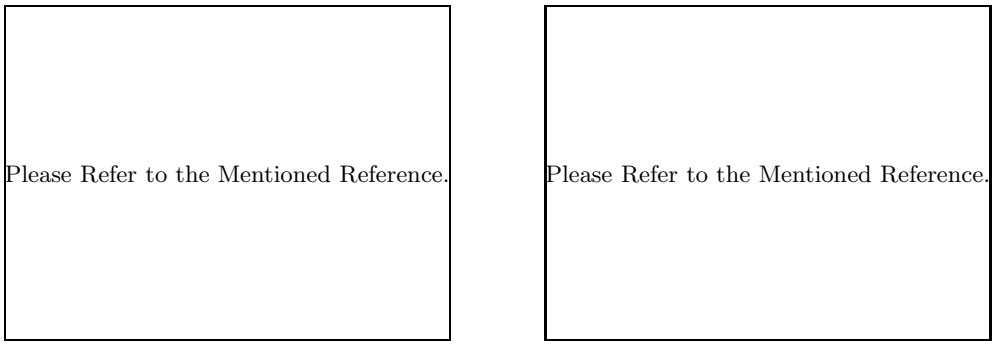

(a) (b)

FIGURE 1.2: Striking gold colour in the cuticle of a species of a beetle produced by a multilayer structure [64].

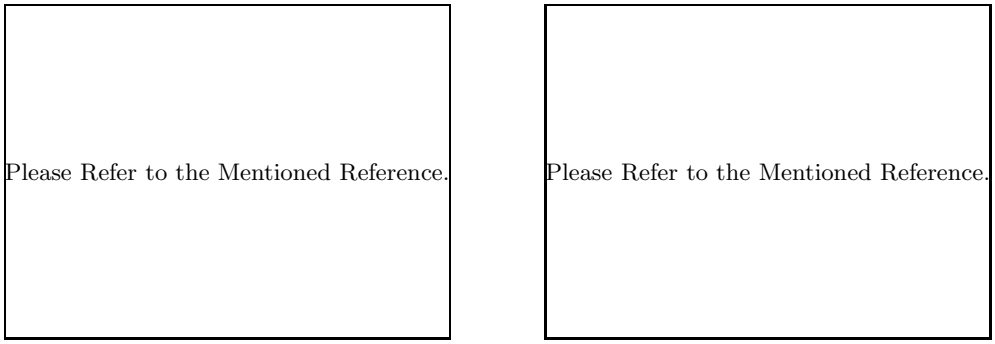

(a) (b)

FIGURE 1.3: The antenna's of a seed-shrimp showing metallic colour produced by the diffraction grating structure [66]

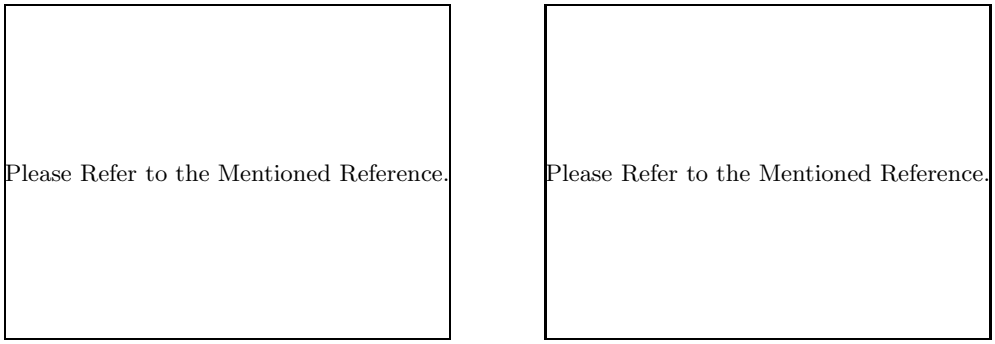

(a) (b)

FIGURE 1.4: The blue colour on the body of a weevil is produced by an opal-like structure [70]

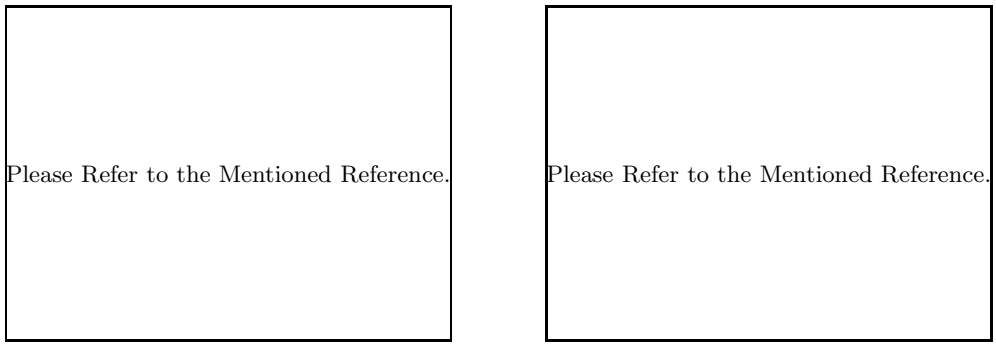

(a) (b)

FIGURE 1.5: (a) Light sensitive brittle star in day (left) and night (right) covered by microlenses (b) [8].

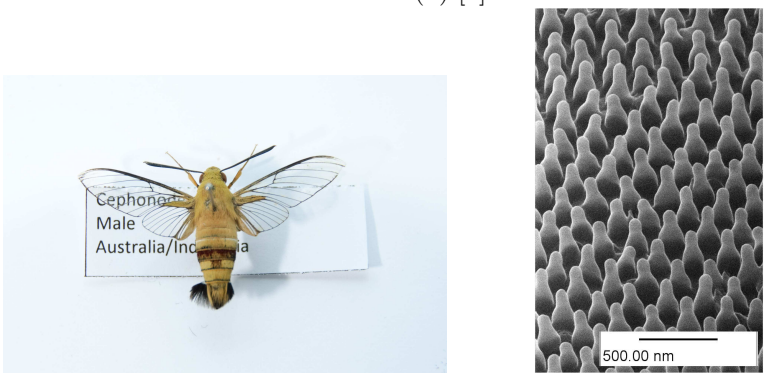

(a) (b)

FIGURE 1.6: Transparent wing of species of moth produced by zero order diffraction grating.

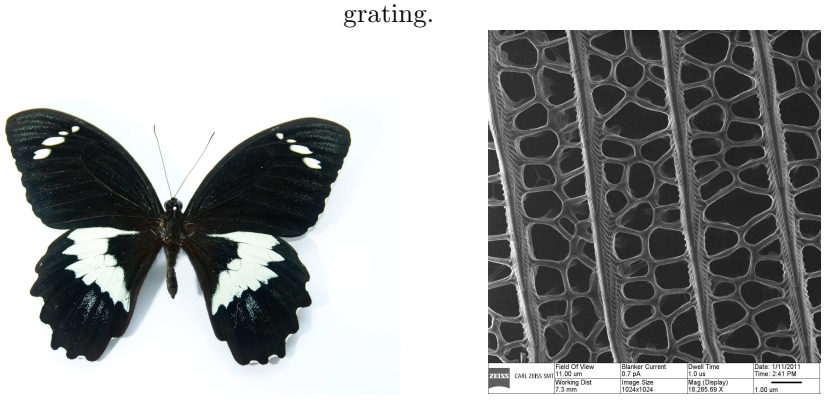

(a) (b)

FIGURE 1.7: Ultra black surface of wings of a butterfly (a) is produced by three dimensional photonic crystal structure. (b) A helium ion microscopy image of an uncoated black wing scale.

fabricated providing a variety of dimensions and parameters within moth-eye structures to be studied. This work has pursued the following objectives:

- To perform a computational study of moth-eye structures with different geometries and dimensions and optimise the reflection properties of silicon moth-eye structures for anti-reflective and anti-glare purposes,
- To study the optical properties of moth-eye structures for a range of angles of incidence and azimuth orientation using computational modelling,
- To study the optical properties of biomimetic moth-eye samples fabricated by Boden [15] for a range of angles of incidence and azimuth orientation,
- To compare the computational and experimental results of reflectance of silicon moth-eyes with other anti-reflective structures researched for photovoltaics.

1.5 Layout of the Thesis

The chapters of this thesis are as follows:

Chapter 2 briefly explains the problem of reflection within the field of photovoltaics and the solutions provided to date by science. It then, introduces nature's solution to this problem by providing a review of the literature on the computational and experimental studies performed on natural moth eyes and biomimetic moth-eye structures. Fabrication techniques used to produce biomimetic moth-eye structures are summarised in this chapter.

Chapter 3 introduces and explains the experimental techniques used in this work.

Chapter 4 reviews the computational method used for simulation of silicon moth-eye structures. The effect of variation of the geometries of moth-eye structure on its optical properties is studied. A moth-eye structure is optimised for anti-reflective purposes within the visible to near infra-red spectrum. Further studies are performed on the optimum structure to evaluate the effect of external conditions to the optical behaviour of silicon moth-eyes.

Chapter 5 employs the experimental techniques introduced in Chapter 3 and studies the optical behaviour of silicon moth-eyes with alternating periodicity.

Chapter 6 performs the same studies as Chapter 5 on a set of samples with a range of pillar profiles. An additional experiment of varying the azimuth orientation of samples on the reflectance of samples is also performed here.

Chapter 7 compares the optical performance of experimental and computational optimum silicon moth-eye structures studied in previous chapters with anti-reflective structures within the field of solar cells.

Chapter 8 provides the main conclusions drawn from this work. Suggestions for further studies and future works are also presented.

Chapter 2

Literature Review

Research in the field of biomimetics starts with the problem definition phase where a specific problem within industry is identified and needs to be solved (Chapter 1). In the field of photovoltaics a well-known problem is the surface reflection from the cell which is one of the main sources of loss of energy in the area of photovoltaic energy harvesting. To solve this problem a few solutions are already given by science and employed in the industry. However, searching the database of natural photonic structures had brought attention to moth-eyes where nature has already solved the problem of reflection efficiently. This chapter explains the current anti-reflective technologies in the field of solar cells which are the solutions given by science to solve the problem of surface reflection in photovoltaic, and later it provides a comprehensive study of the moth-eye structure and reviews the studies performed in this area to date.

2.1 Problem: Reflection

When a beam of light illuminates the interface between two materials, the light is scattered by re-radiation of atoms in the second media and reflects back (Figure 2.1). The proportion of the light reflected back from the interface to the first media depends on the difference in refractive index between the two media; the bigger the difference, the greater the reflectance. The relationship between reflection and the refractive index of the two media is defined by the Fresnel Equations [34]. At normal incidence these equations simplify to:

$$R = \left(\frac{n_1 - n_2}{n_1 + n_2}\right)^2. \tag{2.1}$$

where R is the reflectance at normal incidence, n_1 is the refractive index of the first medium and n_2 is the refractive index of the second medium.

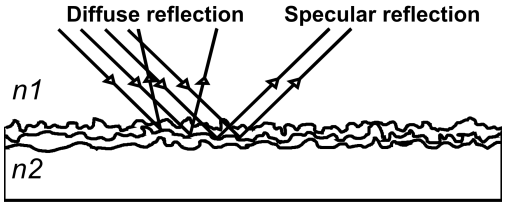

FIGURE 2.1: Reflection from the interface of two materials with the refractive index of n_1 and n_2.

Although reflection underpins the operation of many optical devices and technologies, it is not desirable to have reflection in applications where transmission of light plays the main role. The reflection from the surface of lenses is highly undesirable in optical devices such as telescopes, where low reflection helps to improve the contrast of the image. Reducing reflection from eyeglasses improves the vision of the wearer and makes the eyes appear more visible to others. Many display components suffer from reflection which reduces the sharpness of the displaying image.

Photovoltaics, as one of the main energy harvesting technologies [94, Ch. 3], is another technology in which reflection is identified as a problem. The efficiency of solar cells is far from being close to the maximum theoretical value of $93\% - 95\%$; most commercial single junction solar cells have the efficiency of 5% to 22% [94]. Reflection of the solar radiation from the top surface of a solar cell is among the optical losses that a high efficiency solar cell suffers from. At normal incidence the loss of the solar irradiation due to surface reflectance at the air-silicon interface of silicon solar cells is between 31% to 61% which causes an approximation of 36.2% reduction in the short circuit current produced by a silicon solar cell [15]. Thus it is of great importance to develop effective anti-reflective technologies to reduce surface reflection losses and consequently increase solar cell efficiency.

2.2 Science's Solution

The anti-reflection technologies in the field of solar cells are generally based on one of the mechanisms including: destructive interference, multiple-reflectance, light trapping or the gradual change of refractive index. In solar cells, three main groups of anti-reflective coatings are developed. These three groups are reviewed in the following sections.

2.2.1 Thin Film Coating

Thin film anti-reflection coatings are based on the theory of the destructive interference of electromagnetic waves. If two waves with a phase difference of half a cycle overlap, the waves destructively interfere, meaning that the amplitude of the resultant wave is a subtraction of the amplitude of the two incident waves. If the waves have equal amplitude, the resultant amplitude is zero. The reflectance of the incident light on an interface can be reduced to lower and in some cases to zero values using destructive interference. Employing a layer with a refractive index value between the two surrounding media of the interface (n_0 and n_s), produces two interfaces within the path of the incident light and consequently the reflection of the incident light happens at the two interfaces: one at the interface of the first media(n_0) and the intermediate layer(n_1), and the other one at interface between the intermediate layer (n_1) and the second media(n_s) (Figure 2.2). The latter exits the intermediate layer following the theory of refraction. The path difference between the two reflected rays, caused by the thickness of the intermediate layer, causes a phase difference between the two reflected waves which results in constructive or destructive interference. According to the findings of Rayleigh [55], if the intermediate layer has a thickness of one quarter of the wavelength within the layer, the path difference of the two reflected rays produces a 180° phase difference and hence the destructive interference causes zero reflectance at this wavelength and lower reflectance at neighbourhood wavelengths.

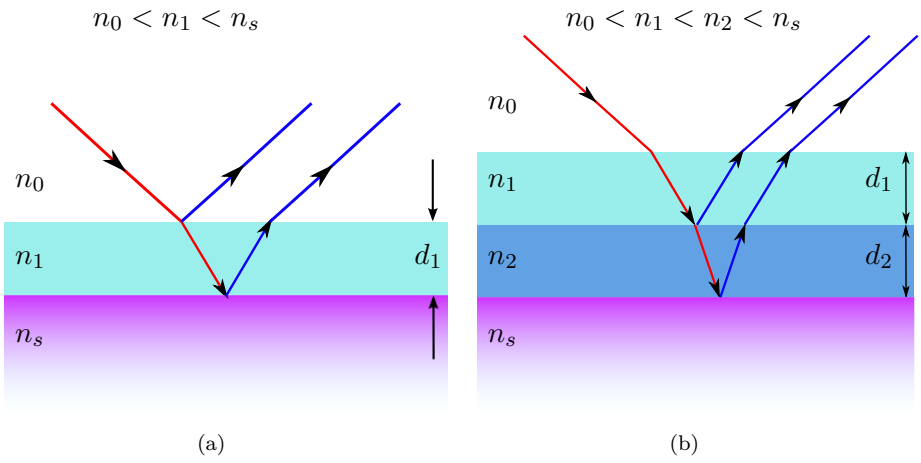

FIGURE 2.2: Destructive interference using (a) a single intermediate layer (SLAR), and (b) double intermediate layers (DLAR).

This technique is used within solar cell anti-reflective coatings to reduce the surface reflection. A Single Layer Anti-Reflective coating (SLAR) with an optical thickness[1] of $d_1' = \frac{\lambda}{4}$ and refractive index of $n_1 = \sqrt{n_0 n_s}$ can be used as a solar cell anti-reflective coating. In this case, n_0 is the refractive index of air and n_s is the refractive index of

[1]Optical thickness is the thickness of the layer considering its refractive index: $d_1' = n_1 d_1$

silicon for an air-silicon interface of solar cells. The efficiency can be improved beyond that of a single layer by using multiple intermediate layers of different refractive index and thickness. Multilayer structures also show better performance for reflection from oblique angles of incidence. In all cases the optical thickness of each layer is $\lambda/4$. For Double Layer Anti-Reflective structures(DLAR) the refractive index of the intermediate layers can be calculated using [15]:

$$n_1^3 = n_0^2 n_s \quad \text{and} \quad n_2^3 = n_0 n_s^2 \tag{2.2}$$

Studies are performed to choose materials with the optimum refractive index as SLAR and DLARs for silicon solar cells [101, 20, 15]. The refractive index of silicon changes with the wavelength. However, solar cells are mostly optimized at the wavelength of 600nm where the intensity of the sunlight is the greatest. At this wavelength the refractive index of silicon is 3.941. In order to provide the optimum refractive index for intermediate layers within SLAR and DLAR, a variety of materials were investigated having the refractive index of between $1.4-2.7$ [49]: SiO, SiO_2 [54, 60], Si_3N_4 [81, 44, 73] (latter for DLAR), TiO_2 [54], ZnS [20, 28], Al_2O_3 [20], Ta_2O_5 [20].

Richards performed an extensive investigation of different SLAR structures and concluded that the most efficient SLAR in terms of anti-reflectivity and solar cell performance is Si_3N_4 while TiO_2 is the second best[78]. The nature of a single layer anti-reflective structure results in low reflectance at a single wavelength. Adding more layers increases the number of minima within the spectra. Hence double layer anti-reflective has two minima within the spectrum which provides a broader range of anti-reflectivity. Structures of SiO_2-TiO_2 [49], MgF_2-ZnS [103] are very common in the field of DLAR to provide such refractive indices. The latter is a double layer used as a coating for the best silicon solar cell with inverted pyramids in micron scale [30, 103]. Studies are also performed to find triple-layer thin films. Structures of $MgF_2/Al_2O_3/ZnS$ and SiO_2/SiO_2-TiO_2/TiO_2 are studied for this purpose. However finding materials providing the required optimum refractive indices in a TLAR structure is even harder than DLAR and thus this structure is not very popular.

Thin film structures are generally fabricated using vacuum processes such as thermal evaporation, reactive sputtering, and Plasma-Enhanced Chemical Vapour Deposition (PECVD). While the fabrication process might not be a complicated process, there is not a wide range of materials which can be used for this purpose to provide the required refractive index. Finding materials for SLAR or DLAR anti-reflective coatings is limited by the optimum refractive index, deposition method, uniformity and thickness of the layer and the properties of the coating [44]. SLARs reduce the surface reflection of silicon to $8\% - 15\%$ in total [45] and show the optimum performance only for a limited range of angles of incidence. Employing DLARs instead of SLARs improves the range of

the incident angle where the AR performs optimally. Figure 2.3 plots the total normal incidence reflectance of various SLARs and DLARs of silicon solar cells which are studied experimentally in literature. SLARs show a a single minimum at the design wavelength, which reaches to near zero for ZnS and and SiN_x. The reflectance spectra of SLARs rise at two other sides of the minimum point. Reflectance of DLARs however show two minima and consequently a wider bandwidth of low reflectance.

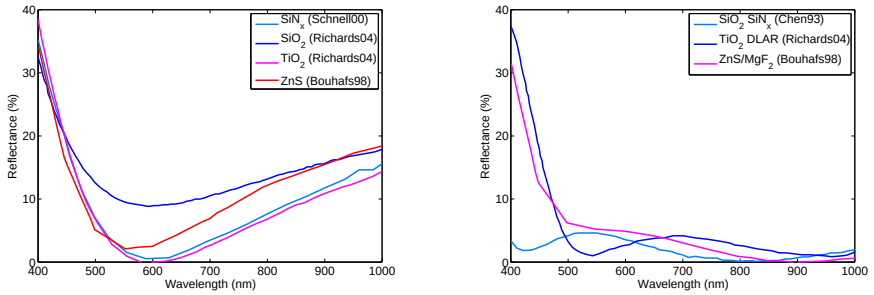

(a) (b)

FIGURE 2.3: Normal incidence hemispherical reflectance of (a) single layer anti-reflective coatings and (b) double layer anti-reflective coatings. Data is taken from literature (Schnell00 [81], Richards04 [78], Bouhafs98 [20], Chen93 [21]).

2.2.2 Micron-scale Texturing

Introducing micron scale texturing at the surface of the air-silicon interface of solar cells is another technique used to reduce the surface reflection. The texturing at the interface causes the incident light to reflect multiple times. At each reflection a portion of the light enters the substrate and thus in overall reduces the surface reflection. The textures also cause the transmitted light to undergo multiple refraction and scattering and to pass through the silicon multiple times. This is known as light trapping and is important in the case of thin film devices where the silicon is thin. Light trapping helps the light to be absorbed and prevents it from being lost within the structure.

The textures are normally in the form of random arrays of pyramids [41, 74, 7], microgrooves [101], random textures [28] and regular inverted pyramids [74, 102]. While anisotropic etching is compatible with single crystalline silicon [41, 63, 103], multi crystalline silicon is textured using laser scribing [7], plasma etching of defined patterns [103], mechanical grooving [51] and isotropic etching[28, 87]. The reflectance of micron scale textured structures is further reduced by SLAR or DLAR coating on top of the texturing [102, 44, 103, 28, 73].

The reflectance of few micron textured solar cell ARs reported in the literature without thin film coating and with thin film coating is plotted in Figure 2.4. ARs without thin film coating show a reflectance of between 10% to 20%. Adding thin film coatings in the form of SLAR or DLAR has reduced the reflectance value to $1\% - 15\%$. In comparison to

DLAR structures, micron textured coatings show a better anti-reflectivity with optimum value between $0 - 5\%$ in a wider bandwidth.

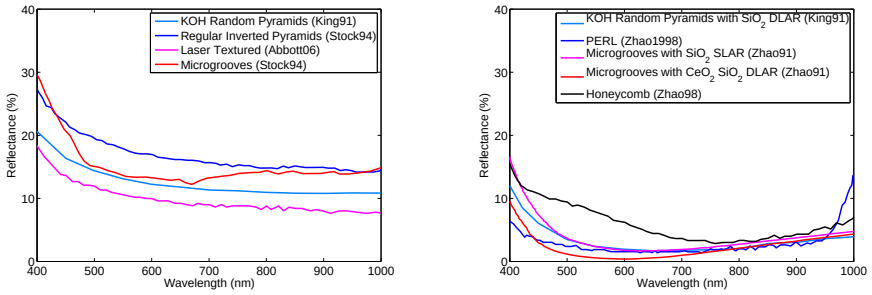

(a) (b)

FIGURE 2.4: Normal incidence hemispherical reflectance of micron textured anti-reflectives (a) without thin film coating and (b) with thin film coatings. Data is taken from literature (King91 [41], Stock94 [87], Abbott06 [7], Zhao98 [103], Zhao91 [101]).

The progress made within anti-reflectivity of silicon solar cells employing micron texturing was good enough to achieve the most efficient crystalline silicon solar cell of inverse pyramid with DLAR coating (PERL) [30, 103]. However, the amount of material etched/removed away from the top of the silicon solar cell is considerable and thus this technique cannot be used for thin silicon solar cells. Also the reflectance of these structures increases with the angle of incidence which is not favourable in solar cells.

2.2.3 Sub-Wavelength Structures

Another approach to suppress the surface reflectance of silicon solar cells is to texture the silicon top surface of the cell with textures of dimensions less than the incident wavelength. These structures are called Sub-Wavelength-Scale structures (SWS) and are explained by Effective Medium Theory (EMT) [46]. The sub-wavelength textures decrease the discontinuity between the two interface by making the textured surface appear blurred to the incident light. The textured surface has an effective refractive index which is the ratio of the volume fraction of the substrate material to the air. In the case of textures of tapered profile, the effective refractive index of the intermediate layer (textured layer) gradually increases from the low refractive index medium to the high refractive index medium. It is easier to imagine there are an infinite number of very thin layers in the intermediate layer, each with a different effective refractive index which increases from the tip of the tapered textures to the bottom. As the light passes through the layer with gradually increasing refractive index, less reflectance takes place.

The fabrication of SWS structures normally include etching to produce a regular array of textures using lithographic or metal masks [80, 89], and chemical etch or reactive ion etch in a maskless procedure to produce random textured structures [36, 81, 79, 45]. The reflectance of the textured layer depends on the shape of features and aspect ratio (height

to spacing of features) which has produced computational optimisation of textured layer in several studies [80, 19].

Various experimental studies of SWS structures were performed previously. Schnell *et al.*[81] fabricated random SWS textures which showed a total reflectance below 5%. Employing this structure as a solar cell coating increased the efficiency of the cell by 2.4% (10.9% in comparison to 8.5%). However, the SWS structure increased the surface area of the solar cell which caused an increase in the surface recombination and decreased the efficiency. Ruby *et al.*[79] employed another etch process and fabricated a similar SWS structure with similar reflectance but with an efficiency of 17.1%. A structure of randomly arranged pyramids of $300 - 400$nm height and 100nm periodicity, gave a surface reflection of 3.6% and lower and an increase of $3.2 - 3.8\%$ in the solar cell efficiency [80]. There is also a structure of random texturing which has zero reflectance, however how well this reduction of reflectance has contributed to the solar cell efficiency is not reported [97].

A problem with random textured SWS structures is the fact that the textures are mainly produced by an etching process. The degree of control over the etching process is not high and hence the control over the shape and spacing of the textures is not controllable. Since the reflectance of sub-wavelength structures is dependant on the periodicity, height and shape of textures, the re-production of the same reflectance behaviour of a SWS structure is not controllable either. Employing a lithographic mask or a metal mask provided more control in the production of a repeatable fabrication process. A successful example of masked fabrication of SWS texturing is the work by Koynov [45] in which reflectance is reduced to $< 5\%$ and the cell efficiency is increased by $36 - 42\%$ in multi-crystalline and tri-crystalline silicon solar cells.

Figure 2.5, shows the reflectance of experimentally studied sub-wavelength structures on silicon. In general the reflectance of silicon surfaces is reduced to as low as 5% using the sub-wavelength texturing. However the influence of SWS structures on the solar cell performance is different from its anti-reflective properties. Moreover, the fabrication techniques are somewhat expensive compared to other AR structures and thus needs more study. The study of employing sub-wavelength structures within the field of solar cell anti-reflectives is an emerging field which is still in the development stage. If the problem of cell efficiency affected by high aspect ratio is solved, these structures will have great potential to be used for solar cell anti-reflectives.

2.3 Nature's Solution

The discovery of anti-reflective structures in insects eyes took place while studying the compound eye's of insects [56]. The study of the underlying anti-reflective mechanism of these natural structures revealed their potential as anti-reflectives in industry and

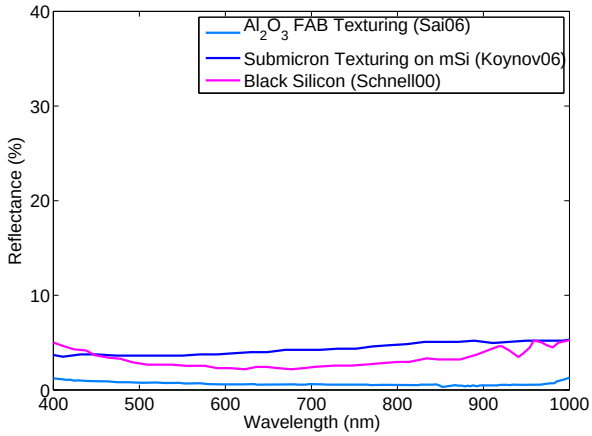

FIGURE 2.5: Normal incidence hemispherical reflectance of sub-micron textured anti-reflectives. Data is taken from literature (Sai06 [80], Koynov06 [45], Schnell00 [81]).

science. The rest of this chapter focuses on moth-eye structures and the studies and discoveries performed to date.

2.3.1 Moth-eye Structure

The moth-eye structure was first discovered by Bernhard, Miller and Moller through their studies on the corneal surface of the eyes of a night moth [13, 11]. Electron microscopy of the cornea revealed that the surface is covered by a number of visual units called ommaditia with a diameter of $15-40\mu$m (Figure 2.6(b)). Each ommaditia is also covered by a large number of minute protuberances, which can only be detected using electron microscopy. The protuberances detected were roughly conical in shape, approximately 200nm tall and arranged in a hexagonal lattice with a center-to-center distance of 200nm (Figure 2.6). Bernhard and colleagues called the protuberances "nipples" and the structure a "nipple-in-air" array [13]. Since the protuberances are smaller than the wavelength of light in the visible regime, they are also known as "sub-wavelength" structures.

The functionality of "nipple-in-air" arrays was studied by two methods: transmission and reflection measurements using a microwave model and spectrophotometric measurements [13, 11]. Nanoscale fabrication techniques in 1960s were not as advanced as today thus fabricating a nipple-in-air array at its actual scale (200nm height and 200nm spacing) was not possible. Instead, a replica of this structure was fabricated on a larger scale to be used at microwave wavelengths. Transmission and reflection measurements of this replica showed that the existence of the protuberances increases the transmission of waves through the structure and decreases the surface reflection. By matching these results to the actual dimensions of the nipple-in-air array it was concluded that the nipples also increase the transmission and reduce the reflection in the visible regime.

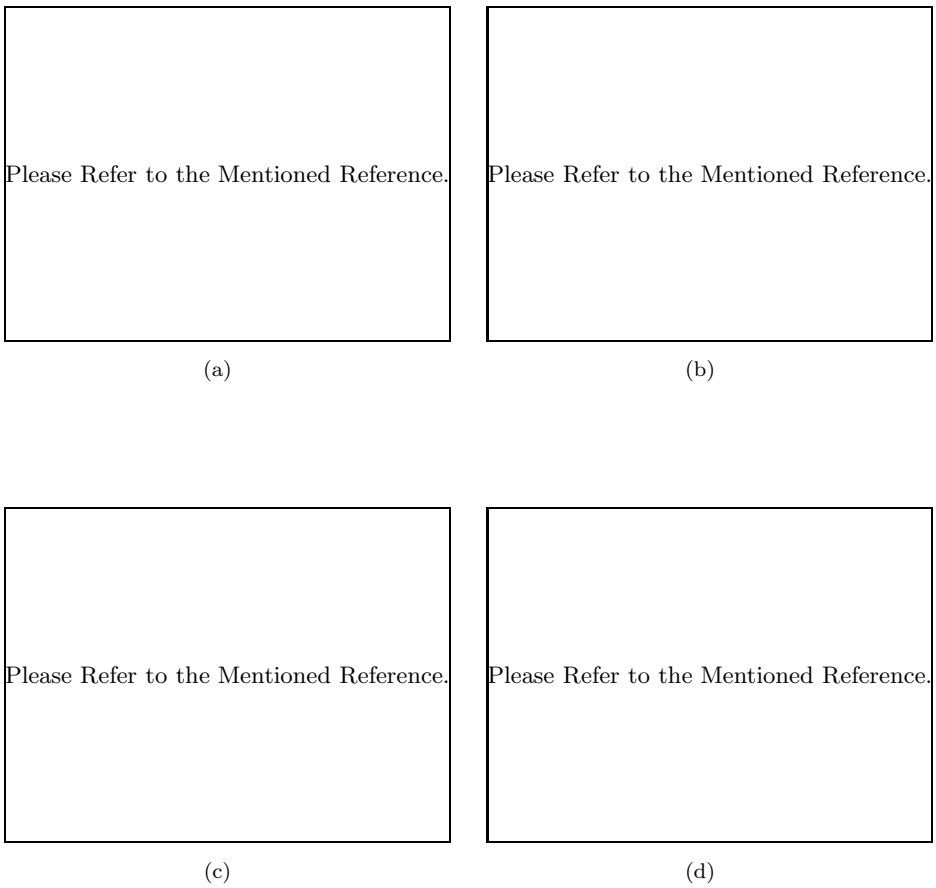

FIGURE 2.6: Scanning Electron Micrograph of (a) the moth eye cornea, (b) ommatidias at the surface of the cornea, (c) protuberances of adjacent ommatidia and (d) protuberances within a single ommatidia ([11])

A spectrophotometric measurement of the cornea with nipple-in-air array, compared with the smooth-surfaced cornea of a grasshopper, supported the microwave results. Microscope images of the nipple-in-air array were also used to study the functionality of this structure. Images of a cornea with nipples were darker compared to a smooth surfaced cornea, which is again a confirmation of low reflection of the surface covered with conical protuberances.

Bernhard and co-workers also modelled the structure mathematically [13, 11]. In their model they replaced the nipple-in-air layer with multiple homogeneous layers with varying refractive indices. The refractive index of the nipple-in-air array layer changes from 1 of air to 1.57 of chitin, the material of the cornea. This is a result of the conical shape of the protuberances giving 0% material at the tip and 100% material at the base. The refractive index transition was modelled by dividing the nipple-array structure into 20 horizontal layers of equal thickness. For each layer the refractive index was calculated for a number of wavelengths. The reflection of the structure at normal incidence was

calculated. The reduction of reflection of nipple-array structure was compared with the reduction of reflection of a quarter wave stack with half the height of nipple-array structure. The nipple-array structure showed better anti-reflectivity over a wider bandwidth. The results also agreed well with the comparative spectrophotometric results of the grasshopper eye and moth eye.

Bernhard also performed a very extensive study on the eyes of other species of nocturnal insects and found similar nipple-array structures. However, the structures differ in topography having different height and arrangement of protuberances. Bernhard used the height (h) to group the nipple-array structures into three classes: class I with minor protuberances ($h < 50$nm), class II with low-sized protuberances ($50 < h < 200$nm), and class III with full-sized protuberances ($h > 200$nm). His studies also showed that the protuberances in class II and III are arranged in a hexagonal lattice, while class I has both irregular and regular hexagonal arrangements [12]. Bernhard also studied the distribution of these three classes in various insect orders including moths and butterflies. The results have helped in understanding the functionality of nipple-array structures in insects and the progress of evolution. He also showed that these three classes of nipple-array also exist in some species of butterflies, although with a density much lower than in moths. Following Bernhard's classification, Stavenga and others[85] performed a similar study on many species of butterflies and observed the same three classes of nipple-array structure (Figure 2.7). However, they performed additional mathematical studies on the performance of nipples in relation to their shape, height and the incident wave polarisation which will be discussed later.

The nipple-in-air array has also been observed on both sides of the wing of a hawk-moth, Cephonodes hylas, making them transparent to the eyes of predators (Figure 2.8). Yoshida *et al.* [98, 99] reported the height of the nipples to be around 250nm and their center-to-center spacing to be around 200nm, an arrangement almost identical to that of the moth-eye structure. The spectophotometry results of smooth wings compared to rough wings also showed more reflection for the case of smooth wings. A reflectance measurement from the surface of this structure showed that the wing of the Cephonodes Hylas Hawk moth gives a reflection of less than 2% for wavelengths from $200 - 800$nm. Although the nipple-in-air array has also been observed on the wing of this and many other species, it is typically known as "Moth-eye" structure since it was first seen on the eyes of moths. The same terminology is used throughout this work.

Andrew Parker *et al.*[71] found a different anti-reflective structure, similar to the moth-eye structure, and called it a fly eye grating. This structure was first seen in the surface cornea of Eocene Dolichioidid dipteran from Baltic Amber (45 million years old) and consists of parallel ridges with a sine wave profile. The ommaditia of this insect are curved and so the ridges have a slight angle with respect to each other, which is known to result in angle independent reflection. They have also found a combination of moth-eye protuberances and fly eye gratings on other species of insects (Figure 2.9).

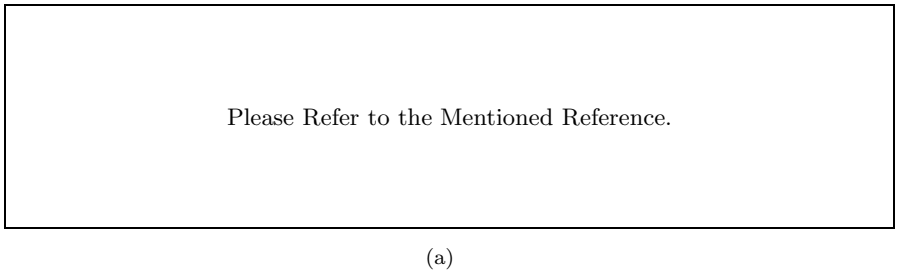

(a)

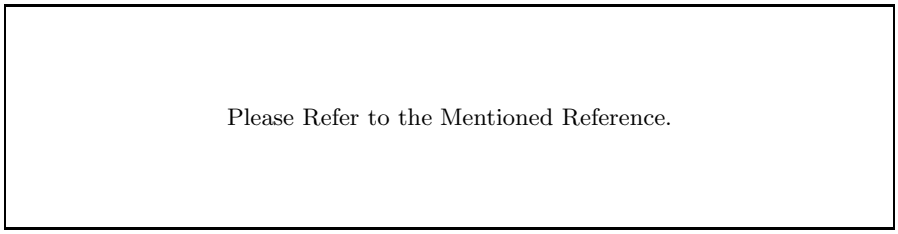

(b)

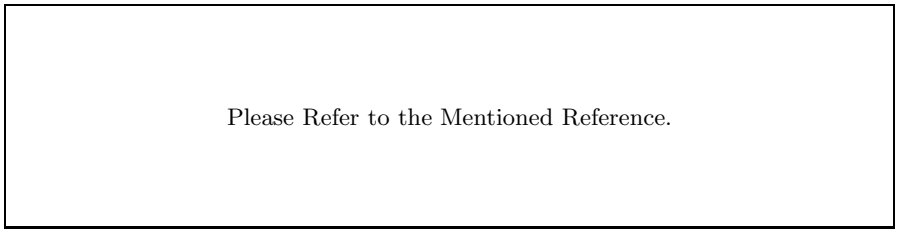

(c)

FIGURE 2.7: Scanning Electron Micrograph of the moth eye structure on butterfly eyes: (a) Bicylus anynana (class III), (b) Pseudozizeeria (class II), and (c) a Papilionid Papilio xuthus (class I). Scale bar:500nm [85].

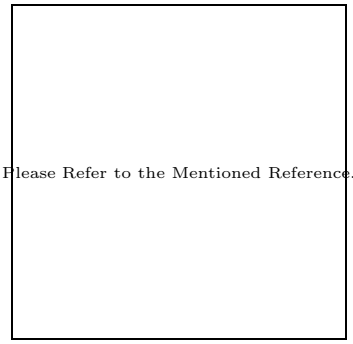

(a)

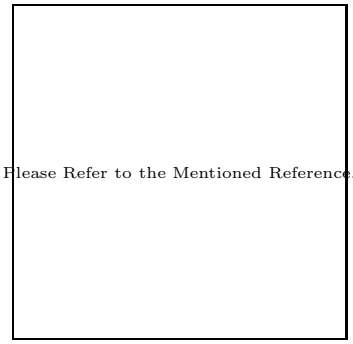

(b)

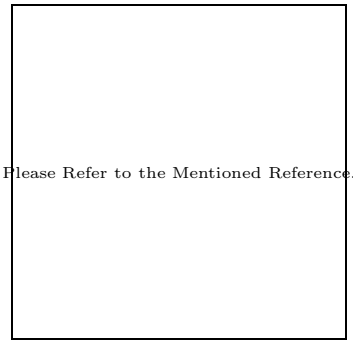

(c)

FIGURE 2.8: (a) Photograph of the hawkmoth Cephonodes hylas. Scanning electron micrograph of the transparent part of the wing (b) Top view, (c) Side view. Scale bar:1μm [99]

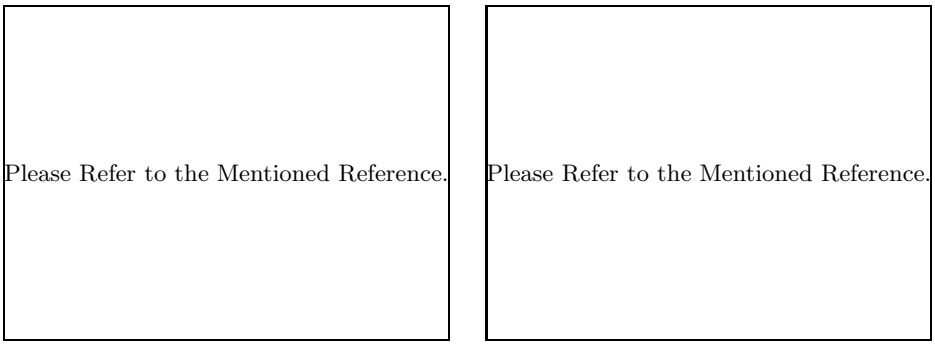

(a) (b)

FIGURE 2.9: (a) SEM image of Eocene dolichioidid dipteran (Scale bar:3μm) (b) SEM image of Z-minor Diptera. "g" shows fly eye grating area and "p" shows protuberances similar to the moth-eye structure (Scale bar:2μm) [71]

The nipple-in-air array is usually seen in the cornea of nocturnal insects. Thus it is thought to help the visual capacity of these insects by resulting in less internal reflection and an increased light transmission into the eye. It is also known that the structure is useful for the purpose of camouflage. For example when moths are resting with folded wings, the minimised reflection from their eyes keeps them safe from predators [13, 11]. The nipple-in-air array has been observed in many species of nocturnal insects like night moths, netwings and caddis flies. Some butterflies also have the same structure covering their cornea [11, 12, 85].

2.3.2 Theoretical Study

Bernhard performed a mathematical study of moth-eye structure, replacing the nipple-array with a stack of individual homogeneous layers of equal thickness producing a varying refractive index from tip to the base of protuberances. Basically, the conical shape of nipples provides a gradual change of refractive index from tip of the nipples to the base. The incident light can transmit through the slow refractive index change without encountering an abrupt change in media and therefore reflection is minimised. This is the basis of the use of effective medium theory [2] used to model the optical behaviour of moth-eye structures [46]. In this method the nipple-array is divided into a number of thin layers in the direction perpendicular to the plane of periodicity. Each layer is assigned an effective refractive index corresponding to the volume ratio of two different media in the layer. Using this simplified structure the reflection and transmission properties of the structure are calculated through Maxwell's Equations.

In a multilayer structure the reflected light is a superposition of waves reflected from many interfaces. Light propagating through the structure hits layer interfaces at different depths, which give reflected waves of different amplitude and phase. Depending on

[2] Also known as homogenisation

the height of the layer, h, and the wavelength of the light reflected waves interfere destructively giving the net reflection of zero. The reflection of the structure varies in response to the value of $^{h}/_{\lambda}$ in which λ is the wavelength of incident light [77, 23, 50, 95]. The plots in Figure 2.10 show theoretical results of the variation of reflectance with $^{h}/_{\lambda}$. When $h \ll \lambda$ the surface looks like a sharp interface to the incoming wave and the reflection is as of a discontinuous interface calculated by the fresnel's equation. As h increases it reaches a point where the reflection is zero (at $^{h}/_{\lambda} = 0.4$). From here, increasing h keeps the reflection still very low (far less than 1%) but with modest fringes. Further, when $h \gg \lambda$ the reflection still stays very small. When the effective refractive index profile of the structure has a shape different from that of Figure 2.10(a) there exist small differences (Figure 2.10(b)) but the overall conclusion is the same: There will be a noticeable reduction of reflection in a structure for which the thickness of the layer is about half or more of the wavelength. Thus in order to keep the reflection constantly low ($< 0.5\%$) in a graded index structure, h should be designed so that the wavelength of the incident light is smaller than $2.5h$. This helps to design a structure for a specific wavelength range; in the case of moth-eye structures which work in the visible regime, the height of the protuberances should be larger than 250nm.

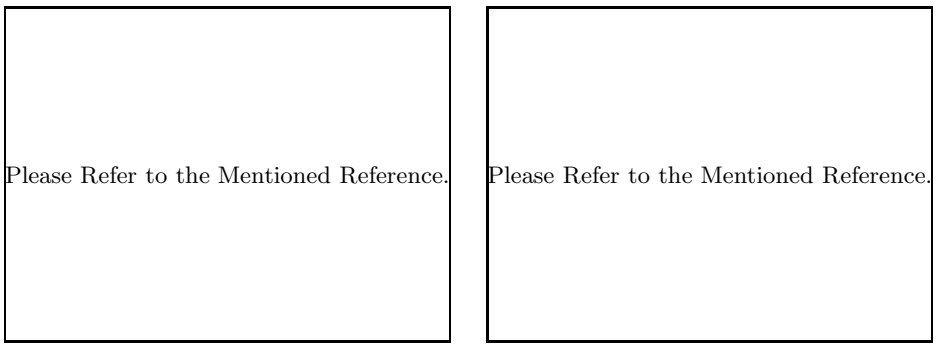

(a) (b)

FIGURE 2.10: Reflection vs thickness to wavlength ratio reported by (a) Clapham and Hutley [23] (b) Lowdermilk and Milam [50]. (The difference in the curves comes from the difference in the profile of the effective refractive index.)

The other important design parameter for a moth-eye structure with a specific application is the spacing between adjacent protuberances. Primarily, this value in the moth-eye structure has to be small enough to prevent the moth-eye acting as a diffraction grating. Equation 2.3 is the diffraction grating equation [61]. In this equation d is the periodicity within the structure, θ_m is the angle of the reflected beam, θ_i is the incident angle, λ is the wavelength of light, and m is the diffraction order (integer values). It is desired to suppress all the diffraction orders except $m = 0$.

$$\sin\theta_m = \sin\theta_i + m\frac{\lambda}{d} \tag{2.3}$$

Considering light at normal incidence, $\theta_i = 0$, the grating equation will be

$$\sin\theta_m = m\frac{\lambda}{d} \tag{2.4}$$

To suppress the $m = 1$ order, $\frac{\lambda}{d}$ has to be more than unity which gives $d < \lambda$. Having this condition the first order is also suppressed even at oblique incident angles. However, there is a possibility of having $m = -1$ orders for negative θ_m. In this case to suppress the $m = -1$ orders $\frac{\lambda}{d} > 2$, which requires d to be smaller than $\frac{\lambda}{2}$. Thus to suppress all diffraction orders and to have the least reflection for the zero order diffraction according to Rayleigh theory, the dimension of the nipple array (height of nipples, h, and centre-to-centre distance of each nipple, d) has to fulfil the requirements in Table 2.1. According to this table the widest bandwidth is available in the presence of the smallest spacing and the largest height.

	Normal Incidence	Oblique Incidence
No Diffraction Zone	$d < \lambda < 2.5h$	$2d < \lambda < 2.5h$

TABLE 2.1: Optimal dimensions of a moth-eye structure in visible regime to suppress diffraction orders.

The effective medium theory provides a computationally simple and cheap method of studying the optical properties of moth-eye structures but it also has limitations. It was shown that for highly modulated structures the nipple-array stops acting like a homogeneous layer and thus EMT is not capable of producing a close approximation to the moth-eye structure [46]. Moreover, the effective medium theory is not capable of predicting the diffraction grating behaviour while studying moth eye structures of different dimensions. This is due to the fact that EMT does not consider the spacing between the protuberances.

Thus there was a need for a different method of mathematical study for the moth-eye structure. Attention turned towards rigorous methods, the most well known and widely used of them being Rigorous Coupled Wave Analysis(RCWA) [59, 61]. Rigorous refers to the fact that there is no approximation and simplification employing Maxwell's Equations to form coupled-wave equations of differential form. The coupled-wave method is commonly used in studying the efficiency of diffraction modes in 2D planar grating structures. Since the moth-eye structures are similar to 2D planar gratings, the same method can be used to study the behaviour of the structure. Coupled wave analysis explains the field inside the modulated area with coupling waves of forward and backward direction. The boundary conditions of Maxwell's equation are then applied to the boundary of the modulated area with the surrounding area of air and substrate. These equations are solved by finding the corresponding eigenvalue and eigenvectors.

RCWA was first used to calculate the diffraction efficiency of 2D grating structures with block or cylindrical protuberances. For more arbitrary profile shapes like conical shapes a method of dividing the profile into a stack of thin layers (staircase approximation) was used. Thus solving the eigenvalue problem for a number of thin layers in the modulated area leads to an expensive numerical method in terms of computational time and memory. Nevertheless, RCWA has been extensively used to perform numerical studies of moth-eye structures. Sun [88] used RCWA to design and fabricate a silicon moth-eye structure with 420nm periodicity and 800nm height which showed 2.5% reflection within the visible spectrum ($400 - 800$nm). Lalanne and Morris [47] also fabricated silicon moth-eye structures of 260nm periodicity and 80nm thickness and their experimental results were found to agree with their numerical results. Also, in a comparison with a single thin-film anti-reflection layer, their moth-eye structure showed similar values in reflection reduction. Min [57] used RCWA to calculate the reflection of a GaSb moth-eye structures to be less than 2%. In a more extensive study, Mirtznik and colleagues[58] implemented a direct pattern search optimization method using RCWA in order to find the optimum moth-eye structure in the millimetre wave frequency range. Boden and Bagnall [17] used RCWA to study the effect of altering periodicity, height and shape of the protuberances on the reflection of moth-eye structures. Other examples of numerical studies of moth-eye structures using RCWA include Toyota and colleagues on fused silica [91], employing moth-eye structures to increase the light efficiency of LEDs [39, 40] and the work by Chuang *et al.* [22] in which they concentrated on the inverse polarisation behaviour of moth-eye structures as opposed to their anti-reflectivity properties.

In other studies, the shape of the protuberances was shown to play an important role in decreasing the reflection. The profile of protuberances affects the distribution of the refractive index within the modulated area. Southwell [83] has studied the reflection of refractive index distributions of linear, cubic and quintic functions and has shown the lowest reflection comes for a quintic function of refractive index as shown in Equation 2.5.

$$n = n_i + (n_s - n_i)(10t^3 - 15t^4 + 6t^5) \tag{2.5}$$

In another study, Southwell implemented this equation for different refractive indices [84]. For glass with a refractive index of 1.52, the shape of protuberances giving a quintic refractive index profile is a flat sided pyramid. For materials with higher and lower refractive index the curvature of the faces change, as shown in Figure 2.11. Stavenga *et al.*[85] also performed a similar study. They compared conical, Gaussian and parabolic shaped protuberances. In their study they concluded that tall paraboloid protuberances and a close-packed arrangement provided the least reflection for normal incidence within the visible regime. However, they concluded that the shape of the protuberances plays the least role in the amount of reflection and it is the height of protuberances which plays the main role while the spacing between the protuberances is the second most important

factor. These studies were all based on the use of an effective refractive index for the nipple-array layer and EMT. Boden and Bagnall [17] have used RCWA to show that the moth-eye structure can be optimized for use within an arbitrary range of angles and wavelengths if the height, spacing and base of the protuberances are tuned accordingly.

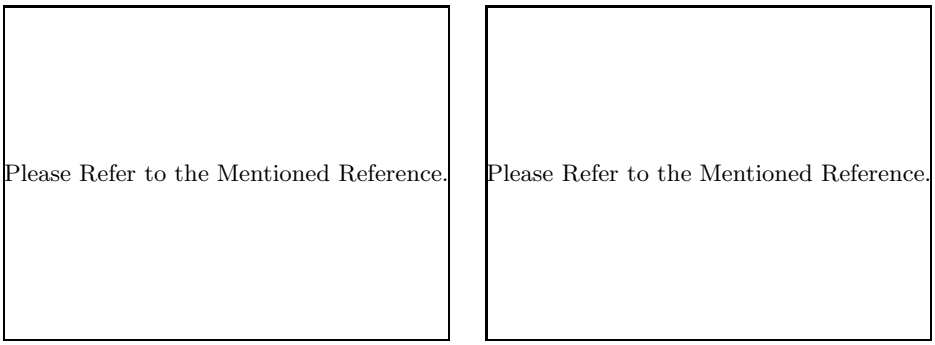

(a) (b)

FIGURE 2.11: Optimised moth-eye protuberances quintic function for (a) glass ($n = 1.45$) and (b) silicon ($n = 3.42$) [84]

2.3.3 Fabrication

The anti-reflective property of moth-eye structures has attracted the attention of the optics, photonics, physics and electronic communities. However, fabricating the moth-eye structure of sub-wavelength dimensions for visible applications was almost impossible in the 1960s and 1970s. As fabrication techniques have improved, many replications of the moth-eye structure have been produced. Many fabrication methods have been attempted. The four most widely used fabrication techniques are reviewed here. A brief explanation of each technique is given along with a detailed example. For each method a few successful examples of fabrication and optical results are presented.

2.3.3.1 Holographic Lithography

The first effort to make a moth-eye structure was by Bernhard who designed structures to work in the microwave spectral range[11]. The model was made from a mixture of beeswax and paraffin in order to achieve a refractive index close to chitin. However, the first fabricated structure to operate in the visible range was made by Clapham and Hutley[23] using interference holography. They used the interference fringes at the intersection of two collimated krypton laser beams (wavelength 351nm) at an angle of 120° to produce sinusoidal protuberances in photoresist on a glass substrate (The photoresist had a refractive index similar to glass). The sinusoidal intensity variation of the beams produced sinusoidal grooves in the photoresist. Thus this technique is only applicable for plane surfaces. The structure had a refractive index of 1.6 and the spacing between protuberances was approximately 210nm. The glass was rotated 90° between

the two exposures. The reflectance of the structure in wavelength range of $400 - 700$nm at normal incidence was measured to be below 0.5%.

For this technique the spacing between the protuberances depends on the spacing between the fringes produced by the intersecting laser beams:

$$d = \frac{\lambda_0}{2 \sin \theta} \tag{2.6}$$

where,

d is the spacing between protuberances

λ_0 is the wavelength of the laser

θ is half the angle of the interfering laser beams.

With the maximum possible angle between the two laser beams, they calculated the minimum value of d as $0.6\lambda_0$, which corresponds to an angle of 120° between the beams. Thus for the krypton laser beam, 210nm is the minimum spacing which can be fabricated. The depth of the grooves, h, is harder to control. The depth varies with the exposure time and the response of the photoresist to the exposure (photoresist is more sensitive at shorter wavelengths). Thus there is a limitation to the ratio of $\frac{h}{d}$ which makes the change of h and d strictly dependent on each other. This is a limitation to this technique especially for making taller protuberances that improve the anti-reflectivity performance of moth-eye structures. Later, they also used an argon ion laser (wavelength 458nm), which produced a similar structure with a minimum spacing of 275nm [95]. The moth-eye structures they fabricated had a different periodicity and depth and showed reflectance values lower than 3%.

Wilson and Hutley [95] also introduced the idea of using a metal replica to transfer the pattern into photoresist. However, in some cases separating the master and the replica was hard and caused damage to the master.

In a comparison between the performance of a fabricated moth-eye structure and a commercial multilayer they showed that such a structure could be a replacement for commercial anti-reflective layers. However, the cost of the technique at that time for mass production and the nature of photoresist made it unsuitable for many applications, such as anti-reflective coatings for high quality optical components, mass produced plastic components, and solar energy. Thus they were hoping that improvements in fabrication techniques and material properties could solve the problems with the delicate photoresist and make the technique more suitable for the target applications.

Later, this technique was used to transfer the moth-eye pattern to substrates made of other materials like glass[62] and silicon[47]. Firstly, the substrate needs to be coated

with a certain thickness of photoresist. The resist is exposed with the two intersecting coherent UV lasers to transfer the pattern of the optical standing wave on to the resist in one dimension. Then the substrate is rotated 90° in order for the pattern to be transferred in the second dimension. Then by means of reactive ion etching the pattern is transferred to the silicon. Finally the remaining resist is removed by immersing the substrate in acids.

Lalanne[47] used the same technique to create a moth-eye pattern on silicon working in the visible regime. However, they used an intermediate layer of SiO_2 between the substrate and resist. This layer ensures that the grooves could be etched deep enough into the photoresist. Not having the intermediate layer limits the thickness of the photoresist layer and also the depth of the grooves which can be transferred onto silicon. Above that limit undercuts take place in the photoresist layer requiring a selective etching of the photoresist from silicon. Since there is not such a technique they have employed an SiO_2 layer as high as the desired protuberances to prevent this problem.

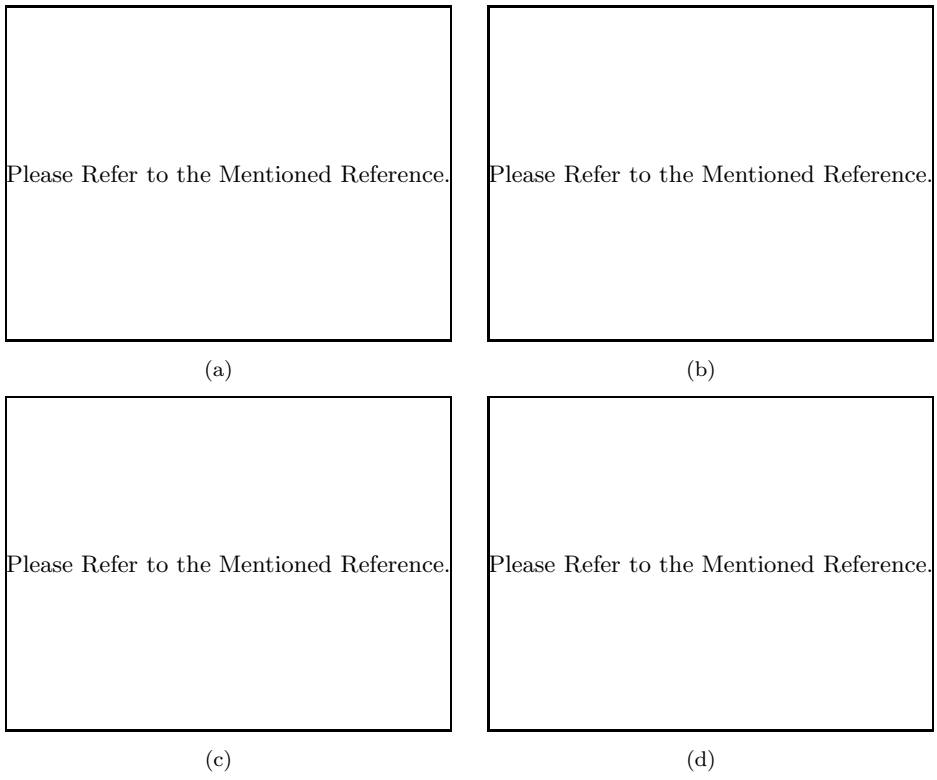

FIGURE 2.12: SEM image of moth-eye structures,(a) made by Holographic interference in silicon(scale bar=1μm)[47],(b) Fabricated by E-beam Lithography in silicon(scale bar=750nm) [38],(c) made by E-beam Lithography in fused silica(scale bar=100nm)[91] (d) made by nanoimpriting in silicon (scale bar 200nm) [100]

The SEM images showed a successful fabrication process (Figure 2.12(a)). This moth-eye sample was compared to a quarter-wave thin film coating on silicon and showed a mean reflection lower than the coated silicon for a wavelength range of $400 - 1000$nm. At $\lambda = 632.8$ nm, the specular reflection of the structure is as low as 1% for incident

angles less than 50°. Furthermore, they reported that the reflection from their moth-eye structure was insensitive to azimuth angle and polarisation. However, in this technique the fast development of the resist prevents the formation of protuberances with a wide diameter at the base, whereas experimental work has shown that a high value of the width of $\frac{h}{d}$ decreases the reflection of the structure. Therefore, when aiming to fabricate high efficiency moth-eye structures this technique is not the best option.

The minimum feature of the final pattern made by holographic lithography is determined by equation 2.6 and depends on λ_0 and θ. According to equation 2.6, the limit to the periodicity is $d = \frac{\lambda_0}{2}$. A patent for the invention of a machine that performs holographic lithography claims θ can be fixed to a maximum of 60°, giving a minimum periodicity of $d = 0.57\lambda$ [9]. This technique is capable of producing structures with a periodicity of 200nm to 4μm and a minimum feature size of 100nm [52]. However, the minimum feature size of techniques like Electron Beam Lithography and Nano-imprint Lithography is even smaller. The other disadvantage of this technique is that it is limited in the design of the protuberances and arrays. Additionally, the height of the grooves and the periodicity depend on each other so the height is limited by the thickness of the resist and the etching ratio of the substrate to resist. However, by using metal replicas or embossing, it is possible to fabricate large areas of the structure at low cost. Thus for structures with a minimum feature size of 100nm and a lattice geometry that can be made by interfering beams (square or hexagonal lattice), holographic lithography is favoured.

2.3.3.2 Electron Beam Lithography

Another technique to make moth-eye structures is electron beam lithography. Figure 2.13 shows a general schematic of this technique. The substrate is coated with a layer of resist. There are two types of resist: positive and negative. If negative resist is used the non-exposed resist is removed. After the resist is developed (removed by exposure and chemical treatment) the pattern is transferred into the substrate by means of etching. The type of the etching process plays an important role on the shape of the transferred pattern. After etching, the remaining resist is removed using an acid wash.

A number of silicon moth-eye structures have been made by e-beam lithography. Kanamori used an e-beam lithography technique along with SF_6 Fast Atom Beam(FAB) etching [38]. They utilised the anisotropic nature of the FAB etching technique to produce deep structures. A 400nm positive resist was deposited on a 200μm thick silicon wafer. A 1.2mm×1.2mm area was exposed with the e-beam machine for about 10hrs to write the pattern into the resist. After developing the resist, the wafer was etched with SF_6 FAB etching and thus the pattern transferred to the silicon. The remaining resist is removed by immersing the wafer into an equal parts solution of H_2SO_4 and H_2O_2. The protuberances have sharp conical shapes with a periodicity of 150nm and height of 350nm (Figure 2.12(b)) Their structure showed a large reduction of reflection within the visible

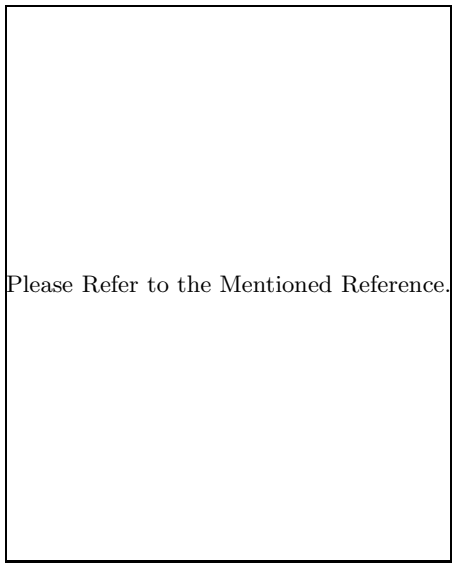

FIGURE 2.13: Fabrication process of E-beam Lithography [38]

regime compared to silicon (less than 3%). Also, at a wavelength of 632.8nm, reflection of s-polarized light at angles of incidence from $5-80^{\circ}$ is lower than that of the silicon. The p-polarized reflected light is also lower than silicon, but only up to an incidence angle of 65°.

Employing different etching processes, removing the resist by means of different etching processes or a lift off process, or adding more layers as an etching mask to the process makes it possible to fabricate moth-eye structures in different materials. Toyota *et al.*[91] used electron beam lithography along with reactive ion etching and a chrome disk array as an etching mask to make moth-eye structures in fused silica. Their structure had conical protuberances with a 250nm periodicity and 750nm height (Figure 2.12(c)). It showed reflection of less than 0.5% for wavelengths of $400-800$nm at normal incidence and 3% for the angle of incidence range of $5-55^{\circ}$ at 632.8nm.

Boden *et al.*[15] made moth-eye structures employing e-beam lithography with dry etching and a dry oxidation at the end, to smooth the surface of the structure. The process they followed starts with spinning a negative resist on silicon substrate. Exposing the desired resist regions removes the resist and thus a resist mask of a hexagonal array of circles was defined. A HBr/Cl_2 dry etch is then performed to produce the tapered profile in the silicon, before stripping the resist. At the end, the structure is dry oxidized to remove the damaged parts of the silicon caused by etching, and to make the surface of the protuberances smoother. They fabricated a number of moth-eye structures with a variety of dimensions and profile shapes in 1mm×1mm area samples. The best moth-eye sample showed reflection of 1% at normal incidence for the wavelength range $520-920$nm and had a height of 450nm and a periodicity of 200nm. It also exhibited a reflection less than 5% for angles of incidence up to 50°.

E-beam lithography provides a smaller minimum feature size compared to holographic lithography. However, the writing process even for small areas takes a long time. Thus this technique is expensive in terms of time and equipment.

2.3.3.3 Nano-imprint Lithography

Making large scale samples using e-beam lithography is expensive and time consuming. Nano-Imprint Lithography(NIL) is a relatively new technique alternative to e-beam lithography [38]. This is a cheaper technique which uses a stamp to transfer the pattern onto a substrate. With the correct coating for the stamp it can be preserved and used many times, making this technique scalable [90].

The fabrication technique starts by making the stamp. The stamp is fabricated by means of ebeam lithography for features smaller than 200nm or optical Interference Lithography (Holographic Lithography) for bigger features. Then it is pressed onto a heated substrate, which is covered with a suitable thickness of polymer. After pressing the stamp with the correct amount of pressure and cooling the substrate, the stamp is removed. The pattern on the polymer is then transferred into the substrate by dry etching. The remaining polymer resist is removed by chemical means. The minimum feature size in this technique is determined by the features on the stamp. However, a minimum feature size of 10nm has been achieved using nano-imprint lithography with e-beam lithography to make the stamp. Since the stamp can be used many times the time needed to make the stamp by e-beam lithography is not that much of a concern. Figure 2.14 shows the stages of fabrication in this technique.

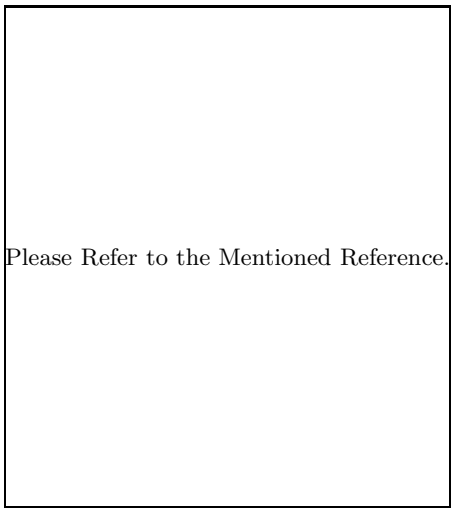

FIGURE 2.14: A schematic of the general Nano-imprint Lithography fabrication method [53].

In an attempt to make anti-reflective silicon layers, Yu *et al.*[100] fabricated silicon moth-eye structures by means of trilayer nano-imprint lithography and a lift off. In their process, a nickel mask of pyramids is made by means of trilayer photoresist nanoimprinting

lithography and lift off. Reactive ion etching (CHF_3/O_2) was then used to etch the underlying substrate through the mask to give a conical moth-eye array with 200nm period and 250nm groove depth (Figure 2.12(d)). This moth-eye structure exhibited a reflection of less than 1% at normal incidence within the visible regime ($400 - 800$nm). Also, at a wavelength of 632.8nm their structure showed a reflection of less than 3% for angles of incidence less than 65°.

Boden *et al.*[18] also fabricated silicon moth-eye structures by means of nano-imprint. They employed dry etching processes to produce protuberances similar to moth-eye structures on 1cm×1cm samples. Reflection was as low as 10% for incident light in the visible regime.

Using the same technique, moth-eye structures have also been fabricated on glass [10, 32, 31] and GaAs [33].

Nano-imprint lithography has the advantage of large scale fabrication along with small feature sizes as small as e-beam lithography. However, like e-beam lithography, the control over the shape of protuberances is still very poor, and remains dependent upon the etching process.

2.3.3.4 Nanosphere Lithography

The nature of some materials makes it hard to use fabrication techniques described above. Thermal mismatch between the substrate and coatings is one of these issues. Also, for some applications, the moth-eye structure only works efficiently for a narrow range of wavelengths, which makes the fabrication technique expensive for such a low throughput. Thus a cheaper technique is desirable to transfer the pattern into the substrate. One approach is to use nanospheres as masks to transfer the pattern directly to the substrate. In this technique the arrangement of nanospheres is due to self assembly (a number of spheres on a flat surface form a hexagonal lattice). This is a bottom-up technique, which does not include the expensive pattern writing of e-beam lithography. Thus in the sense of equipment it is much cheaper compared to previous techniques. In general, the fabrication process follows the stages in Figure 2.15. At the first stage, a monolayer of nanospheres is deposited on the substrate. The size of the nanospheres is tailored according to the desired feature size. The next process is etching the substrate to produce the hexagonal pattern of protuberances in the substrate. There may be a need to add additional etching steps to smooth the profile of the protuberances.

Sun *et al.*[88] employed monolayer silica colloidal crystals with non-close-packed structures as masks to etch the silicon and produce moth-eye shape protuberances. A spin-coating technique is used to create the non-close-packed arrangement of 360nm silica spheres on silicon. Then a SF_6 dry etch was performed to etch the underlying silicon

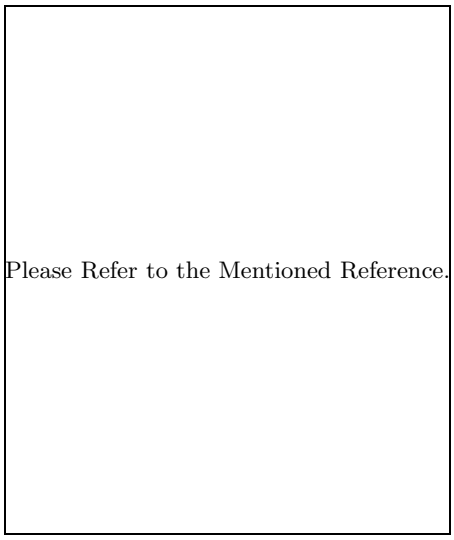

FIGURE 2.15: Fabrication steps of Nanosphere Lithography to produce moth-eye structures [22].

through the nanosphere mask. The etching time determines the height of the protuberances. At the end, the remaining silica particles are removed by a hydrofluoric acid wash. The protuberances have a height of 800nm and a base radius of 210nm (Figure 2.16(a)). Their pattern showed reflection of less than 2.5% for a wavelength range of $400 - 800$nm. Chuang *et al.*[22] used the same technique to produce silicon moth-eye structures. One of their best samples had a base diameter of 90nm and a height of 150nm and showed a reflection of less than 5% for incidence angles from $5 - 70^{\circ}$ at $\lambda = 632.8$nm. The same technique has been used to make GaSb moth-eye structures to be used in thermophotovoltaic applications [57]. The fabricated structures were etched for 2.5min and showed a reduction of reflectance from 35% for the GaSb flat surface to just 2% for the etched surface.

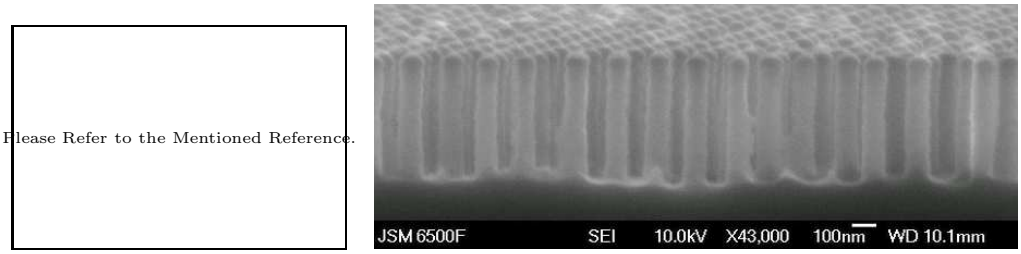

FIGURE 2.16: SEM image of moth-eye structures made by Nanosphere Lithography in silicon,(a) by Sun et al. [88],(b) by Stavroulakis (The image is a courtesy of Mr Petros Stavroulakis, University of Southampton)

Silicon moth-eye structures have been fabricated using this technique at the University of Southampton[86]. Polystyrene nanospheres were self assembled and deposited on silicon to make a hexagonal lattice. At the next step, the silicon was etched with SF_6 in a deep reactive ion etch process in order to achieve a 400nm groove depth. The diameter of nanospheres was 200nm to achieve a 200nm periodicity in the structure (Figure 2.16(b)).

The sample with the best result had the pillar diameter of 100nm and was etched for 15 cycles (the deepest groove). This sample showed a significant reduction of reflection at wavelength of $400 - 500$nm. However, the reflection increases up to a less impressive 25% as the wavelength increases, though this is still lower than flat silicon.

Other examples of silicon moth-eye structures fabricated by means of nanosphere lithography are found in the work by Xu *at al.*[96] and Li *et al.*[48].

This technique has the advantage of not using the expensive pattern writing techniques. It is also a fast technique compared to e-beam lithography. Plus, nanospheres have been used to make arbitrary protuberances such as holes, cones, rings and nanotubes. However, in order to produce samples with larger area, more spheres are needed which makes the technique expensive. Also, this technique is only capable of making hexagonal lattices of protuberances, while sunflower patterns and aperiodic structures are also attracting some research work [35, 86].

2.3.4 Optical Properties

Optical studies of fabricated moth-eye structures confirm the resulting reduction in reflectivity at the interface between two different mediums. In the case of tapered protuberances the reduction in reflection is greater. The optimum shape of the protuberances was confirmed to be the actual shape found on the moth eye cornea: a parabolic profile[11, 91, 17]. This is not rejecting the findings of Southwell [83, 84] where a quintic profile was found to be the most efficient shape of moth-eye protuberances; fabricating quintic structures has not yet been possible. Experimental studies along with theoretical studies show that an optimum structure with the least reflection has the protuberances arranged base to base [11]. EMT explains this effect with the sudden change of the effective refractive index in a case where there is a slight distance between protuberances. Less reflection is also observed in protuberances with greater heights.

Specular reflection studies of moth-eye structures showed that the existence of protuberances at the interface harmonizes the s and p polarisation reflection from the surface, while at a flat interface between two different media the s polarisation reflection is more than the p polarisation. Also, at p polarisation, a Brewster's angle exists for which the reflection of light is zero. However, moth-eye structures show similar reflection values for light of different polarisations. Furthermore, it was found that reflection from moth-eye surfaces is independent of the incident polarisation for quite a wide range of incident angles (up to 40°)[100].

Recently Chuang *et al.* [22] found that for moth-eye structures with a height of about 400nm, an inverse behaviour of polarisation is observed. This phenomena was found in a moth-eye structure of non-close packed hexagonal array of conical protuberances. In these structures for angles of incidence greater than the Brewster angle, the s polarized

light reflection increases until it crosses the p polarisation reflection value and continues to increase. The suggested that in order for a moth-eye structure to show inverse polarisation in the visible spectrum, the base diameter of the protuberances should be smaller than 100nm. Such a unique behaviour might not be of interest in the field of anti-reflectivity but has the potential to be studied in more detail.

Since the discovery of moth-eye structures in 1962 by Bernhard [11], there have been many studies on applying moth-eye structures in anti-reflection applications. Experimental studies of moth-eye samples have confirmed their suitability for this purpose. In the photovoltaic industry, reducing the surface reflection of the cell is one of the approaches to increase the efficiency. Silicon-based solar cells can have a moth-eye silicon layer as the anti-reflection layer replacing the conventional anti-reflection layers. According to the literature, silicon layers which have a moth-eye layer have a reduced reflection compared to a smooth surfaced silicon(Figure 2.17). It has been observed that introducing a moth-eye structure reduces the reflection by $30 - 40\%$.

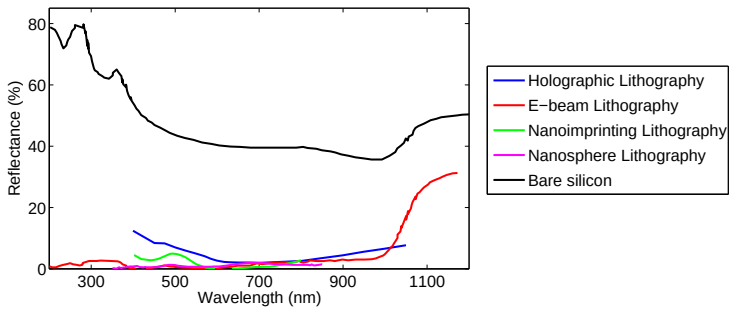

FIGURE 2.17: Normal incidence reflectance of silicon moth eyes fabricated by Holographic Lithography(period= 260nm, height= 80nm) [47], E-beam Lithography (period= 150nm, height= 350nm)[38], Nanoimprinting lithography (period= 200nm, height= 520nm) [100] and Nanosphere lithography (period= 210nm, height= 800nm) [88]. The reflectance of bare silicon is also plotted to provide a better comparison [38].

2.3.5 Applications

As an anti-reflective layer, the moth-eye structure performs similarly to conventional commercial multilayers at normal incidence. However, it shows much less reflection in exposure to light at oblique incidence. So it can be applied to components which have to work when exposed to light over a wide range of angles. The moth-eye technique has the advantages of stability and possible control of the optical properties of the material. The stability is due to the ability to make the moth-eye in a solid material. The optical properties of the material can be controlled by changing the geometry of the structure. Shifting the operating range simply needs change in the height of the protuberances. This gives the advantage of more flexibility in choosing the material and changing its optical properties according to the application needs.

Some potential applications of moth-eye structures include increasing the efficiency of low-quality optical components and plastic optical components like a hand-held magnifying glass, glass cover of laboratory instruments, cars, and aircraft, where the mass production of the structure compensates for the cost of the fabrication. Replacing greenhouse double glazing with a plastic sheet covered with moth-eye structures on both sides can help in delivering crops on time [95]. Substituting the multilayer anti-reflective layers in thermophotovoltaic cells because of stronger thermal stability of moth-eye layers is another proposed application [57]. Also, the longer stability and durability of moth-eye structures makes them suitable to be used in space [47]. In solar thermal applications, moth-eye structures can specifically be useful to enhance the performance of collectors [47, 95]. The flat collectors in cells are typically protected by cover glasses to reduce heat loss in the form of convection. Due to reflection losses, only one or two glass covers are normally used. Covering both sides of the glass with the moth-eye structure can help to reduce the reflection loss and increase the number of glass covers in order to increase the equilibrium temperature. In photovoltaic solar cell applications, the silicon surface of solar cells causes a 20% to 50% reflection loss. Employing a moth-eye layer as the cover can dramatically reduce this percentage [95]. Moth-eye structures are also very good replacements for thin film coatings. Thin film coatings exhibit problems caused by material selection, adhesion, thermal mismatch or diffusion of one material into another, which are not present in moth-eye structures [47].

Boden and Bagnall[16] studied the advantage of having moth eye anti-reflective layers in the field of photovoltaic solar cell coatings by simulation and experiment. Their results show that a moth eye anti-reflective layer with a protuberance height of 500nm gives a reflection of less than 0.5% in a broad band of wavelengths, which corresponds to a 12% increase in energy production compared to single layer anti-reflective coating. In another study, Han *et al.* [33] studied the effect of employing GaAs moth-eye coatings for a triple junction solar cell and observed a 1% efficiency increase. This value was observed to be around 3% for Si-based thin film solar cells having a moth-eye glass cover for arbitrary incident angles [31, 32].

Coating a moth-eye structure with a layer of metal gives the ability to choose a spectrum for reflectance/transmission of light [95]. Having the anti-reflective spectrum at longer wavelengths requires the moth-eye structure to be made at larger scales than sub-wavelength dimensions. However, the anti-reflective spectrum of a certain moth-eye structure can be shifted to the desired wavelength spectrum by coating the moth eye with a thin layer of a certain metal. This might be useful in applications where space is an issue.

Many studies have concentrated on using moth-eye structures to increase the efficiency of light emitting diodes [39, 40, 37, 76].

These anti-reflective layers have recently been used in glare reduction applications and for enhancing the transmission of light, specifically in window panes, cell phone displays and camera lenses [85]. A company in the UK, MacDermid Autotype, has produced Moth-eye Anti-Reflection and Anti-Glare (MARAG) films for flat panels [2].

In some other studies, moth-eye structures also showed hydrophobic properties, which is promising for self-cleaning surfaces for optical devices [10, 25, 31].

2.4 Conclusion

A review of photovoltaic anti-reflectives was provided in this chapter. Thin film coatings, micron textured structures and sub-wavelength-scale structures are the three groups of anti-reflectives in the field of photovoltaics. Optimum examples of each group with low reflectance and high cell efficiency, have already made their way into industry. The drawbacks of thin film coatings and micron textured structures do not exist in sub-wavelength structures. However, sub-wavelength structures themselves are suffering from expensive fabrication technologies. It is interesting that the path science started to produce optimum anti-reflectives has led to sub-wavelength structures, similar to moth-eye structure which is what nature had chosen to use as anti-reflectives.

Moth-eye structures improved by Nature provide the best anti-reflection structure used for camouflage or eye sight in various insects and butterflies. This structure is the result of many years of evolution and has been optimised by Nature to meet Nature's needs. It has also found its way into human needs where reflection is not desired.

In order to model the behaviour of moth-eye structures, EMT is an effective and easy method. However, it is not applicable to structures with larger periodicity. In these cases the features are not resolved by the incident wavelength and thus do not produce an effective refractive index. Thus RCWA is a more suitable tool to be used in this case.

Moth-eye structures lie within the category of sub-wavelength structures to provide anti-reflectivity. Fabricating sub-wavelength structures is hard and expensive. However, improvements in fabrication methods have allowed successful moth-eye samples to be produced. The commercial availability of moth-eye anti-reflective structures suggests that the cost of fabrication can be reduced to an acceptable degree. However, for different laboratory and commercial applications one has to find a compromise between time, cost, and the perfection of the fabricated sample. Table 2.2 summarizes the properties of fabrication methods.

Optical properties of artificial moth-eye structures in silicon, GaAs, GaSb, glass and silica show that moth-eye structures can be an efficient anti-reflection structure to be employed for many technological needs. It is easy to optimise the structure for use in an arbitrary wavelength regime by changing the size, periodicity, or even material of the

Method	Minimum feature size	Notes
Holographic Lithography	100nm	•Fast • Can be replicated using metal replicas • The height and spacing between protuberances relate to each other which limit the geometry • It is not capable of making different shape of geometries • Relatively fast and cheap
E-beam Lithography	1nm[53]	• High resolution • Capable of making a variety of lattices and cross sectional shapes • Low speed, so only used for small areas (couple of microns) • Expensive in terms of time and cost
Nanoimprinting Lithography	10nm	• Capable of making a variety of lattices and cross sectional shapes • Scalable to be used for large areas • Much faster than E-beam Lithography
Nanosphere Lithography	90nm	• Cheap(in small scales) • Fast(compared to E-beam Lithography) • Only capable of producing hexagonal lattices • Only capable of making circle, or ring cross sections

TABLE 2.2: Summary of nano-fabrication methods in the field of moth-eye structures

structure. Also, introducing a coating on top of the structure can compensate for space problems and shifts the working wavelength range of the structure up or down in the wavelength spectrum.

Chapter 3

Experimental Techniques

In this work biomimetic moth-eyes, fabricated in silicon, have been studied and measured. Scanning electron microscopy is used to image the fabricated structure and measure their dimensional properties. The optical characterisation of the structure is done by means of two sets of measurements: Normal incidence and oblique incidence specular measurement. Reflectance of the structure at normal incidence is measured through the first technique, where the second measures the specular reflectance of the structure at a range of incidence angles. In this set-up the sample is also rotated in the azimuth plane to look at the influence of the azimuth rotation of the structure into its reflectance behaviour. Samples are designed so that the effect of changing the dimensions of the structure on the reflectance of the structure can be examined. This chapter introduces the techniques used for the characterisation of the structure.

3.1 Scanning Electron Microscopy

Scanning Electron Microscopy (SEM) can be used to image structures with feature sizes down to tens of nanometers. A beam of high energy electrons scans the surface of the structure. Electrons interact with the atoms at the surface of the structure and produce back scattered or secondary electrons. The backscattered or secondary electrons are in fact the signals which carry information about the surface composition, topography and electrical properties. Since the information is produced by the interaction of particles at an atomic scale, the resolution of this type of microscopy is as low as 1nm, however due to scattering this value differs within different devices. This work has used a Jeol JSM-7500F SEM. Samples with patterned silicon moth-eyes are attached to an aluminium stub using a carbon pad. Images are taken once from the top of the sample, and once when the sample is slightly tilted. The latter gives an image from the side of the samples, which include the profile shape of protuberances. The height of protuberances can also be determined from the tilted images.

In the case of biological samples, a small section of the wing/eye is separated and attached to a small aluminium stub. Natural samples also need to be coated by a thin layer of conductive material to prevent sample charging. If charging occurs the features are not visible. Thus a thin layer of platinum or gold is sputtered onto the sample before inserting it into the SEM. However sputtering metal particles on to the features of a natural structure can cause features to bend or compress. Consequently the images which are produced from these structures can have distorted features.

The voltage of the beam has to be adjusted according to the nature of the sample to achieve a clear image. For silicon moth-eyes the beam has the voltage of 10kV and for natural samples it is set to 5kV. The difference is because of the conductivity of the material interacting with the incoming electron beam.

SEM images were later analysed by means of "Digital Micrograph" or "ImageJ" software to characterize the features of the structure.

3.2 Spectroscopy

3.2.1 Normal Incidence: Probe Measurement

In order to study the reflectance properties of moth-eye samples at normal incidence, a specular reflectance measurement is carried out using a probe measurement system. A fibre optic reflection probe is used to illuminate the sample and carry the reflected light to the spectrophotometer for detection. The optical probe has three terminals. At one terminal, it consists of seven optical fibres bound tightly together with one fibre at the center and the other six fibres are arranged around it. The other two terminals of the probe are to connect to the spectrophotometer and light source. One terminal only has a single fibre and the other terminal consist of the ring of six fibres. The single fibre acts independently to the ring of six fibres; one shines the light onto the sample and the other collects the reflected light and takes it to the spectrophotometer. The probe fibre is kept normal to the sample holder where samples are placed and can be moved in x-y-z directions (Figure 3.1).

The output of the spectrophotometer is processed in the spectrophotometer software where the relative reflectance of each sample (R_{sample}) is calculated by

$$R_{sample} = R_{ref}\left(\frac{I_{sample} - I_{dark}}{I_{ref} - I_{dark}}\right) \tag{3.1}$$

where

R_{ref} is the absolute reflection of the reference sample

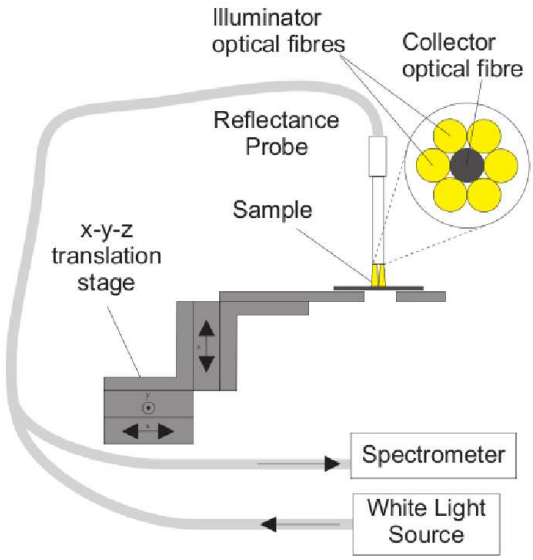

FIGURE 3.1: Probe measurement set-up (The image is a courtesy of Dr Stuart Boden, University of Southampton).

I_{sample} is the intensity of light detected at normal incidence from the sample

I_{dark} is the dark intensity (with the absence of the light source)

I_{ref} is the intensity of light detected at normal incidence from the reference.

The reference sample is a reflective sample with a known absolute reflection. Silicon is used in this work thus the absolute reflection of silicon, R_{Si} is used for normalisation. The absolute reflection of silicon is calculated from Fresnel equation (Equation 3.2). The refractive index of silicon in Equation 3.2, n_{Si}, is taken from literature [6]. This equation is only applicable to calculate the reflection coefficient of silicon at normal incidence.

$$R_{Si} = \left(\frac{n_{air} - n_{Si}}{n_{air} + n_{Si}} \right)^2 \tag{3.2}$$

The light source used through this measurement was a tungsten halogen light produced by HL-2000 (Wavelength range of $360 - 2000$nm). The spectrophotometer was an HR4000CG which can detect a wavelength range of $200 - 1050$nm with an optical resolution of 0.75nm. The data was entered into the Ocean Optics spectral software (SpectraSuite) for post-processing and plotting. The probe fibre used in this measurement was an Ocean Optics QR400-7-VIS-BX which can carry light of wavelength $200 - 1100$nm.

Figure 3.2 shows the operation of the probe during the measurement. The probe fibre is connected to the source and spectrophotometer so that the light shines from the ring of the six fibres around the centre fibre of the probe and illuminates the patterned area.

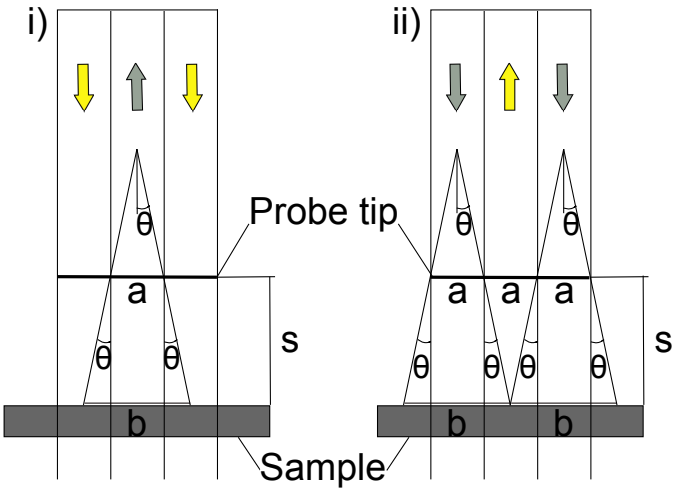

FIGURE 3.2: The operation of the probe fibre at normal incidence at (i) the illumination state and (ii) collection state. b represents $d_{collection}$.

The reflected light is collected by the central fibre. The collection area of the central fibre should not exceed the area of the sample that is patterned by moth-eye structure and is illuminated by the incident light. The diameter of the collection cone on the sample is

$$d_{collection} = a + 2s \tan\theta \tag{3.3}$$

where s is the distance between the probe and the sample, a is the diameter of the fibre and θ is the numerical aperture of the fibre. The probe fibre is kept at a distance from the sample where the illumination cone of the 6-bundled fibres do not overlap. Thus according to Figure 3.2,

$$2s \tan\theta = a \tag{3.4}$$

Thus,

$$d_{illumintation} = 2a \tag{3.5}$$

Having identical fibres around the core fibre has the advantage that the illumination cone of each fibre is identical to the collection cone of the inner fibre. The total diameter of the illumination area is:

$$d_{illumination} = 2s \tan\theta + 2a + 2s \tan\theta \tag{3.6}$$

$$d_{illumination} = 4a \tag{3.7}$$

In the case of the probe used in this experiment the core diameter of the fibre is $400\mu m$. Thus the diameter of the total illumination area is $1600\mu m$ (the illumination area is a series of touching circles).

The numerical aperture of the fibre corresponds to an illumination/collection angle of θ. Hence the incident light on to the sample spreads over a cone with angle of θ. According to the manufacturers, the QR400-7 probe has a numerical aperture of 0.22. The numerical aperture is the sine of the illumination/collection angle of a fibre. Thus a numerical aperture of 0.22 corresponds to an illumination/collection angle of 12.7°. Accordingly the incident angle of light onto the sample changes from 0° to 12.7°. So the light collected by the collection fibre is an integration of reflection from incident angles of near 0° to 12.7°.

In order to increase the signal-to-noise ratio, the illumination cones must be arranged to closely touch each other without overlapping. This will happen by setting the distance between probe and the sample to be according to

$$2s \tan\theta = a \tag{3.8}$$

For the probe used in this experiment a equals to $400\mu m$, which gives the optimized value of $887.5\mu m$ for the distance between the probe and the sample.

To provide a better signal shape and eliminate noise within the experiment, the integration time in the SpectraSuite program can be set appropriately. Also in order to smooth the data, the Boxcar Width[1] is another parameter to be set. The value of these parameters for each measurement is mentioned within the chapters.

Figure 3.3 shows the reflectance of silicon at normal incidence measured via this set-up along with the theoretical value of silicon reflectance. The integration time is set to 100ms and Boxcar width to 1. The noise within the measurement has produced a difference of maximum magnitude of 1.26%. Increasing Boxcar Width reduces this value.

3.2.2 Angle-Resolved Reflectance Measurement: Reflectometer

Angle-resolved reflection measurements are performed in a custom built motorised goniometer system (Figure 3.4). The device can be used for specular reflection measurements, and angular scattering in transmission or reflection. The light source is a white laser beam. The laser beam is passed through a cross polariser, which determines the power, and sets the polarization of the beam to two linear polarizations: "s" where the electric field is perpendicular to the plane of incidence (TM), and "p" where the electric field is parallel to the plane of incidence (TE). The first polariser in front of the laser

[1]Boxcar Width calculates an average of a number of pixels while transmitting the data. Specifying n means the pixels are being averaged by n pixels to the right and n pixels to the left.

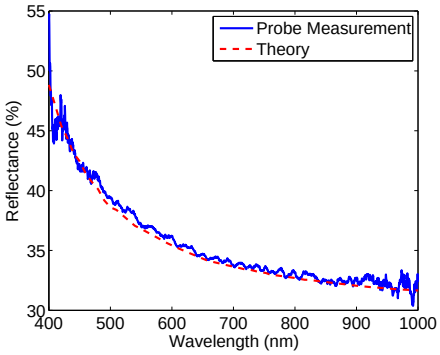

FIGURE 3.3: Normal incident reflectance of silicon measured by probe set-up (solid line) and achieved from theory (dashed line).

aperture is called the "analyser" and the second polariser is called the "polariser". The polariser is fixed to produce either s or p polarised light and the analyser is rotated to change the light intensity. The value of the light intensity resulting by the combination of two polarisers follows Malus's law[34]. According to Malus's law when one polariser is placed on the path of a polarised beam, the intensity of the resulting light equals to:

$$I = I_0 \cos^2(\theta) \tag{3.9}$$

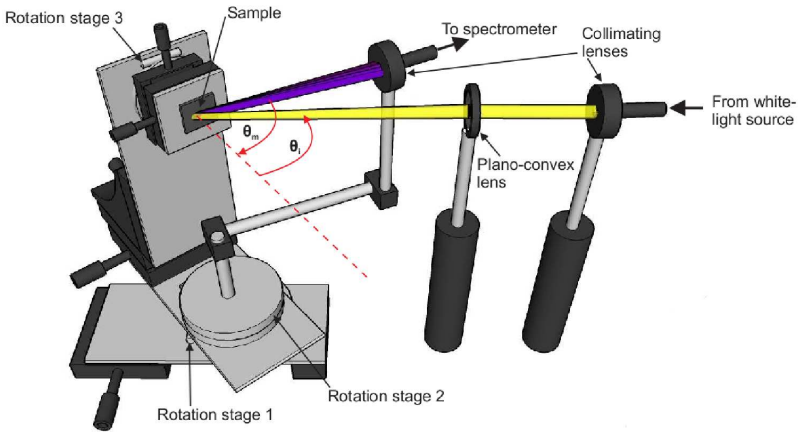

FIGURE 3.4: Reflectrometer setup used for specular reflection measurements (The image is a courtesy of Dr Stuart Boden, University of Southampton).

where I_0 is the light intensity entering the polariser, I is the light intensity after passing through the polariser and θ is the phase difference between the polarised light and the polarisation angle of the polariser. In a cross polariser the initial polarised light (I_0) is produced by placing another polariser on the path of the non-polarised light before it enters the main polariser. According to Equation 3.9 the intensity of the light entering the measurement system by cross polarisers is at minimum power (zero) when the angle between the polarisers is 90° and maximum when the polarisers are parallel to each

other. Figure 3.5 shows how the laser power changes with changing the position of the polarisers. To produce s and p polarised light, the second polariser is kept constant at 5° and 95° respectively. The polarisation angle of the analyser is changing from $-10°$ to $-190°$ for s polarisation and from 80° to $-100°$ for p polarisation to produce a complete sweep of 180°. The shape of both the plots confirms that the cross polarisers follow a $\cos^2 x$ function. Thus it is expected to show the maximum laser power when the two polarisers are parallel to each other, at $-100°$ for s polarisation and 0° for p polarisation. But there is a difference in the value of the maximum power between s and p polarisation. This difference is because of the different response of optical components to each polarisation state.

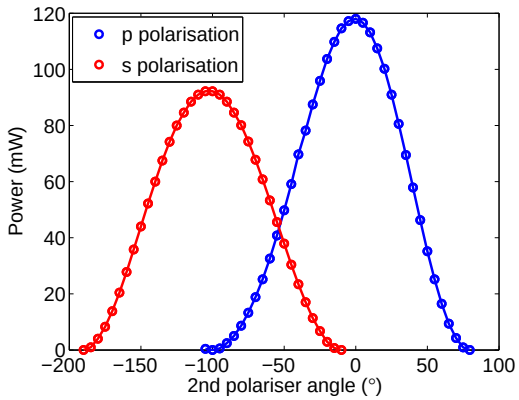

FIGURE 3.5: Laser power produced by the cross polarisers for s and p polarisation. The second polariser is kept fixed while the position of the first polariser determines the laser power.

After light has passed through the cross polarisers it is guided upwards by means of a periscope. It goes through an aperture and optionally a lens to change the beam spot size, then it hits the mirror and deflects 90° to illuminate on to the sample holder. The sample holder is set on a rotating stage which rotates 90° and also has translating stages to move the sample in X,Y and Z directions. The sample holder is also capable of rotating the sample in the azimuth plane from 0 to 360 degrees. The sample is attached to the sample holder by means of double sided tape. The detector fibre is fixed on a rotating bar which rotates around the sample relative to the center of the sample holder stage. Zero angle for the sample rotation stage is set to be when the light from the mirror is shining onto the sample at normal incidence. At this point the detector fibre is behind the mirror and thus cannot receive the reflected beam. After a few degrees the light from the sample can enter the detector fibre. The position of the mirror (source) is fixed. Thus the angle of incidence (AOI) changes when the rotational angle of the sample stage changes. A change in the rotation of the sample stage is followed by a rotation in the detector by an angle double that of the sample rotation angle. The light collected by the fibre is then guided to the spectrophotometer. A LabView program is designed to control all the stages and polarisers and also to plot the light intensity and

record the data. A lens can be placed on the path of the beam from sample to the fibre to collect and focus the light into the centre of the fibre aperture.

To start the experiment the sample is attached to the sample stage. While the sample holder is set at 0° the sample has to be fixed flat and perpendicular to the incident beam coming from the mirror. This is achieved by ensuring that the reflected beam from the sample is reflecting back on the same path as the incident beam (by fixing an aperture on the path of the laser beam). Using the two screws on top of the sample holder, the tilt of the sample at X and Z direction can be changed. Once the sample is set flat, the Y distance of the sample from mirror and consequently detection fibre has to be set to the optimum value where the reflected light goes directly into the detector aperture. This value is set when AOI equals to 45°. By varying the Y-distance slowly the intensity of detected light changes. Where the light intensity is maximum the Y-distance is at its optimum position. However tests still have to be performed at other angles to make sure the reflected light enters the fibre. Slight changes in the Y-distance and the tilt of the sample in the X-direction helps to achieve the correct alignment. An inaccurate value of the Y-position prevents the reflected light to enter the detection fibre at an arbitrary angle of incidence and thus inaccuracies occur in the measurement. This is equivalent to making sure the detection fibre is exactly on the path of the reflected light for all angles of incidence, in other words the system is aligned. The next and final step is to set the laser power (rotation of the analyser) and integration time. These values must be fixed so that there is enough signal and so that it does not saturate. Since each sample has a different reflectance behaviour, the laser power and the integration time varies between samples. Once the set-up is aligned and the power intensity and the integration time is set, the measurements are performed.

The laser source is a Fianium Continuum laser producing light of $450-2000$nm wavelength with a spot size of $\approx$ 2mm width. The beam size hitting the sample must be set not to exceed the size of the sample to be measured. Otherwise the reflected light would involve reflections from the non-patterned area of the sample which would result in inaccurate results. As the sample is rotated to alter the angle of incidence the width of the beam spot extends. According to Figure 3.6, the width of the spot changes by a ratio of $\frac{1}{\cos\theta}$ in which θ equals to the angle of incidence. Increasing θ causes $\frac{1}{\cos\theta}$ to increase and consequently the width of the beam increases. Thus while performing measurements use of an appropriate lens to reduce the beam size according to sample size, should be considered.

The fibre which carries the light to the spectrophotometer is a multi mode fibre AFS50/125Y (Thorlabs) which operates over the wavelength range of $450-1450$nm. The core diameter of this fibre is 50μm and its numerical aperture is 0.2. With this numerical aperture the collection cone of the fibre is 11.53°. The distance between the fibre and the sample is fixed at 17cm. Thus the diameter of the collection cone of the fibre at sample point, with similar calculations to the previous section, is 6.986cm. This value is bigger than

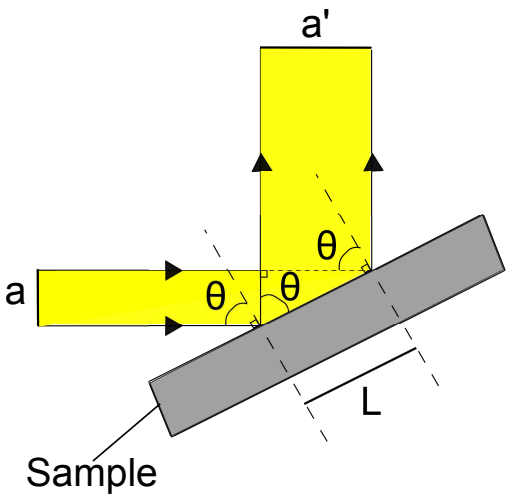

FIGURE 3.6: The width of the beam on the sample at the incident angle of θ.

the larger moth-eye sample available (1cm×1cm) which means light reflected from other components around the apparatus can also enter the fibre. However similar to probe measurement, this measurement is also performed in a dark room to minimise errors rising from unwanted light entering the fibre. Also increasing the laser power and integration time increases the signal to noise ratio and reduce the effect of the error caused by unwanted light entering the fibre. The spectrophotometer is a BWTEK BTC112E which detects light in the wavelength range of $200 - 1050$nm and has an optical resolution of up to $0.3 - 10$nm. This spectrometer is equipped with a thermoelectric cooled linear CCD array that offers much higher dynamic range, greatly reduced dark counts and superior long term operation, making it ideal for low light level detection and long term monitoring applications of up to 16 minute.

The angle of incidence is altered from 0° to 85° in steps of 0.1°. For the specular reflectance to be measured, the detector is set at an angle of $2 \times \theta$ (θ being the angular position of sample rotation axis to the source, in other words the angle of incidence). Thus the detector angle changes from 0° to 170°. However presenting the measurement of reflection from a sample at normal incidence ($\theta = 0°$) is not possible. Detecting the reflection of normal incident light needs the detector to be at $\theta = 0°$; however having the detector and the source both at 0° angle means each of them is blocking the other. Hence the normal incidence measurements are presented for angles close to normal where the detector and source are not blocking each other's light path. For this set-up the start angle is set to 1.5°. Also when the angle of incident increases to values of 75°, depending on the size of the sample, the beam tends to be larger than the patterned area of the sample and thus results are no longer entirely from the moth-eye structure and thus inaccurate. The value of the AOI where the results are not acceptable depends on the size of the sample.

The reflection measurement results are normalised to the incident beam. To measure the laser beam spectrum, the detector is rotated to the angle of 180° and the sample holder is

moved out of the way. The normalization equation can still be explained by Equation 3.1 used in the probe measurement: if an ideal sample which has a reflectance coefficient of unity is used as the reference sample, thus R_{ref} equals to 1 and I_{ref} equal to the laser beam. Under the same conditions as a probe measurement, a dark measurement is also performed with the laser light off.

Since the laser can have slight output power fluctuations over time (a few mW in a 24 hour period), while performing the measurements, attention should be paid to keep the laser power to a constant value by adjusting the analyser accordingly. Also, these fluctuations over time should be monitored and included in post analysis. In order to do this, the laser power is measured before and after each experiment. While performing the normalisation, an average of the laser power from before and after is used as I_{ref}.

During the work of this thesis it was noticed that the equipment is very alignment sensitive. Due to the small aperture of the fibre, $50\mu m$, the Y distance between the sample and the detection fibre has to be set accurately to ensure the reflected beam goes into the fibre at all angles of incidence. Figure 3.7 shows results of reflectance measurement for silicon using the reflectometer.

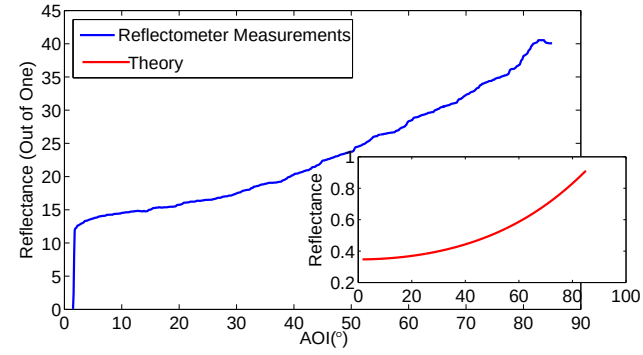

(a)

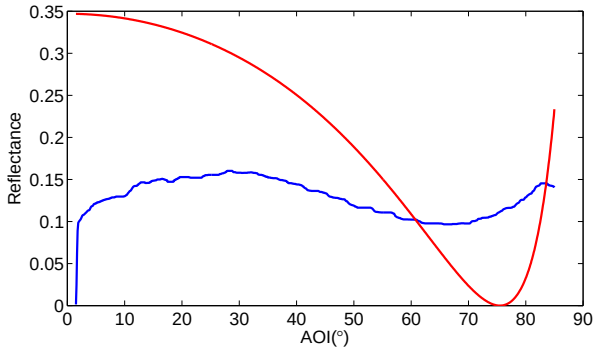

(b)

FIGURE 3.7: Comparing the reflectance of silicon at $\lambda = 632.9$nm for AOI$= 3 - 85$ measured with reflectometer set-up and calculated from Fresnel equation(theory) for (a) s polarisation and (b) p polarisation.

The first point to notice is the value of "reflectance" axis for Figure 3.7(a). This value is more than "1" while measurements are normalised to 1. This suggests that the intensity of measured light reflected from silicon is higher than the intensity of measured laser power. Also looking at reflection at p polarised light, it is clear that it shows low reflection behaviour at the Brewster angle, however the whole spectrum does not show correct values. For angles lower than 60°, the measurement shows lower values, compared to theory, while for higher angle of incidences the reflectance was higher than theory. Both of these discrepancies suggest that the system is not aligned correctly. To tackle this problem a mini integrating sphere was designed to be added to the set-up at the detecting fibre. Light enters the sphere from one port and is sent to the spectrometer by means of the fibre at the other port. The front port of the aperture of the integrating sphere is larger than the aperture of the fibre, thus light with a slight mis-alignment enters the sphere and is still collected by the fibre and sent to the spectrometer. The design images and real images of the integrating sphere are provided (Figure 3.8) and show the parts and features in the sphere. The sphere is built in a cube of size $30 \times 30 \times 35\text{mm}^3$. Four front ports with different hole size are designed for the front of the sphere; 1, 2, 3, and 4mm diameter. The largest front port will ease the alignment, however it reduces the angular resolution of the system. Different detectors can be connected to the sphere to collect the light. The integrating sphere is made of Poly Tetra Fluoro Ethylene (PTFE). It is highly reflective and almost all of the light is diffusely reflected from its surface. There is a small round disc which is inserted at the back of the sphere. The existence of this disk is very important as it prevents light from escaping out of the sphere and reducing the measured reflectance. The light shining into the integrating sphere will hit the back surface of the sphere and will reflect back into the front port and data will be lost, thus this disc which is fixed with a slight angle of 8°, prevents the light from reflecting back to the front port and exiting the sphere. The disc reflects the light with a slight angle and guides it to shine onto the sphere and then gets reflected again within the sphere. The disc works very similarly to the reflectance port in big integrating spheres and thus it is labelled as the "reflectance" port in Figure 3.8(c). In order to provide a homogeneous distribution of the light within the sphere the light needs to be reflected within the sphere many times before it transmits through the fibre to the spectrometer so a baffle situated between the detector port and the back disk is used to prevent the light signal shining straight into the detector. In this way the light shines back from the disc, reflects many times within the sphere and only after being homogeneously distributed, it enters the fibre.

Apart from reducing the angular resolution of the system, the integrating sphere needs the intensity of the laser power to be quite high and large integration time to be set so that the signal gets detected by the spectrometer (high signal-to-noise ratio). However high laser power is not favourable with all samples and might damage the sample, especially for natural samples. Thus it is favourable to cover the outer surface of the sphere by reflective materials to increase the signal to noise ratio and reduce the laser

power required. In this way even the small amount of light transmitted through the sphere walls gets reflected back to the sphere and will be collected by the fibre. Thus the signal detected by the spectrometer is stronger which means the value of laser power can be reduced to prevent possible harm to the sample. Having the detected reflectance at lower intensity also has the disadvantage that the reflectance spectrum is accurate for a smaller wavelength range: $450-850$nm as opposed to $450-1050$nm in the absence of integrating sphere.

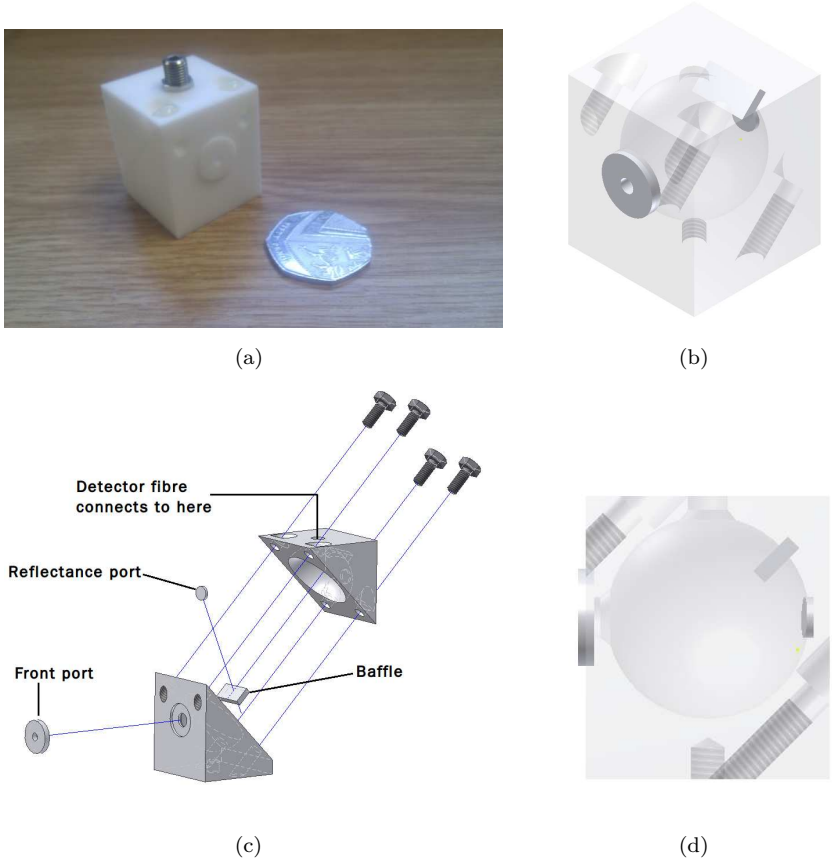

(a) (b) (c) (d)

FIGURE 3.8: Mini integrating sphere designed as the detector port for the reflectometer set-up. (a) shows the real image of the integrating sphere compared to a 50 pence British coin. (b) three dimensional image of the integrating sphere design figure (c) different parts of the integrating sphere (d) a cross section cut of the integrating sphere design image. (Images are courtesy of Mr David Payne, University of Southampton)

Figure 3.9 shows the results of silicon reflectance measured by the reflectometer employing the integrating sphere at the detector point. The reflectometer results are plotted in colour while the theory is plotted in black. A comparison between results from Figure 3.7 and Figure 3.9 reveals that measurements with the mini integrating sphere are much more accurate than without. In this measurement, the port with the entrance hole size of 3mm is used. The integrating sphere is kept at a distance of $\approx$ 16cm which achieves the angular resolution of 0.4°; meaning the system can be 0.4° out of alignment while the signal will still be detected. However this also has some disadvantages. It will reduce the sensitivity of the set-up by 0.4° which means small features in the reflectance pattern

within angles of 0.4° will be lost. With this set-up the results are acceptable from the angle range of $1.5-83°$. Figure 3.10 shows the specular reflectance of silicon at the two orthogonal polarisations for the wavelength range of $450-850$nm for the aforementioned AOI range. The theoretical results are calculated through Equation 3.10. Equation 3.2 is extracted from this equation for $\theta_i = 0$

$$R_p = \left(\frac{n_1 \sqrt{1 - \left(\frac{n_1}{n_2}\sin\theta_i\right)^2} - n_2 \cos\theta_i}{n_1 \sqrt{1 - \left(\frac{n_1}{n_2}\sin\theta_i\right)^2} + n_2 \cos\theta_i} \right)^2$$

$$R_s = \left(\frac{n_1 \cos\theta_i - n_2 \sqrt{1 - \left(\frac{n_1}{n_2}\sin\theta_i\right)^2}}{n_1 \cos\theta_i + n_2 \sqrt{1 - \left(\frac{n_1}{n_2}\sin\theta_i\right)^2}} \right)^2 \tag{3.10}$$

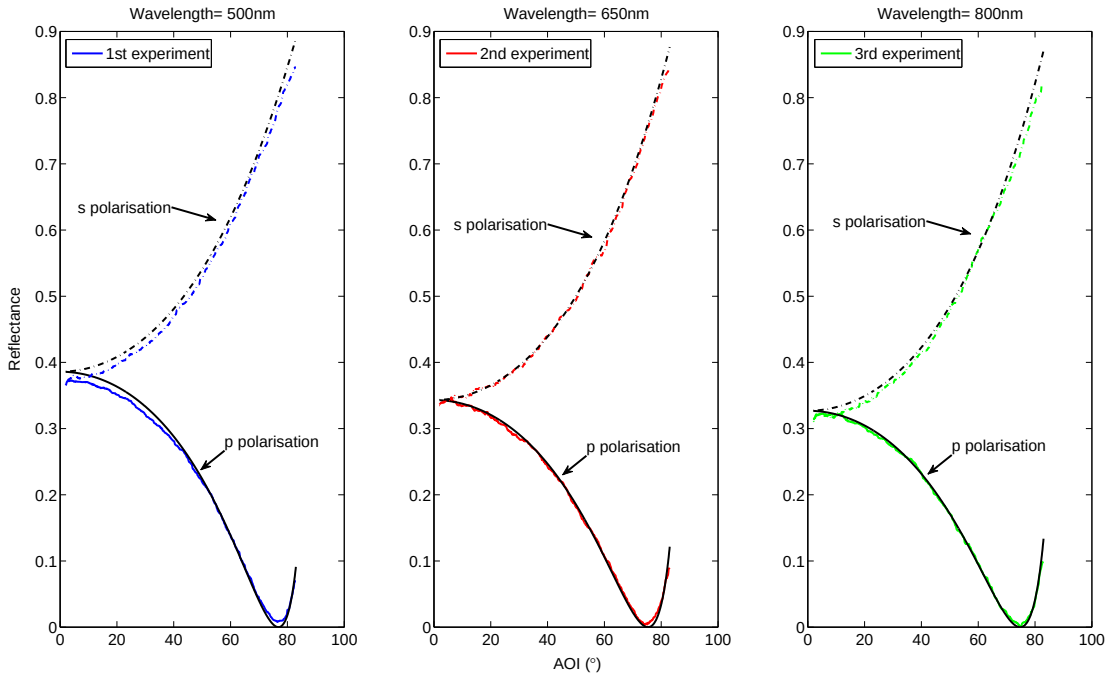

FIGURE 3.9: Results of reflectance measurement from silicon using the reflectometer set-up equipped with integrating sphere at the detector port. The experiments are compared with theory (black). Each plot is showing the results from a different measurement and a single wavelength compared with theory.

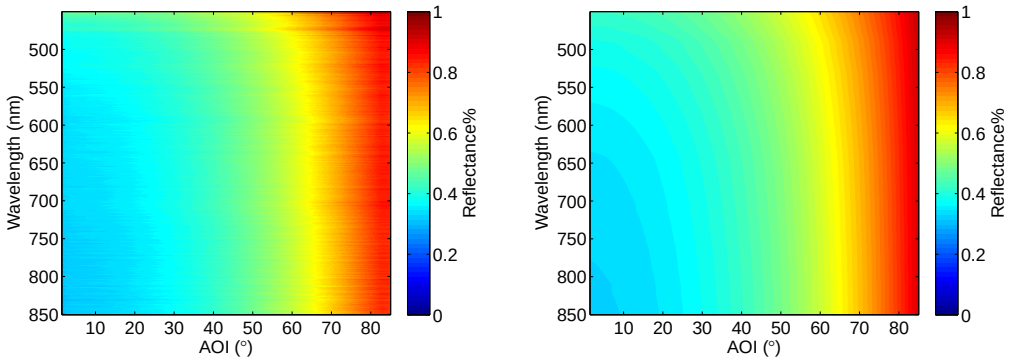

(a) s polarisation - Experiment

(b) s polarisation - Theory

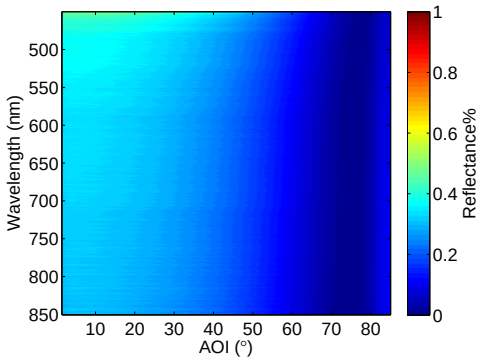

(c) p polarisation - Experiment

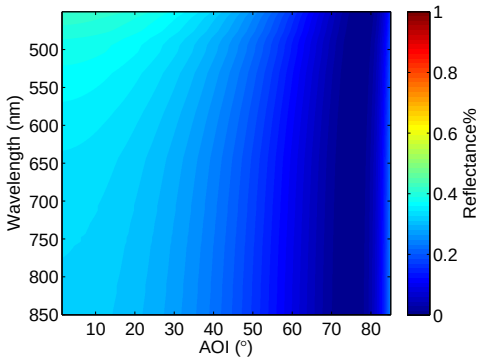

(d) p polarisation - Theory

FIGURE 3.10: Specular reflectance of silicon for s and p polarisation measured using the reflectometer and the mini integrating sphere at the detector point. The theory is calculated from Fresnel equation.

3.3 Conclusion

This chapter explained the techniques used for characterization and experimental studies performed in this work. SEM imaging was used to study the shape and geometrical properties of the samples fabricated previously and studied in this thesis. Reflectance of samples at normal incidence was studied using the probe measurement technique. Specular reflectance of samples were studied using the reflectometer set-up. The latter was also used to rotate the sample in the azimuth plane, so that the specular reflectance of samples could be measured at arbitrary azimuth orientation of the sample.

The initial measurement performed in this thesis using the reflectometer set-up showed values of no sense. This was due to the fact that the set-up was very alignment sensitive. Also, for the same reason producing repeatable measurement results was of a great difficulty. Hence, the setup was modified to overcome these difficulties. A mini integrating sphere was added at the detector port to collect the reflected beam while easing the alignment of the system. Reflectance of silicon samples were repeated with the new set-up and results of close approximation with theoretical values were achieved.

Chapter 4

Simulation of Silicon Moth-eye Structures

Numerical simulations of biomimetic photonic structures provides a better understanding of their optical behaviour. In general, using numerical simulations as a virtual model can allow us to study the effect of changing geometrical parameters on the optical behaviour of biomimetic photonic structures. Experimental parameters such as angle of incidence and polarisation can be varied so that the optical behaviour of the structure can be studied in different experimental environments. Reflectance, transmission and absorption spectra, electric and magnetic fields, reflectance and transmission diffraction orders can be investigated to show the optical behaviour of the structure. Theoretical study can be used before fabrication of a biomimetic structure to create an optimised structure matching required purposes, and it can also be used after experiments are performed to examine unforeseen behaviour and to confirm a hypothesis derived from experimental data.

It was shown in Chapter 2 that Rigorous Coupled Wave Analysis (RCWA) is an appropriate numerical method to model and simulate moth-eye structures. RCWA employs the full vectorial form of Maxwell's equations. Electromagnetic waves in the form of a sum of coupled waves are related to a periodic Fourier function, which represents the periodic permittivity of the structure. Thus Maxwell's equations are solved in the Fourier domain. Field distributions are derived from Fourier harmonics and diffraction efficiencies are calculated at the end of the simulation.

Modelling and simulations performed and presented in this work used an RCWA modelling package called RSoft [4]. RSoft includes several photonic and optical structure simulation packages. Among them DiffractMOD is a package using RCWA along with Modal Transmission Line (MTL) theory to calculate the diffraction efficiency and field distribution of 2D and 3D periodic structures. MTL is an enhanced version of RCWA where the electromagnetic fields are represented by summation of individual modes. The

periodicity of the structure in the X-Y plane is expressed by means of the Bloch Theorem. Employing the Bloch theorem within Maxwell's equations results in an eigenvalue problem. The structure is divided into thin layers where the permittivity of the structure is homogeneous in the Z direction. The eigenvalue problem at each individual layer is solved and thus integrated into adjacent layers by means of MTL.

The model of the structure is created in DiffractMOD by means of a built-in CAD package. The CAD package makes it possible to create arbitrarily shaped structures and simulate them using one of the several modelling packages within RSoft.

In this chapter, a detailed explanation of using the CAD layout to produce silicon moth-eye structures is presented. The design of silicon moth-eye structures is taken step by step. Results are presented to verify the structure and the simulation method. Once a silicon moth-eye structure is produced satisfactorily, the simulation file is used to study the influence of geometrical parameters on the optical properties of the structure. Further, silicon moth-eyes are optimised for the visible wavelength and their optical behaviour is studied as angle of incidence and azimuth rotation of the structure is changed.

4.1 DiffractMOD Initialization

At the start of a new design a start up window is presented so that the user specifies the package to be used, in this work DiffractMOD (Figure 4.1). The dimension of the simulation domain also has to be set: two dimension or three dimension. Other parameters can also be set in this dialogue box:

Free Space Wavelength Wavelength of wave in free space

Background Index The refractive index of the background material

Component Index The refractive index of the component

Component Width The default width of a component in X direction in μm

Component height The default width of a component in Y direction in μm

Index Profile Type The type of the index profile

DiffractMOD can output the reflection and transmission for each diffraction order, total reflected, transmitted and absorbed power. These values can be plotted against wavelength or incident angle.

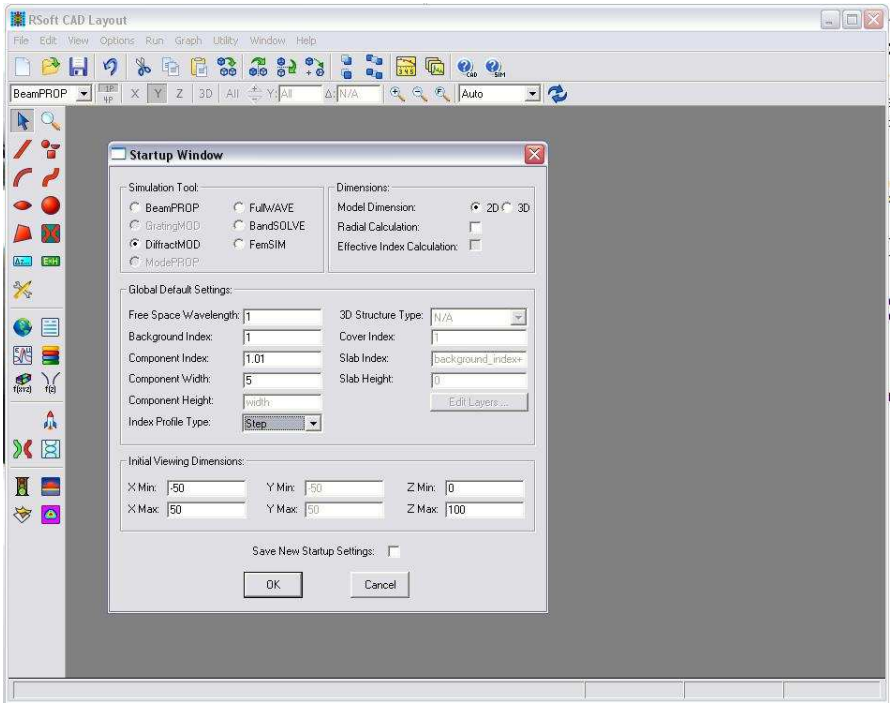

FIGURE 4.1: Print screen of RSoft start-up window.

4.1.1 Defining the Structure

To start, a simple simulation of reflection from a flat interface of air-Silicon was set up. From the start-up window, the DiffractMOD package is selected and the simulation dimension is set to two. In 2D it is assumed that the structure is not varying in the Y direction and thus the structure is defined in the X-Z plane. The rest of the variables were left as default and changed through the designing process of the simulation. A "segment" is drawn in the X-Z plane using the mouse. The dimensions of the component can be changed later by right-clicking on the component and opening the "Properties of Segment" box (Figure 4.2). The refractive index of the component can also be defined in this dialogue box. It can be set to a constant number, or for materials with dispersion relation a data file of the refractive index changing with wavelength can be added to both real and imaginary values of the refractive index separately. "width" and "height" are defined in the X-Y plane and thus irrelevant in 2D simulation, however they can be reset in this window. In order to reset these values new parameters can be defined in the "Symbol Table Editor" dialogue box. This dialogue box can be found on the "properties for segment" or on the left hand bar as is shown in Figure 4.2. In the Symbol Table Editor dialogue box, the values for "width" and "height", are both set to 10μm [1]. These values are later assigned to the width and height of the segment in segment properties box. To define an air-silicon interface, the background index in the start-up dialogue box is set to 1. For silicon, the refractive index data from literature is used [6]. "index" and "alpha" are global variables which define the real and imaginary part of the silicon

[1]The default dimension in RSoft is set as microns

refractive index. These are inputs to Properties of Segment refractive index values. Two separate data files are used for index and alpha. The size of the segment in the Z direction can be specified through to the Z value in "Starting Vertex" and "Ending Vertex" in "Properties of Segment" box. The starting and ending vertex values of Z are set to 0μm and 10μm respectively.

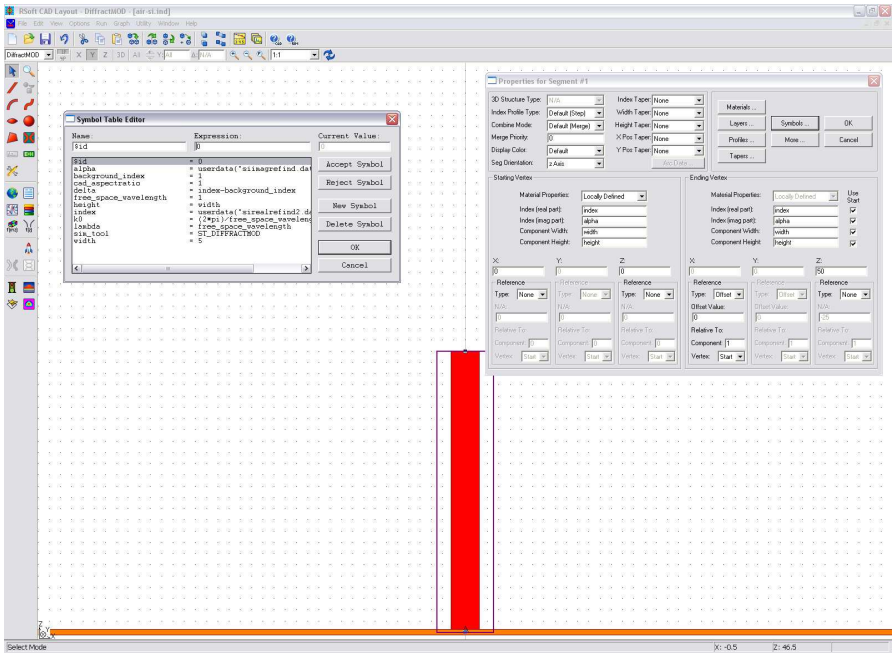

FIGURE 4.2: Specifying the structure parameters through "Properties of segment" dialogue box in DiffractMOD

4.1.2 Defining the Unit-Cell

Once the design of the structure is finished, the simulation unit-cell has to be specified. This is the space in which DiffractMOD performs the calculation. The size of the unit-cell in the Y direction is infinity as it is assumed that the refractive index of the structure is independent of Y. The unit-cell is defined using the button on the left hand bar "Display index profile" (Figure 4.3). Domain Min and Max in X and also Z (and Y in 3D simulation) define the boundaries of the unit-cell. DiffractMOD shows the default unit-cell by the purple rectangle around the structure. The unit-cell must be specified to include at least one periodic unit of the structure. In this example, since the reflection from a simple flat interface of air and silicon is being calculated, the size of the unit-cell does not affect the results, however it affects the time of the simulation. Hence, since the air-silicon interface does not have any features in the unit-cell and the refractive index of both media across the boundary are constant in all Cartesian directions, a small unit-cell of 0.2μm$\times$0.02μm is specified.

"Grid Size" and "Slice Grid" are two parameters of great importance when defining the simulation grids. Grid size sets the grid used during the simulation for each dimension.

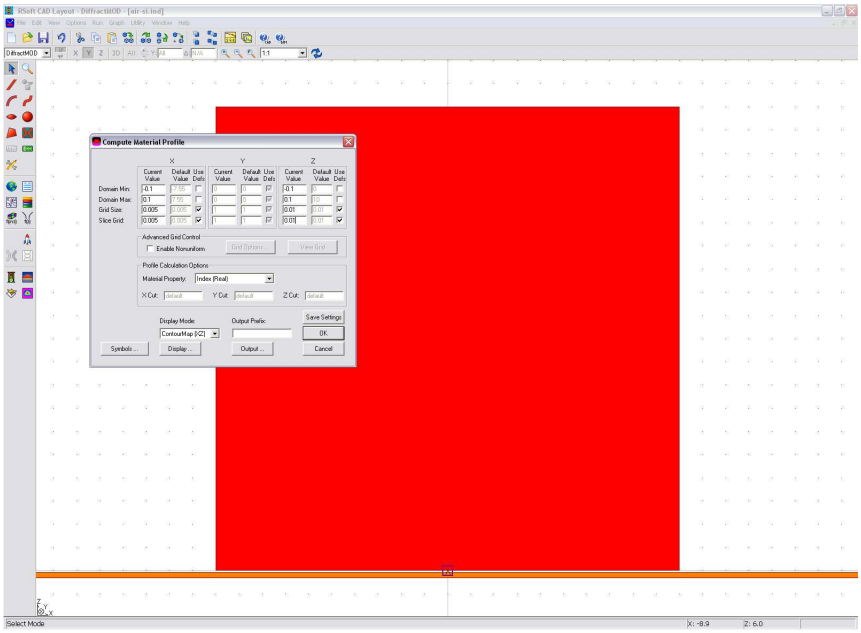

FIGURE 4.3: Specifying the computational unit-cell in DiffractMOD

Slice grid specifies the grid point in which the simulation is saved and displayed. It is better to set these two values equal in order to save all calculated data; having a larger slice grid than grid size can hide some useful information.

The X-min and -max values are set to -0.1 and 0.1 respectively, and the size of the cell in the Z direction has a length of 0.02 (-0.01 to 0.01). Leaving the grid size and slice grid to default, the refractive index of the interface in X-Z plane can be observed by choosing the "XZ counter map" option and pressing OK. Figure 4.4(a) shows the refractive index counter map of the unit-cell. It can be seen that the air-silicon interface which was set to be at $Z = 0$ is actually at $Z = -0.005$. Changing the Z grid size from the default value of 0.01 to 0.005 and 0.001 shows that the interface moves closer to $Z = 0$. In this simple simulation, since only a flat interface is simulated, the coarse or fine setting of the grid size does not affect the results. However in structures with features the grid size has to be set properly to define the interfaces accurately.

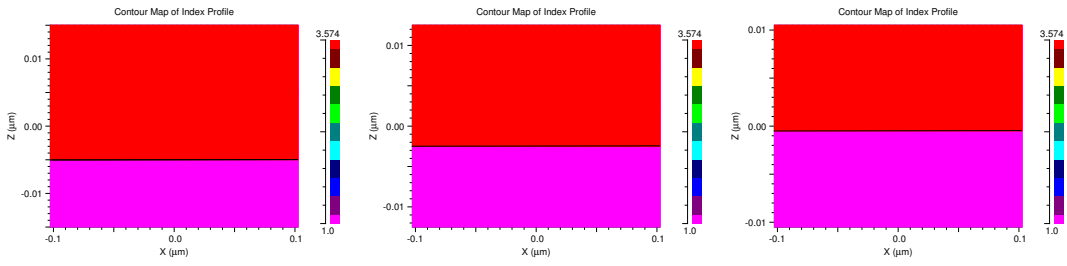

(a) (b) (c)

FIGURE 4.4: Changing the grid size in Z direction and defining correct interfaces.

Index Resolution	Time(sec)
0.1	0.2
0.01	0.3
0.001	2.9
0.0001	28.7

TABLE 4.1: Wavelength sampling vs simulation time

4.1.3 Defining Simulation Parameters and Running the Simulation

Figure 4.5 shows the dialogue box where the simulation parameters and outputs can be specified. The first box is the primary direction which specifies the direction in which the plane wave travels. It is left as the default value, +Z, which means the waves are travelling in the +Z direction and incident on the air-silicon interface from the air side. In this dialogue box "Domain Min and Max" are the same values as in the unit-cell dimensions. Number of harmonics specifies the number of harmonics while expanding the fields in Fourier transform. A greater number of harmonics gives greater accuracy while increasing the simulation time, thus a convergence test must be performed to optimise this value. "Index Resolution" is different from simulation grid. It specifies the number of layers in each direction with a homogeneous refractive index. These layers are used by RCWA through simulation to resemble the structure in a series of stacked layers and perform the calculations. A convergence test is also necessary to optimise the index resolution. The "Launch" box in this menu specifies the polarisation of incident light and the angle of incidence. The "Output" button specifies the field to be calculated and displayed. In this example, the plot type of "Vs. Wavelength" is chosen. The wavelength ranges from 0.3 to 1μm. "Step" specifies the steps with which the wavelength is changing. This value also has to be specified wisely to ensure neither time nor accuracy is being sacrificed. It was initially set to 0.1. The refractive index of silicon [**?**] input into the simulation, includes the dispersion relation of the silicon and so the box "Account Material Dispersion" has to be ticked so that DiffractMOD takes it into account. The rest of the fields specify the values to be calculated and outputted. Total reflected power was chosen to be calculated. The dashed green line in Figure 4.6 shows the results of this simulation.

To ensure the number of wavelength steps is set so that all the details in the reflectance spectrum are visible, the simulation is performed with smaller step values. It can be observed that decreasing the step value (increasing the number of steps) converges the results to the theoretical value (red line in Figure 4.6). However, as it increases the number of wavelengths it also increases the simulation time (Table 4.1). In this example the simulation is a basic modelling of reflectance from a flat interface and thus does not take a long time. However, for more complicated structures and simulations a balance has to be struck between accuracy and simulation time.

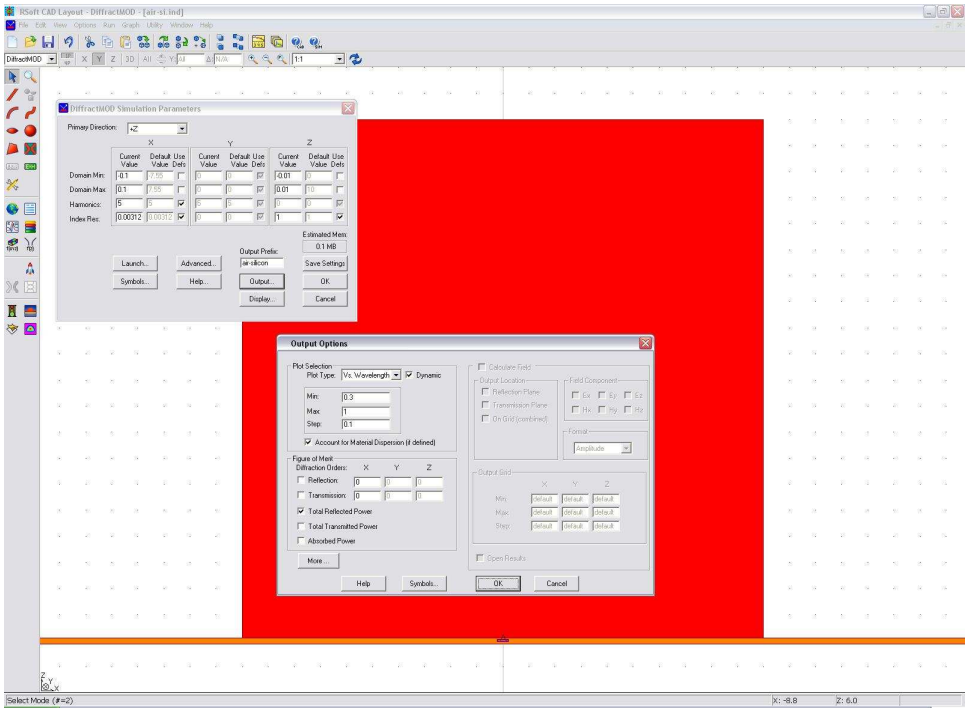

FIGURE 4.5: Setting simulation parameters in DiffractMOD

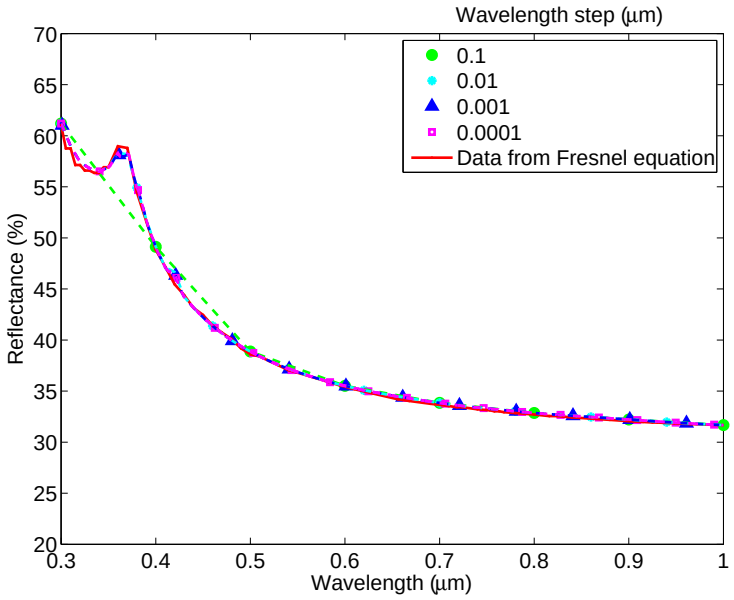

FIGURE 4.6: Reflectance at air-silicon interface calculated by DiffractMOD. The legend shows how changing the wavelength sampling value converges the results to the experimental value.

4.1.4 Simulation in 3D

The same simulation can be performed in 3D. In "Global Setting Window" (Figure 4.7) the dimensions of the simulation was changed to 3D. The structure can be viewed in 4 planes; this option is available on the toolbar at the top of the window. The image in the Y-Z plane and the X-Y plane shows that the unit-cell in the Y-direction has a large value compared to the X and Z values set previously, which is not essential. The unit-cell has to be redefined through "Display Material Profile". Y-max and -min are set to -0.1 and 0.1 respectively. The grid spacing and slice grid will be left as default values along with other simulation and segment values. The unit-cell can be observed in 3D plot, changing the Display Mode into 3D Volume.

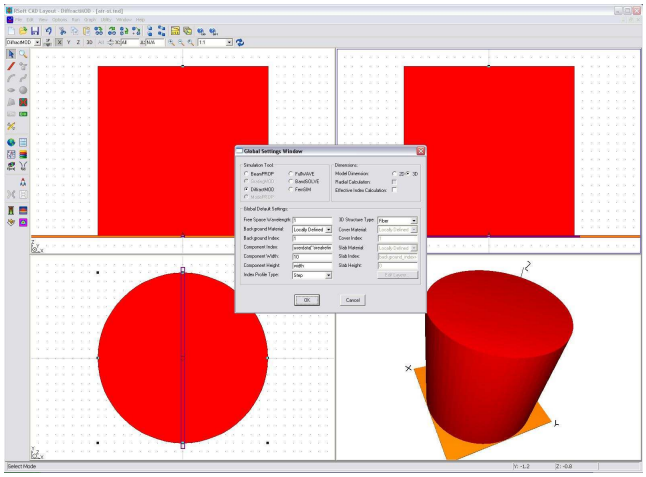

FIGURE 4.7: The simulation in 3D and the new unit-cell.

The simulation is performed with similar settings to the 2D simulation. The wavelength step is set to 0.001. The results are identical to the results of the 2D simulation (Figure 4.8). Having the unit-cell at the interface changed from a square shape to a rectangular shape does not affect the calculated results.

4.1.5 Defining the Moth-eye Structure

This structure formed the basis of making a moth-eye structure. Thus new components were added to this structure gradually to make the moth-eye structure. Gradual changes were monitored with simulation tests to ensure settings were correct.

The cross section of a component can be chosen to have square, circle or polygon shapes. In order to change the shape of the cross section to square/rectangle, "channel" is chosen as the 3D structure type in the properties of segment. New symbols are defined in the symbol dialogue box as below. The height of the substrate is also changed to 2μm. The

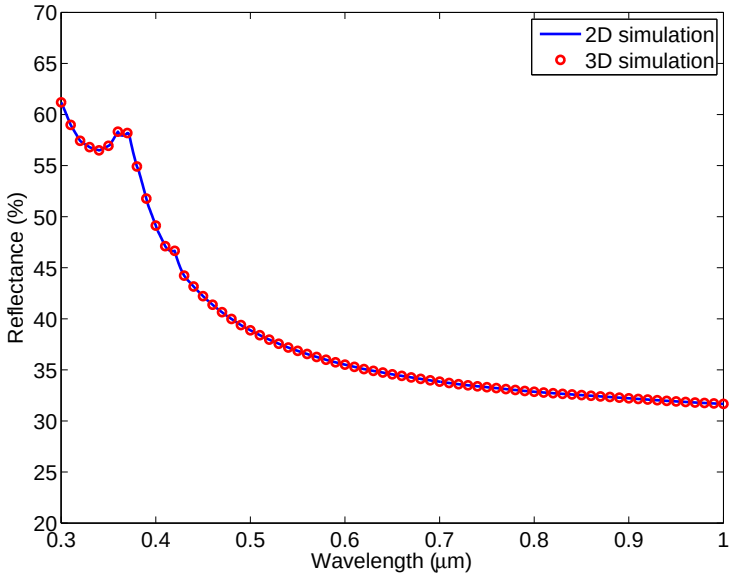

FIGURE 4.8: Reflectance of silicon-air interface in 2D and 3D simulation in Diffract-MOD

refractive index of the rod is set to silicon. The new values are chosen to be close to moth-eye dimensions (Chapter 2).

rod-width width of the rod in the X direction, set to "0.1μm"

rod-height width of the rod in the Y direction, set to "width"(to give square cross section)

period periodicity of the square lattice (spacing between adjacent rods), set to "0.25μm"

Z-height height of rods in Z direction, set to "0.2μm"

The structure consists of a rod arranged in a square lattice. The periodicity has to be set for the unit-cell. In order to define a square unit-cell with the periodicity of 0.25μm, the minimum and maximum values for X and Y are both set to $-\frac{period}{2}$ and $\frac{period}{2}$ respectively. The Z-min and -max values have to be set so that it includes the height of the rods and the interface between the rod and the substrate. Thus a value of 0.01 is added to the top and bottom of the length of protuberances. Keeping the grid size and slice grid value as default, 0.005, for X and Y and 0.01 for Z, the refractive index counter map of the structure is plotted in three planes to ensure the structure is correctly set (Figure 4.9). The counter-map of the X-Y plane is plotted at the plane Z= 0.1. The refractive indices are calculated in the wavelength of 1μm which was set in the global settings dialogue box ("free space wavelength"). The red colour represents the value of the refractive index at $\lambda = 1\mu$m. The pink colour represents the background, in this case air with the refractive index of 1. As can be observed in the images, at the edge

of the structure in the X and Y direction, the refractive index is presented with a green colour with a value between that of the red and pink. This indicates that the software has averaged the refractive index of the material at these edges resulting in a coarse grid size in X and Y directions. They are left at the default value in this work. The structure to be simulated in DiffractMOD, is presented in Figure 4.10.

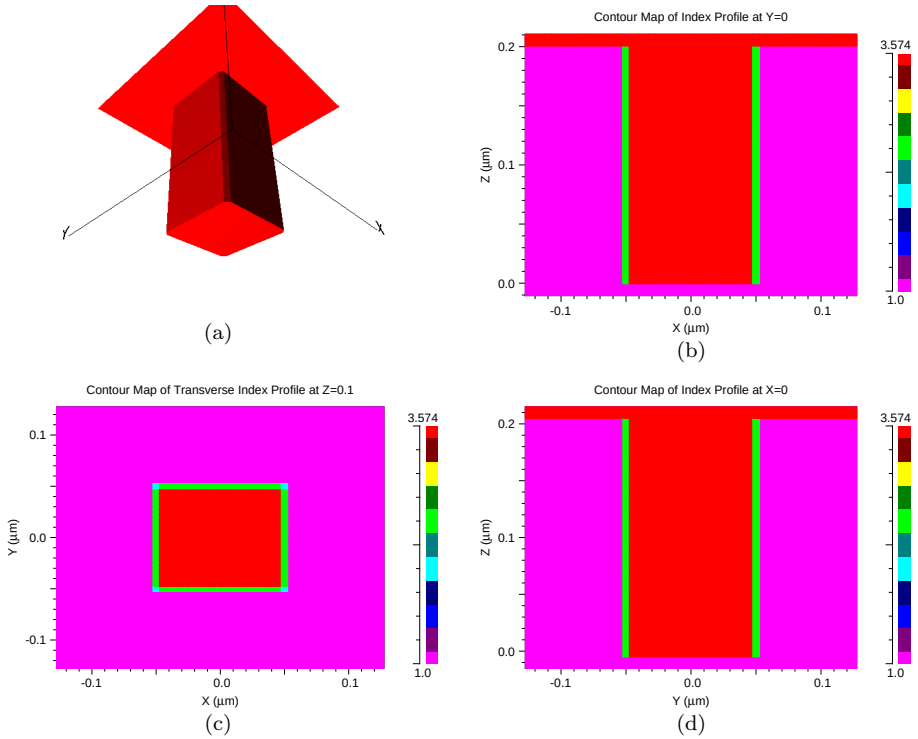

FIGURE 4.9: Counter-map of the unit-cell of a square rod in square lattice in DiffractMOD

To ensure that the simulation runs correctly, a test is performed in which the size of the square rod is gradually increasing until it covers the whole unit-cell. The last configuration gives an air-silicon interface like the previous example, where the height of the substrate is slightly bigger (substrate + height of the rod). Thus the results have to resemble the air-silicon reflection pattern as the size of the rod increases. Figure 4.11(a) shows the reflectance spectrum of the structure while the width of the rod increases. The width of the rod changes from 0.05μm to 0.25μm, in steps of 0.05μm. The last value is equal to the width of the unit-cell produces a block of silicon covering the whole unit-cell, giving a flat interface of silicon at higher Z point. The reflectance value for rods of width 0.25μm is similar to the reflectance value of silicon. The other interesting feature of this diagram is that for the rod of smallest width, the reflectance spectrum at higher wavelengths is close to the reflectance of silicon. This is because at higher wavelengths the width of the rod is quite small and can be resolved in the wavelength, thus the structure seems like a flat silicon-air interface to the light. For rods of width between these two values, the rods cause the reflectance at the interface to decrease, and introduced fluctuations in the reflectance spectrum along the wavelength.

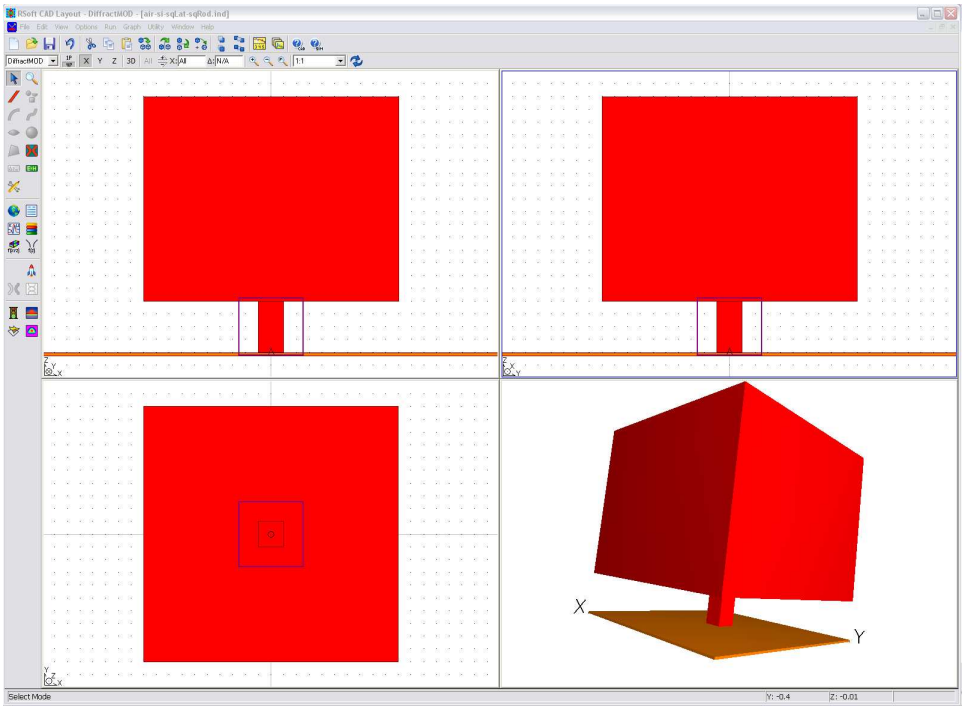

FIGURE 4.10: Simulation window for a square lattice of rods on a substrate in DiffractMOD

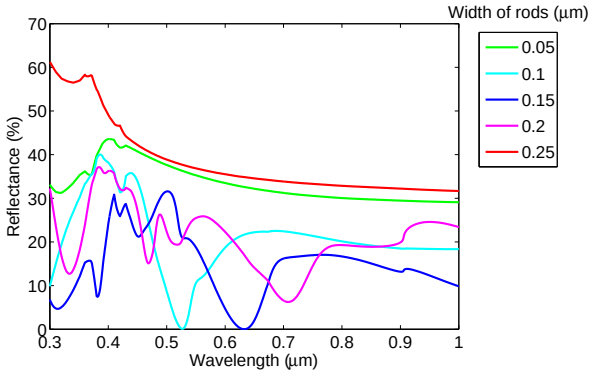

(a)

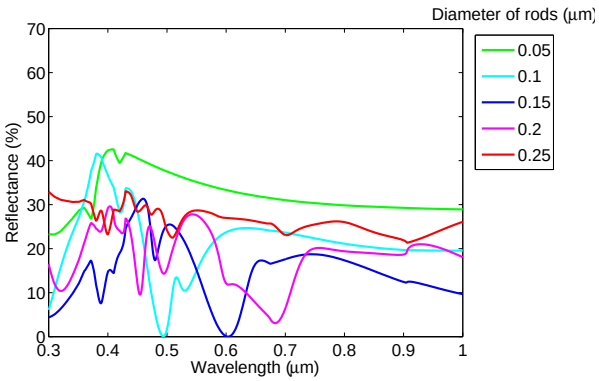

(b)

FIGURE 4.11: Reflectance value for a width scan for rods in a square lattice with (a) square cross section (b) circle cross section

The base of the protuberances in a moth-eye structure has a circular shape, thus the shape of the cross section of the rods are to change from a square shape to a circle shape. The diameter of the circles are equal to the width of the sides of the square rods. The unit-cell is kept constant as shown in Figure 4.12. Results are presented in Figure 4.11(b). The results for the diameter of 0.05μm to 0.2μm are quite similar to the previous structure with square-shaped rods of the same width, however, for the diameter of 0.25μm there is a significant difference in reflectance spectrum. As the diameter increases the circular rods cover a larger portion of the unit-cell, however the circles cannot cover the unit-cell completely and some space will be left uncovered at the edge of the unit-cell. Thus unlike the previous structure, when the width of the circle rods equals to the width of the unit-cell, the homogeneously flat interface of air-silicon is not produced. Hence it is expected to see a behaviour different from an air-silicon flat interface (or square cross sectional rods with width of 0.25μm).

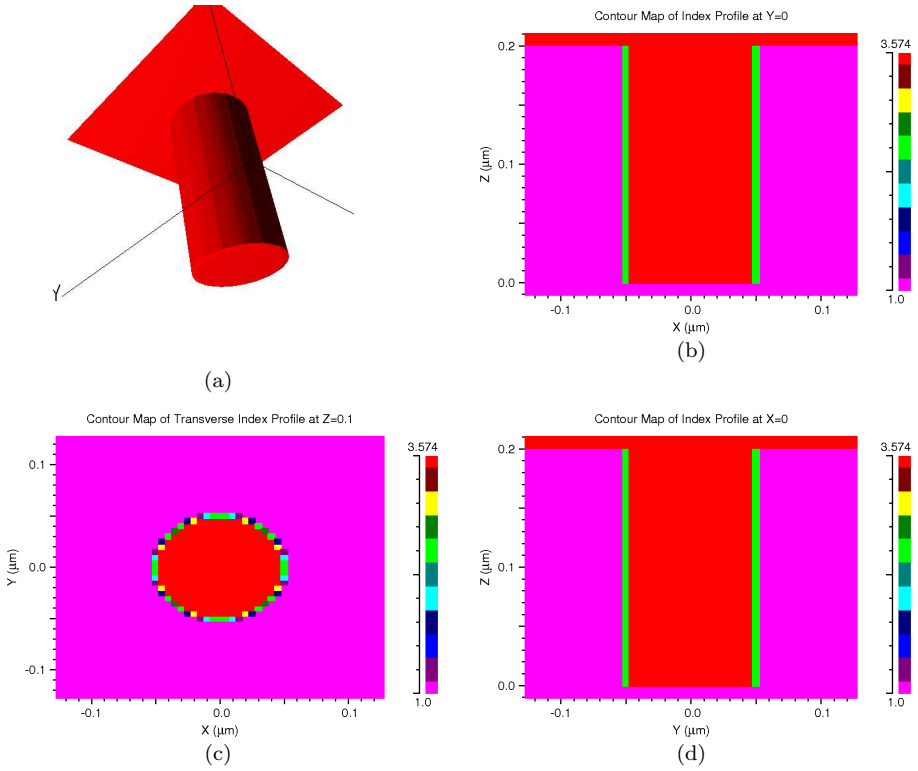

FIGURE 4.12: Counter-map of the unit-cell of a cylindrical rod in square lattice in DiffractMOD

In the moth-eye structure the rods are arranged in a hexagonal lattice. A hexagonal lattice has a unit-cell of rectangle shape with two or four rods (Figure 4.13). Thus the unit-cell was changed from square to rectangle. Later more rods were added to the unit-cell. The height of the unit-cell in the Y direction is changed to $\sqrt{3}a$ where a is the periodicity of the hexagonal lattice, and the width of the cell in the X direction. The unit-cell in 3D is plotted in Figure 4.14(a). The width of the circle-shaped rods change from 0.05μm to 0.25μm and reflectance results are plotted in Figure 4.14(b). The reflectance spectrum of rods with larger width values is showing a more different

behaviour comparing to previous structures. This is caused by the larger empty space between rods as the unit-cell in the Y direction is larger than previous unit-cells. However, in the case of the smaller rods, there is still a similarity between the cylinder rods in the rectangle unit-cell and the square unit-cell.

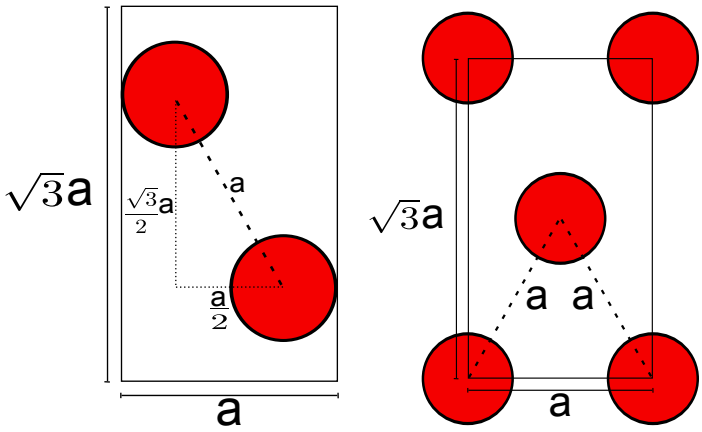

(a) (b)

FIGURE 4.13: A unit-cell of hexagonal lattice of (a) two rods completely in the unit-cell, and (b) one rod in the center and four quarters at each corner. The unit-cell is shown by the black rectangle.

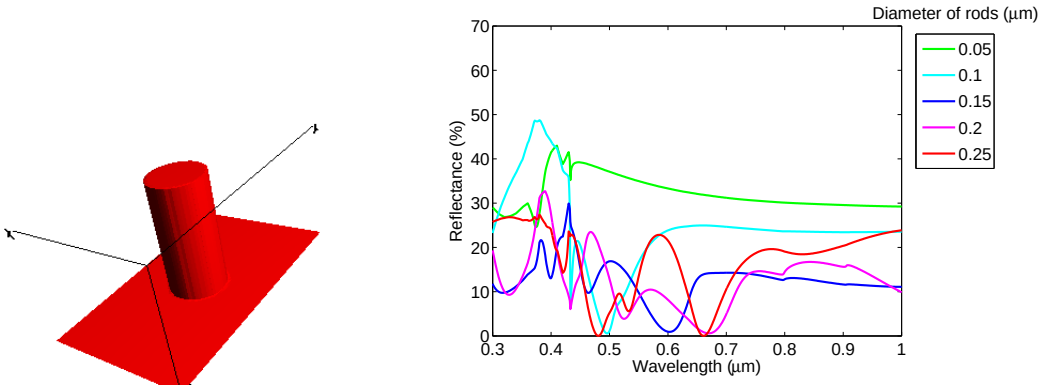

(a) (b)

FIGURE 4.14: (a) Cylindrical rod with a rectangle unit-cell in 3D (b) Reflectance of the structure for a scan of rod's radius.

In order to produce the hexagonal lattice, additional rods were added according to the unit-cell arrangement (Figure 4.13). A hexagonal unit-cell can be defined either with two rods in the unit-cell, or one rod in the unit-cell and 4 quarters at each corner of the unit-cell. However the arrangement of the two rods fully in the unit-cell is limited in the maximum radius of rods. In this arrangement the radius of the rods cannot have values larger than $\frac{a}{4}$ as they will cross the boundaries of the unit-cell. This limitation does not exist for the other arrangement (Figure 4.13(b)).

Simulations were performed employing the two unit-cells, with the diameter of the rods set to 0.0625μm and 0.05μm and periodicity of 0.025μm. Since the diameter of the rods

were less than 100nm, the index resolution in the X and Y direction was set accordingly so that DiffractMOD distinguished the interfaces correctly. Reflectance results are plotted in Figure 4.15(c). The match between the results of two the different unit-cell arrangements shows that DiffractMOD implements a correct hexagonal lattice independent of the unit-cell.

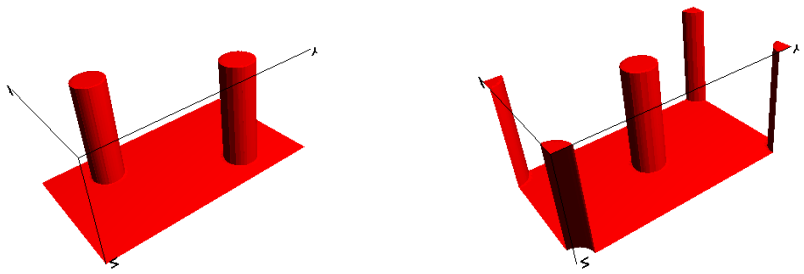

(a) (b)

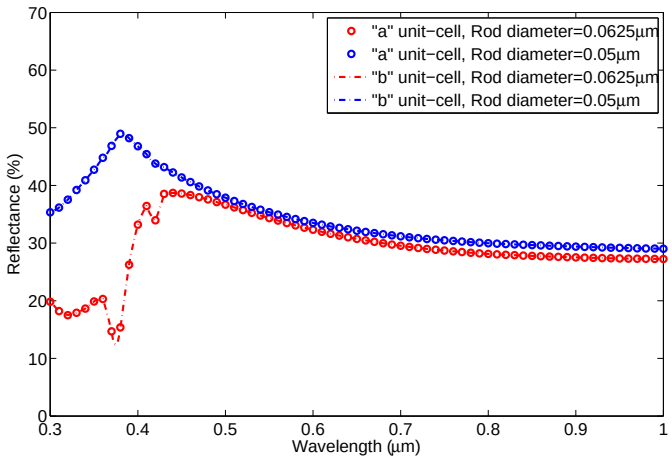

(c)

FIGURE 4.15: 3D volume demonstration of the unit-cell of a hexagonal lattice with the arrangement of (a) two rods in the unit-cell, (b) one rod in the unit-cell and four quarters at each corner. (c) Comparison of the reflectance of (a) and (b) structures with the periodicity of 0.25μm, and rod diameter of 0.0625μm and 0.05μm.

4.2 Simulation of Silicon Moth-eyes in DiffractMOD

4.2.1 Profile and Topography

The profile of protuberance has to provide a gradual change in the refractive index at the existing interface to reduce the reflectance from the surface. A variety of protuberances' shapes was studied to fulfil this aim: cones, tapered cylinders, paraboloids, Gaussian and sinusoidal shapes [85]. The optimum protuberance profile was reported to be a quintic shape (Section 2.3.2), however such a structure is hard to fabricate as the

etching stage will remove the sharp tip. Thus, a rounded tip profile similar to Gaussian, sinusoidal or paraboloid is more likely in practice. Sinusoidal profiles have a mirror symmetry along the horizontal axis and provide the same profile in both directions in the vertical axis. Such a profile provides a gradual increase of the refractive index in either vertical direction. This similar refractive index change has proven to be effective to decrease the reflectance from an interface. Since a similar mirror symmetry does not exist at Gaussian or sharp-tipped profiles, this work employs a sinusoidal profile to mimic the protuberances in a moth-eye structure. The profile of the structure is proportional to Equation 4.1. The protuberances are arranged in a hexagonal lattice (Figure 4.16) similar to that of the actual moth-eye structure. The lowest reflectivity is observed in a hexagonal lattice where the protuberances are close-packed and touching at the base. Thus the diameter of the base of protuberances are set to be half of the periodicity to provide a close-packed arrangement of protuberances in the hexagonal lattice. Figure 4.17 shows the moth-eye structure set in DiffractMOD.

$$z = \cos(x, y) + 1 \tag{4.1}$$

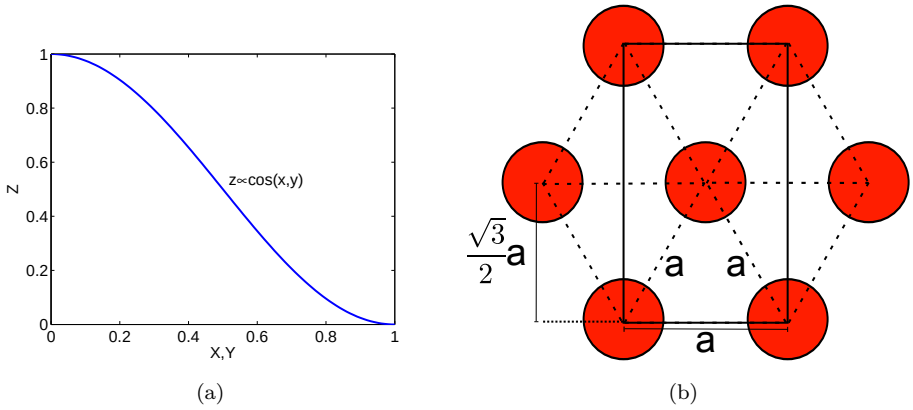

(a) (b)

FIGURE 4.16: (a) $z = \cos(x, y) + 1$, the profile of moth-eye protuberances in DiffractMOD (b) arrangement of protuberances in a hexagonal lattice with the rectangular unit-cell of $a \times \sqrt{3}a$.

4.2.2 Convergence Test

To perform accurate computational studies it is essential to determine the optimum value of the simulation parameters. In DiffractMOD the index resolution value in the Z direction and the number of harmonics are the two parameters that determine the accuracy of the simulation results. Index resolution in X and Y directions determine the level of accuracy with which the structure defined in the CAD layout is imported into DiffractMOD. However, these values are dependent on the number of harmonics to be used within the simulation, the dimensions of the structure and the size of the

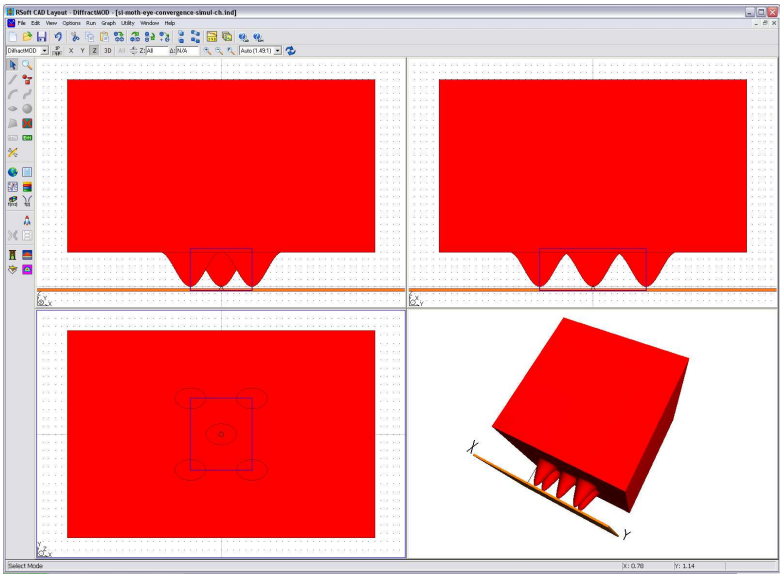

FIGURE 4.17: Moth-eye cosine profile in DiffractMOD

simulation domain (unit-cell) in X and Y directions. RSoft default values of X and Y index resolution were used for simulations throughout this work.

A new parameter, "the number of layers in the Z direction", was defined to determine the value of the index resolution according to Equation 4.2.

$$\text{Index Resolution} = \frac{\text{Height of Structure in the Z direction}}{\text{Number of Layers in the Z direction}} \tag{4.2}$$

Convergence results are plotted in Figure 4.18. The mean average of reflectance from a silicon moth-eye structure with a height of 100nm and periodicity of 100nm is plotted against the number of layers in the Z direction and the number of harmonics. Figure 4.18(a) shows that results converge when the number of layers in the Z direction reached the value of 60. However, the simulation time increased as more layers were added along the Z axis. To provide an optimum balance between time and accuracy, the number of slices was chosen as 60 where the mean average of reflectance differs by a value of 0.02% from the converged value.

Increasing the number of harmonics, increased the simulation time by a greater value, reaching almost four days at the number of harmonics of 10. Thus only a limited number of harmonics ($2-10$) were tested and the results are plotted in Figure 4.18(b). The value of the mean average of reflectance spectrum at normal incidence was tending to converge at the number of harmonics of 6 with the third decimal point changing. At this point the simulation takes 6hours. The height of the moth-eye structure in these simulations is set to 100nm while the natural structures are as tall as 200nm and literature has reported the theoretical study and fabrication of moth-eyes of taller protuberances (Chapter 2). It has to be considered that moth-eye structures of higher protuberances need more time for

simulations and consequently the total simulation time will increase to higher values than Figure 4.18(b). Interpolation of the curve in Figure 4.18(b) gives the "pseudo-converged" value of 16.8% for the mean average reflectance. At the number of harmonics of 4, the average reflectance value is 16.4%, 0.4% less than the pseudo-converged value, which is 2.3% of the pseudo-converged value. An accuracy of ±2.3% is accurate enough to gain a good qualitative understanding of the reflectance behaviour of moth-eye structures. Hence, a value of 4 was chosen to balance the time and accuracy for all the simulations performed throughout this work.

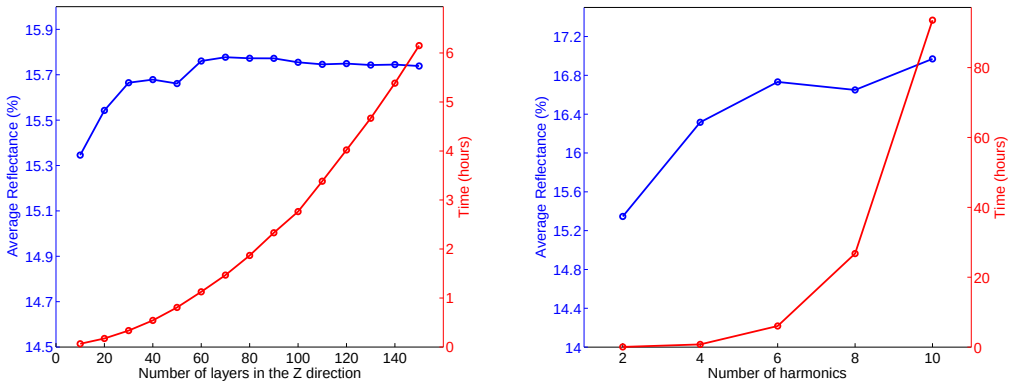

(a) (b)

FIGURE 4.18: Convergence test for moth-eye simulation in DiffractMOD (a) number of slices in the Z direction (b) number of harmonics in the Fourier transform

4.2.3 Results

4.2.3.1 Height and Periodicity at Normal Incidence Reflectance

The effect of changing the periodicity and height on the reflectance behaviour of silicon moth-eye structures at normal incidence for un-polarised light was studied using DiffractMOD and the results are presented in Figure 4.19. The periodicity ranges from 0.1 to 0.4μm in steps of 0.01μm. The maximum limit of the periodicity, 0.4μm, was chosen as the cut-off value to prevent the occurrence of diffraction orders at normal incidence (Table 4.2). The height was varied between 0.1 and 0.8μm in steps of 0.1μm. It can clearly be seen that increasing the height reduces the overall reflectance. The low reflectance values of 2% or less (dark blue) expand and cover a greater area of the graph as the height increases.

The influence of periodicity on the reflectance spectra of moth-eye structures can be extracted from the same graphs. Figure 4.19 shows that increasing the periodicity shifts the low reflection region (dark blue) towards longer wavelengths, this is more clear in (a), (b) and (c) plots where the height is set to 0.2 and 0.3μm respectively. In these two plots, for shorter periodicities the low reflection spectrum is in lower wavelength ranges and as

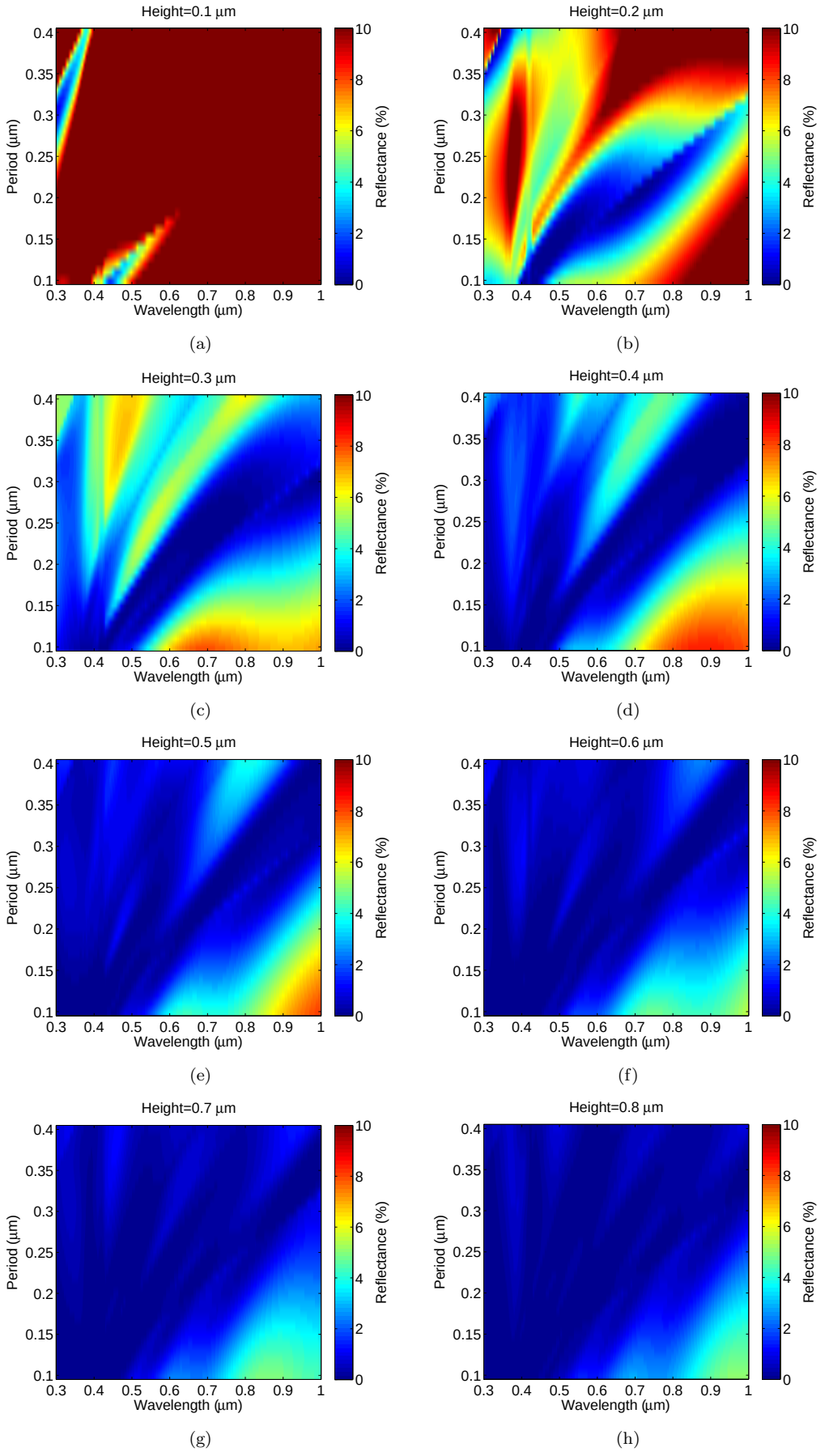

FIGURE 4.19: Reflectance of silicon moth-eye structures at normal incidence for periodicity range of 0.1 to 0.1μm in steps of 0.01μm, and the height of 0.1 to 0.8μm in steps of 0.1μm, for the wavelength range of $0.3 - 1\mu$m.

	Normal Incidence	Oblique Incidence
period(d)	$d < 400$nm	$d < 200$nm
height(h)	$h > 320$nm	$h > 320$nm

TABLE 4.2: The range of period and height of moth-eye structures so as to prevent occurrence of diffraction orders in the reflectance spectrum for the incident wavelengths of between $400 - 800$nm according to Table 2.1

the period increases on the vertical axis the low reflectance region travels towards longer wavelengths. This is also the case for structures with taller protuberances, however it is less clear as the reflectance value is reduced as a result of the height increase.

In Figure 4.19 the profile of the plots do not change shape and only change value. This is more clearly seen in Figure 4.20 where the reflectance spectrum of certain periods at all scanned heights is plotted against wavelength. In each plot the height is kept constant while the periodicity changes. Comparing the reflectance of structures with the same periodicity while the height is increased confirms that the reflectance spectrum is reduced towards lower reflectance values but the position of peaks and troughs in terms of wavelength is not changed. However, it seems the reduction of reflectance is of greater magnitude at wavelengths shorter than 0.7μm. The reduction of the reflectance value implies that the difference between the reflectance minimum and maximum value reduces and the oscillation of the reflectance within the whole spectrum is smoother compared to low height structures.

The mean average of reflectance of these structures is presented in Figure 4.21. Structures with shorter pillars show high values of reflectance starting from 20%. This value decreases with the increase in the height of protuberances until it reaches 1% at the height of 0.47μm for the periodicity of 0.28μm. The mean average is less sensitive to the value of periodicity, especially for short protuberances of $0.1 - 0.2\mu$m height, but as the height increases the mean reflectance is more affected by the value of periodicity.

4.2.3.2 Optimisation of Silicon Moth-eye Structures

The results of the previous section showed that the height and periodicity of the moth-eye structure can be designed to set the low reflectance region of the spectrum to a desired wavelength range and value. Hence optimization of moth-eye structure depends on the application needs. This section aims to optimise the moth-eye structure in the visible regime while exposed to solar irradiance. The intensity of solar irradiance during a twenty four hour varies with wavelength and time of the day (angle of incidence). In order to include the effect of such variations on the reflectance properties of anti-reflective structures, weighted reflectance (R_w) is used. It is calculated by Equation 4.3,

$$R_w = \frac{\Sigma(R(\lambda) \times I_T(\lambda))}{\Sigma I_T(\lambda)} \tag{4.3}$$

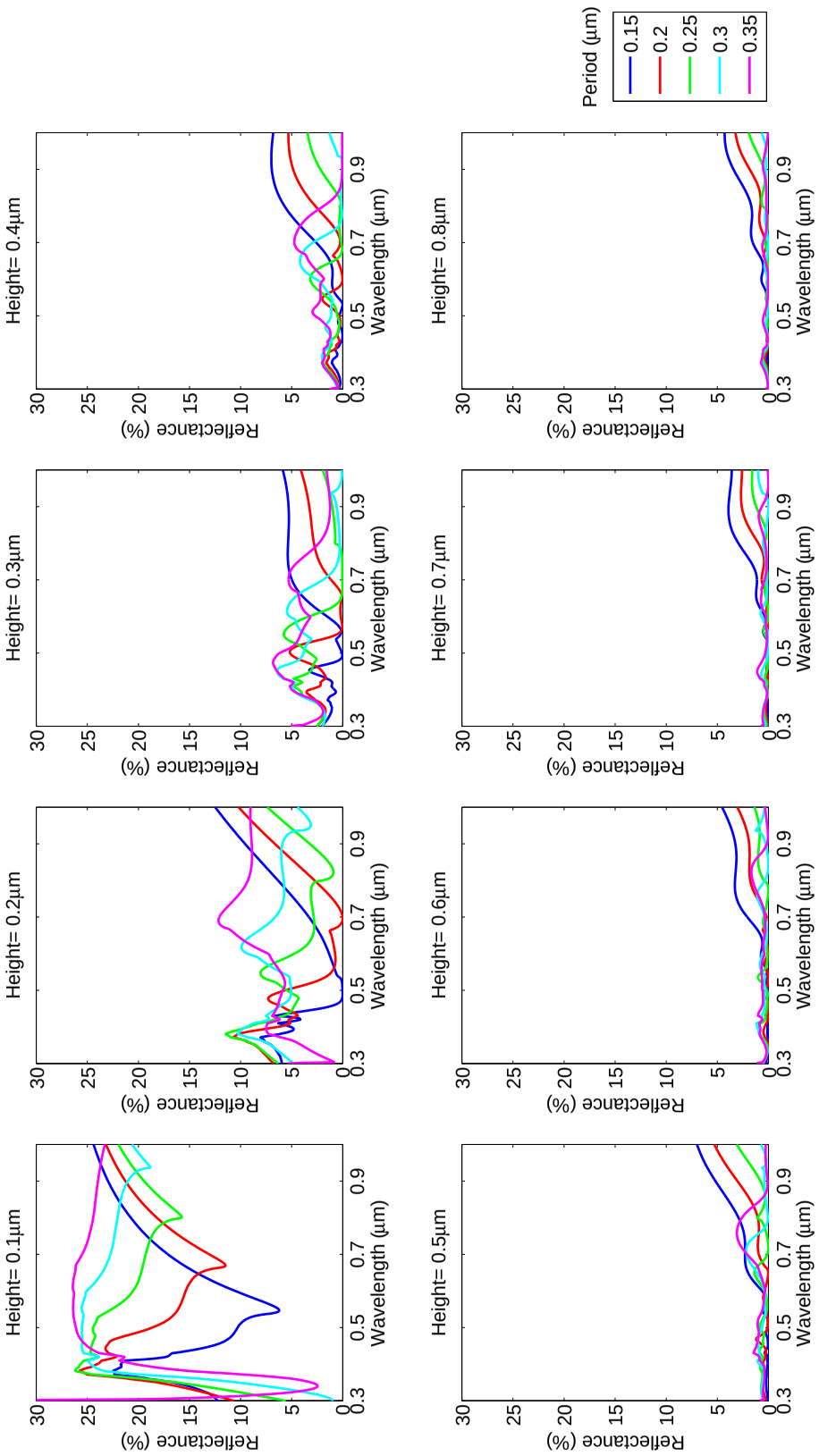

FIGURE 4.20: Reflectance of silicon moth-eyes at normal incidence for the periodicity range of $0.15 - 0.35\mu$m in steps of 0.5μm and height of $0.1 - 0.8\mu$ m in steps of 0.1μm.

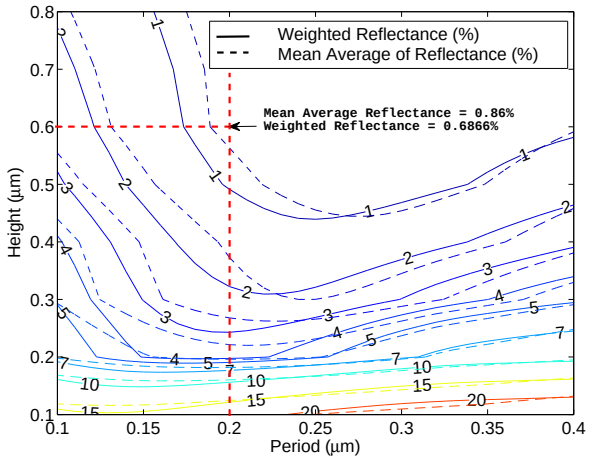

FIGURE 4.21: Contour plot of mean average reflectance and weighted reflectance of silicon moth-eye structures with periodicity of $0.1-0.4mu$m and height of $0.1-0.4\mu$m. The mean average is the dashed line and the weighted reflectance is the solid line. The point marked with the arrow is chosen as the optimised point with no diffraction orders and the mean reflectance and weighted reflectance value lower than 1%.

Where $R(\lambda)$ is the reflectance of the silicon moth-eye structure, I_T is the total irradiance illuminated on the structure, in the case of photovoltaics, the solar spectrum. The solar spectrum data provided by SPCTRL2 from National Renewable Energy Laboratory (NREL) was used previously to produce the total irradiance from 6 am to 12 am (half a day), corresponding to an angle of incidence changing from 90° to 0° [14, 15], and is presented in Figure 4.22. The photon flux density (Figure 4.22(b)) is calculated by dividing the total irradiance by the energy of a photon at each wavelength, $h\nu$.

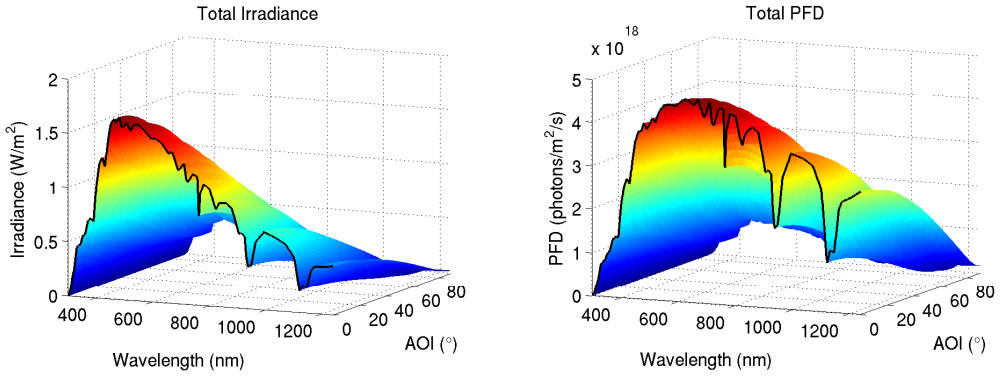

(a) (b)

FIGURE 4.22: (a) Total solar spectral irradiance (b) Total photon flux density of the solar spectrum [15].

The weighted reflectance value of the moth-eyes studied in the previous section is shown in Figure 4.21 along with the mean average reflectance. There is a close correlation between the mean average and the weighted reflectance for shorter heights, but the difference increases as the height increases. For a height of 0.47μm the weighted reflectance can be as low as 1%, provided the periodicity is optimised. As the height increases the

area in which the reflectance is less than 1% expands into shorter and longer periods and in fact more into longer periods. Thus it can be understood that as the height increases above 0.8μm, the reflectance decreases and reaches lower values while the periodicity range which covers the reflectance value of under 1% also expands. However, attention should be paid that fabrication of pillars with high aspect ratio (height of pillars to radius) is difficult and not practical. In the field of photovoltaics, high aspect ratio increases the surface area of the cell and recombination of holes and electrons and thus decreases the short circuit current which reduces the efficiency of the cell. Also, in thin film solar cells, pillars of tall height are not desirable. These limitations will limit the available range of the design parameters for moth-eye structures. In structures with periodicity above 400nm and 200nm, diffraction orders occur at normal incidence and oblique incidence respectively (Table 4.2). Considering the aforementioned limitations on moth-eye structures with high aspect ratio, along with limitations within the parameter choice to suppress diffraction orders, the periodicity is chosen to be on the border of the no diffraction order limit, at 200nm. For this value of periodicity the mean average and weighted reflectance are both under 1% when the height is 0.6μm (Figure 4.21). Thus these parameters are suitable to achieve reflectance under 1% without diffraction at any angle of incidence (AOI) across the wavelength range of $400 - 800$nm.

The reflectance spectrum of this structure for un-polarised light, and the two orthogonal polarisations of s and p, is shown in Figure 4.23. The reflectance is less than 1% until it reaches a wavelength of 0.748μm. Above this wavelength, the reflectance value increases to 3% at the end of the wavelength range (1μm). There is a difference of less than 0.5% between the reflectance at the two orthogonal polarisations which is greatest below 0.4μm and above 0.7μm. Since the plane of periodicity is a hexagonal lattice and there is not a 90 degree symmetry in the structure a slight difference is expected. Electric and magnetic fields encounter different rod arrangement at the two orthogonal polarisations and thus such a difference exist.

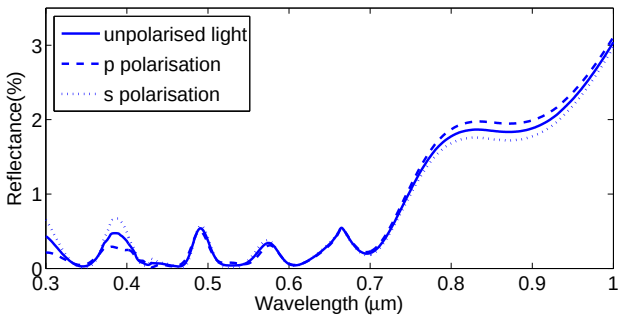

FIGURE 4.23: Normal incidence reflectance of silicon moth-eye structure with periodicity of 200nm and height of 600nm, for unpolarised (solid line), p polarised (dashed line) and s polarised light (dotted line).

4.2.3.3 Reflectance at Arbitrary Angle of Incidence

The previous section considered reflectance at normal incidence. However in practical situations the incident light comes from a range of angles. Thus it is essential to study the behaviour of an anti-reflection structure at different angles of incidence. The reflectance of the optimised structure was calculated at angles of incidence from 0° to 80° in steps of 10°, for both s and p polarisation, and is presented in Figure 4.24. The plane of incidence is kept constant. The change in the orientation of the plane of incidence is similar to changing the azimuth angle of the sample under the incident light and will be discussed in the Section 4.2.3.4.

Figure 4.24(a) and Figure 4.24(b) show that as the angle of incidence increases the value of the reflectance of the structure also increases for both polarisations. This is clear when looking at the total reflectance at different AOIs, Figure 4.25(a). The total reflectance is constant up to an AOI of 40°, after which it increases sharply. The general shape of the spectrum remains constant and the fluctuations become more significant as the AOI is increased.

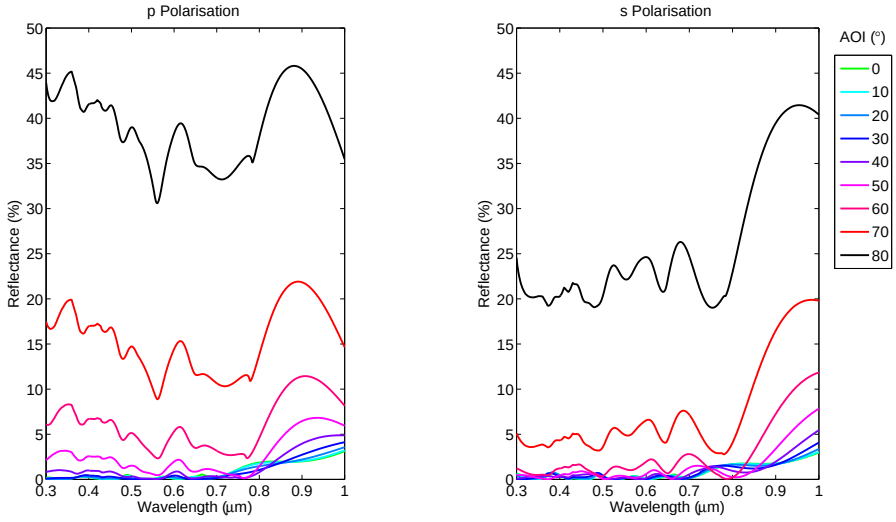

(a) (b)

FIGURE 4.24: Reflectance spectrum of silicon moth-eye structure with periodicity of 200nm and height of 600nm at AOI of 0° to 80° in steps of 10° for (a) p polarisation and (b) s polarisation.

Figure 4.25 plots the total reflectance, maxima and minima values of the reflectance spectrum at different AOIs for each polarisation. All values are increasing for both polarisations as AOI increases. While the rate of increase of maxima for both s and p polarisation is very similar, the rate of increase of minima is smaller for the p polarised light compared to s polarised light. Hence, the total reflectance at p polarisation has higher values than the s polarisation. The total reflectance of this moth-eye structure

at AOI of 0 to 80° increases from ≈ 1% to 40%, 26% and 33% for p, s and unpolarised light respectively.

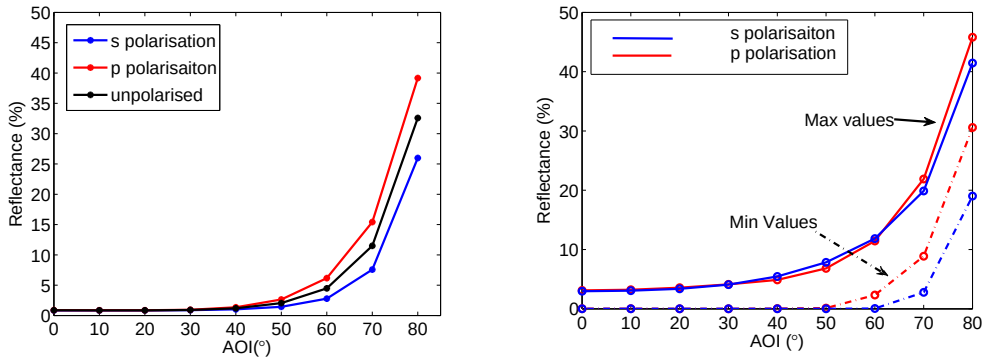

(a) (b)

FIGURE 4.25: (a) Total reflectance at AOI changing from 0 to 80° for s and p polarisation and unpolarised light (black). (b) The plot of maxima (solid line) and minima (dot-dash line) of reflectance spectrum for each AOI and polarisation (s polarisation in blue and p polarisation in red).

The reflectance value of the structure for s and p polarisation against AOI at certain wavelengths is presented in Figure 4.26. At p polarisation the reflectance remains constant until the AOI of 40° for wavelengths of under 0.8μm, but for longer wavelengths the reflectance is more sensitive to AOI. However at s polarisation the value of reflectance stays constant up to AOI of 60° for the wavelength of lower than 0.5μm but the range over which the reflection is insensitive to AOI reduces to 40° and is even lower for longer wavelengths. For the most of the spectra the reflectance of p polarisation shows higher values compared to s polarisation. However at a wavelength of 1μm the behaviour of s and p polarisation changes and p polarisation has lower values. This is a remarkable feature in the angular reflectance of this moth-eye structure. The angular reflectance of silicon at s polarisation normally has larger values of reflectance compared to p polarisation. This is because the particles oscillating in the direction of polarisation at p polarisation cannot radiate light in the direction of oscillation and thus at a certain angle there is no reflectance from the surface of the material at p polarisation. This angle is called the Brewster angle. However the silicon moth-eye structure presented in this chapter shows higher values of reflectance for p polarisation compared to s polarisation for wavelengths lower than 1μm which means that the moth-eye structure has cancelled the Brewster angle effect and has produced an inverse polarisation behaviour. The inverse polarisation was observed in literature [22] at wavelengths of 1250μm. However the optimized moth-eye structure studied in this chapter shows the inverse polarisation within the whole visible spectrum.

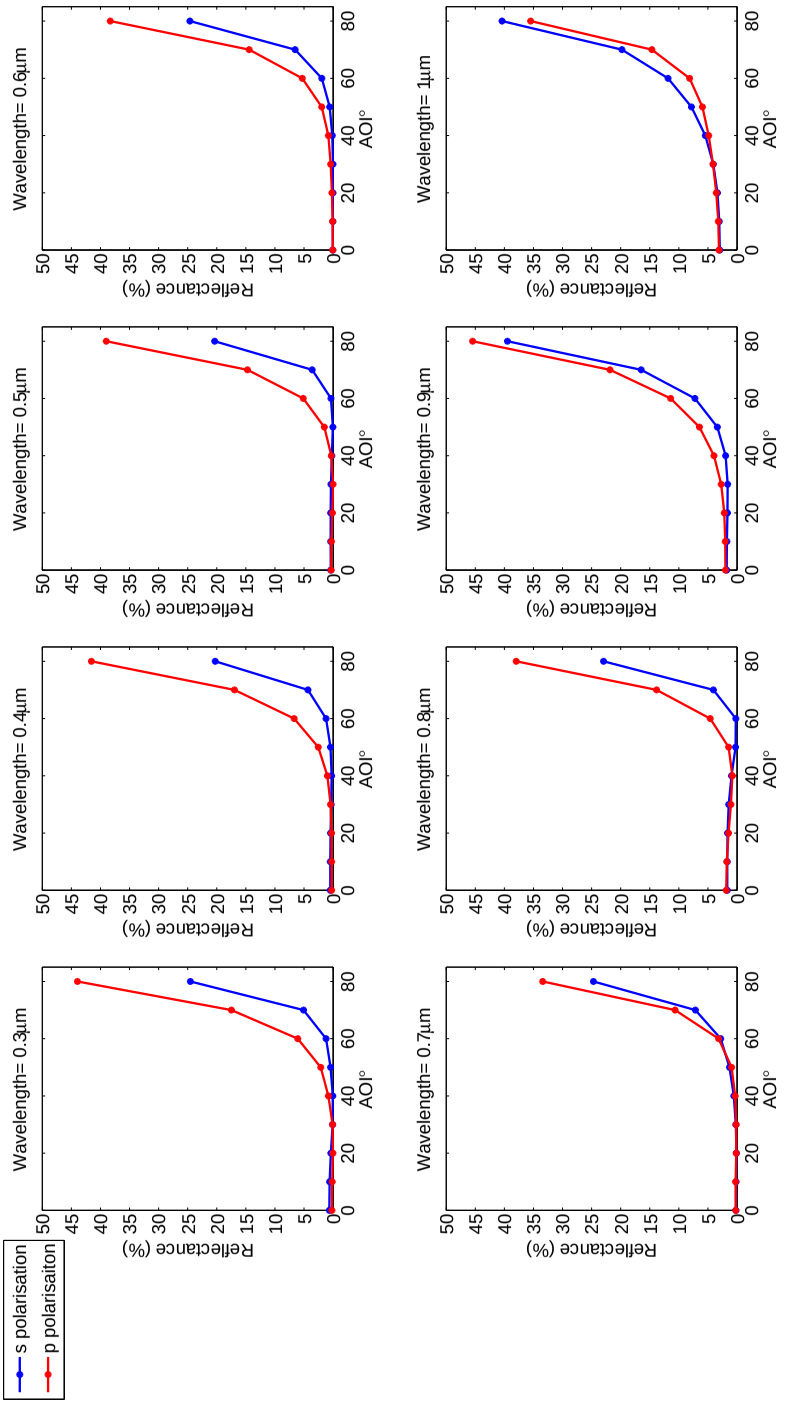

FIGURE 4.26: Reflectance of silicon moth-eye structure with periodicity of 200nm and height of 600nm at AOIs of 0° to 80°, at wavelengths of 0.3μm to 1μm in steps of 0.1μm, for p polarisation (red) and s polarisation (blue).

4.2.3.4 Azimuth Angle

The angle of incidence variations studied in the previous section was studied while maintaining a constant plane of incidence. However, the plane of incidence can also rotate. This is the same as rotating the sample and changing the azimuth angle. The protuberances are arranged in a hexagonal lattice in a moth-eye structure. Therefore if the azimuth angle is changed and the sample is rotated, the electric and magnetic field of the incident beam observe a different profile of the refractive index and would be expected to produce a difference in the reflectance spectra (Figure 4.27). Computational work was performed to investigate the influence of the azimuth orientation of moth-eye structures on their reflectance spectra. The reflectance spectra of the optimized silicon moth-eye structure was studied for two orthogonal polarisations and angles of incidence from 0° to 80°. The results are plotted in Figure 4.28 for s and Figure 4.29 for p polarisation. A hexagonal lattice is a 6-fold symmetric plane, thus the behaviour of the sample is unique at azimuth angles between 0° and 30°, and repeats every 60°. In this section the azimuth angle has varied from 0° to 45° to cover the 30° of symmetric unit and confirm the repetition of the results for azimuth angles greater than 30°.

In Figure 4.28 and Figure 4.29, the change of the azimuth angle of the lattice does not show a significant change in the reflectance spectrum, except at wavelengths lower than 0.4μm. The reflectance at wavelength of 0.3μm as a function of AOI and azimuth angle is plotted in Figure 4.30. For both s and p polarisation the reflectance value only changes for AOI larger than 40°. For p polarisation there is a slight jump of the reflectance at AOI of 50° for azimuth of 25° and 35°, and AOI of 60° for azimuth of 15° and 45°. The reflectance value at these points increases by $6-8\%$. The occurrence of these discrepancies might seem to contradict the fact that the structure is optimised not to have diffraction orders. However it should be considered that these discrepancies exist at the wavelength of 0.3μm, which is beyond the visible range (0.4μm−0.8μm) where the structure is optimised. Figure 4.30 shows that the reflectance of azimuth angles of 25° and 35°, 15° and 45° show a similar behaviour to each other and follow the same trend. This is because of the symmetry of the hexagonal lattice which is repeating around the azimuth of 30°, meaning that electric and magnetic fields are observing the same refractive index profile in the azimuth angles of 25° and 35°, and also 15° and 45°.

A comparison of the mean reflectance at each azimuth angle and wavelength and AOI, demonstrates that the mean value only varies by 0.05%. This can be explained by effective medium theory. Since the dimensions of the structure are much smaller than the incident wavelength, the $\overrightarrow{E}$ and $\overrightarrow{H}$ field do not sense the protuberances and thus the moth-eye layer appears as a homogeneous layer, with a thickness equal to the height of protuberances and the refractive index changing from top to the bottom. In a homogeneous layer where no features exist on the structure, changing the azimuth rotation does

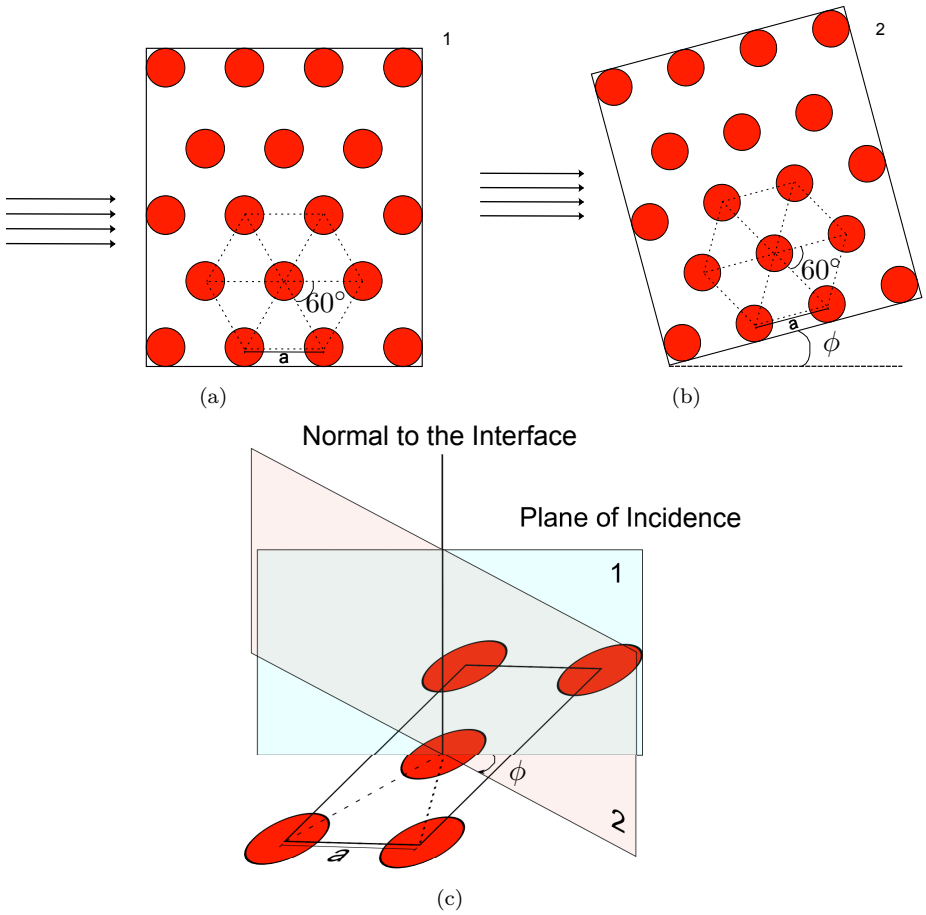

FIGURE 4.27: (a) Top view of a hexagonal lattice of rods illuminated by light. This arrangement is considered as zero reference for azimuth rotation of the sample. (b) Top view of a hexagonal lattice of rods, illuminated by light. The sample is rotated $\phi°$ in the azimuth plane in respect to the reference situation. (c) Shows a hexagonal lattice of rods constant in the azimuth plane. The plane of incident "1" corresponds to the situation of zero azimuth rotation, and the plane of incidence "2" corresponds to the situation where the sample is rotated $\phi°$ in azimuth plane.

not change the reflectance behaviour of the sample. If a significant discrepancy occurs it is a sign of diffraction orders.

4.2.4 Comparison between Silicon Moth-eye and Single Layer and Double Layer Anti-Reflective Coatings

Boden [15] had performed a study on optimization of thin film structures for photovoltaic applications and reported that a single layer anti-reflective coating of Si_3N_4 (80.6nm) and a double layer anti-reflective coating of SiO_2/TiO_2 (108.74/57.45nm) are the optimum anti-reflectives. Thus a comparison of the optimized silicon moth-eye and the

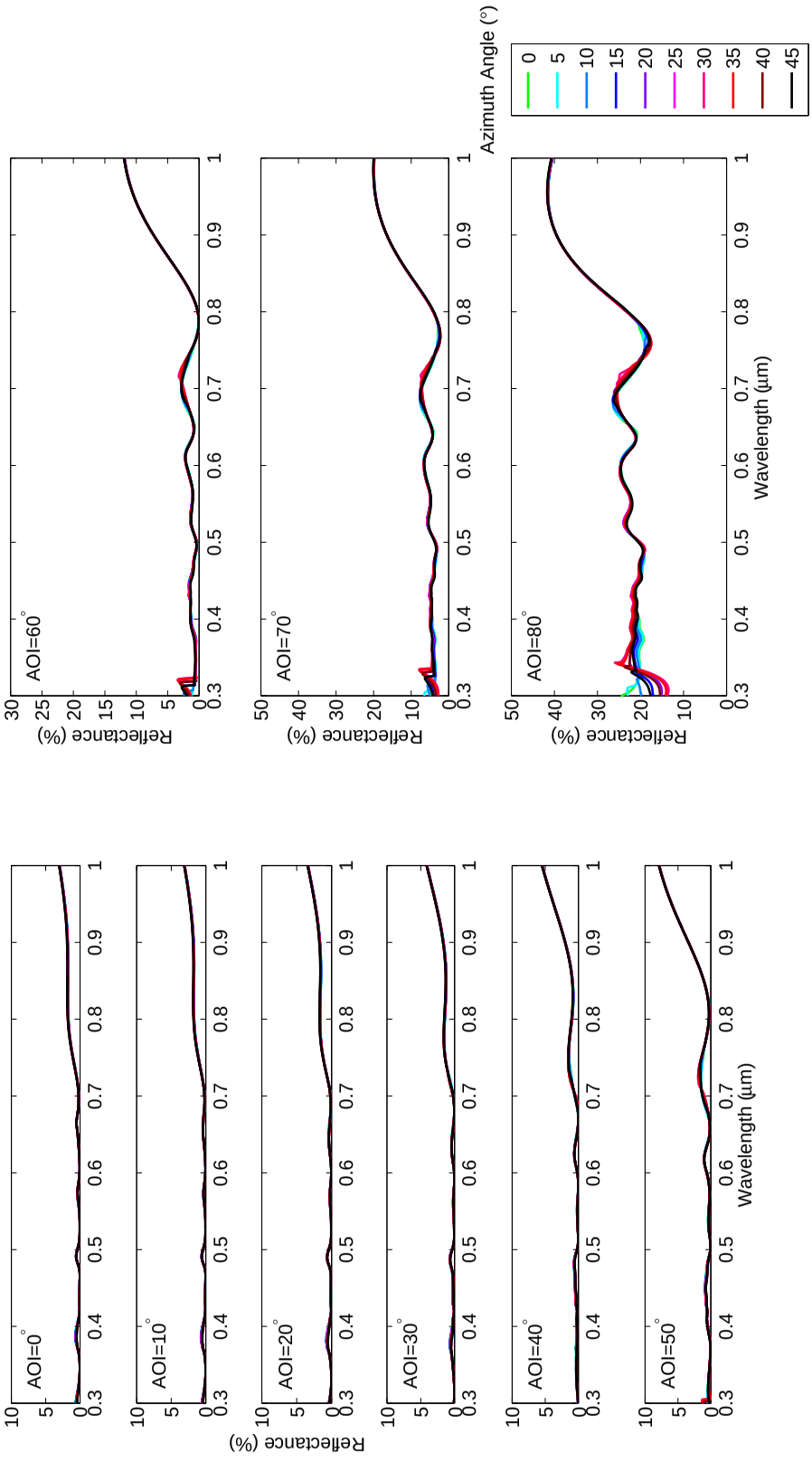

FIGURE 4.28: Comparison of the s polarisation reflectance of silicon moth-eye structure with periodicity of 200nm and height of 600nm at AOIs of 0° to 80°, at wavelengths of 0.3μm to 1μm in steps of 0.1μm, for azimuth angle changing from 0° to 45° in steps of 5°.

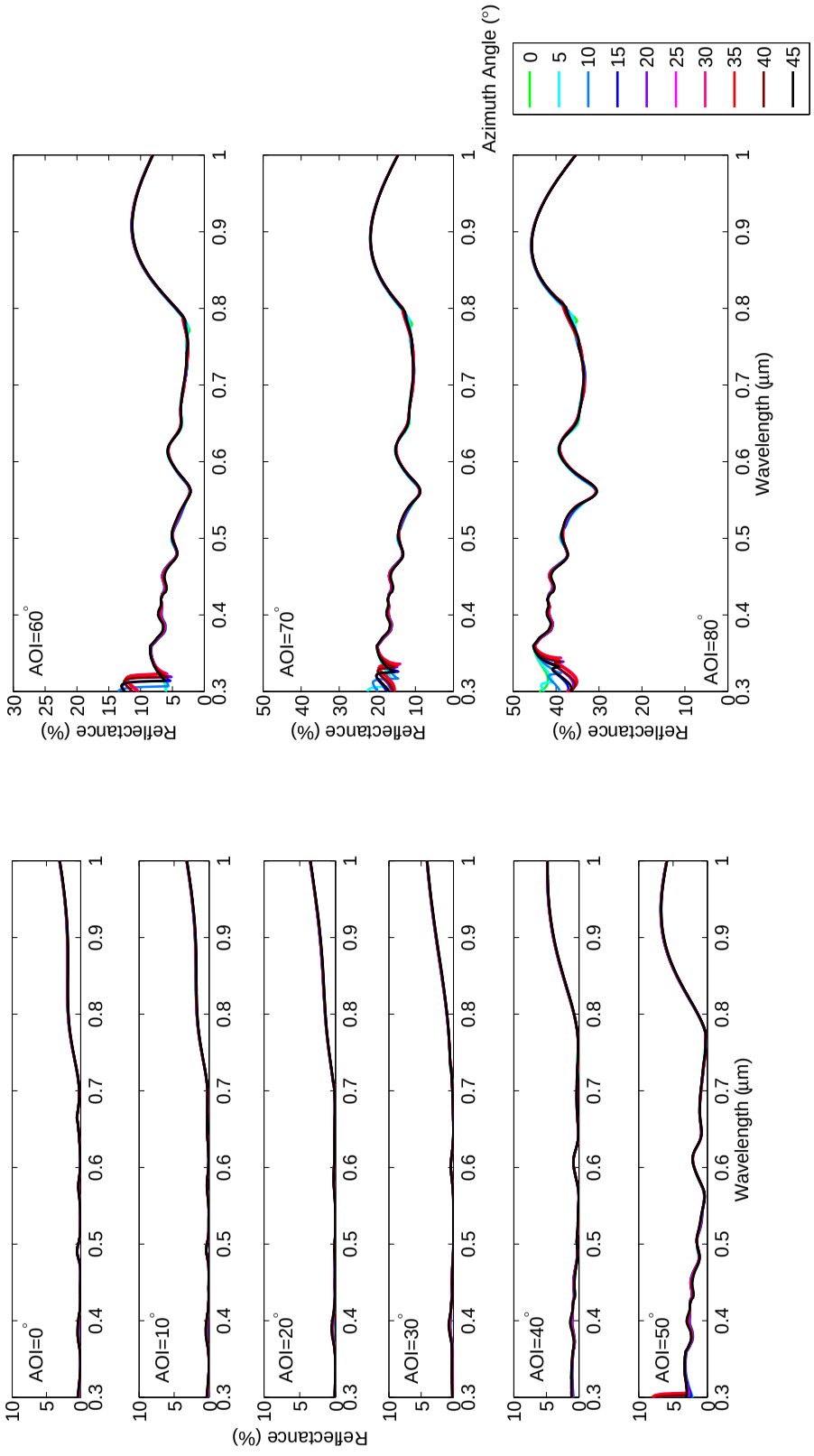

FIGURE 4.29: Comparison of the p polarisation reflectance of silicon moth-eye structure with periodicity of $200nm$ and height of 600nm at AOIs of 0° to 80°, at wavelengths of 0.3μm to 1μm in steps of 0.1μm, for azimuth angle changing from 0° to 45° in steps of 5°.

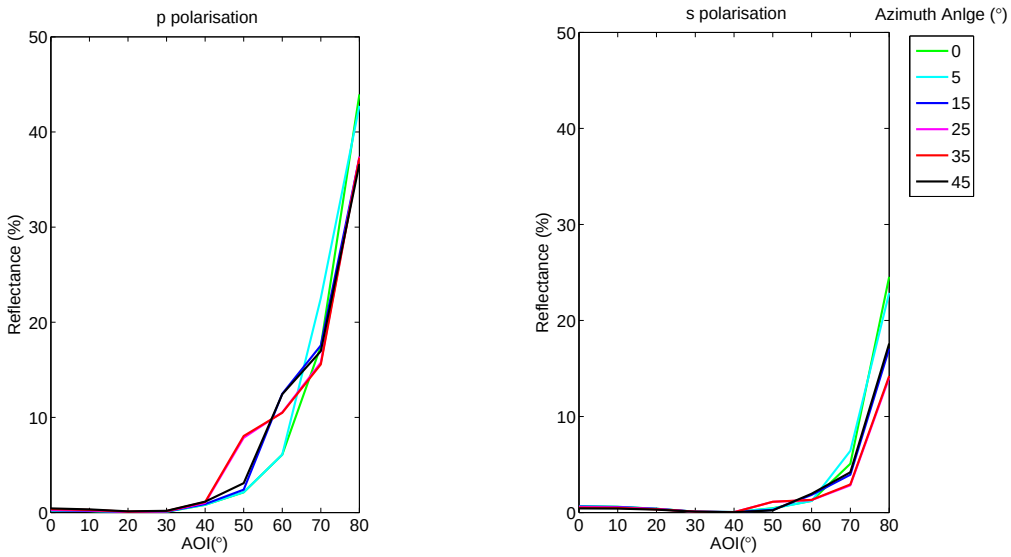

(a) (b)

FIGURE 4.30: Reflectance values of the optimized silicon moth-eye structure at wavelength of 0.3μm, for AOI from $0-80°$ and azimuth of $0, 5, 15, 25, 35, 45$. The inset is zooming to the plots at AOI of $60°-70°$ to show the similarity between the reflectance of similar lattice orientation in respect to the mid point of symmetry.

two SLAR and DLAR layers is essential to understand the advantages of silicon moth-eye structure. Reflectance of the Si_3N_4 SLAR and SiO_2/TiO_2 DLAR were calculate by RSoft. Refractive index data of Si_3N_4, SiO_2 and TiO_2 were taken from [26], [29] and [78] respectively.

Figure 4.31(a) compares the reflectance of the three structures at normal incidence. For short wavelengths, below 0.4μm there is a large difference between the reflectance of silicon moth-eye and that of the SLAR and DLAR. SLAR and DLAR have a maximum reflectance of $\approx 56\%$ at wavelength of 0.36μm, whereas the reflectance of silicon moth-eye at this point is 0.1%. However the reflectance value of SLAR and DLAR reduce to ≈ 0 at $\lambda = 0.472\mu$m for DLAR and $\lambda = 0.614\mu$m for SLAR, where the reflectance value of silicon moth-eye has not changed significantly and shows a reflectance of $\approx 0.1\%$. At longer wavelengths the reflectance of silicon moth-eye remains lower than the other two ARCs. However for wavelengths longer than $\approx 0.8\mu$m DLAR has lower reflectance of about 10 times lower, while the reflectance of silicon moth-eye remains slightly above 1%. Thus the silicon moth-eye at normal incidence outperforms the SLAR structure, and DLAR for wavelengths of up to 0.8μm.

Comparison of the mean reflectance of these three structures at AOI from normal to 80° for wavelength range of $0.32-0.84\mu$m (where the data is available for all structures), Figure 4.31(b), shows that the reflectance of SLAR is highest for all AOIs. The silicon moth-eye shows a reflectance value around 10% lower than DLAR, and 15% lower than

SLAR for all AOIs. All three ARs are sensitive to AOI in the same way: showing close to constant reflectance from AOI of 0° to 40° before increasing at AOIs greater than 40°.

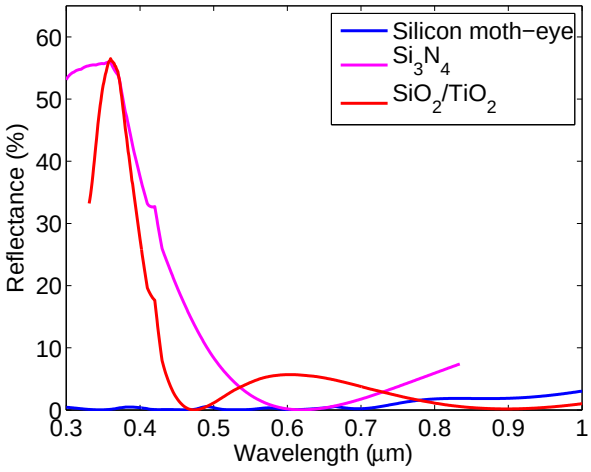

(a)

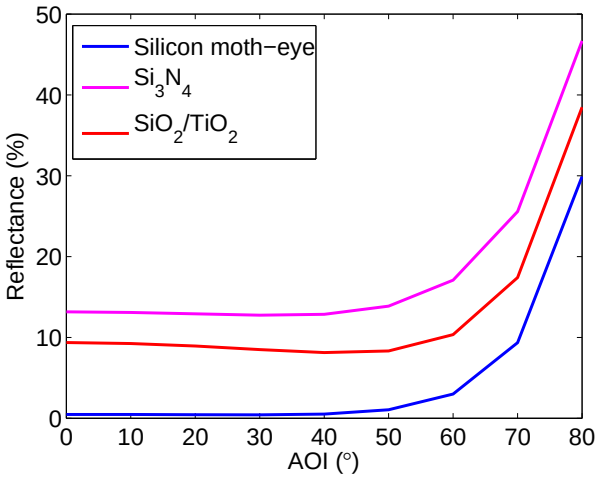

(b)

FIGURE 4.31: (a) Reflectance of SLAR, DLAR and optimised silicon moth-eye at normal incidence. (b) Total reflectance of SLAR, DLAR and silicon moth-eye for AOI of $0° - 80°$ insteps of $10°$, and for the wavelength range of $0.32 - 0.84\mu$m.

Figure 4.32 shows the reflectance spectrum of the SLAR and DLAR for AOIs between 0° and 80°. Comparison between the pattern of the reflectance spectra of SLAR, DLAR and silicon moth-eye (Figure 4.24) shows that SLAR and DLAR are less wavelength dependent and show less fluctuations than the silicon moth-eye structure, particularly at wavelengths greater than 0.4μm. Silicon moth-eye shows more fluctuations, but these are of lower magnitude (Figure 4.24). Thus a moth-eye structure introduces more fluctuations into the reflection spectrum, however it reduces the reflectance by a larger value compares to SLAR and DLAR.

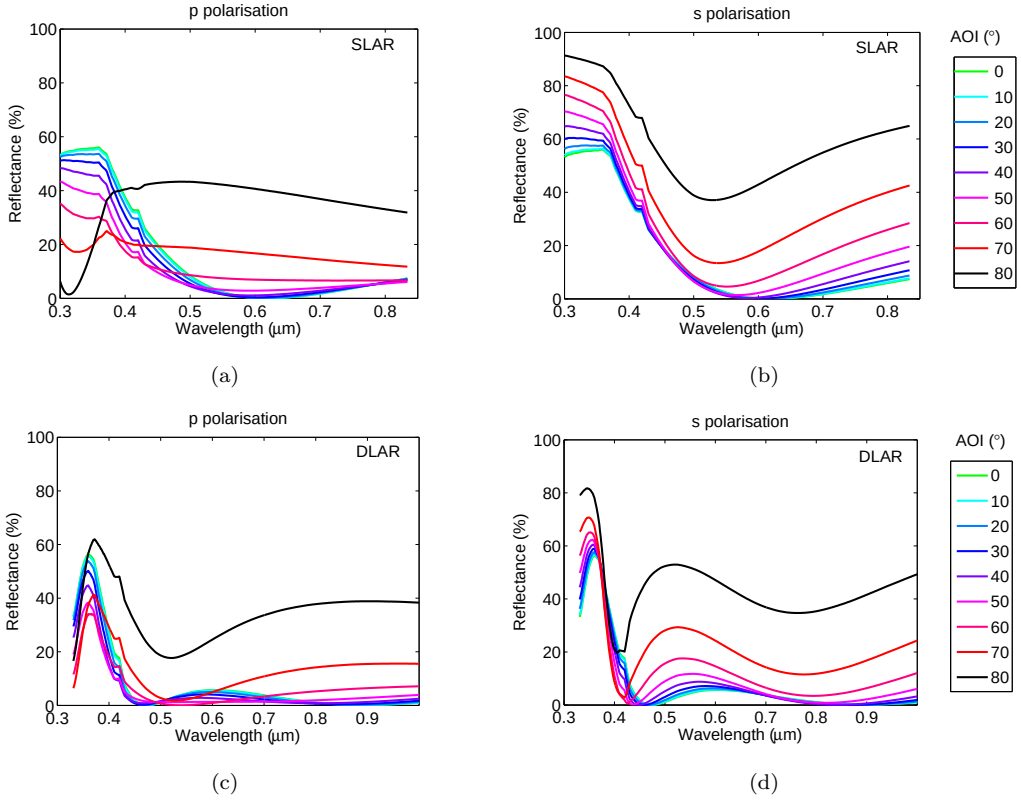

FIGURE 4.32: Reflectance of SLAR Si_3N_4 at (a) p and (b) s polarisation for AOI of $0° - 80°$ in steps of 10°. Reflectance of DLAR SiO_2/TiO_2 at s and p polarisation for the same AOI sweep is plotted in (c) and (d).

Figure 4.33 compares the weighted reflectance of SLAR, DLAR and optimised silicon moth-eye. The weighted reflectance is calculated using Equation 4.3. However, at this stage the AOI is also taken into account. Thus the value of the weighted reflectance demonstrates the ratio of the reflected solar energy to the incident beam energy. The SLAR of Si_3N_4 has a weighted reflectance of 12.2%. This value is 8.1% for DLAR (SiO_2/TiO_2). Silicon moth-eye shows a lower weighted reflectance of only 2.2%. Compared to SLAR and DLAR, the moth-eye structure shows a great improvement in reducing the surface reflectance.

4.3 Conclusion

A simulation package of RCWA was used in this chapter to study reflectance behaviour of moth-eye structures. Details of starting the design of the simulated structure, setting the simulation parameters and setting the grid was explained. The simulation technique was then used to study the reflectance behaviour of biomimetic silicon moth-eye structures of close-packed protuberances with different periodicity and height. It was shown that the performance of the structure is highly dependent on these two parameters: period specifies the wavelength in which low reflectance occurs and height affects the average,

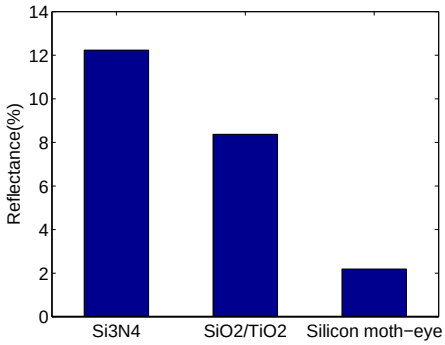

FIGURE 4.33: Weighted reflectance of SLAR (80.6nm of Si_3N_4), DLAR (SiO_2/TiO_2 at 108.79nm/57.45nm) and silicon moth-eye (0.2μm period and 0.6μm height.)

maximum and minimum values of the reflectance. The effect of height and periodicity in a structure with a constant packing density are independent, hence the reflectance performance of the structure can be tuned to a desired wavelength and value according to the needs of a given application. This finding extends the findings of Boden [15] to close-packed moth-eye structures and concludes that the effect of the periodicity and height on reflectance of moth-eye structures at normal incidence does not depend on the packing density of the structure.

The reflectance performance of silicon moth-eyes in response to the solar spectrum was optimised using RCWA. A structure of 0.2μm periodicity and 0.6μm height was found to show weighted reflectance of 0.86%. This structure showed an insensitive behaviour to AOI up to 40°. The maximum reflectance of 33% is observed at an AOI of 80°. It was found that the effect of reflectance in response to AOI in moth-eye structures is very wavelength dependent, especially for wavelengths longer than the height of the structure. Also for the first time computational study of moth-eye structures showed an inverse polarisation behaviour within the visible spectra for a silicon moth-eye structure with pillars of the base diameter of 200nm, bigger than the predicted value of 100nm in literature [22].

Increasing the angle of incidence showed an increase in the reflectance of the moth-eye structure for both s and p polarisation. At larger angles of incidence the reflectance spectra showed more pronounced fluctuations which means the moth-eye structure is more wavelength selective at larger incident angles. Comparison between the reflectance of moth-eye structure at p polarisation with a flat silicon surface shows that moth-eye structures are capable of removing the Brewster effect. Whether this is a property of only moth-eye structures or sub-wavelength structures in general needs more studies.

The specular reflectance simulations were repeated at different azimuth orientation of moth-eye structures. It was observed that the azimuth orientation of moth-eye structures does not affect the specular reflectance (reflectance at normal incidence and oblique incidence) at wavelength above 0.4μm. A slight difference was predicted at wavelengths

lower than 0.4μm where the ratio of the wavelength becomes comparable to the dimensions of the structure and can recognize the variation of features within the azimuth plane.

The reflectance of the optimized silicon moth-eye structure was compared to the predicted performance of the optimum SLAR and DLAR reported by Boden[15]. The silicon moth-eye structure outperformed SLAR and DLAR by approximately 10% and 15% respectively. Showing a better reflectance performance than the SLAR and DLAR while still keeping the advantage of no influence by the azimuth angle is a great advantage of the moth-eye structure which makes it very promising for all antireflection applications, where diffraction has always been a problem.

The RCWA limitations in setting the correct simulation parameters for moth-eye structures, reveals a general big challenge in simulating sub-wavelength structures. Since sub-wavelength structures have features of dimensions less than the incident wavelength, the grid spacing, resolution of features and number of harmonics in the Fourier transform have to be set into high values so that acceptable convergence is achieved. However, increasing these values will consequently increase simulation time and memory, which will make simulation of sub-wavelength structures to be expensive. Thus RCWA predictions of reflectance properties of sub-wavelength structures is qualitatively acceptable while accurate values will only be achieved if the expenses of time and computational memory are provided. Unless supercomputers of high computational power are available, simulating sub-wavelength structures will always remain a challenge.

Bio-photonic structures are sub-wavelength structures of two and three dimensional arrangement of more complicated structures than moth-eye structures. Thus the problem of setting simulation parameters of moth-eye structures extends to bio-photonic structures with a greater degree. It seems that improving computational methods for studying two dimension and three dimension sub-wavelength structures remains a strong requirement in the field of nano-photonic biomimetics.

Chapter 5

Moth-eye Samples and Periodicity

The influence of the period and height of silicon moth-eyes on their reflectance properties were studied in the previous chapter using computational analysis. In this chapter reflectance of samples with different periodicity at normal and oblique incidence are investigated by means of the experimental methods introduced in Chapter 3. Measurements are compared to simulation results to evaluate the validity and accuracy of the simulation technique.

5.1 Samples: Silicon Moth-eyes Fabricated by E-beam Lithography

A set of samples with different periodicity were fabricated using e-beam lithography [15]. The procedure of the fabrication process is presented in Figure 5.1. A 105nm layer of e-beam resist (ZEP 520) was spun on the surface of silicon substrate. The resist was patterned by electron beam lithography so that arrays of holes in the resist remained after developing the resist. 15nm of aluminium was then deposited by electron beam evaporation. Resist was stripped using an 80° stripper and 10 minute sonication. The remaining aluminium was used as a mask to define the moth-eye pillars. An anisotropic dry etch of SF_6/C_4F_8 was used to etch the silicon substrate to 400nm depth to form the pillars. This step gave pillars of vertical walls. After the Aluminium mask was removed, the pillars were etched so that a tapered profile was achieved. This is performed via an isotropic etch using SF_6/ CHF_3/O_2 for 2 minutes. The last step was a high temperature oxidation of $20 - 40$nm thickness which was later stripped off to smooth the shape of pillars, correct sharp and square edges, and remove any damage.

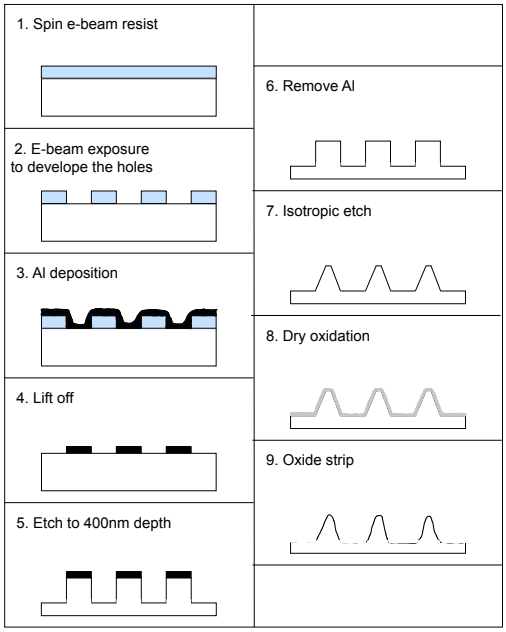

FIGURE 5.1: Fabrication steps of silicon moth-eye structures with e-beam lithography.

Samples were designed to have the periodicity of $150 - 350$nm in steps of 50nm and 400nm height and were labelled as C1 to C5 respectively. The radius of pillars were designed so that the packing density of samples is 50%. Packing density was defined as the ratio of the base of the pillars in a unit-cell to the area of the unit-cell and was calculated using Equation 5.1 (r is the radius of the base of the pillars and a is the periodicity).

$$p = \frac{2\pi r^2}{\sqrt{3}a^2} \tag{5.1}$$

The area of the wafer patterned by the moth-eye structure was designed as 2mm×1mm, to be used for specular reflection measurements. SEM images of samples are provided in Figure 5.2. The sample with the shortest periodicity, 150nm has pillars slanted towards each other and in some cases attached to each other from the top. This shows that the last stages of either isotropic etch or oxide strip was not performed successfully and thus pillars were not formed correctly. This sample was not used for optical characterization. SEM images of C2 and C3 also show that residue of material, thought to be oxide, was left on top of a few pillars.

The etching stage was designed to produce a smooth profile at the top of the pillars. However this was not achieved during the fabrication and the pillars have flat tops. Dimensions of pillars were extracted from SEM images and are presented in Table 5.1. It shows that the height of pillars varies between 483nm and 600nm and the design height of 400nm was not achieved. Since the packing density of these samples was high, the pillars were packed together and thus the height was only observable at the edge

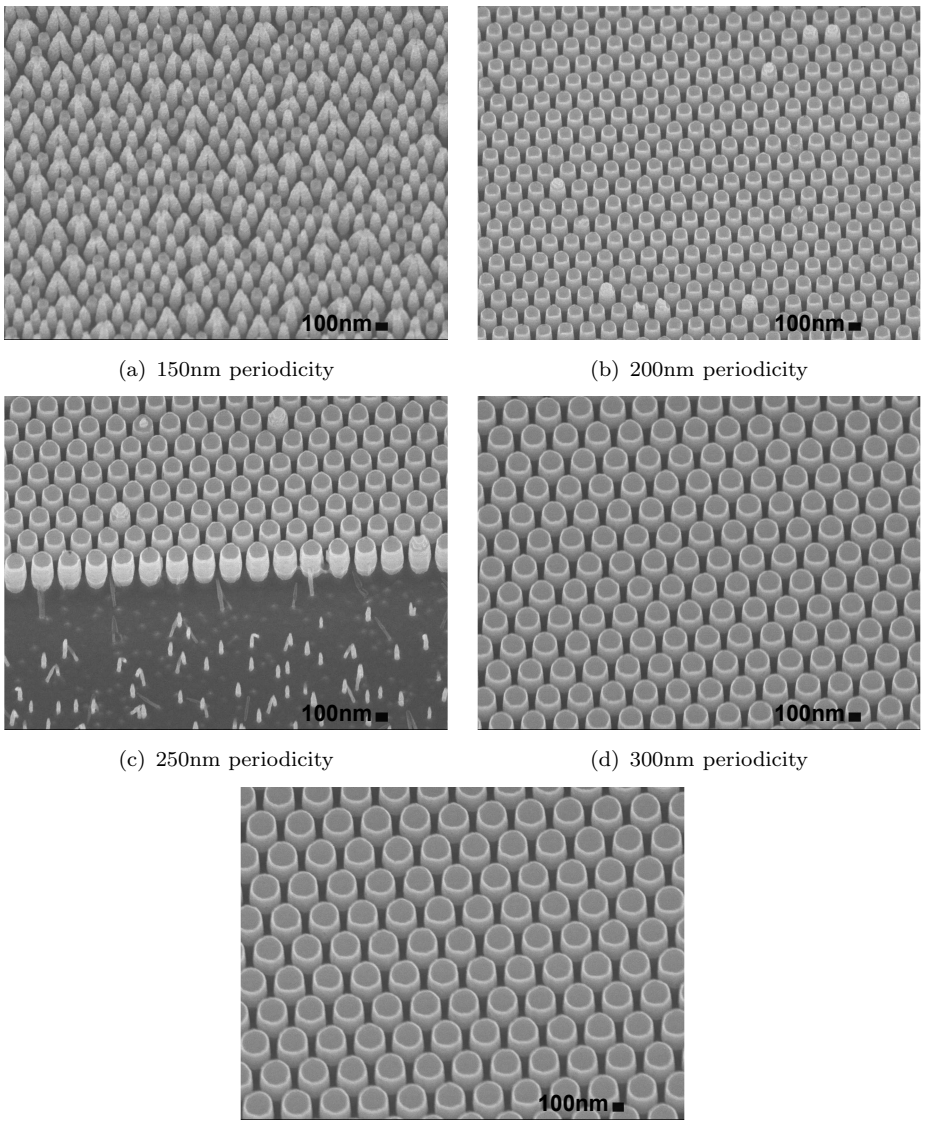

(a) 150nm periodicity

(b) 200nm periodicity

(c) 250nm periodicity

(d) 300nm periodicity

(e) 350nm periodicity

FIGURE 5.2: SEM images of silicon moth-eyes fabricated by e-beam lithography having height of 400nm, packing density of 50% and periodicity of (a) 150nm, (b) 200nm, (c) 250nm, (d) 300nm and (e) 350nm. Samples were tilted 20° and the scale bar of all images is 100nm.

of the sample. However the SEM images show the pillars to be thicker at the edge of samples than the center. Thus measurement of height is from an edge pillar and not representative of all the pillars.

Sample name	Period (nm)	Pillar Width Top - (nm)	Pillar Width Bottom - (nm)	Est. Packing Density (%)	Height (nm)
C2	201	113	146	47	553
C3	253	164	189	50	600
C4	294	191	224	52	483
C5	351	235	266	52	578

TABLE 5.1: Dimensions of silicon moth-eyes of e-beam lithography, C series extracted from SEM images.

5.2 Normal Incidence Measurement

5.2.1 Experimental Set-up

The probe measurement technique was used to measure the reflectance of silicon moth-eye samples at normal incidence. Light is shone through the 6 fibres around the center of the probe and is collected by a single fibre in the center of the probe. In order to make sure the collection spot is entirely within the patterned area, the sample is moved horizontally in every direction. Observing no change in the reflection pattern means that the detected light is reflected from the patterned area of the sample. The acceptance cone of the fibre is 12.7°. The HL-2000 light source and HR4000CG spectrometer are used to produce the light and detect the reflected light respectively. The integration time is set to 1ms and Boxcar width is set to 1.

5.2.2 Results

The reflectance spectrum of the silicon moth-eye samples of the C series (Table 5.1) are plotted in Figure 5.3. The reflectance of the samples goes as high as values of 40%. This is caused by the flat top of the pillars which produces a discontinuous interface between the air and silicon substrate as opposed to a graded index interface produced by pillars with a round top (Chapter 2). As the periodicity increases from C2→C3→C4→C5, the reflectance spectrum moves to longer wavelengths. The minimum reflectance point of the C2 sample is marked as point "A" and tracked in other images. The reflectance of this point and the corresponding wavelength is summarized in Table 5.2. The average wavelength shift of this point within the samples is 93nm. The shift of the reflectance spectrum towards higher wavelengths with increase in the periodicity agrees well with simulations performed in the previous chapter.

The reflectance spectrum of moth-eye structures are wavelength dependant. Figure 5.4 plots the average, maximum and minimum reflectance values of C2, C3, C4 and C5. The large difference between minimum and maximum of each individual sample confirms the oscillations of the reflectance within the wavelength spectrum. C4 with the periodicity of 300nm has the largest difference between minimum and maximum values, $\approx$ 40%.

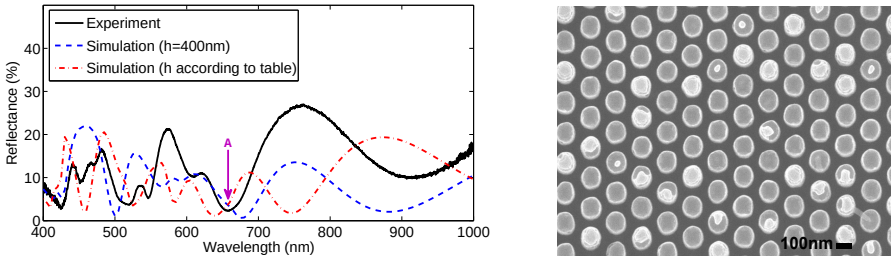

C2 (Period= 200nm)

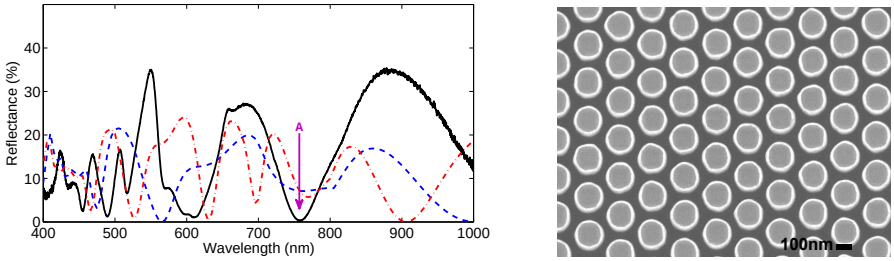

C3 (Period= 250nm)

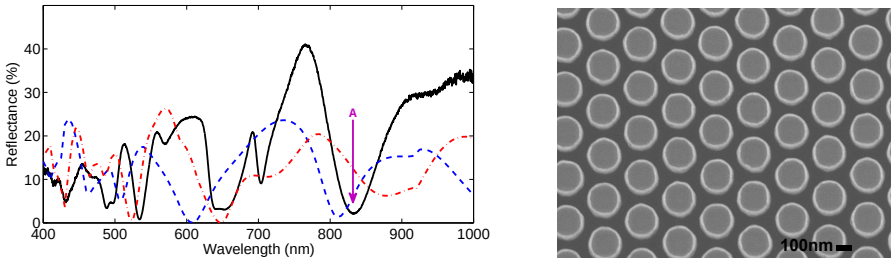

C4 (Period= 300nm)

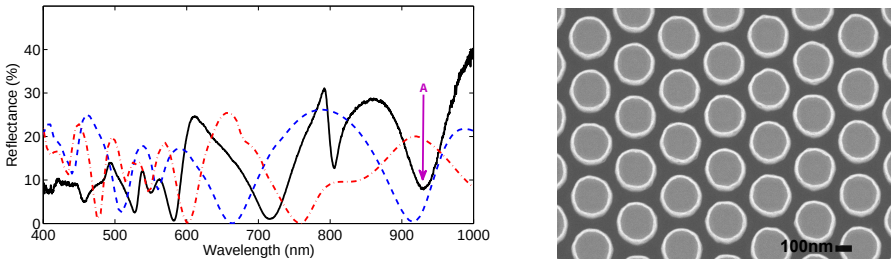

C5 (Period= 350nm)

FIGURE 5.3: Reflectance of silicon moth-eye samples of e-beam lithography, C series, for the wavelength range of $400 - 1000$nm measured by the probe measurement (black solid line). Point "A" is a trough in C2 chosen and tracked in other samples. Its corresponding wavelength and reflectance value is for each sample is summarised in Table 5.2. Two sets of simulation is also performed employing the periodicity and the base and top diameter from dimensions from Table 5.2, with h= 400nm (blue dash line) and h from the Table 5.2 (red dash dot line). The periodicity of samples was varied from 200nm to 350nm. The SEM images are taken from the top of samples. The scale bar of all images is 100nm.

Sample	**Refl(%)**	**λ(nm)**
C2	2.53	656
C3	0.39	756
C4	2.09	830
C5	7.7	935

TABLE 5.2: Corresponding reflectance and wavelength values of point A in Figure 5.3

The mean average of reflectance of the samples increases as the periodicity increases, $\approx 4\%$, however for the sample with largest periodicity it shows a decrease of 3% and shows a similar value to C2 of 200nm period.

The large fluctuations in the reflectance spectrum of silicon moth-eyes is caused by the fact that the incoming light encounters dimensions of height, periodicity and the diameter of pillars which change from base to the top of the moth-eye layer. Moth-eye structures as sub-wavelength structures have the dimensions in a similar range to the incident wavelength. In the wavelength spectrum, dimensions less than the incident wavelength are not sensed by the incoming wave and thus are ignored, whereas the features with dimensions comparable to the incident wavelength affect the reflectance. As an example, the periodicity of a moth-eye structure might not significantly affect the reflectance of a large wavelength of 800nm but would affect an incident wavelength of 400nm. However the exact comparison ratio between wavelength and dimensions is not necessarily one to one.

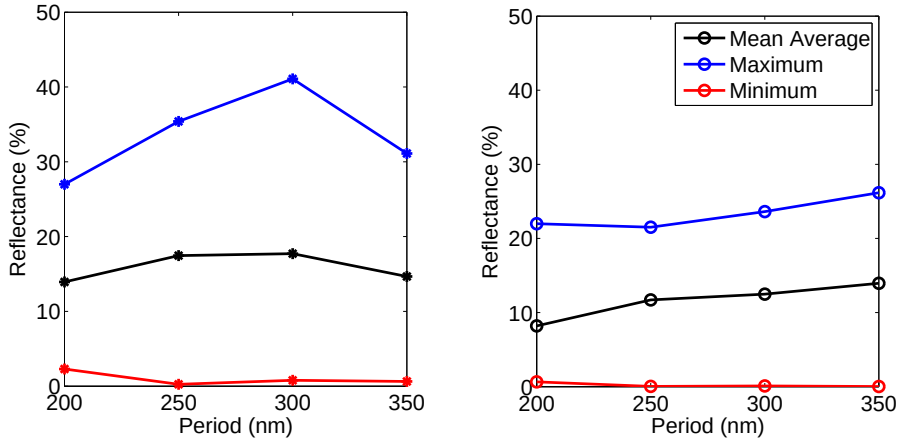

(a) Experiment (b) Simulation

FIGURE 5.4: The values of mean average, maximum and minimum reflectance of silicon moth-eyes of C series extracted from (a) experiment, and (b) simulation.

5.2.2.1 Comparison with Simulation

To model the fabricated moth-eye structures, pillars of similar dimensions (Table 5.1) were defined in DiffractMOD. The red coloured lines in Figure 5.3 present the simulation results of reflectance of silicon moth-eye structures.

Comparison between the reflectance pattern of simulation results and measurement for C2 and C3 show a poor agreement. In the case of C4 and C5 however the simulated reflectance spectrum shows better agreement with the measurements. The reflectance features at wavelengths of $500-650$nm for C4 and $600-700$ for C5 are well predicted by simulations. At longer wavelengths the pattern of the reflectance spectrum is approximately predicted by simulations but with lower values, and the reflectance spectrum of C5 modelled by simulations is slightly shifted to higher wavelengths compared to measurement. It was mentioned previously that the height of samples is not an accurate representation of all the pillars of the sample. Thus new simulations were performed employing the dimensions of Table 5.1 for periodicity and diameters but changing the height to 400nm. These results are plotted with blue colour lines in Figure 5.3. In this case for C2 and C3 a better agreement is observed between simulation and experiment. The reflectance pattern is approximately predicted by simulations for wavelength above 500nm for C2 and 650nm for C3. C4 and C5 simulation results show a reflectance pattern similar to measurements for wavelength above 500nm, but with a slight shift to shorter wavelengths. In the simulations with $h=$ 400nm, the wavelength position of point "A" is estimated closely even though for C3 the reflectance value is greater. A comparison between the two simulations shows that the height of C4 and C5 are values between the values in Table 5.1 and 400nm. For C2 and C3 however the height value is far from the values of Table 5.1 and closer to 400nm.

Figure 5.4 shows the mean average, maximum and minimum of the reflectance of simulations of silicon moth-eyes with a height of 400nm (blue lines in Figure 5.3). The figure shows that the maximum value of the simulated structures is lower than the experiment. Thus the mean average of reflectance in the simulations is slightly lower than measured in the experiments. The mean average of samples in the simulation however show an increase as the periodicity increases. Since this behaviour is not observed in the experiment, it supports the observation that the height of the fabricated samples is not uniform and varies for individual samples.

The discrepancies between reflectance measured in the experiment and calculated in the simulation does not reject the ability of RCWA to model the reflectance of silicon moth-eyes. The discrepancies had taken place because the dimensions were extracted from SEM images, however each image is only from a small part of the sample. Dimensions are averaged over a small number of pillars of the whole sample. Also the SEM image of C2 shows the existence of residue of a material on the top of the pillars which is not accounted for in the model.

5.2.3 Summary

Normal incidence reflectance measurements of silicon moth-eye samples fabricated by e-beam lithography with varying periodicity was carried out. The SEM images reveal that through the fabrication process, the samples were not fabricated according to design parameters. The results show that periodicity's effect on reflectance is that increasing the periodicity shifts the reflectance towards higher wavelengths. The peaks and troughs of reflectance spectrum shift towards higher wavelength as the periodicity increases. This is in agreement with the simulation results of previous chapter.

Simulation of silicon moth-eyes employing the approximate models extracted from SEM images show that the measured height value is not representative of the whole sample. At the edge of the samples the pillars have greater height. This resulted from difficulties achieving dimensions close to the design profile during fabrication. Changing the height of pillars to 400nm (design parameter) the simulations showed a better agreement with experiment; a close approximation of the reflectance pattern was observed. Since the height is not accurate and the accurate value cannot be measured from SEM images a firm decision on the accuracy of the simulation method cannot be concluded. However it seems RCWA is able to predict the pattern of the reflectance of silicon moth-eye structures even though the modelled structure was an approximate structure. This agreement of pattern was observed at longer wavelengths above 500nm.

5.3 Angular Reflectance Measurement

Angular reflectance measurement is of great importance to show the effect of increasing the incident angle on the optical behaviour of a moth-eye structure. In the literature, angular reflectance measurements were performed using single wavelength lasers. This work employs a white light laser of wavelength of $400 - 1000$nm to study the angular reflectance of samples across a wide wavelength range. This technique is uniquely applied to the field of moth-eye structures in this work.

5.3.1 Experimental

The reflectometer was used to investigate the reflectance properties of silicon moth-eyes (C series) at oblique angles of incidence. Table 5.3 lists the laser power and integration time for each sample for s and p polarisation measurements. The laser power used for each sample was chosen according to the behaviour of the sample and whether or not the signal could be detected by the spectrometer. The integration time also differs in order to provide a high enough signal-to-noise ratio. The normalisation process and calculation of the reflectance of samples were performed as was explained in Chapter 3.

	***s* polarisation**		***p* polarisation**	
	Laser Power (mW)	Int. Time (ms)	Laser Power (mW)	Int. Time (ms)
C3	25.25	1000	27.5	1000
C4	25.84	1500	42.6	1500
C5	25.58	1500	28.9	1500

TABLE 5.3: The laser power and integration time set for reflectance measurements performed on silicon moth-eye samples using the reflectometer

The angle of detector was varied between 2° and 170° in steps of 0.2°, giving a fine scan of the specular beam over the angle of incidence from 1° to 85°. The smallest incident angle where the beam was not blocked by the mirror and entered the mini integrating sphere was at 1.5°. After processing data and cancelling the noise, the results are acceptable between angles of incidence of 2° and 83°. The signal-to-noise ratio causes the wavelength range of $450 - 980$nm to be acceptable.

The reflectance of silicon moth-eye samples of C series, C3, C4 and C5 were investigated at arbitrary angles of incidence using the reflectometer set-up. In this set-up as the sample was rotated to vary the AOI, the incident beam on the sample widened. However C2 has scratches on its corner and as the beam expanded on the sample it illuminated areas of different properties, slanted and broken pillars (Figure 5.5). Therefore the results would not be acceptable and measurement was not performed on this sample.

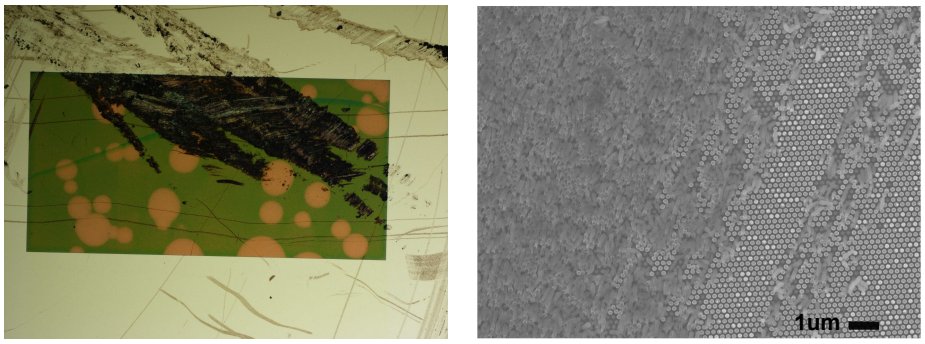

FIGURE 5.5: Image of the silicon moth-eye C2 sample showing the scratches on the sample (left). SEM image of an area of scratches showing the broken pillars in the sample (right).

5.3.2 Results

5.3.2.1 Reflectance at Normal Incidence

Reflectance of silicon moth-eye samples at near normal incidence, $\theta = 2.5°$, at s and p polarisation are extracted from reflectometer measurement and plotted in Figure 5.6. The reflectance of un-polarised light, R, is an average between the two orthogonal polarisations of s and p, calculated from Equation 5.2.

$$R = \frac{R_p + R_s}{2}. \tag{5.2}$$

where R is the reflection coefficient for un-polarised light, R_s and R_p are the reflection coefficient for s and p polarisation respectively.

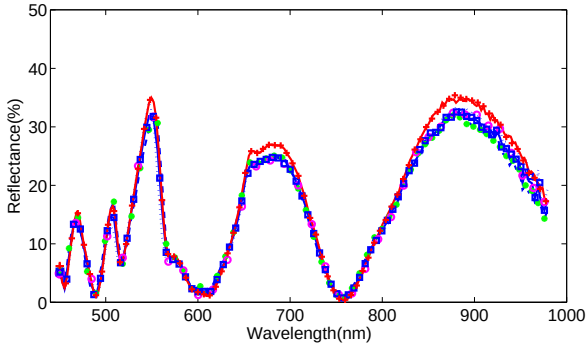

(a) C3 (Period= 250nm)

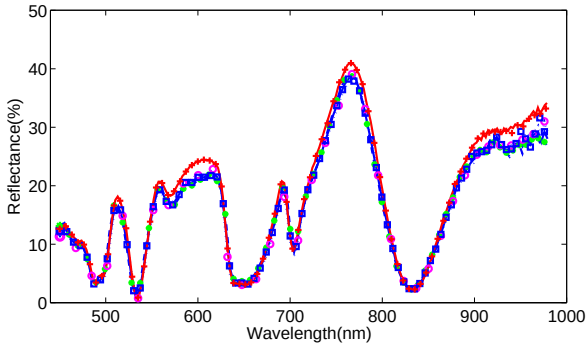

(b) C4 (Period= 300nm)

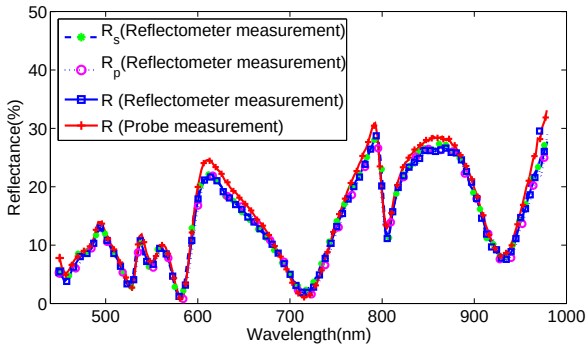

(c) C5 (Period= 350nm)

FIGURE 5.6: Reflectance of silicon moth-eyes (a) C3, (b) C4 and (c) C5, at near normal incidence ($\theta = 2.5°$) for s, p and un-polarised light extracted from reflectometer measurement (blue) compared to normal incidence measurements from probe measurement (red). Markers of different colour are used to distinguish the overlapping lines.

At normal incidence, the reflectance of the two orthogonal polarisations and consequently the unpolarised light, show almost equal values of reflectance. The s and p polarised light are different in the orientation of $\overrightarrow{E}$ and $\overrightarrow{H}$ field. At normal incidence the reflection of a

homogeneous medium is not affected by the polarisation of the incident light. However, if the sample has an asymmetric structure within an azimuth angle of 90°, the reflectance of the two orthogonal polarisations is also different. The moth-eye structure of a hexagonal lattice has a 6-fold symmetry (the unit cell repeats every 60°). The similarity between the reflectance of s and p polarisation implies that the two orthogonal polarisations sense similar structure in the plane of periodicity which can be explained by effective medium theory. The periodicity, height and profile of pillars provide a structure where the incident light cannot resolve the features and consequently interacts with the effective refractive index of the moth-eye layer, constant in the plane of periodicity. Therefore light of different polarisation incident on these structures behave similarly. An equal reflectance value for s and p polarisation was also observed in simulations.

The near normal incidence results of the reflectometer measurement are compared to the results of the probe measurement in Figure 5.6. The difference in the collection angle of the probe measurement and reflectometer measurement is only 0.8° and thus a very small difference between these two measurement at the peak of plots is observed. The similarity between the normal incidence results of these two measurements confirms the validity of the reflectometer results.

5.3.2.2 Reflectance at Arbitrary Angles of Incidence

Figure 5.7 shows the reflectance of silicon moth-eyes C3, C4 and C5 at arbitrary angles of incidence ($2 - 83°$) and wavelengths ($450 - 980$nm) for s and p polarisation. The angular reflectance spectrum of all three samples show small features of low reflectance values (dark blue) which in some cases stay at a constant wavelength as AOI increases and in other cases they move to longer or shorter wavelengths. A comparison between the three samples shows that increasing the periodicity affects these features in two ways:

- The features shift towards longer wavelengths.
- The spectrum features expand. In other words the distance between adjacent features is increased.

These observations show that the effect of periodicity on the reflectance spectrum at normal incidence is also true at arbitrary angles of incidence meaning that increasing the periodicity of the silicon moth-eye structures moves the angular reflectance spectrum towards higher wavelengths.

For each sample, the angular reflectance spectrum at s and p polarisation are different. The majority of the plot of p polarisation is covered by blue colour which represents reflectance of lower than 40% whereas reflectance of s polarisation has higher values

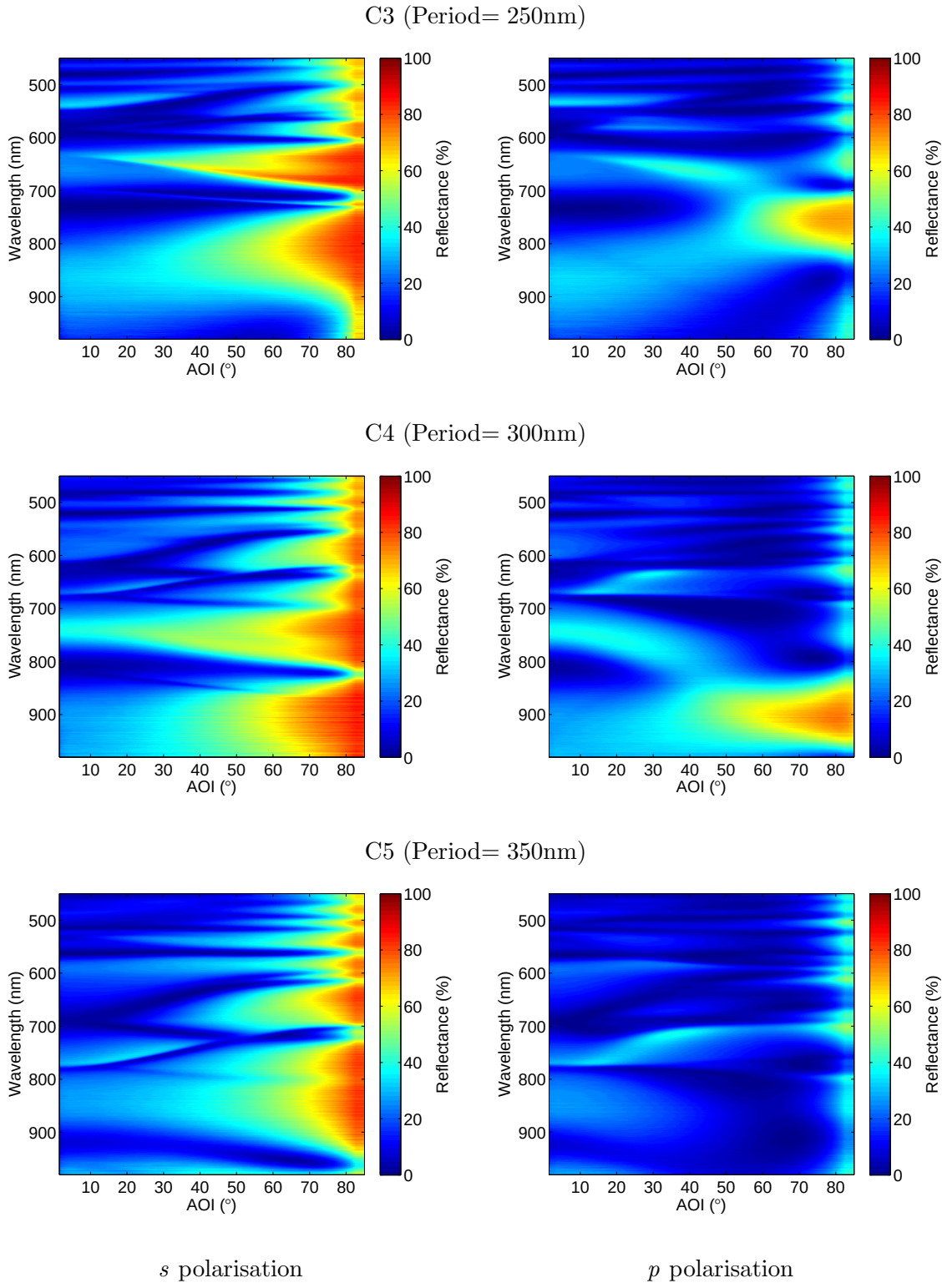

FIGURE 5.7: Reflectance of silicon moth-eye samples C3, C4 and C5 for s and p polarisation at AOI between $2-83°$ in steps of $0.1°$ and wavelength range of $450-980$nm.

of reflectance especially for AOIs greater than 50°. This is similar to the behaviour of silicon where the reflectance at s polarisation is higher than reflectance at p polarisation. Plots of p polarisation reflectance show a dark blue colour region at AOIs of 65° and above which is similar to zero reflectance of silicon at p polarisation at Brewster's angle. However to make a firm conclusion the reflectance values at s and p polarisation has to be compared quantitatively. The reflectance spectrum of silicon moth-eye samples have large fluctuations and plots of reflectance spectrum for individual AOIs are not easy and convenient to interpret. Thus the reflectance of samples at individual wavelengths are plotted against AOI for C3, C4 and C5 in Figure 5.8, Figure 5.9 and Figure 5.10 respectively.

The angular reflectance of all three samples varies with incident wavelength which confirms that the fluctuations within the reflectance spectrum observed at normal incidence also exist at arbitrary angles of incidence. At normal incidence the reflectance of s and p polarisation are equal at all wavelengths, however as the angle of incidence increases differences take place between the reflectance of the two polarisations. However, this difference between the reflectance of the two polarisations does not follow a homogeneous trend within the wavelength.

It was mentioned earlier that the 3D plot of the angular reflectance spectrum shows that reflectance of s polarisation is higher than p polarisation in general. However the detailed observation of the reflectance at the two polarisations at individual wavelengths shows that at some wavelengths the reflectance value of p polarisation is higher than s polarisation; at $\lambda = 550 - 600$nm for C3, at $\lambda = 650$nm for C4 and at $\lambda = 750$nm for C5 for AOIs above 40°.

There are remarkable results in the angular reflectance of the silicon moth-eye samples at some wavelengths. These are, constant reflectance of s polarisation at $\lambda = 750$nm for C3, and at $\lambda = 460$nm for C4 (with maximum 2% fluctuations), constant angular reflectance of p polarisation at $\lambda = 460$nm for C5 and almost equal angular reflectance value of s and p polarisation at $\lambda = 900$nm for C4.

Total angular reflectance is an average of the reflectance of samples at each wavelength. This obscures the details of the angular reflectance as the wavelength changes. However it provides an overview of the optical behaviour of a sample as the AOI changes. Hence the total angular reflectance of C3, C4 and C5 for s, p and un-polarised light is plotted in Figure 5.11. An outstanding feature of all three plots is the almost similar and in some cases equal value of reflectance for s and p polarisation from normal incidence up to the incident angle of 30°; C3 and C4 show almost equal values while C5 shows a similar values with 5% maximum difference. Although Figure 5.8, Figure 5.9 and Figure 5.10 showed that at some wavelength the angular reflectance of s polarisation is lower than p polarisation, the total reflectance of all samples show higher values of reflectance for s polarisation than p polarisation. The total angular reflectance of all samples at s

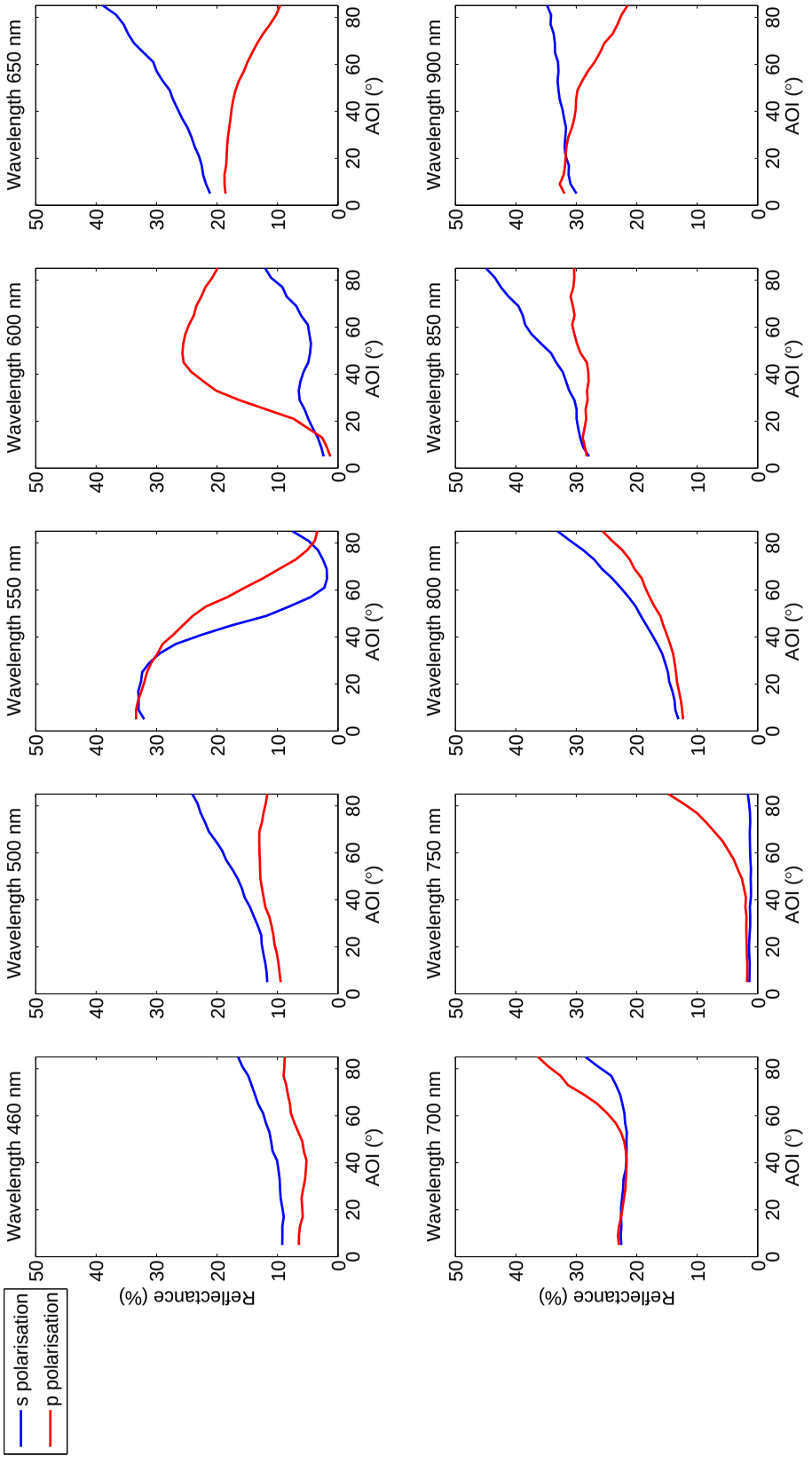

FIGURE 5.8: Angular reflectance of silicon moth-eye, C3, at wavelength intervals of 50nm from $450 - 900$nm, at AOI of $2 - 83°$ for s and p polarisations.

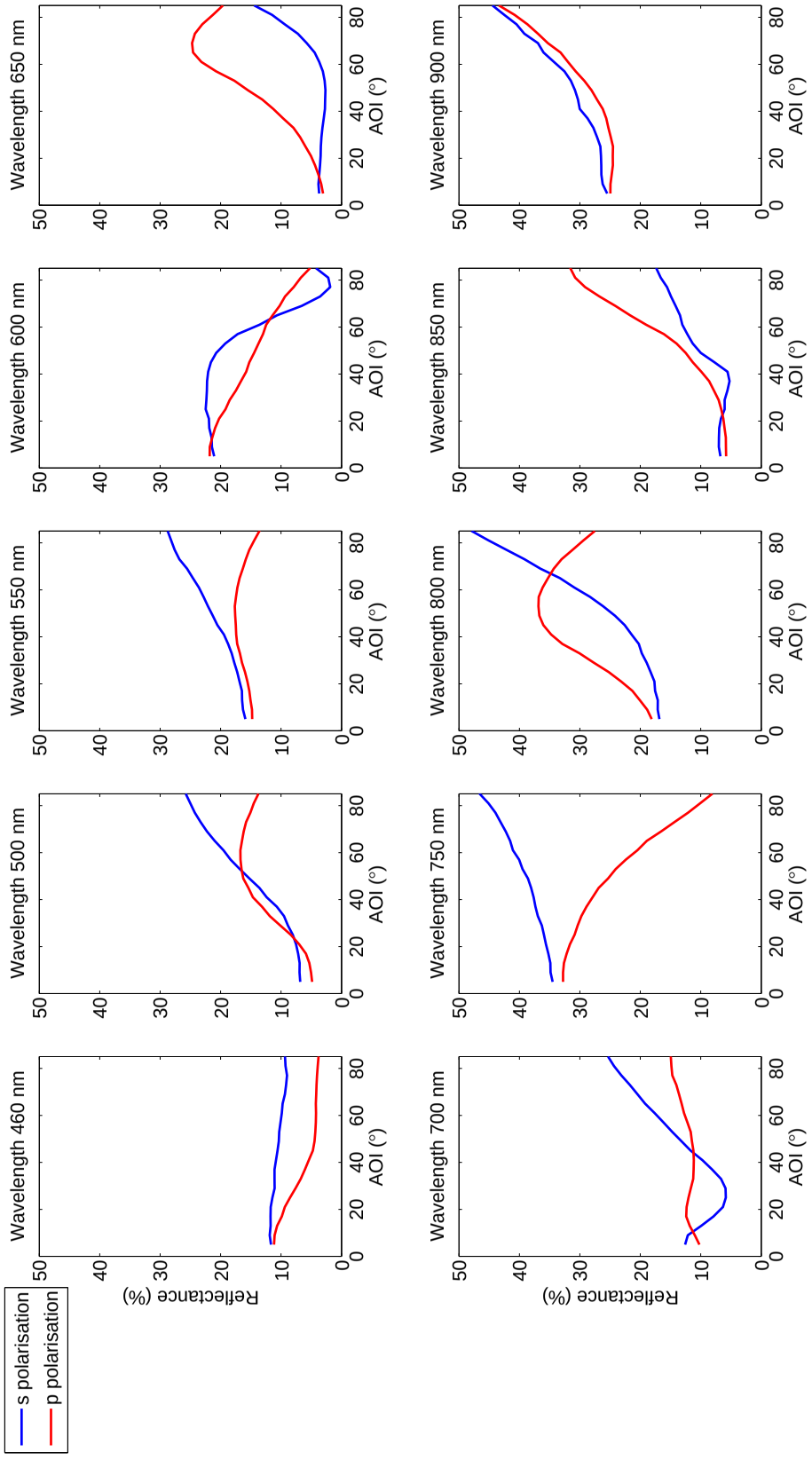

FIGURE 5.9: Angular reflectance of silicon moth-eye, C4, at wavelength intervals of 50nm from $450 - 900$nm, at AOI of $2 - 83°$ for s and p polarisations.

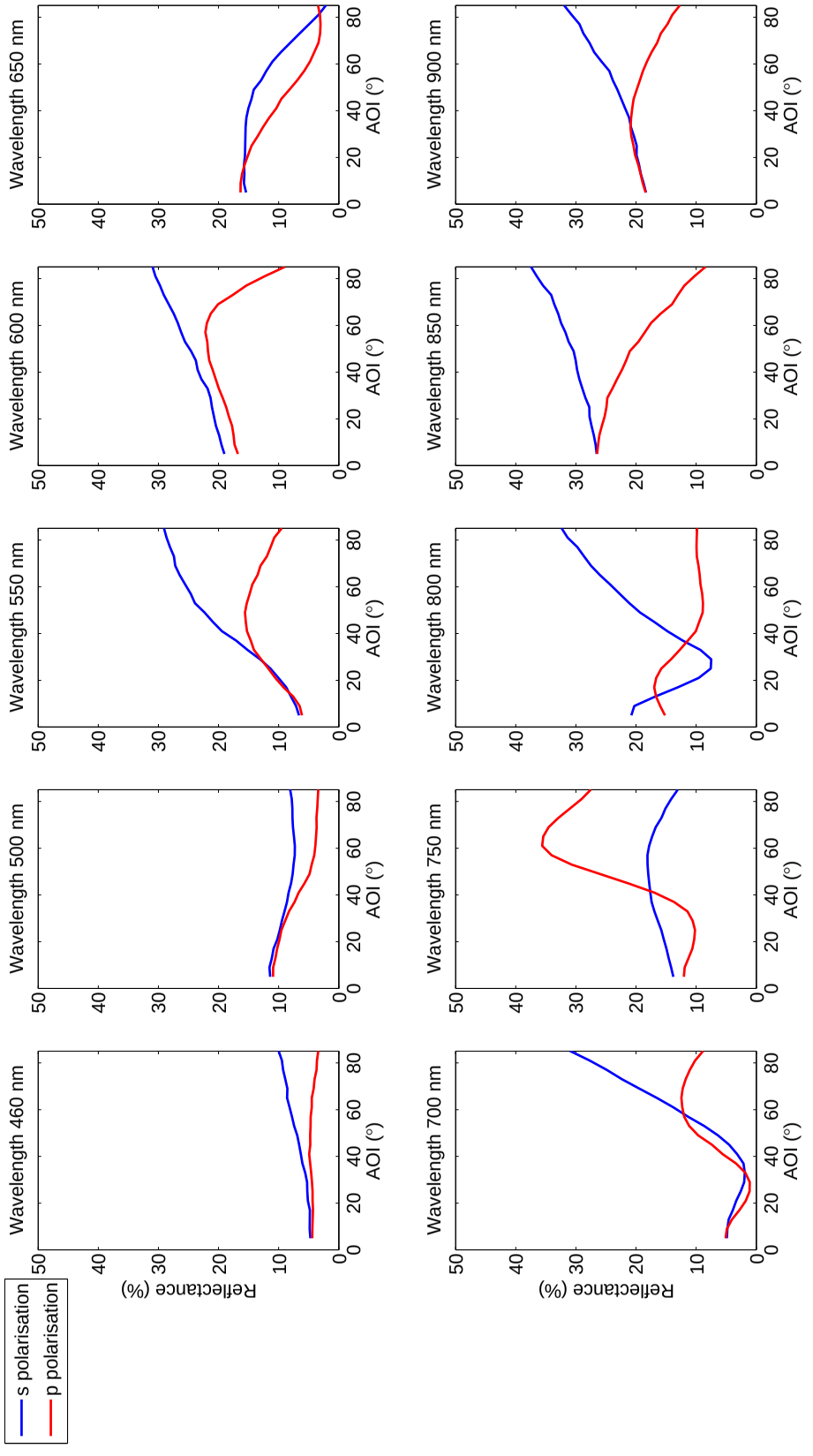

FIGURE 5.10: Angular reflectance of silicon moth-eye, C5, at wavelength intervals of 50nm from $450 - 900$nm, at AOI of $2 - 83°$ for s and p polarisations.

polarisation is similar, starting from ≈ 14% at normal incidence reaching up to ≈ 72% at AOI of 83°. For p polarisation, C4 and C5 have similar angular reflectance behaviour starting from normal incidence to ≈ 33% at AOI= 83° after reaching a minimum of ≈ 6.5% at AOI of 64° for C4 and 60° for C5. However, angular reflectance of C3 does not reduce to a minimum and only increases from 13.3% at normal incidence to the reflectance value of 45% at 83°. A comparison between the reflectance of the unpolarised light (black line) for all three samples reveals that the reflectance of all samples increases as AOI increases. However increasing the periodicity reduces the maximum reflectance value achieved at the greatest AOI. The angular dependence of the reflectivity of the samples are different. C4 shows a constant angular reflectance for AOI of $30-40°$ while C5 shows a constant angular reflectance for AOI of normal incidence to 40° and C3 is significantly angle dependant compared to the other two samples. Thus increasing the periodicity has reduced the rate of the change of the angular reflectance. In other words as the periodicity is increased the reflectance is less angle dependant.

The angular reflectance of silicon is also presented in Figure 5.11, showing the effect of introducing moth-eye structure to the angular reflectance of a flat surface. Comparison between the angular reflectance of C3, C4 and C5 with silicon shows that all three samples have an angular reflectance less than silicon at s polarisation. This difference however reduces as the AOI increases and has its maximum at normal incidence with 21% difference and its minimum difference at the AOI of 83° with 12%. For p polarisation however this is not the case. Reflectance of silicon decreases from normal incidence until it reaches a zero value at the Brewster angle, 78°. The angular reflectance of C3 increases continuously as AOI increases. Thus at the AOI of 50° it matches the total reflectance of silicon and from there it has higher values than silicon. C4 and C5 show a similar behaviour to silicon at p polarisation but with a smoother profile. Their reflectance value reaches a minium but never the zero value. Thus at an AOI of ≈ 62° the mean reflectance of C4 and C5 of p polarisation is equal to silicon and from there it has higher values than silicon. A comparison between the total angular reflectance of silicon and silicon moth-eyes shows that the total angular reflectance of silicon moth-eyes is lower than silicon for AOIs of normal incidence up to 71° for C3 and slightly higher AOI of 80° for C4 and C5.

The weighted reflectance provides a useful comparison of the performance of silicon moth-eyes exposed to sunlight during a day. Thus the weighted reflectance of silicon moth-eyes is calculated using Equation 4.3 from Chapter 4 and presented in Figure 5.12. C5 with the greatest periodicity (350nm) shows the lowest weighted reflectance of 15.81%. C4 has a higher value of 18.57% and C3 is slightly higher at 19.39%. Therefore the weighted reflectance of samples reduces as the periodicity of the samples increases.

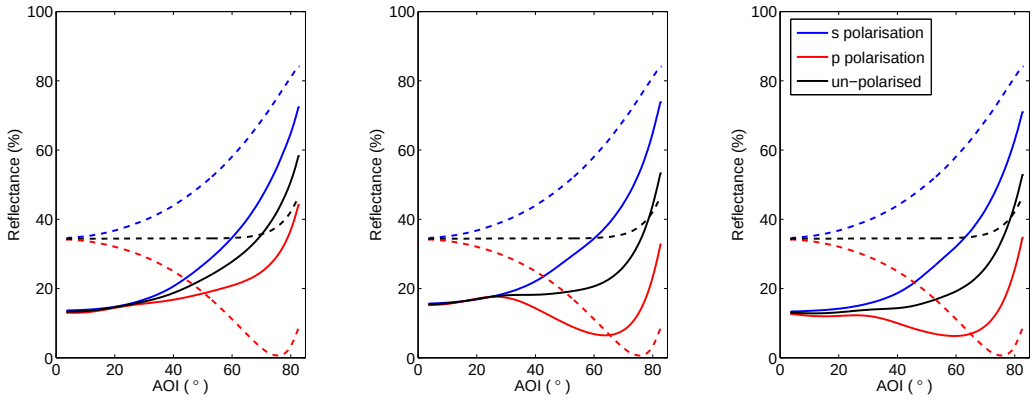

(a) C3 (period= 250nm) (b) C4 (period= 300nm) (c) C5 (period= 350nm)

FIGURE 5.11: Total angular reflectance of silicon moth-eyes (a) C2, (b) C3 and (c) C3, at AOIs of $2.5 - 83°$, for s polarisation (blue), p polarisation (red) and averaged of both to represent un-polarised light. Solid lines shows the angular reflectance of the moth-eye structure and dashed lines show the angular reflectance of silicon.

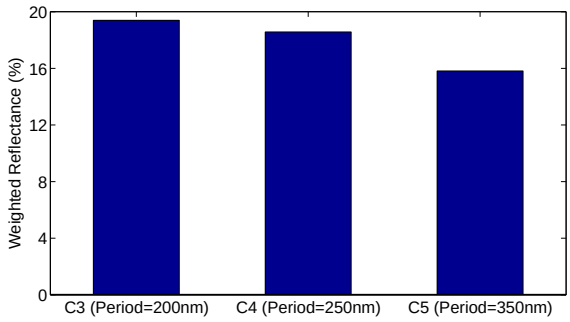

FIGURE 5.12: Weighted reflectance of silicon moth-eyes C3, C4 and C5 with AOIs of $2 - 83°$ and wavelengths of $450 - 900$.

5.3.3 Summary

Silicon moth-eyes of different periodicity were studied under the illumination of s and p polarised light at arbitrary AOIs. The orthogonal polarisation of light does not affect the reflectance of silicon moth-eyes at normal incidence. This was also observed previously while performing simulations for the optimized silicon moth-eye. However at arbitrary angles of incidence the reflectance of samples at s and p polarisation is different.

The effect of the periodicity on the reflectance spectrum of silicon moth-eyes at normal incidence is also evident at arbitrary angles of incidence: the angular reflectance spectrum moves to higher wavelengths as the periodicity increases.

The angular reflectance of silicon moth-eyes was shown to be sensitive to the incident wavelength and to differ between the two orthogonal polarisations. Unlike silicon with a smooth surface (at the sub-micron level) which has higher values of angular reflectance for s polarisation compared to p polarisation at all wavelengths, silicon moth-eyes show

an inverse behaviour at some wavelengths. However the total angular reflectance of moth-eye structures showed higher values for s polarisation than p polarisation.

The angular reflectance of silicon moth-eyes at s polarisation increased as AOI increased for all samples. At p a different behaviour was observed among samples: C3 with a periodicity of 250nm showed a constant increase of the angular reflectance, while C4 and C5 showed a decrease of angular reflectance up to an AOI of ≈ 62 and increased from there. However the total angular reflectance of the un-polarised light showed an increase with AOI for all samples but with a different angular dependency. C3 is very angle dependent while C4 is less and C5 is almost constant up to an AOI of 40°.

The silicon moth-eyes were compared to silicon and a reduction of reflectance at arbitrary AOI of up to a certain AOI was observed; however the AOI where the reflectance of silicon moth-eyes starts to be higher than silicon changes with different periodicities. AOIs greater than 70° are almost at the Brewster angle where silicon shows zero reflectance for p polarisation and thus the reflectance of the silicon moth-eye is higher. However C3 showed that silicon moth-eye structures can also cancel the effect of the Brewster angle. As a result the reflectance of silicon moth-eyes is higher than silicon at this AOI.

5.4 Conclusion

This chapter examined the influence of the periodicity on reflectance of silicon moth-eyes at arbitrary AOIs. Two sets of measurements were performed on silicon moth-eye samples:

- Normal incidence measurements using a probe fibre.
- Specular reflectance measurement using a goniometer reflectometer.

It was shown that increasing the periodicity does not have a noticeable effect on the average and weighted reflectance, however it shifts the angular reflectance spectrum towards higher wavelengths. This is in agreement with the simulation results performed in Chapter 4. This phenomena is an advantage in the design process where the minimum reflection region can be designed by choosing the right periodicity according to the system needs.

The reflectance of silicon moth-eyes is significantly wavelength and angle dependant. However these samples showed an independence to polarisation for AOIs of up to 30°. Moreover it was shown that increasing the periodicity reduces the angular dependency of the reflectivity of silicon moth-eye samples.

Comparison of the angular reflectance of silicon moth-eyes with silicon confirmed that introducing moth-eye structures at an interface reduces the reflectance of the surface at

normal incidence and also arbitrary angles of incidence. In the case of one sample it also removed the Brewster angle effect of silicon surfaces.

Silicon moth-eyes were simulated using two models, one with pillar heights calculated from SEM images and the other using a design height of 400nm for all samples. A better agreement was shown between the model with a height of 400nm and the experimental results. This may be because samples at the edges showed taller pillars than the other areas. Employing pillars of 400nm height in the model showed that RCWA is capable of predicting the reflectance of silicon moth-eyes qualitatively.

The samples investigated in this chapter were not optimised samples, they were used to study the effect of the periodicity. Also the flat top of the pillars caused the reflectance of these structures to reach high values (40%). The next chapter implements the same experimental study on silicon moth-eyes which were previously optimized for solar cell anti-reflective purposes.

Chapter 6

Reflectance Properties of Silicon Moth-eyes with Changing External Conditions

Computational studies have been performed to optimize silicon moth-eye structures for anti-reflective purposes [15]. A moth-eye structure with a periodicity of 280nm was identified as an optimum anti-reflective to deliver the least reflectivity at normal incidence at a wavelength of 628nm. A height of 400nm was chosen to provide a balance between fabrication difficulties, low reflectance and surface area of the structure. The packing density was fixed at 50%. Accordingly, silicon moth-eyes were fabricated using nano-imprint lithography, employing different etching stages to alter the shape of the pillars. This chapter investigates the reflectance properties of these silicon moth-eyes. The reflectance of samples at normal incidence and arbitrary angles of incidence was studied using the probe and reflectometer measurement techniques. Further study of the effect of rotating the azimuth orientation of samples on their angular reflectance was also performed using the reflectometer to investigate the performance of silicon moth-eye structures for anti-reflective applications and stealth applications.

6.1 Samples: Nano-Imprinted Silicon Moth-eyes

Silicon moth-eye structures investigated in this chapter were fabricated using nano-imprint lithography [15]. A stamp was fabricated with cylinders in a hexagonal lattice of 280nm periodicity and density of 50%. The stamp fabrication process was similar to steps 1 to 6 used in e-beam lithography in Chapter 5 (Figure 5.1). After the removal of Al disks, an anti-adhesion coating covers the stamp to prevent the stamp from sticking to the substrate. The stamp is made from silicon. The imprinting process is presented in Figure 6.1. The e-beam resist of 170nm thickness is spun on a silicon wafer. The

stamp is then placed on top of the wafer coated with resist and placed into the hot embossing tool. The wafer is heated to 190°C. A pressure of 40 bar is then applied for 5 minutes. After the sample is cooled to room temperature the pressure is released and the stamp is separated from the sample. The pattern of the stamp is imprinted on the resist producing cylindrical holes in the resist. An oxygen plasma etch is performed to remove the remaining resist at the bottom of the holes. The remaining steps are the same as from step 3 to the last step of the e-beam fabrication process in Chapter 5. 15nm of aluminium is deposited which is later removed by a liftoff process to produce disks of aluminium on the silicon substrate. Dry etch is then performed to produce 400nm tall pillars with vertical walls. After the Al mask is removed, isotropic etch and oxidation are performed to give a tapered shape to the pillars and to smooth the profile. Finally, the oxide is stripped from all wafers.

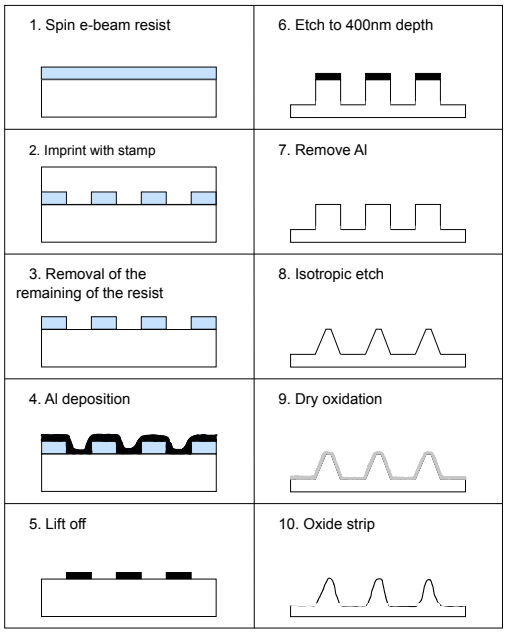

FIGURE 6.1: Fabrication steps of silicon moth-eye structures with the nano-imprinting process.

The oxidation time is varied for each of the three wafers to produce different pillar shapes:

- Wafer 1: Isotropic etch 90s, no oxidation.
- Wafer 2: Isotropic etch 90s, oxidation 5 mins.
- Wafer 3: Isotropic etch 90s, oxidation 10 mins.

This imprinting step is repeated on the surface of the wafers to produce an area of 1cm×1cm of the moth-eye structure. Figure 6.2 shows top view SEM images of the samples. The periodicity of all three of the structures is extracted from SEM images

and approximated to 270nm. Unfortunately the pillars from the top view show a square cross section as opposed to a circular cross section. SEM images of the imprinting stage (Figure 6.3) shows that the stamp and the Aluminium disks produced circular shape holes and rods respectively. Thus the square shapes are due to the effect of etching stages on the crystalline structure of the silicon, either during the Anisotropic etch to produce vertical wall cylinders or during the isotropic etch to produce tapered cylinders. SEM images of the horizontal direction of samples are shown in Figure 6.2. Pillars in wafer 1 are thicker than the other wafers and have vertical walls, the base diameter of pillars is approximately 155nm and the top diameter is 147nm. Wafers 2 and 3 have pillars with tapered walls, however the pillars in wafer 2 are sharper than pillars in wafer 3 and have a smaller diameter at the top compared to wafer 3. An outline of the pillars' profile is extracted from SEM images and plotted in Figure 6.2. The specifications of the pillars are noted in the image.

6.2 Normal Incidence Measurement

6.2.1 Experimental Set-up

The probe set-up was used to measure the normal incidence reflection of the silicon moth-eye samples. The specifications of the set-up was explained in Section 3.2.1. The integration time was set to 100ms and Boxcar width to 10.

6.2.2 Results

Figure 6.4 shows the reflectance results of the silicon moth-eye structures at normal incidence. Wafer 1, with protuberances with vertical walls shows higher reflectance compared to the other two samples with tapered walls. It also shows more sensitivity to wavelength. Wafers 2 and 3 show lower reflectance values across the whole spectral range and a wider low reflectance region in the spectra. However, the near to zero reflectance region is between $550-650$nm for wafer 2 and $650-750$nm for wafer 3. The mean average of the reflectance of these three samples at normal incidence is plotted in Figure 6.5. The mean average reflectance of wafer 1 is greater than the other two samples, 9.21%, whereas wafers 2 and 3 have a very close mean average reflectance of 6.75%.

The comparison between the reflectance spectra of the three silicon moth-eye samples shows that samples with finer protuberances and of tapered profile show less reflectance. This is a result of the discontinuity that the shape of the profiles produce in the transition of refractive index from the top to the bottom of the moth-eye layer. Protuberances with a flat top produce a larger discontinuity at the interface which produces more reflection.

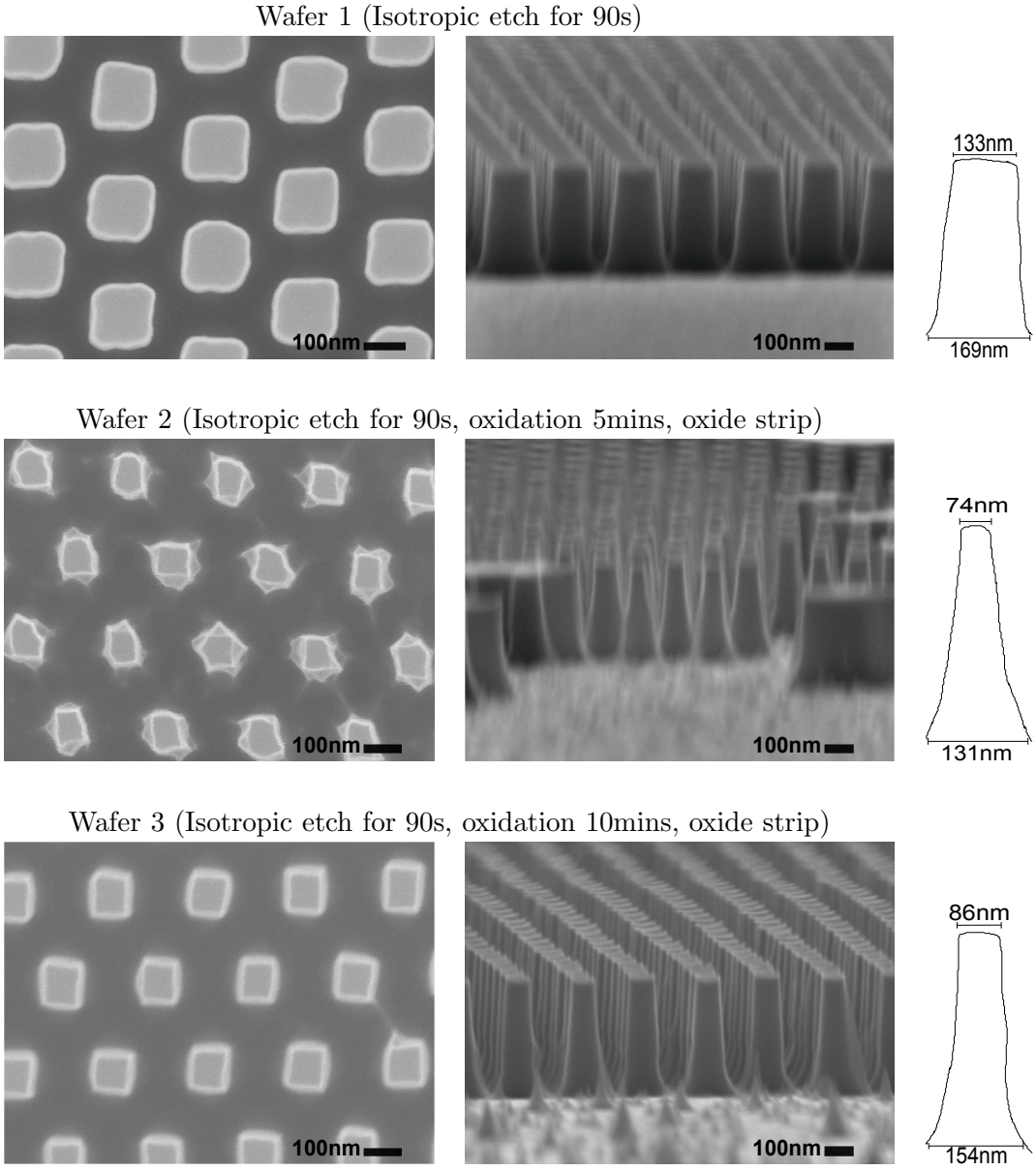

FIGURE 6.2: SEM images of silicon nano-imprinting lithography silicon moth-eye structures with the periodicity of 280nm, height of 400nm and packing density of 50%. The etching time differs among the samples, producing a different profile shape. The etching time is noted for each wafer. Images are taken from top view (left) and horizontal view (right). The outline profile is taken from a pillar in the horizontal view. (The images from horizontal view are courtesy of Dr Stuart Boden)

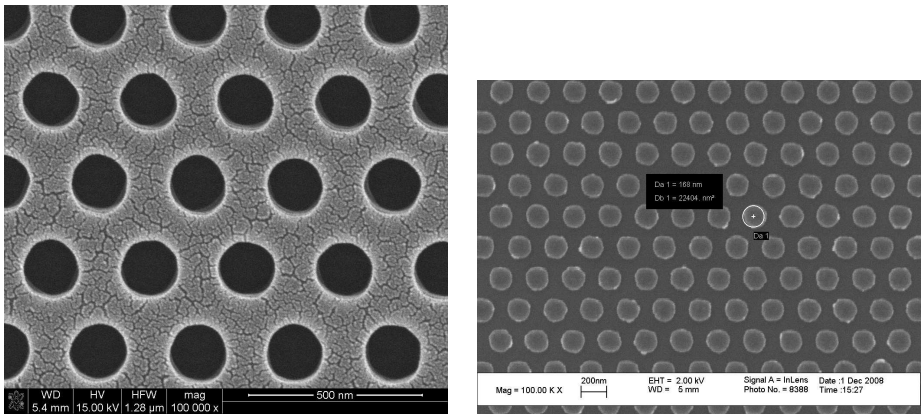

(a) (b)

FIGURE 6.3: (a) SEM images of stamp imprinted into the e-beam resist. (b) SEM images of Al disks after removal of resist. (Images are courtesy of Dr Stuart Boden.)

However, thinner protuberances with a tapered profile have a sharper tip and reduce the extent of discontinuity in the refractive index between the two layers and consequently reduce the reflectance. The mean average reflectance of wafers 2 and 3 are the same, however the reflectance spectrum is different within the wavelength range. The low reflectance region for the two wafers is within a different wavelength range. Since the height and period of the two wafers are the same, the only difference between them is the profile of the pillars and the base diameter. The difference between the shape of the pillars has caused the reflectance spectra to change, while the base diameter difference has shifted the low reflectance region to higher wavelengths in wafer 3.

6.2.3 Comparison with Simulations

Silicon moth eyes were modelled using the dimensions presented in Figure 6.2. Results are presented in Figure 6.4. The first model employed tapered profile pillars (red dashed line). However the pillars in the SEM images do not have a tapered profile. So a sinusoidal profile for pillars was employed (Figure 6.6). Results are presented in black dashed dotted lines. The model shows qualitative agreement with the measurements. Differences between modelling results and experimental results may be due to the assumed dimensions which may not be fully representative of the structure. In addition, the profile of the actual pillars are not necessarily a linearly tapered or a sinusoidal and thus the difference between model and experiment may be expected.

To model the pillars, the profile of a pillar of wafer 3 was taken from the SEM image from the edge of the sample (Figure 6.2). However, it was noticed that pillars at the edge of samples have greater values of height and diameters than the average values calculated from SEM images. An outline of the pillar is first created in "InkScape" and saved as ".bmp" file format. The file was given to a Matlab script (created by Boden in [15]) where the pillar along the height is divided into thin layers of disks with

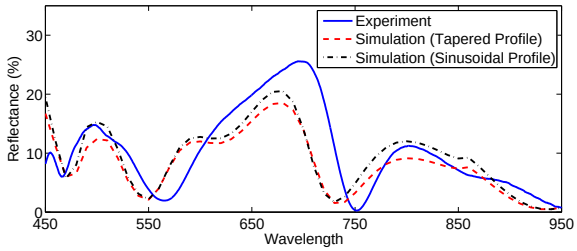

(a) Wafer 1

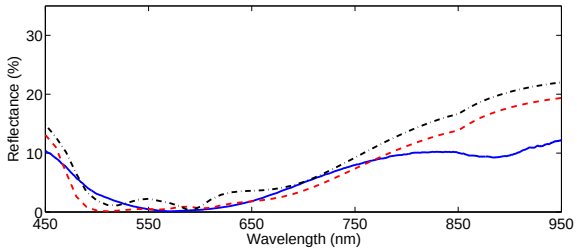

(b) Wafer 2

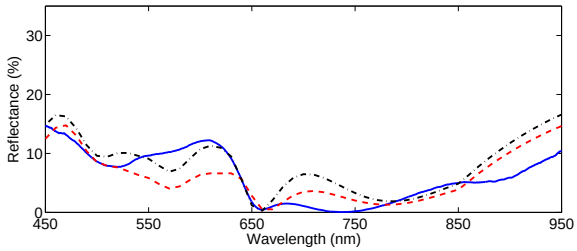

(c) Wafer 3

FIGURE 6.4: Reflectance of silicon moth-eye samples, wafers 1, 2 and 3 at normal Incidence (solid blue line). Silicon moth-eyes have a period of 270nm and height of 400nm. The profile of pillars of each wafer is different and presented in Figure 6.2. The simulation results of normal incidence reflectance of samples for tapered profile (dashed red line) and sinusoidal profile (black dash dot line) are also presented.

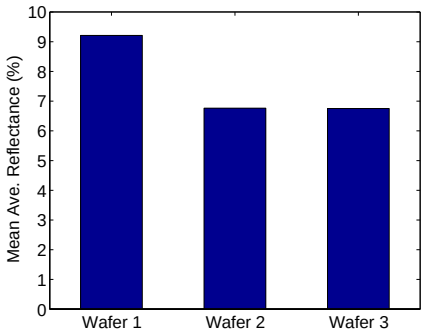

FIGURE 6.5: Mean average reflectance of silicon moth-eyes presented in Figure 6.2.

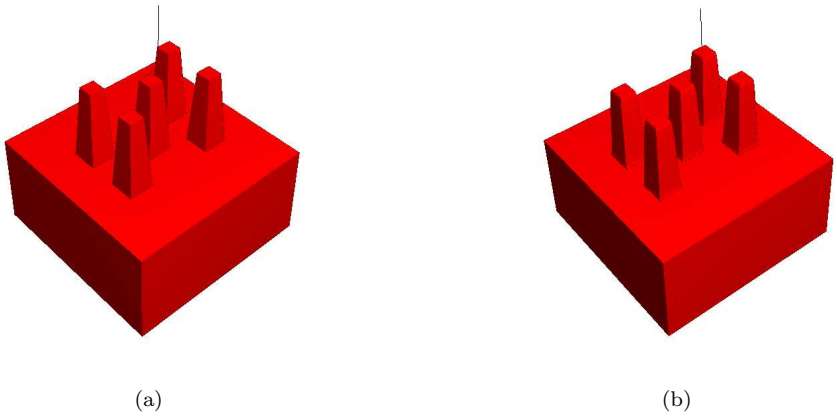

(a) (b)

FIGURE 6.6: The structures used in RSoft to model silicon moth-eyes with (a) tapered pillars and (b) sinusoidal pillars.

varying radius from the top of the pillar to the base of the pillar. These disk layers are then plotted in RSoft to produce the pillar profile. Modelling results are presented in Figure 6.7. The difference observed between the modelling and experimental results are bigger than previous modelling results which is due to the over sized pillars at the edge of the samples. Thus in order to model the pillars accurately, a profile from the inner part of the sample should be chosen. However, in order to extract the profile of a pillar further from the edge of the sample, the sample should be cut across a cross section which is not favourable.

6.2.4 Summary

The normal incidence reflectance of three silicon moth-eye structures of the same dimensions were measured using the probe measurement technique. The etching time was varied between the three samples and moth-eye structures with different pillar profiles were produced. Therefore the reflectance behaviour of samples was also different: samples with vertical walls and wider pillars showed higher reflectance and more sensitivity to wavelength. Samples with protuberances with tapered walls and sharper tips showed less reflectance and were less sensitive to wavelength. This shows that sharper pillars provide a smoother refractive index transition from the top to the bottom of the moth-eye structure and thus reduces the surface reflectance. This confirms the study of Southwell [84] where the optimum profile for a silicon moth-eye structure was suggested to be a tapered pillar with a sharp tip (Figure 2.11).

The modelling of moth-eyes investigated in this chapter agree qualitatively with experimental results at normal incidence. The pattern of the reflectance spectrum was approximately predicted by the models, however the differences between the model and experiment are due to the fact the structures used in the model are an approximation of the structures and not the exact profile of the pillars.

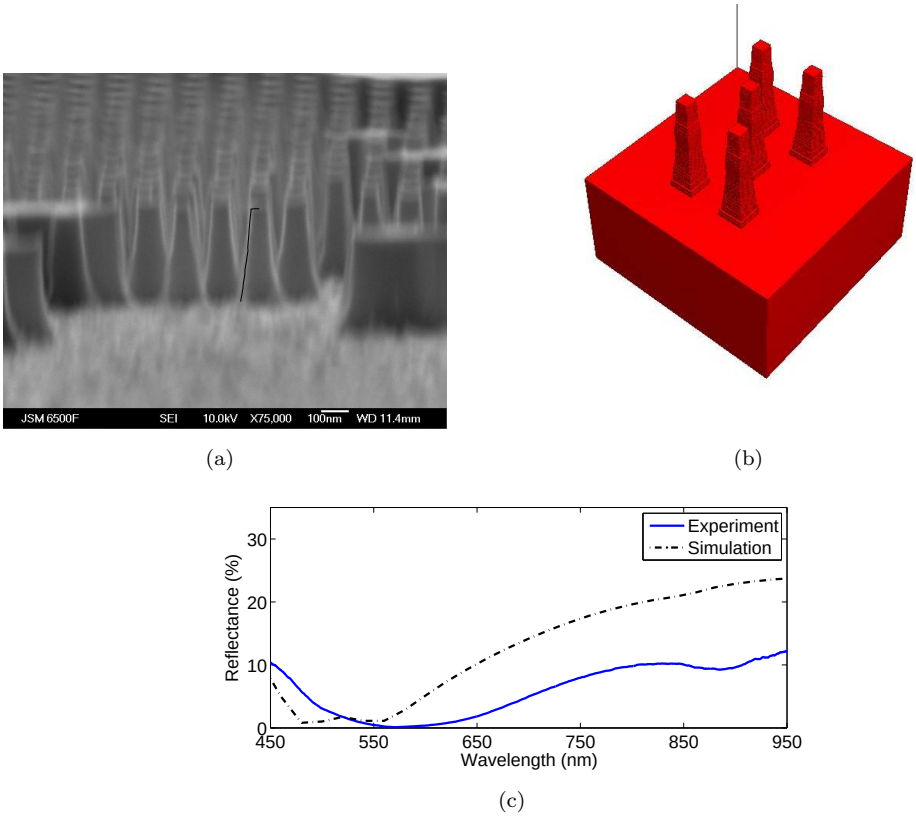

FIGURE 6.7: (a) An outline of a pillar in the SEM image of wafer 2 is drawn. (b) Pillars are modelled using the outline presented in (a). Figure shows the unitcell used in RSoft to model wafer 2. (c) Normal incidence reflectance of wafer 2 using the profile of a pillar of SEM image (black dash dot line) compared with experimental results.

6.3 Angular Reflectance Measurement

6.3.1 Experimental

The reflectometer set-up was used to measure the reflectance of samples at arbitrary angles of incidence and arbitrary azimuth angles. The laser power used for each sample was chosen according to the behaviour of the sample and whether or not the signal could be detected by the spectrometer. The integration time also differs in order to provide a high enough signal-to-noise ratio. Table 6.1 lists the laser power and integration time for each sample for s and p polarisation measurement. The normalisation process and calculation of the reflectance of samples were performed as described in Chapter 3.

The angle of the detector was changed from 2° to 170° in steps of 0.2°, giving a fine scan over the angle of incidence from 1° to 85°. The smallest incident angle where the beam was not blocked by the mirror and entered the mini integrating sphere was at 1.5°. After processing data and cancelling the noise away, the results are acceptable between angle of incidence of 2° and 83°. The signal-to-noise ratio causes the wavelength range

	***s* polarisation**		***p* polarisation**	
	Laser Power (mW)	Int. Time (ms)	Laser Power (mW)	Int. Time (ms)
Wafer 1	39.1	1000	68	1000
Wafer 2	48.9	2000	79.7	1000
Wafer 3	53.4	1800	65.8	1500

TABLE 6.1: The laser power and integration time set for reflectance measurements performed on silicon moth-eye samples using the reflectometer

of $450-850$nm to be of acceptable results. The sample was rotated in the azimuth plane in steps of 5° from a reference angle 0° to 75°.

6.3.2 Results

6.3.2.1 Reflectance at Normal Incidence

The reflectance of silicon moth-eye samples of 270nm period and different pillar profile was measured using the reflectometer. The reflectance spectrum for s and p polarisation at near to normal incident angle, extracted at an AOI equal to 2°, is plotted in Figure 6.8. Average reflectance at s and p polarisation is calculated and presented as the reflectance of unpolarised light, R. The reflectance of samples at the two orthogonal polarisations have similar values and thus overlapped by the average value. The normal incidence results of the probe measurement is also plotted. A close similarity between the probe and reflectometer measurement results exist which shows the amount of light collected by the probe fibre and the mini integrating sphere in the reflectometer set-up are approximately equal and confirms the validity of both measurements. The reflectance of silicon moth-eye samples have almost equal values for s and p polarisation, a result similar to Chapter 5.

6.3.2.2 Reflectance at Arbitrary Angles of Incidence

The reflectance of silicon moth-eyes at arbitrary angles of incidence $(2-83^\circ)$ and wavelengths $(450-850\text{nm})$ for s and p polarisation are presented in Figure 6.9. Similar to the silicon moth-eye structures of Chapter 5, the angular reflectance of wafer 1 has narrow bandwidth features of low reflectance (below 10%) at both s and p polarisation at certain wavelengths which either stay at a constant wavelength as AOI increases or move to neighbouring wavelengths (shorter or longer). However, wafers 2 and 3 do not have such features and instead have a broader wavelength range of low reflectance. The width of the low reflectance regions are wider at p polarisation than s polarisation. Results show that the reflectance of wafer 1 stays under 30% up to the AOI of 50° for s polarisation, but up to an AOI of 75° for p polarisation. Wafer 2 has a reflectance above

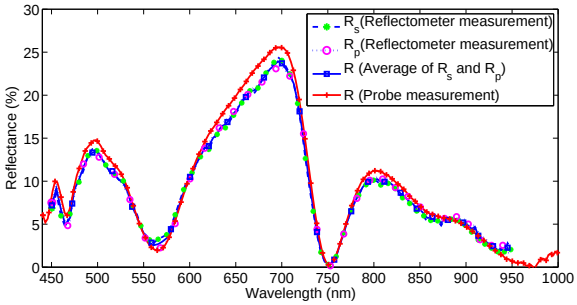

(a) Wafer 1

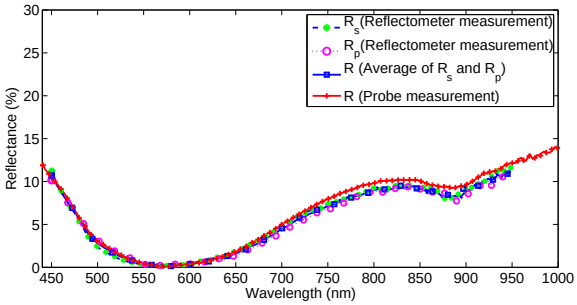

(b) Wafer 2

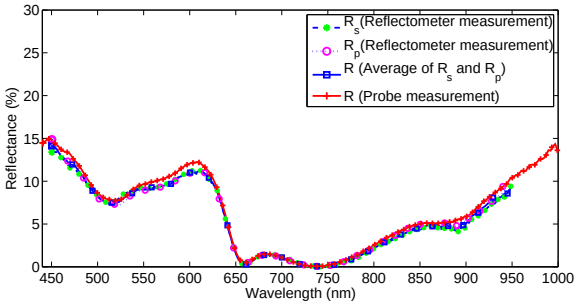

(c) Wafer 3

FIGURE 6.8: Comparison of reflectance of silicon moth-eye samples, (a) Wafer 1, (b) Wafer 2, (c) Wafer 3, measured by reflectometer measurement at near normal incidence (AOI= 2°) with probe measurement.

30% for a wavelength of $450 - 700$nm only for AOIs larger than 75° for s polarisation and 70° for p polarisation. For wafer 3 the boundary between reflectance below and above 30% is at an AOI of 60° for s polarisation and 65% for p polarisation.

In order to study the influence of the AOI on reflectance more quantitatively, the reflectance spectrum of samples at certain AOIs is extracted from Figure 6.9 and plotted in Figure 6.10 for s and p polarisation. At s polarisation, increasing the angle of incidence causes the reflectance spectrum to shift to higher values of reflectance for the majority of the wavelength spectrum for all three samples. At p polarised light, this is only the case for wafer 2. The reflectance of wafers 1 and 3 reduces as the angle of incidence increases until it reaches a minimum at AOI= 50° for wafer 1, and AOI= 30° for wafer 3. From this angle, increasing the angle of incidence increases the reflectance. The reflectance

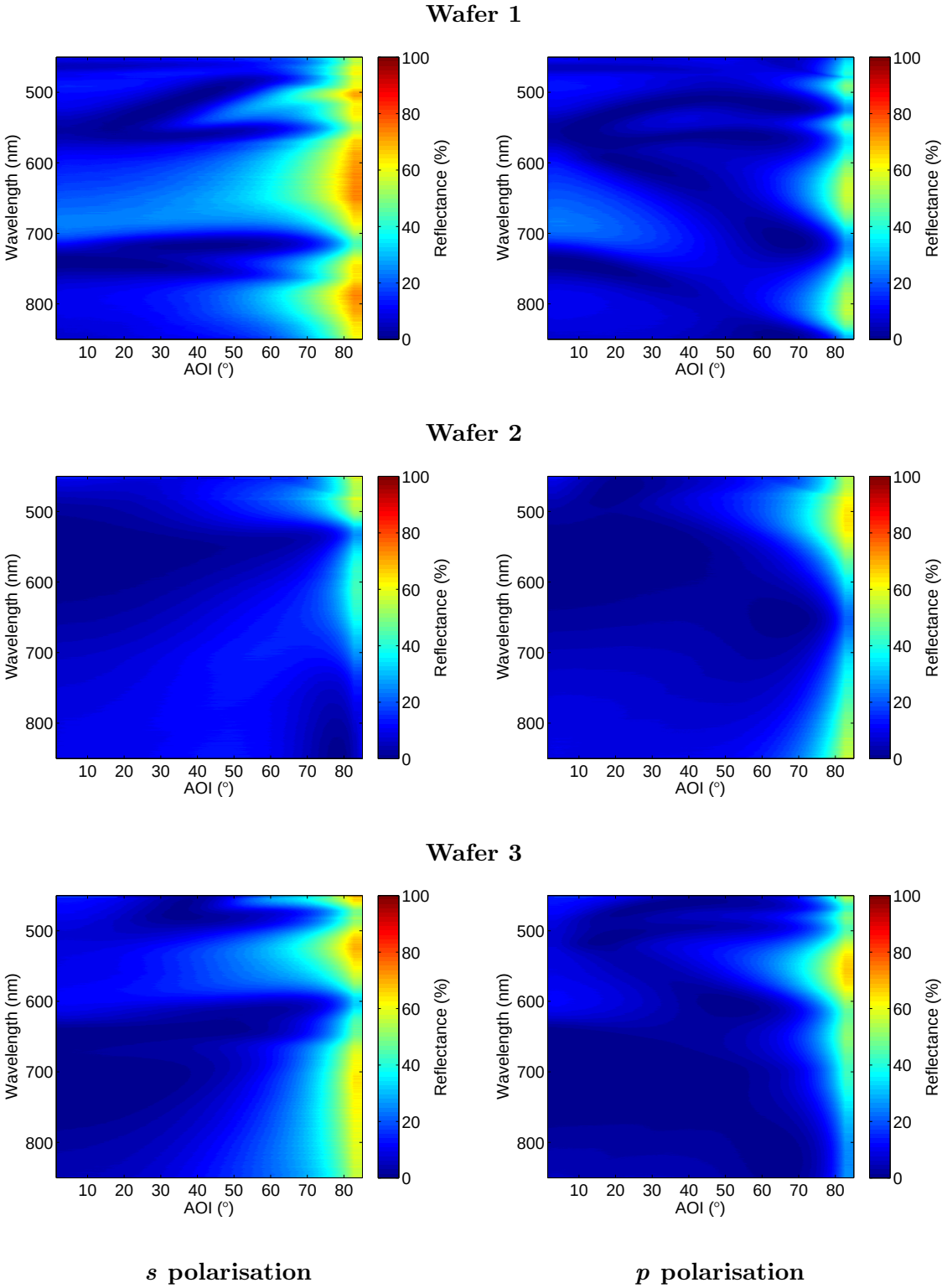

FIGURE 6.9: Reflectance spectrum of silicon moth-eye samples presented in Figure 6.2, at the angle of incidence of 1.5° to 83°, and wavelength range of $450-850$nm at s and p polarisation. The periodicity and height of moth-eye structure is 270nm and 400nm respectively for all samples. These measurements are performed at the 0° azimuth orientation.

spectrum of wafer 2 at wavelengths above 650nm are approximately overlapped from normal incidence to the AOI of 60°. Similar behaviour is observed for wafer 3. It shows that the reflectance of wafers 2 and 3 at higher wavelengths is not sensitive to AOI up to an AOI of 60°.

Figure 6.11 shows the value of maxima and minima of each sample at both polarisations as the angle of incidence increases. It confirms that the maximum reflectance value of wafer 1 and 3 of p polarisation decreases until it reaches a minimum value where it starts increasing again. The minima of all samples at p polarisation does not show a significant change influenced by the AOI, whereas at s polarisation minima value slightly increases at AOI= 50° and above and reaches to values of up to 10% for wafer 1 and lower for wafers 2 and 3 at AOI= 70°. The difference between the minima and maxima at s polarisation is greatest for wafer 1 and lowest for wafer 2 at all AOIs, while for p polarisation it varies as AOI changes. Wafer 2 has similar values of maxima and minima at the two polarisations. The highest increase of maxima from near normal incidence to AOI= 70° is observed for wafer 3, 35% while wafer 1 only shows an increase of 25% and wafer 2 shows only 20%.

Figure 6.12, Figure 6.13 and Figure 6.14 show the reflectance of wafer 1, 2 and 3 respectively for incidence angles of $2 - 83°$ in steps of 0.1° for s and p polarisation, at wavelength intervals of 50nm. The angular reflectance at individual wavelengths shows a different behaviour for all samples. Wafer 1 (Figure 6.12), shows significant changes of the angular reflectance with wavelengths; the maximum and minimum values of reflectance and shape of the line plots are varying arbitrarily with the wavelength. The reflectance is very angle dependant at all wavelengths for both polarisations, except at wavelength of 700nm and 900nm where the reflectance of s polarisation is constant up to the AOI of 60° and 40° respectively. Also for most of the spectra s and p polarisations show significantly different reflectance values. Wafer 2 (Figure 6.13) however, shows a closer similarity between angular reflectance of s and p polarisation. For wavelengths higher than 750nm angular reflectance at s polarisation shows a drop of reflectance at AOI of $\approx$ 80°. At the wavelength of 850nm, the s polarisation reflectance value at AOI= 79° reaches zero. This implies the existence of an inverse polarisation behaviour for this sample; silicon reflectance value reaches zero at the Brewster angle for p polarisation whereas at wafer 2, the zero reflectance is observed for s polarisation. The angular reflectance of wafer 3 also varies with wavelength. At wavelengths of 650nm and above, reflectance at p polarisation is less sensitive to angle of incidence up to AOI of 50°, however the value of the reflectance varies with wavelength. An almost equal reflectance value of s and p polarisation also exist for wafer 3, at wavelengths of 500nm and 650nm. Wafer 3 shows zero reflectance at AOI= 63° for p polarisation, similar to silicon.

The angular reflectance of silicon moth-eyes is averaged over all wavelengths and presented in Figure 6.15. The difference between reflectance of s and p polarisations is

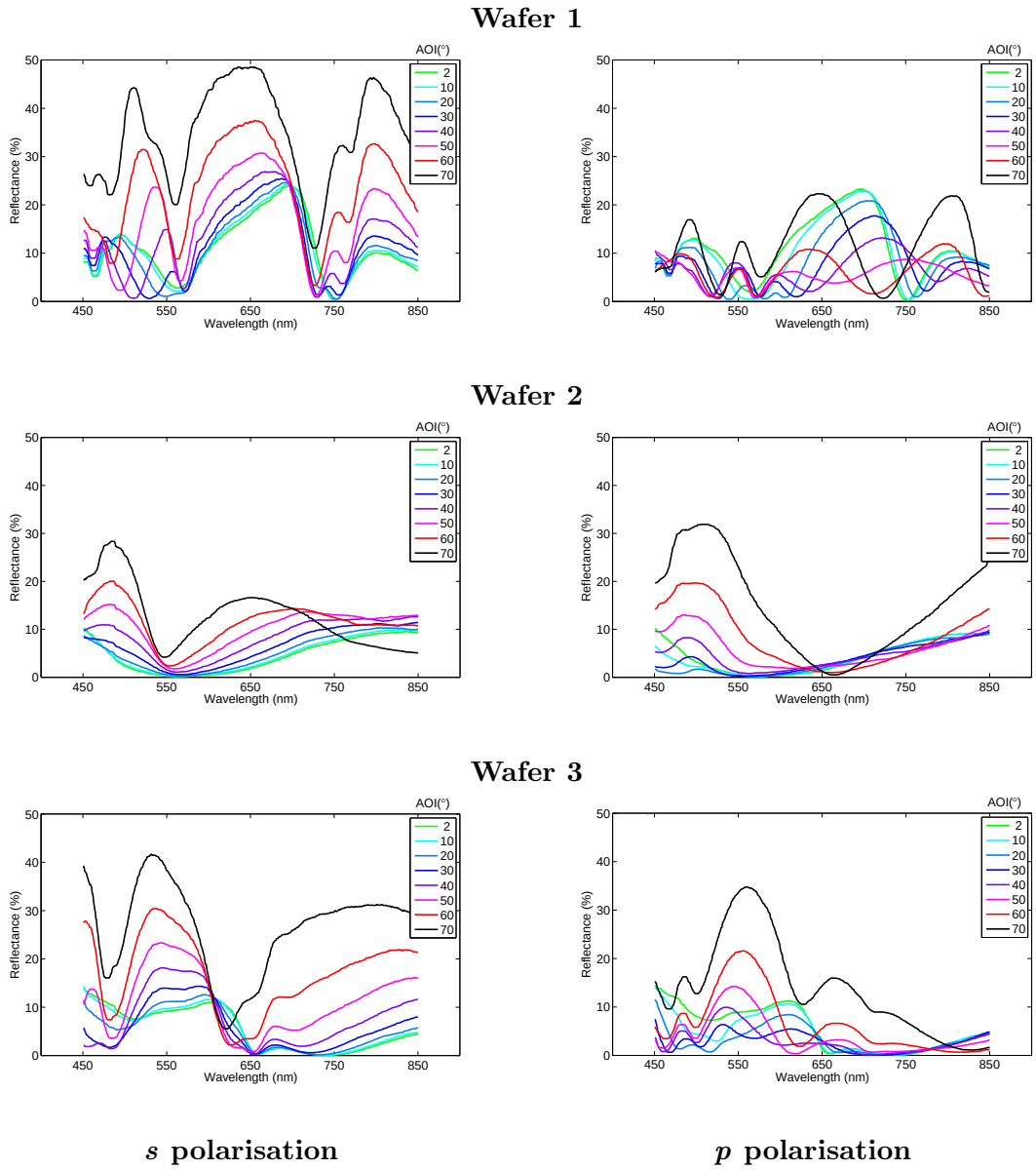

FIGURE 6.10: Reflectance of silicon moth-eye structures with the periodicity of 270nm, height of 400nm and different pillar profile shapes, at AOI intervals of 10° for the wavelength spectrum of 450 − 850nm.

biggest for wafer 1. Wafer 1 shows higher reflectance values at s polarisation compared to wafers 2 and 3, reaching the value of above 60% for AOI of 80° as opposed to 25% for wafer 2 and 48% for wafer 3. Reflectance of p polarisation has the highest increase along the angle of incidence at wafer 2, almost 40%, and it is lower at wafers 1 and 3, approximately 30%. Wafer 1 shows the biggest range of angular insensitivity while comparing the angular reflectance of unpolarised light, from normal incidence to 40°. Whereas wafer 3 shows a constant reflectivity for total reflectance of unpolarised light only up to AOI of 20°. The angular reflectance of wafer 2 at unpolarised light is not constant, however for p polarisation the reflectance stays constant up to AOI of 40°. The inverse polarisation behaviour of wafer 2 is also clear: at AOI= 62° the reflectance of s

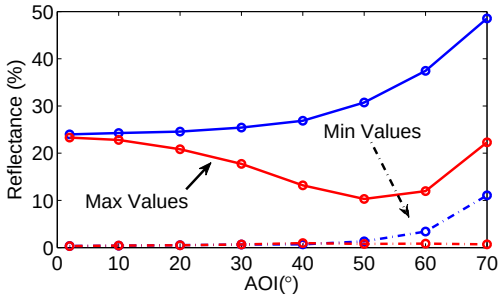

(a) **Wafer 1**

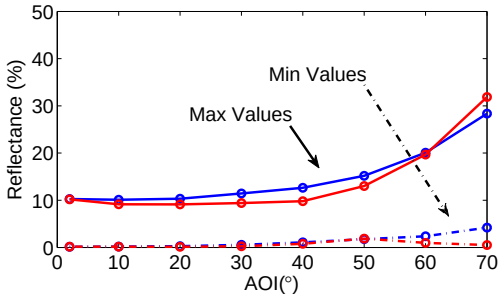

(b) **Wafer 2**

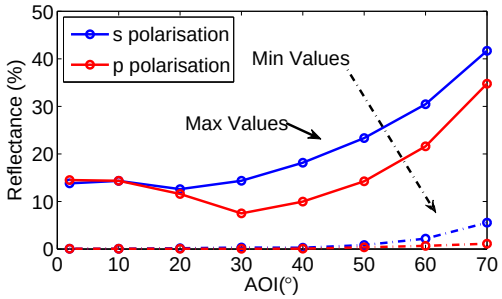

(c) **Wafer 3**

FIGURE 6.11: Maxima (solid line) and minima (dash-dot line) of silicon moth eyes (a) wafer 1, (b) wafer 2 and (c) wafer 3 at AOIs extracted from Figure 6.10 for s (blue) and p (red) polarisation.

polarisation is lower than reflectance value of p polarisation. The inverse polarisation behaviour was previously reported by Chuang *et al.*[22]. They showed silicon moth-eye structures with periodicity of 350nm, base diameter of 245nm and height of 400nm show inverse polarization at wavelength of 1250nm. Chuang *et. al* claimed that an inverse polarisation at visible regime will occur in a moth-eye structure with sub-100nm diameter base. However, wafer 2 has the periodicity of 270nm and base diameter of 130nm and shows an inverse polarisation at the incident wavelength of 750nm and higher. It should be considered that pillars in wafers 1 and 3 are arranged in the same periodicity as wafer 2, 270nm, and height, 400nm. The only difference between pillars of these samples, is the pillar profile (base diameter and top diameter). Thus the inverse polarisation does not necessarily depend on the periodicity; the height of the structure, the shape of the pillars and the ratio of the periodicity to diameter can play a significant role.

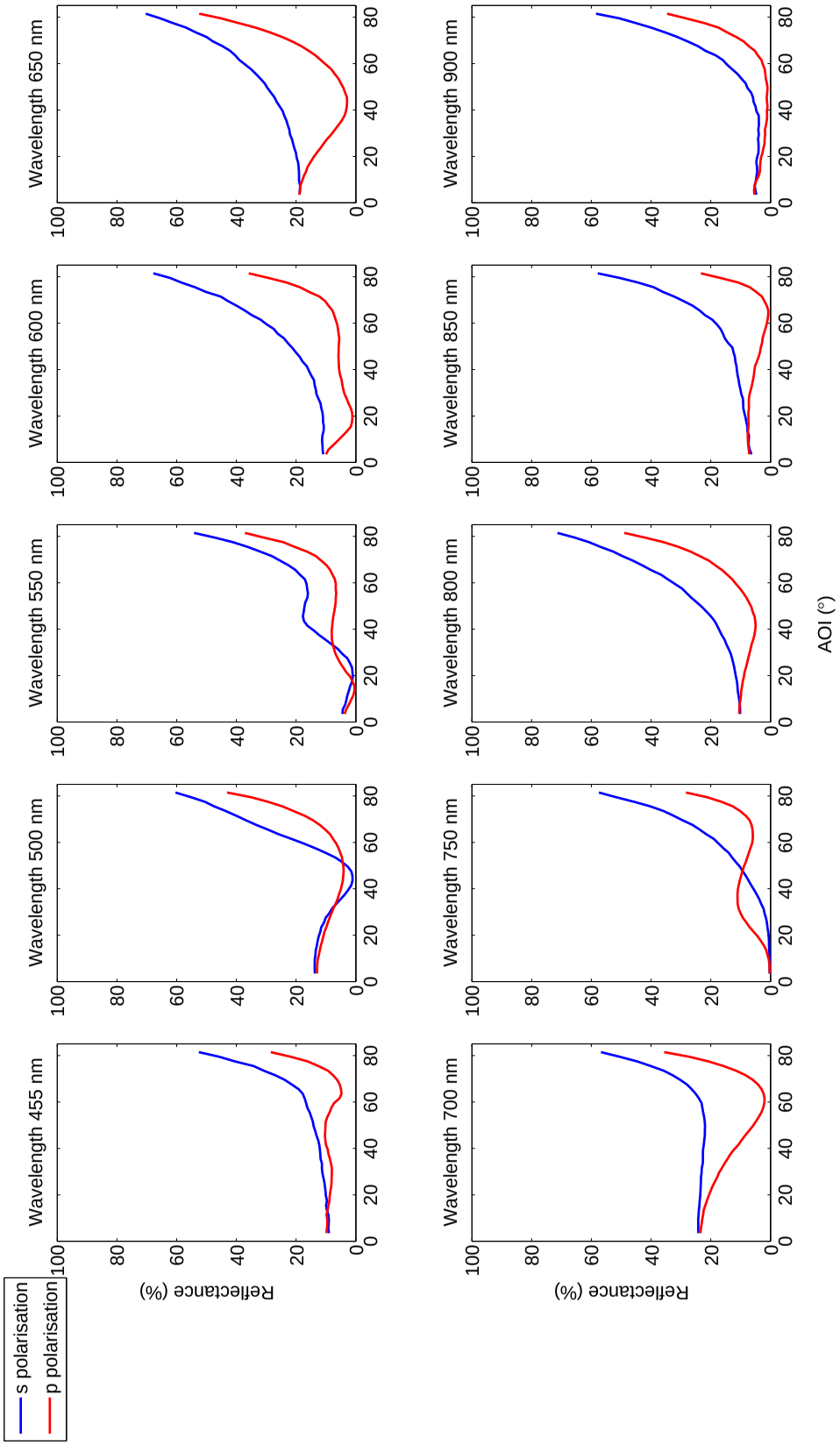

FIGURE 6.12: Angular reflectance of silicon moth-eye, wafer 1, at wavelength intervals of 50nm from $450 - 900$nm, at AOI of $2 - 83°$ for s and p polarisations.

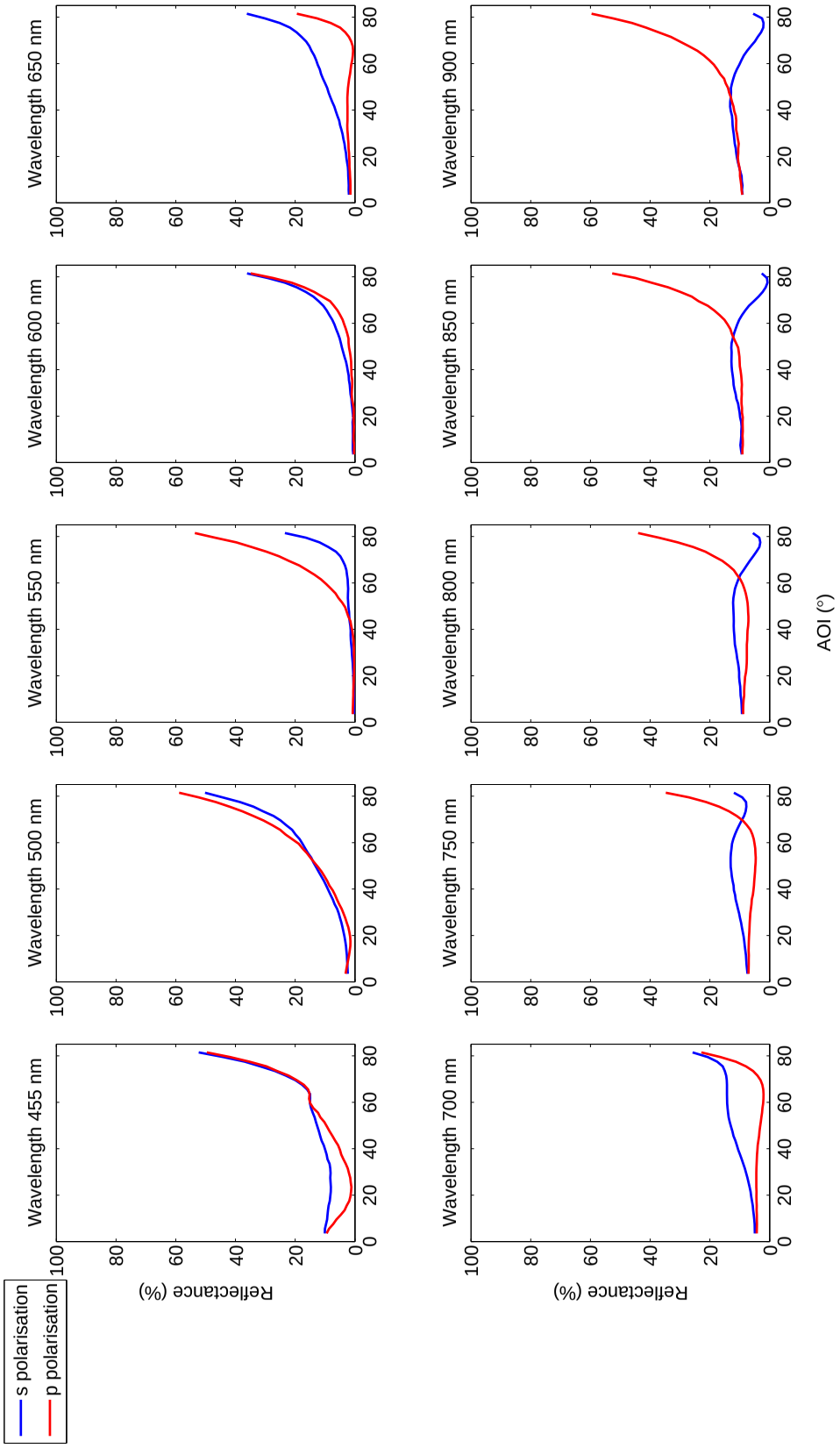

FIGURE 6.13: Angular reflectance of silicon moth-eye, wafer 2, at wavelength intervals of 50nm from $450 - 900$nm, at AOI of $2 - 83°$ for s and p polarisations.

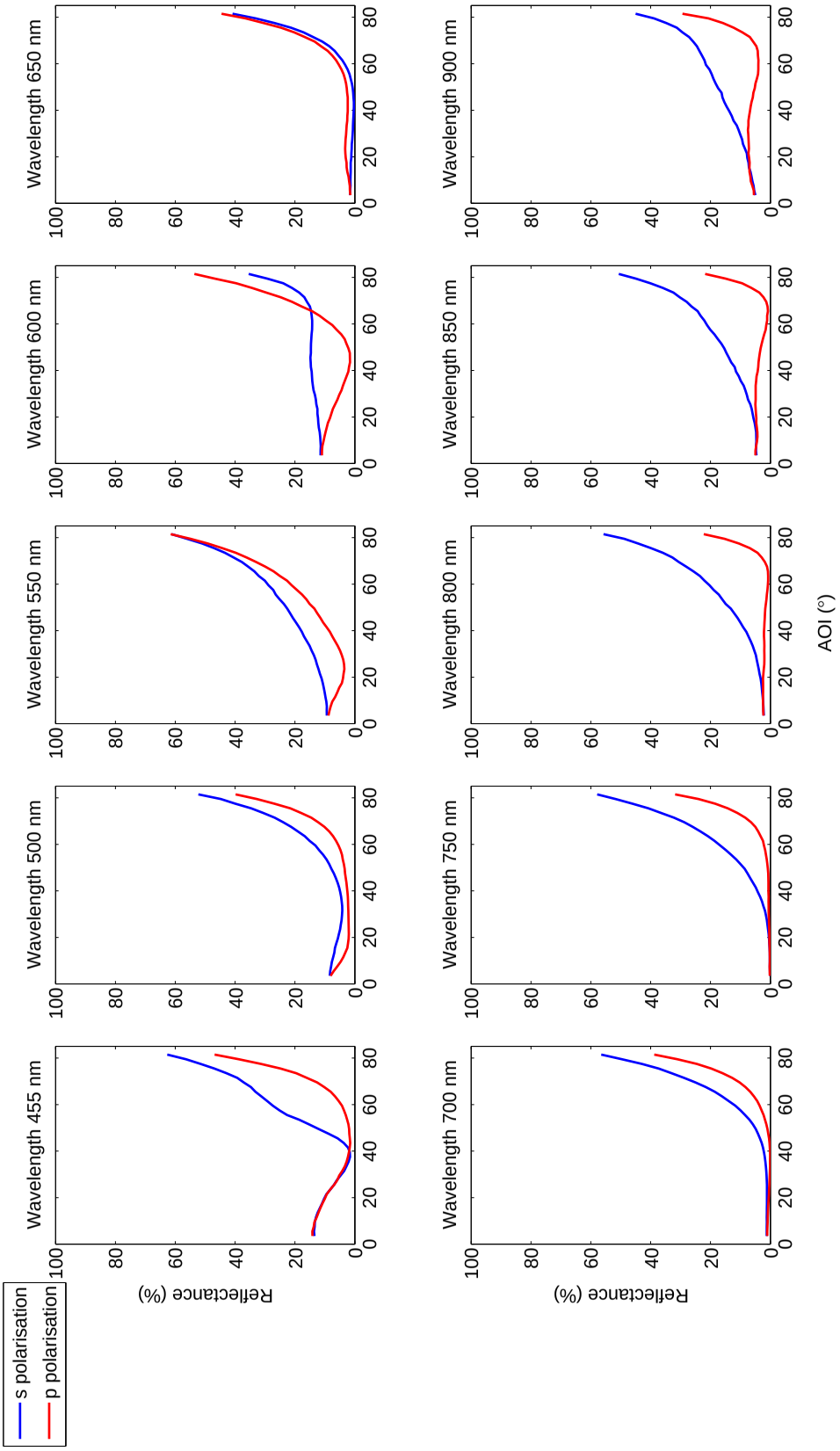

FIGURE 6.14: Angular reflectance of silicon moth-eye, wafer 3, at wavelength intervals of 50nm from $450 - 900$nm, at AOI of $2 - 83°$ for s and p polarisations.

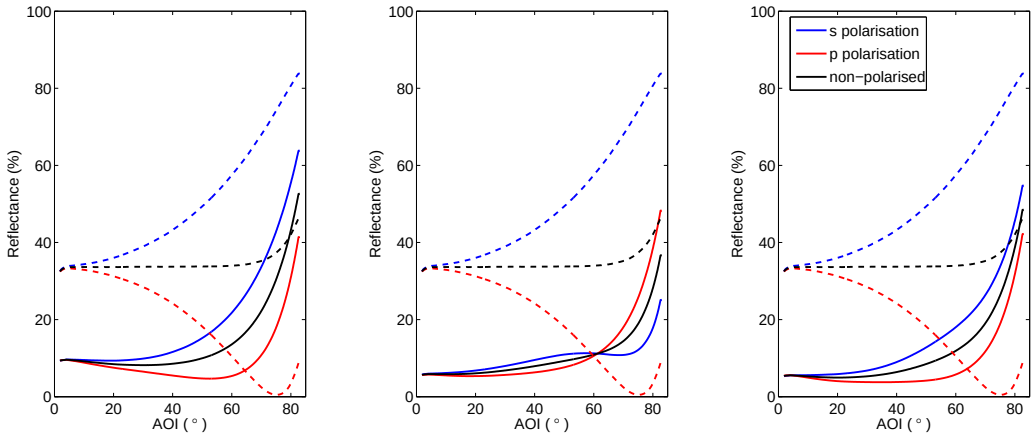

(a) **Wafer 1** (b) **Wafer 2** (c) **Wafer 3**

FIGURE 6.15: Total angular reflectance of silicon moth-eyes, (a) wafer 1, (b) wafer 2 and (c) wafer 3 at AOIs of $2 - 83°$ for s (blue) and p (red) polarisations. An average of the two orthogonal polarisations is calculated and presented (black). The legend in figure (c) is also valid for (a) and (b).

Comparison between the total angular reflectance of silicon moth-eyes with a flat interface between silicon and air, shows a great reduction of reflectance at normal incidence for all samples, $\approx 20\%$. Among all the samples, wafer 2 has total reflectance lower than silicon for all angles of incidence while wafers 1 and 3 show reflectance values slightly higher than silicon at AOI= 79.6° and 82.1° respectively. The difference between total reflectance of all samples with silicon reduces as the angle of incidence increases. This is due to the fact that for an un-polarised light, total angular reflectance of silicon is constant up to AOI of 60° while the total angular reflectance of silicon moth-eyes are almost constant only up to AOI of 40° and increases further from this angle.

6.3.2.3 The Effect of the Azimuth Rotation on Angular Reflectance Spectra

The arrangement of silicon moth-eye protuberances in a hexagonal lattice provides a 6 fold symmetry in the plane of periodicity. Rotation of the structure in the azimuth plane changes the topology of the structure for the incident light, and affects the surface reflectance. Thus using the reflectometer measurement technique, the angular reflectance of silicon moth-eyes is measured at different azimuth rotations. Since the moth-eye structure has sub-wavelength dimensions, the orientation of the hexagonal symmetry of samples is not known while performing the measurement. Thus the first position of the sample on the stage is taken as azimuth angle= 0° and the sample is rotated 5° to change the azimuth angle. Measurements are repeated on each sample for azimuth angles of 0° to 75°. The maximum azimuth rotation angle is chosen as 75° so a full symmetry unit of the hexagonal lattice is covered (60°) and the repetition of reflectance spectrum

with repeated symmetry is verified (from 60° to 75°). The results are presented in Appendix B for wafers 1, 2 and 3 for s and p polarisation. Extracted data at AOI intervals of 10° and azimuth angle intervals of 10° is presented in this chapter. Figure 6.16 and Figure 6.17 present the results for wafer 1, Figure 6.18 and Figure 6.19 for wafer 2, and Figure 6.20 and Figure 6.21 for wafer 3.

Wafer 1 shows similar reflectance as the azimuth angle changes at all wavelengths and AOIs. There is a slight difference at s polarisation when the AOI goes above 60°, and also at p polarisation for wavelengths of less than 500nm for AOIs above 60°. However the magnitude of the reflectance differences is only up to 5%. Wafer 2 also shows no change in its angular reflectance spectrum as the azimuth angle changes at s polarisation, however at p polarisation the reflectance of incident light of wavelength below 500nm has higher reflectance values at azimuth angles of 60° and 70°. The inset in Figure 6.18 shows the angular reflectance of wafer 2 at the wavelength of 455nm as the azimuth angle varies. The shift of the angular reflectance at azimuth angles above 60° is shown. However as the angle of incidence increases, the distance between the angular reflectance of the azimuth angle of 70° and 0° increases; At AOI= 0° this difference is almost less than 10% and at AOI= 80° it increases to 30%. Wafer 3 shows similar behaviour to wafer 1, no significant change in the angular reflectance as the azimuth angle changes, except differences of less than 5% at AOIs greater than 60° at s polarisation, and wavelengths shorter than 500nm at p polarisation.

In Chapter 4 it was shown and explained by EMT that the angular reflectance of moth-eye structures of hexagonal lattice does not depend on the azimuth orientation of the plane of periodicity unless the periodicity of the structure and the profile of pillars are set such that the incident wavelength can resolve the features. The moth-eye structures in this chapter have the periodicity of 270nm, and diameters of $130-150$nm at the base and much smaller at the top. At long wavelengths, above 500nm the features are not resolved by the incident wavelength and the moth-eye layer appears as a thin film with a thickness equal to the height of pillars and an effective refractive index changing from the air to the silicon substrate. In a thin film layer, the rotation of the sample in the azimuth plane does not change the refractive index and thus no change of reflectance occurs. However, at shorter wavelengths the small features become visible to the incident wavelength. Hence the moth-eye structure with varying refractive index in the plane of periodicity and perpendicular to the plane of periodicity is not homogeneous in the azimuth plane, and rotation of the sample in the azimuth plane changes the orientation of the refractive incident exposed to the incident wavelength and thus changes occur in the reflectance spectrum. However changes of reflectance are only observed at AOIs above 60°or in other words the features become visible to the incident wavelength at these AOIs.

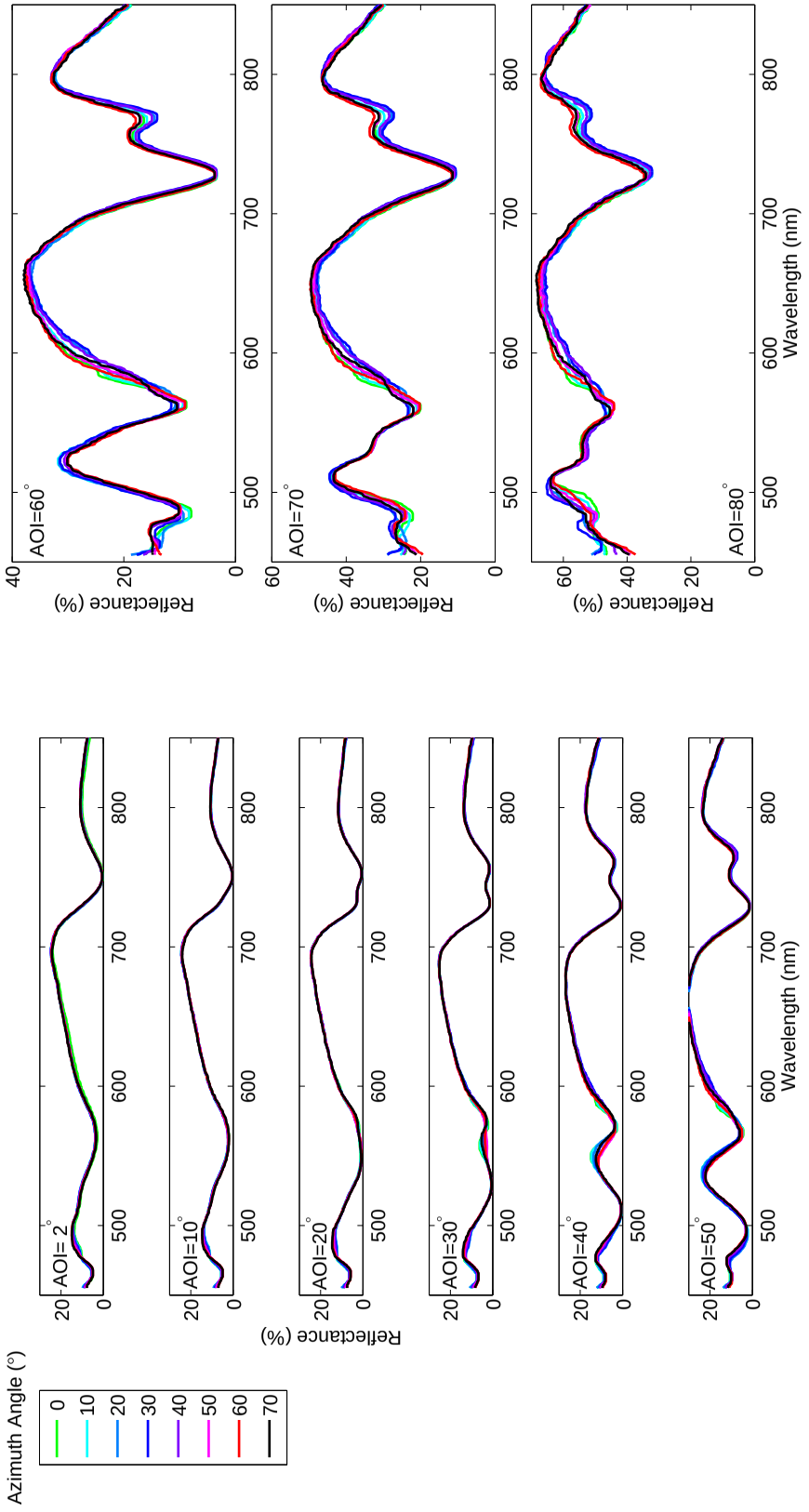

FIGURE 6.16: Reflectance spectrum of wafer 1 at s polarisation at AOI intervals of 10° from $2-80°$ and azimuth angle intervals of 10° from $0-70°$.

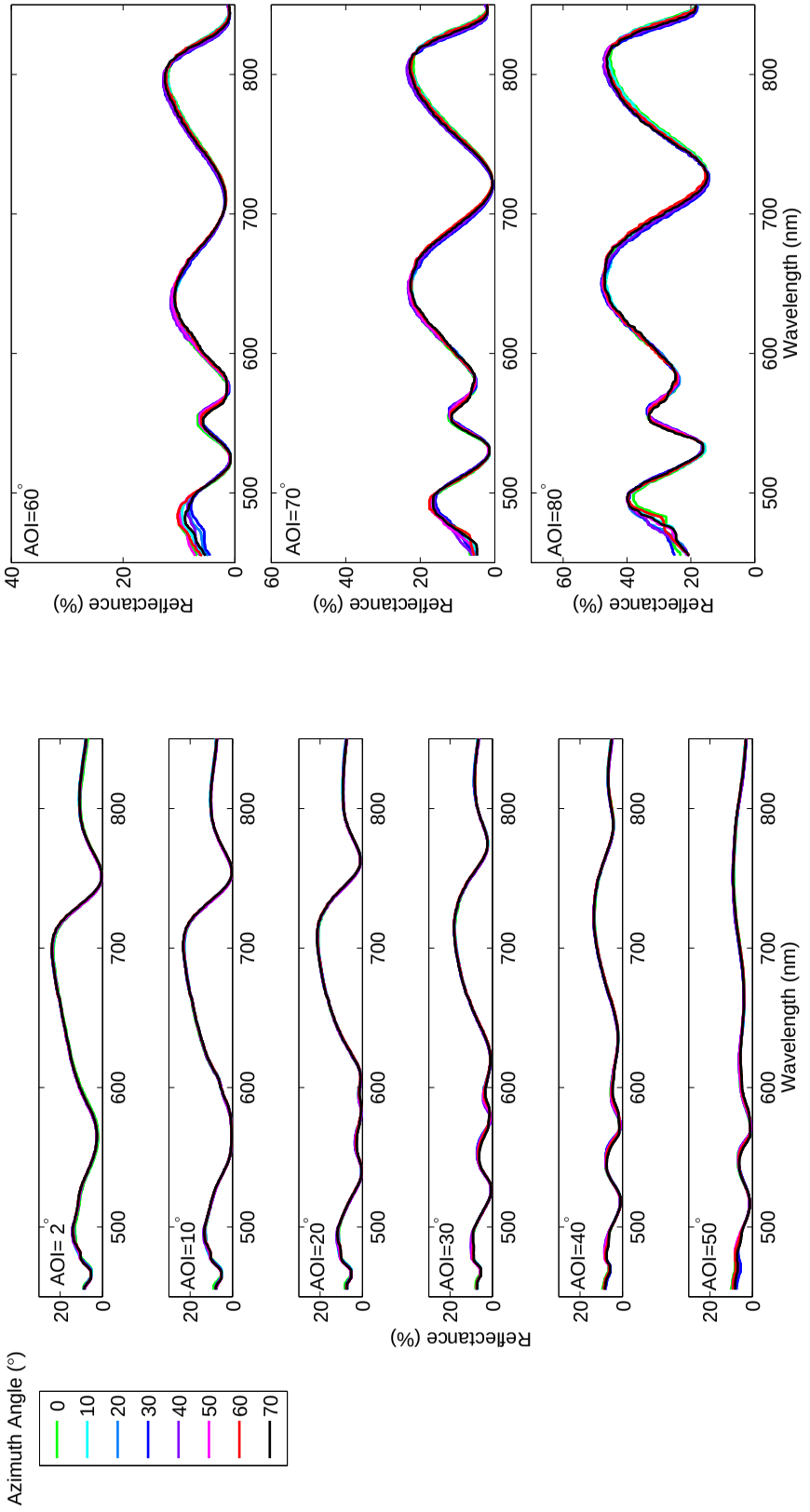

FIGURE 6.17: Reflectance spectrum of wafer 1 at p polarisation at AOI intervals of $10°$ from $2 - 80°$ and azimuth angle intervals of $10°$ from $0 - 70°$.

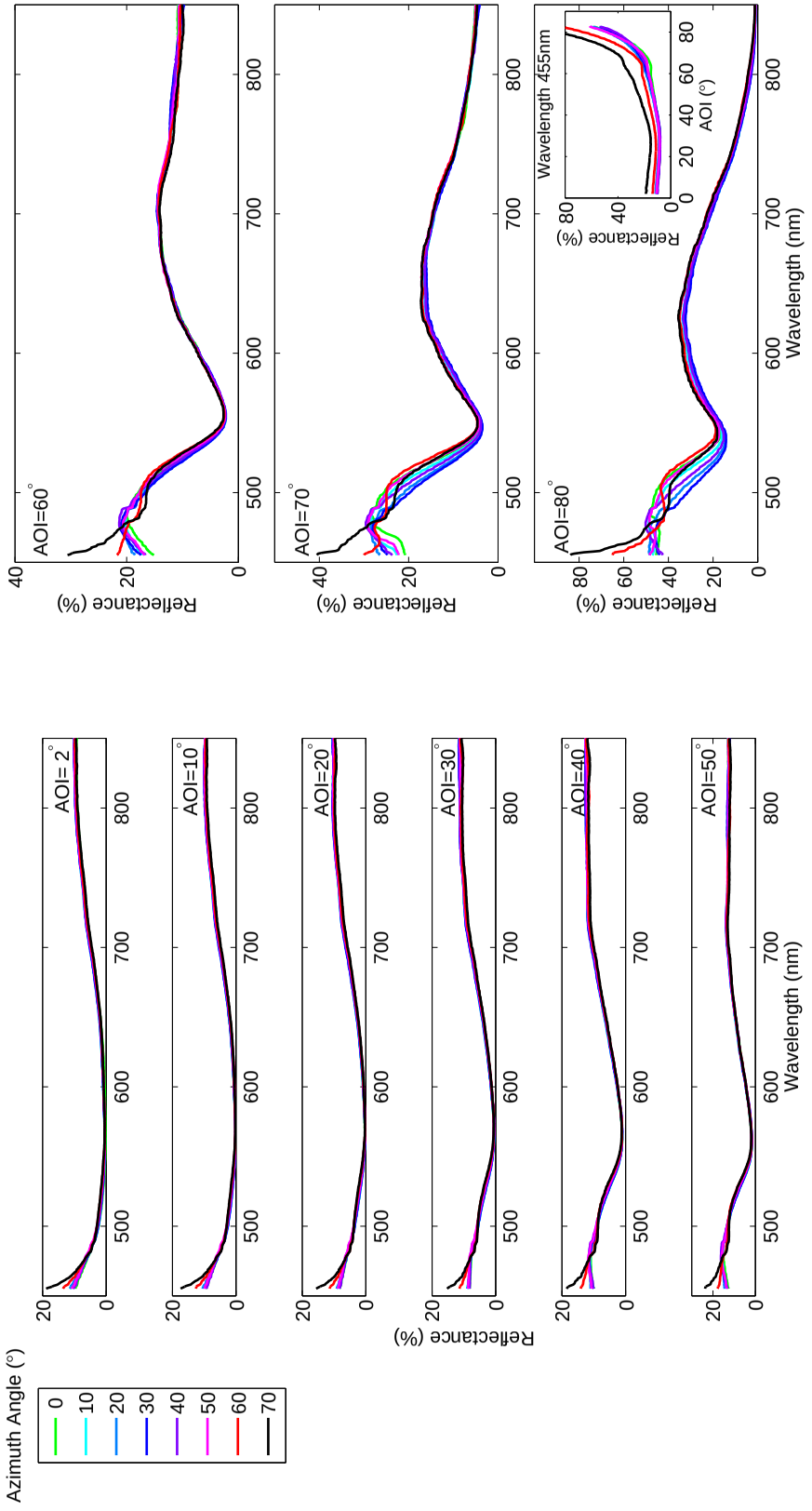

FIGURE 6.18: Reflectance spectrum of wafer 2 at s polarisation at AOI intervals of 10° from $2 - 80°$ and azimuth angle intervals of 10° from $0 - 70°$.

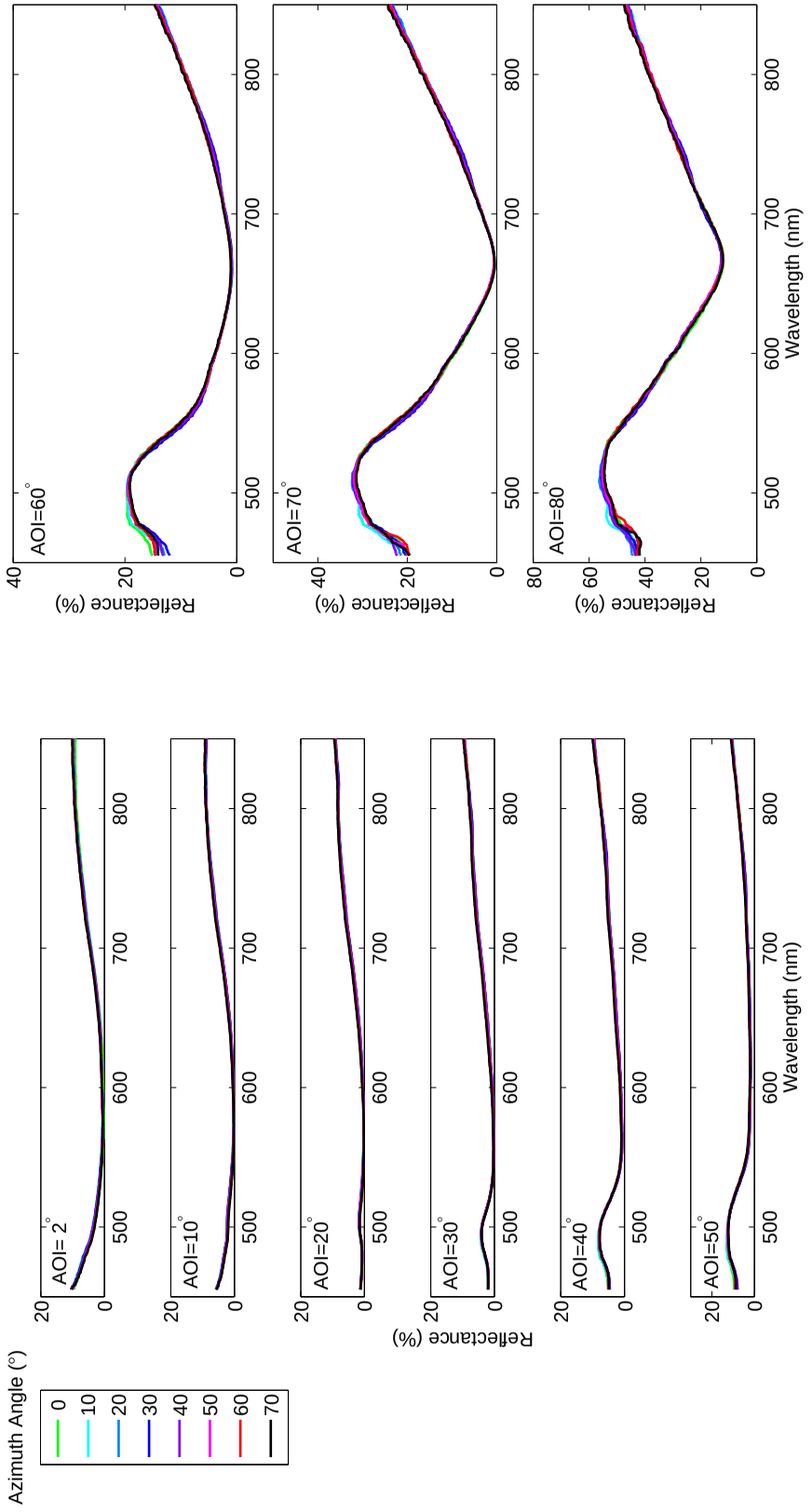

FIGURE 6.19: Reflectance spectrum of wafer 2 at p polarisation at AOI intervals of $10°$ from $2 - 80°$ and azimuth angle intervals of $10°$ from $0 - 70°$.

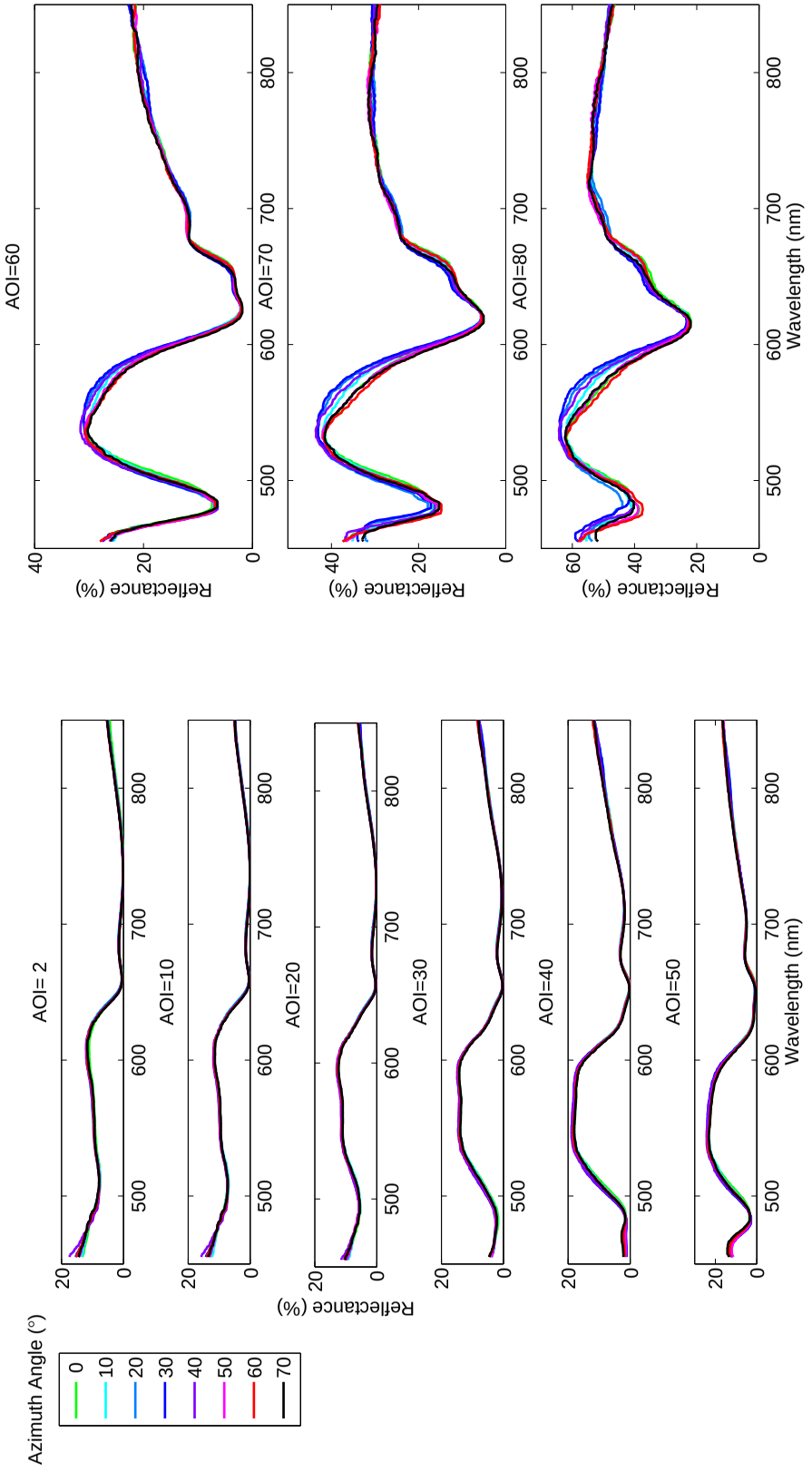

FIGURE 6.20: Reflectance spectrum of wafer 3 at s polarisation at AOI intervals of 10° from $2-80°$ and azimuth angle intervals of 10° from $0-70°$.

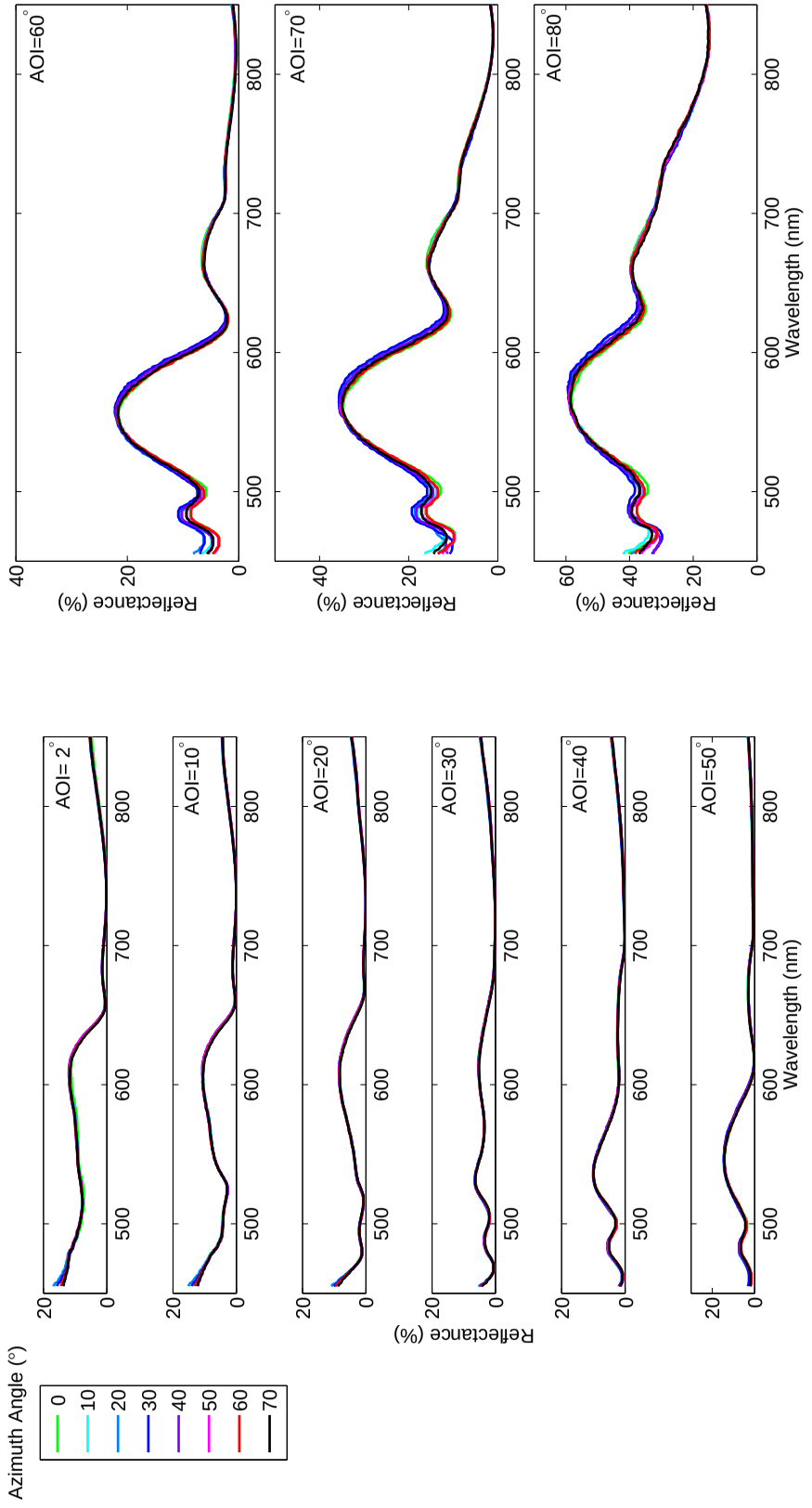

FIGURE 6.21: Reflectance spectrum of wafer 3 at p polarisation at AOI intervals of $10°$ from $2 - 80°$ and azimuth angle intervals of $10°$ from $0 - 70°$.

	No. of Photons/m^2 Reflected Over a Day	**% of Incident Photons Reflected Over a Day(%)**
Wafer 1	5.24×10^{23}	8.18
Wafer 2	2.91×10^{23}	4.54
Wafer 3	4.10×10^{23}	6.39

TABLE 6.2: Percentage and number of photons reflected from the surface of silicon moth eyes, wafers 1,2 and 3 in a full day, calculated using the photon flux density of the solar spectral from Figure 4.22.

6.3.2.4 Weighted Reflectance

The performance of silicon moth-eyes of wafers 1, 2 and 3 exposed to the solar spectrum in a full day are compared in Table 6.2. The number of photons reflected from the surface of a wafer is calculated by multiplying the full reflectance spectrum of the wafer to the photon flux density of the solar spectrum. The ratio of the number of photons reflected from the surface of a moth-eye structure to the sum of the number of photons of the solar spectrum is also calculated and presented in Table 6.2. This will give us a similar value to the weighted reflectance. The performance of the wafers can be rated as wafer 2 being the most optimum anti-reflective structure, reflecting 4.54% of incident photons. Wafer 3 reflects 6.39% of incident photons and wafer 1 shows the highest value of number of photons reflected, 8.18%.

6.3.3 Summary

The reflectance of silicon moth-eyes presented in this chapter were studied at arbitrary angles of incidence for s and p polarisation. The reflectance of the two polarisations at normal incidence showed similar values. The reflectance of wafers 2 and 3 were less wavelength dependant than wafer 1. This is due to the higher extent of tapering of the pillars in the moth-eye structure.

The angular reflectance of the silicon moth-eyes investigated were less angle dependant and less polarisation dependant compared to samples investigated in Chapter 5. The mean average of the reflectance of all samples at s polarisation is higher than p polarisation, except wafer 2 which shows greater values of reflectance at p polarisation at AOIs greater than 62° where an inverse polarisation was observed.

The effect of the azimuth orientation of moth-eye structures on their angular reflectance were studied experimentally. Apart from small changes of 5% maximum at higher AOIs, the angular reflectance does not change with azimuth angle.

A comparison between the weighted reflectance of wafers 1, 2 and 3 showed that wafer 2 has the lowest weighted reflectance among all.

6.4 Conclusion

The reflectance of silicon moth-eye structures optimized for solar cell anti-reflective applications were studied at arbitrary angles of incidence and azimuth orientations.

A comparison of the reflectance of silicon moth eyes with pillars of tapered profile (this chapter) and moth-eye structures of vertical pillars (Chapter 5) shows that tapered pillars produce a greater reduction in the reflectance of silicon at normal incidence and oblique incidence. Tapered pillars also reduce the sensitivity of moth-eye structures reflectance to the incident wavelength, angle and polarisation; constant angular reflectance was observed up to an AOI of 40°.

An inverse polarisation was observed in one case with the base diameter of 131nm, for AOIs above 62° at visible wavelengths. This new experimental finding confirms the computational prediction of Chapter 4 and rejects the prediction of Chuang [22] that an inverse polarisation in the visible spectrum only happens in moth-eye structures of base diameter under 100nm.

The moth-eye structures studied in this chapter had similar height and periodicity and were only differing in the shape of the pillars and the base diameter. However, their optical behaviour showed different properties. In the fabrication of silicon moth-eyes producing a certain pillar profile is not yet a controllable stage; it is managed through the etching stage, which is affected by the etchant and crystal plane of the silicon. Therefore to design a moth-eye structure of optimum behaviour, the emphasis should be on dimensions where there is more control such as periodicity, height and base diameter, rather than the shape of pillars.

The modelling results compared with experiments, showed that RCWA is capable of modelling silicon moth-eye structures qualitatively. There are discrepancies between the simulation results and experimental results which does not reject the applicability of the RCWA. However simulation of structures of slightly different pillars confirms that the reflectance of silicon moth-eyes are very sensitive to the shape of the pillars. Until finding a solution to the problem of controlling the shape of the pillars during fabrication, achieving a structure which delivers the exact results as simulation predictions is a great challenge for moth-eye structures. This conclusion can be extended to other biomimetic sub-wavelength structures as well.

Reflectance measurements of silicon moth-eye structures at different azimuth orientation revealed that the azimuth orientation of a moth-eye structure does not affect its reflectance at normal incidence and oblique incidence. The reflectance only changes at lower wavelengths (under 500nm) where diffraction orders exist. This result is in agreement with simulations presented in Chapter 4. Having such a property is an advantage for anti-glare applications and means that silicon moth-eye structures are suitable for stealth applications.

Among the moth-eye structures studied in this chapter an optimum structure was specified with weighted reflectance of 4.54% (wafer 2). The next chapter compares the optical properties of wafer 2 with anti-reflective structures within the field of solar cells.

Chapter 7

Application to Solar Cells

Moth-eye structures have the potential to replace conventional solar cell anti-reflective coatings. Boden has performed a computational optimisation study on silicon moth-eyes of 50% packing density and accordingly fabricated silicon moth-eyes [15]. The etching time was varied to provide a variation of pillar profiles. Optical characterisation of these silicon moth-eyes were performed in Chapter 6. Wafer 2 showed the lowest reflectance values while comparing the weighted reflectance. However, Boden had a limitation in his simulations; simulation of moth-eye structures with close-packed pillars (90% packing density) were not possible in the software that was used. Therefore a computational study of the optimisation of moth-eye structures of 90% packing density was performed in Chapter 4. Silicon moth-eye structures with a periodicity of 200nm and height of 600nm were identified as an optimum anti-reflective moth-eye structure within the visible wavelength range. This chapter compares the optical performance of the silicon moth-eye sample (wafer 2), optimized silicon moth-eye structure of Chapter 4 with conventional anti-reflective coatings within the field of solar cells presented in Chapter 2. It should be emphasised that the silicon moth-eye optimized computationally in this work was optimised for a wide purpose of anti-reflectivity within the visible spectrum and not necessarily for solar cell applications. The comparison is performed in 4 aspects: total reflectance spectra, angular reflectance spectra, angular reflectance spectra as the azimuth orientation of the sample changes and weighted reflectance.

7.1 Total Reflectance

Total reflectance measurements within the literature are limited to hemispherical reflectance at normal incidence. The angular reflectance measurement used in this thesis is capable of producing results of the specular reflectance at arbitrary angles of incidence. The hemispherical reflectance is a sum of specular reflectance and diffuse reflectance. The sub-micron nature of moth-eye structures reduces the diffused reflectance of the

structure to an extent where the diffused reflectance is negligible. Hence the total reflectance results presented in literature are compared with normal incidence reflectance results presented in this thesis (Figure 7.1).

SLAR Wafer 2 has lower total reflectance than almost all single layer antireflective coatings within a wavelength range of $500-680$nm. However, the silicon moth-eye optimised computationally is far better than all structures at all wavelengths. A close correlation between reflectance spectra of SiN_x, TiO_2 and silicon moth-eye wafer 2 implies that the effective refractive index of the silicon moth-eye is similar to SiN_x and TiO_2.

DLAR Within the wavelength range of $500-650$nm silicon moth-eye wafer 2 shows better anti-reflectivity compared to all DLARs, however for wavelengths longer than this range all DLAR structures show less reflectance while for wavelengths shorter than 500nm only SiO_2/SiN_x has lower reflectance values. The computationally optimized silicon moth-eye shows the least reflectance values up to the wavelength range of 700nm. At wavelengths above this limit the reflectance of other DLARs is reduced and is lower. An addition of an intermediate layer to SLAR structures has reduced the refractive index discontinuity from air to silicon substrate in DLAR structures and improved their anti-reflective performance.

Micron Texturing without ARCs Micron textured layers which are not coated by SLAR or DLAR show higher reflectance values compared to SLAR, DLAR and silicon moth-eye structures. Therefore silicon moth-eye structures are by far a better replacement for these structures.

Micron Texturing with ARCs Covering the micron textured layers with SLAR/DLAR reduces their reflectance by a great extent. Silicon moth-eye wafer 2 shows lower reflectance within wavelength range of $500-650$nm comparing to these structures, however the structure with microgrooves and coated with DLAR is still a better anti-reflective structure than silicon moth-eye wafer 2. At wavelength longer than 650nm the reflectance of wafer 2 is higher than other structures. The computationally optimised structure has the lowest reflectance value at all wavelengths and as wavelength increases its reflectance becomes similar to micron textured structures which are coated with SLAR/DLAR.

Sub-micron Texturing In comparison to other sub-micron anti-reflective techniques the silicon moth-eye structure is showing less reflectivity at wavelength between $500-700$nm. At wavelengths outside this range, the reflectance of other techniques is less than wafer 2. However the textured silicon structure fabricated by Sai [80] shows the least reflectance among all the samples from SLAR, DLAR to sub-micron structures. The computationally optimized silicon moth-eye shows less reflectance compared to sub-micron structures. It also shows slightly lower reflectance values

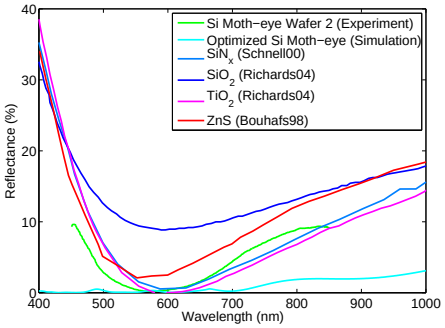

(a) **Comparison with SLAR**

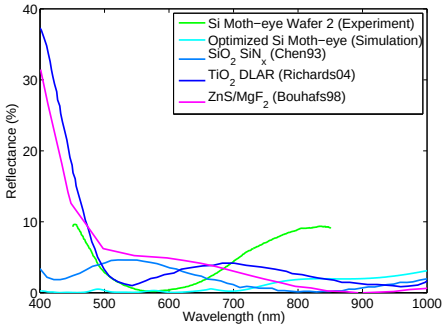

(b) **Comparison with DLAR**

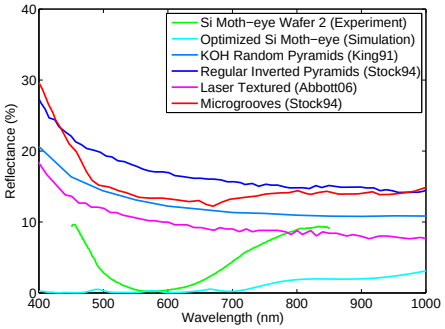

(c) **Comparison with Micron Texturing Layer without SLAR/DLAR**

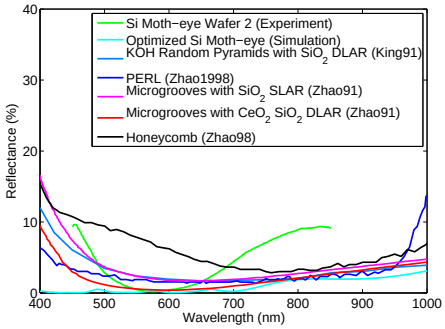

(d) **Comparison with Micron Texturing Layer with SLAR/DLAR**

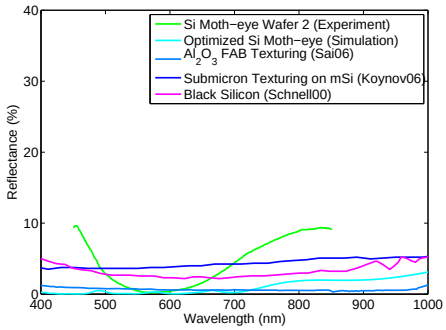

(e) **Comparison with Sub-micron Texturing**

FIGURE 7.1: Comparison of normal incidence hemispherical reflectance of silicon moth-eye wafer 2 and optimised silicon moth-eye (Chapter 4) with ARs of different fabrication techniques taken from Chapter 2.

compared to the aforementioned textured silicon by Sai up to the wavelength of 700nm. For wavelengths above this value, the reflectance of this textured silicon [80] is lower than the optimised silicon structure.

Results show that the silicon moth-eye wafer 2 is optimised for the wavelength range of $500 - 650$nm. The computationally optimized silicon moth-eye structure shows lower reflectance compared to all anti-reflective structures up to the wavelength of 700nm. From this wavelength reflectance of a type of textured silicon and SiO_2/SiN_x, TiO_2 and ZnS/MgF_2 DLARs is lower than this structure.

7.2 Angular Reflectance

Angular reflectance results of anti-reflective structures are not conveniently available in the literature to perform a comprehensive comparison. However the angular reflectance of a double layer of SiO_2/TiO_2 coating on Silicon, textured silicon with SLAR (TiO_2) and PERL structure with DLAR at wavelength of 633nm is taken from [74] and presented in Figure 7.2(a). The effect of the grids of the solar cell is taken out of the reflectance of all the structures. The angular reflectance of the silicon moth-eye wafer 2 is by $\approx 8\%$ lower than the TiO_2/SiO_2 DLAR structure at arbitrary AOI, and similar to the textured silicon up to the AOI of 60°. At AOI= 60° the reflectance of the moth-eye increases rapidly while the textured silicon shows a very smooth profile angular reflectance. In comparison to the PERL structure, the silicon moth-eye wafer 2 has almost equal angular reflectance up to the AOI of 20°. However, the angular reflectance of the PERL structure stays constant up to an AOI of 70° while the silicon moth-eyes reflectance increases as AOI increases. The computational results of the optimised silicon moth-eye structure show lower reflectance compared to all other structures up to the AOI of 50°. At this angle the reflectance of the computationally optimised silicon moth-eye increases and at AOI of 70° shows higher values than the textured silicon and almost equal to Silicon moth-eye wafer 2.

The total angular reflectance is an average of the reflectance over all wavelengths. Results of the silicon moth-eye wafer 2 and the computationally optimised structure is plotted in comparison with PERL and Honeycomb structures where the data was available, within a wavelength range of $450 - 850$, and AOI of $10 - 70°$. The Silicon moth-eye structure, wafer 2, has the highest total angular reflectance compared to the other two structures at AOIs above 45°. However the computationally optimized moth-eye structure has lowest angular reflectance up to AOI of 60° where it is outperformed by the PERL structure. The data is not available for reflectance at an AOI of 80°, but the interpolation of the plots imply that the angular reflectance of the optimised silicon moth-eye will exceed the angular reflectance of the honeycomb structure for AOIs above 70°.

7.3 Azimuth orientation

The rotation of a structure in azimuth plane does not affect the angular reflectance of SLAR and DLAR structures, where the structure is homogeneous in the azimuth plane. However it affects the reflectance of PERL, Honeycomb and micron-scale textured surfaces. The angular reflectance data at arbitrary azimuth angle for a PERL structure at $\lambda = 633$nm is taken from [74]. The PERL structure consists of arrays of inverse pyramids etched into silicon in a square lattice. So the structure had a four fold symmetry, the unit-cell repeating itself at every 90°. Therefore reflectance at azimuth rotation of $0°, 45°$ and 90° was measured in [74] and is presented in Figure 7.3. It was expected to

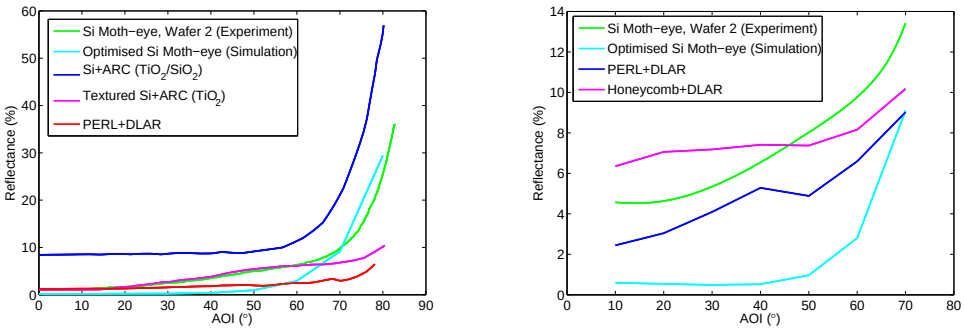

(a) (b)

FIGURE 7.2: (a) Angular reflectance of Silicon moth-eye wafer 2 Chapter 6, optimised silicon moth-eye Chapter 4, DLAR (TiO2SiO2) [74], textured Silicon+DLAR [74], PERL+DLAR [74] at wavelenght of 633nm and AOI of $0-80°$. (b) Total angular reflectance of Si moth-eye wafer 2 Chapter 6, optimised Si moth-eye Chapter 4, PERL+DLAR [74] and Honeycomb+DLAR [74] at wavelength range of $450-850$nm and AOI of $10-70°$.

observe similar reflectance at the azimuth rotation of 0° and 90° however, it is suggested that the difference is a result of a non-symmetrical structure caused by lithography and etching. There is a slight discrepancy between angular reflectance of the PERL structure at azimuth of 0° and 45°, about 1% at maximum. The angular reflectance results of the silicon moth-eye wafer 2 is presented in Figure 7.3 at azimuth rotations of 0°, 30° and 60° due to the 6-fold symmetry of the hexagonal lattice within moth-eye structures Figure 4.27. Unlike the PERL structure the azimuth orientation does not affect the angular reflectance of the moth-eye structure at all and shows a homogeneous similarity.

Therefore even though the lithography and etching stages of fabricating silicon moth-eyes might have caused a non-symmetric structure, the sub-micron nature of silicon moth-eyes cancels the effect of the non-symmetric components and thus the angular reflectance at arbitrary azimuth orientation is not affected.

7.4 Weighted Reflectance

The total reflectance spectra is a useful comparison to investigate the reflectance properties of anti-reflective structures within a wavelength range. However the weighted reflectance helps to analyse the performance of ARs in response to the incident light, in the case of solar cells, the solar irradiance. Hence weighted reflectance of structures studied in Section 7.1 are calculated and presented in Figure 7.4.

The weighted reflectance is calculated using the weighted reflectance equation (Equation 4.3) in Chapter 4. However since the data of other ARs at arbitrary angle of incidence is only available at a single wavelength, the weighted reflectance is only calculated at normal incidence. The incident photon flux density ($I_T(\lambda)$) is taken from

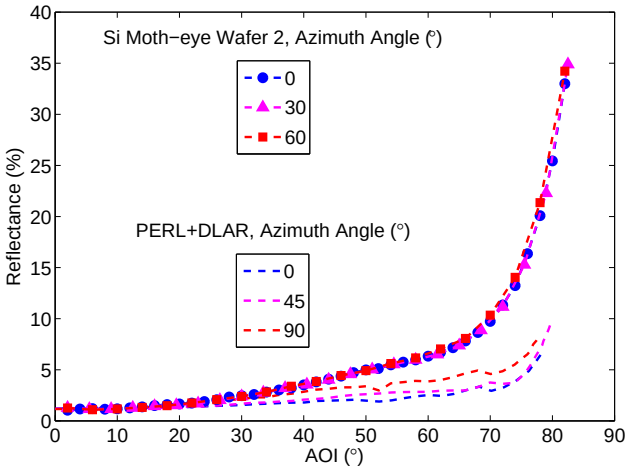

FIGURE 7.3: Comparison of the angular reflectance of silicon moth-eye wafer 2 from Chapter 6 and PERL+DLAR structure taken from [74] at the wavelength of 633nm and the AOI of $0-83°$. The azimuth angle of the Si moth-eye is varied between $0°, 30°$ and $60°$ and for the PERL+DLAR is varied between $0°, 45°$ and $90°$.

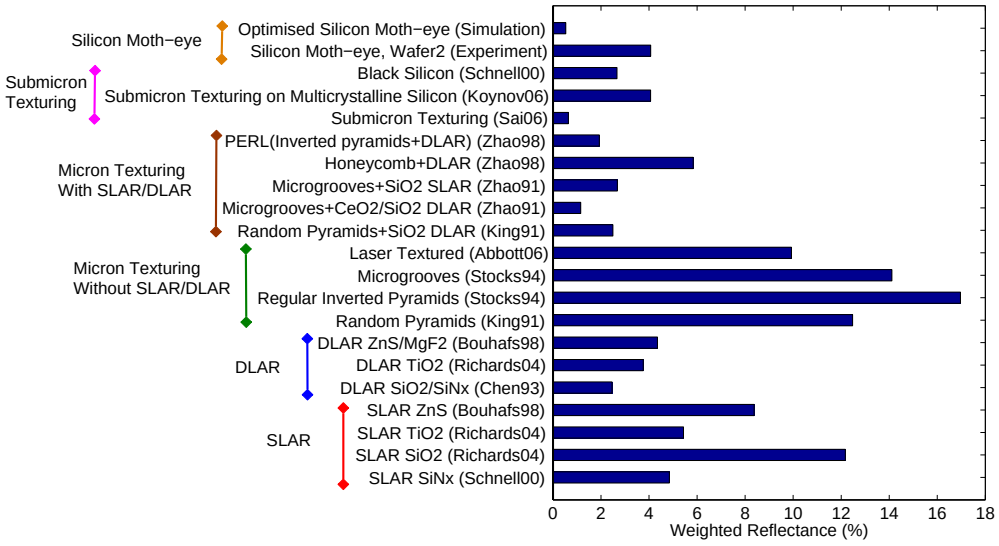

FIGURE 7.4: Weighted Reflectance of silicon moth-eye in comparison with ARs of different fabrication technology presented in Figure 7.1.

ASTM G173 [5] to provide a set of data which can be used globally and compared with other structures.

Micron textured structures without SLAR/DLAR coating have the highest weighted reflectance while the most optimum anti-reflective structures are among the micron textured structures coated by SLAR/DLAR, and sub-micron textured silicon from studies of Sai [80]. The silicon moth-eye sample (wafer 2) with the weighted reflectance of 4% is a medium anti-reflective layer which is outperforming SLAR and DLARs to some extent, all micron textured structures without SLAR/DLAR and other sub-micron structures.

The computationally optimised silicon moth-eye is comparable to the sub-micron textured silicon from Sai [80]. They both show a weighted reflectance of under 1%.

7.5 Conclusion

The silicon moth-eye computationally optimised in Chapter 4 and the optimum silicon moth-eye sample investigated in Chapter 6 (wafer 2) were compared with solar cell anti-reflective structures within literature. The silicon moth-eye wafer 2 was optimised for the wavelength of 628nm [15] and it showed an optimum anti-reflective behaviour within the wavelength range of $500 - 650$nm compared to all other AR structures. The angular reflectance of this silicon moth-eye shows better performance compared to a solar cell DLAR coating and is comparable to a textured silicon and honeycomb structure. However the PERL structure is a better anti-reflective structure by $\approx 2\%$.

The computationally optimised silicon moth-eye structure outperforms all other AR techniques up to the wavelength of 700nm, where the reflectance of sub-micron textured silicon is the lowest. However, the angular reflectance of this silicon moth-eye is by far the best of all structures up to an AOI of $60°$.

The comparison between reflectance of the silicon moth-eye and the PERL structure shows that even though the lithography and etching errors can damage the symmetry of the moth-eye structure, the reflectance of the moth-eye structure is independent of azimuth orientation of the sample. This property of the silicon moth-eye brings new promises into the world of stealth applications and anti-glare along with solar cell anti-reflective coatings.

The weighted reflectance of silicon moth-eye wafer 2 shows that this structure can be ranked as a medium AR structure among all ARs fabricated by other techniques. Therefore the comparable results of the silicon moth-eye wafer 2 with other AR structures, and the computationally optimum results of a newly proposed silicon moth-eye shows that achieving a moth-eye structure which can outperform other AR structures is possible.

Chapter 8

Conclusion and Future work

8.1 Conclusion

A review of the literature revealed that the problem of surface reflection on solar cells is still seeking a solution to provide low reflectance at normal incidence and oblique incidence for a wide wavelength bandwidth. Approaching this problem from biomimetics showed that moth eyes have great potential to be used for anti-reflective purposes. Moth-eye structures can be fabricated with a wide variety of materials, from metals to semiconductors, to be used for solar cell, photovoltaic, stealth and anti-glare applications. Experimental and computational studies have discovered that the optimum moth-eye structure has densely packed pillars of tapered profile with rounded top. The periodicity and height of pillars can tune the anti-reflective region of the spectrum to a desired wavelength range.

Experimental techniques used in this work were introduced in Chapter 3. A new angle resolved set-up is introduced to be used for measuring the specular reflectance of silicon moth-eye samples. This set-up has the advantage of providing measurement results from near normal incidence (2°) to near parallel incidence (83°). The latter is determined by the size of the sample, using samples of 1cm×1cm and bigger gives the maximum available angle of incidence of 85°. This device can be used to study the specular reflectance of a variety of samples at arbitrary angles of incidence. The azimuth orientation is an extra parameter to be changed in the set-up to provide studies on the effect of the azimuth angle on optical properties of the structure.

The main body of this thesis has pursued the objectives introduced in Chapter 1. The contributions made to each aspect is presented in this chapter.

8.1.1 Computational Study of Moth-eye Structures

It was shown in moth-eye structures of close-packed pillars that setting the height and the periodicity can tune the low reflectance region of the spectrum to a desired wavelength range. Adding this finding to what has been studied from literature, it can be concluded that irrespective of the packing density of the moth-eye structure, the periodicity and the height can be used to tune the low reflectance region of a moth-eye structure according to the objectives of an application. (See Chapter 4)

8.1.2 Optimise Moth-eye Structures for Anti-reflective Purposes

A silicon moth-eye structure was optimised to be used for solar cell anti-reflective purposes and general anti-glare purposes. This structure showed omnidirectional low reflectance up to the incident angle of 40° and insensitivity to the linear polarisation of the incident light. (See Chapter 4)

8.1.3 Computational and Experimental Studies of the Optical Properties of Silicon Moth-eye Structures at Arbitrary Angles of Incidence and Azimuth Orientation

Increasing the angle of incidence increases the reflectance of silicon moth-eye structures and their selectivity in absorbing light of certain wavelength. Furthermore, the novel study of the effect of azimuth orientation on the angular reflectance of a moth-eye structure showed that the azimuth orientation of silicon moth-eye structures does not affect the angular reflectance of the structure at either polarisations. (See Chapter 4, Chapter 5, Chapter 6)

A moth-eye structure with a diameter above 100nm, is identified to show inverse polarisation behaviour. To the knowledge of the writer this is a new finding within the field of moth-eye structures. (See Chapter 4 and Chapter 5)

The effect of periodicity on the angular reflectance of silicon moth-eyes is similar to the effect at normal incidence; increasing the periodicity shifts the angular reflectance spectrum towards longer wavelengths. (See Chapter 5)

Tuning the low reflectance region of a silicon moth-eye structure at normal incidence to a certain wavelength region is not applicable for applications where the low reflectance at arbitrary angles of incidence is of interest. This is due to the observation that an increase in the angle of incidence might move the low reflectance region to shorter or longer wavelengths. (See Chapter 5)

Moth-eye structures are capable of removing the effect of single polarisation reflection at the Brewster angle. This effect is stronger in moth-eye structures with lower periodicity. (See Chapter 4 and Chapter 5)

The profile of pillars in moth-eye structures is highly influential on the reflectance properties of the moth-eye structure. Pillars of more tapered profile show lower angular reflectance and less sensitivity to the incident wavelength. Also the high sensitivity of moth-eye structures' angular reflectance to the incident wavelength reveals that the experimental study of the angular reflectance of moth-eye structures at a single wavelength is not enough to determine the extent of omnidirectional reflectance of moth-eye structures. (See Chapter 6)

The etching stages used within the fabrication processes were not able to produce pillars in structures of low periodicity, under 200nm. Even at structures of higher periodicity, there is no control of the profile of the pillars in the etching processes; this is a general concern and not specific to the stages used in this work. Thus until such control can be achieved, the concentration in the design of moth-eye structures should be on the dimensions: periodicity, diameter and height of pillars. (See Chapter 5)

8.1.4 Comparison of the Anti-reflectivity of the Silicon Moth-eye Structure and Other Anti-reflective Technologies within the Field of Solar Cell Anti-reflective Coatings

The success in producing a moderately ranked silicon moth-eye structure plus the promising results of the computational modelling means that moth-eye structures of low reflectance across a broad bandwidth and omnidirectional is possible. Silicon moth-eyes posses positive properties of a variety of ARs; the low reflectance as low as the PERL structure, the omnidirectional extent similar to thin film structures and no sensitivity to the azimuth orientation of the structure on angular reflectance. However, the expensive fabrication techniques used for fabricating silicon moth-eyes is not favourable for the field of solar cell anti-reflectives where the patterned area is of few meters. (See Chapter 7)

8.2 Future work

Based on the work performed in this thesis, the following suggestions for further work are made:

- It was shown that RCWA is able to predict the reflectance behaviour of nano-photonic biomimetic structures qualitatively, however it should be considered that

the simulations were performed having the simulation parameters not entirely converging. This problem might be solved by employing less coarse wavelength steps to employ different simulation parameters which will shorten the simulation time, or allocating more time and computational power to the simulation work to perform more accurate simulations with more accurate simulation parameters. In both cases with accuracy or cost is being sacrificed. Thus the search for a suitable computational method for the field of nano-photonic biomimetics still continues.

- The etching process used previously to fabricate the silicon moth-eye structures needs to be optimised for structures of lower periodicity. Also it is of great interest to achieve better control over the resultant profile of pillars through the etching process. Such improvements within the etching stage will help to fabricate new silicon moth-eye structures. The promising computational result of this work suggests the fabrication of the optimised silicon moth-eye structure. The optical properties of the structure should then be studied using the same measurement techniques to evaluate the performance of the structure.

- The measurement techniques used in this work can be used to perform similar studies on other anti-reflective structures. This will deliver better understanding of the optical performance of those structures.

- This work solely studied the optical properties of silicon moth-eyes. The effect of the moth-eye structure on the electrical properties of silicon solar cells was not in the scope of this work, however it is an aspect which has to be considered when optimising moth-eye structures for solar cell anti-reflective applications.

- Moth-eye structures to be used in other applications are fabricated in other materials. The computational software used in this work is capable of employing a variety of materials. There are no limitations within the experimental techniques to use samples of other material either. Thus using the same methodology presented in this work, similar detailed study of other anti reflective structures can be performed.

- It was found that the sub-micron nature of the moth-eye structure causes the angular reflectance of the structure to be insensitive to the azimuth orientation of the structure. Performing similar measurements on sub-micron anti-reflective structures of other techniques can help to provide a better understanding of this property.

- Moth-eye structures showed to be capable of removing the single polarisation effect at the Brewster angle. Whether or not this is a property specific to moth-eye structures or to sub-wavelength structures in general can be studied by performing similar simulations and experimental study of other sub-wavelength anti-reflectives.

Appendices

Appendix A

Conferences and Publications

- S. Boden and A. Asadollahbaik and H. Rutt and D. Bagnall. *Helium Ion Microscopy of Lepidoptera Scales.* The Journal of Scanning Microscopies, 33:1-14, 2011.

- A. Asadollahbaik, S. Boden, M. Molinari, S. Cox, D. Bagnall. *Modelling Biomimetic Moth-eye Structures for Anti-reflective Surfaces.* In Photon10 Conference, 23-27 August 2010, Southampton, UK.

- A. Asadollahbaik, M. Molinari, S. Cox. *Modelling and Simulation of Moth-eye Photonic Crystal Structures.* In Photon08 Conference, 26-29 August 2008, Edinburgh, Scotland.

Appendix B

Azimuth Plots

The angular reflectance measurement of silicon moth-eyes in Chapter 6 was performed at azimuth orientations of 0° to 75° in steps of 5° for each sample. Results at all azimuth orientations for each sample is presented here.

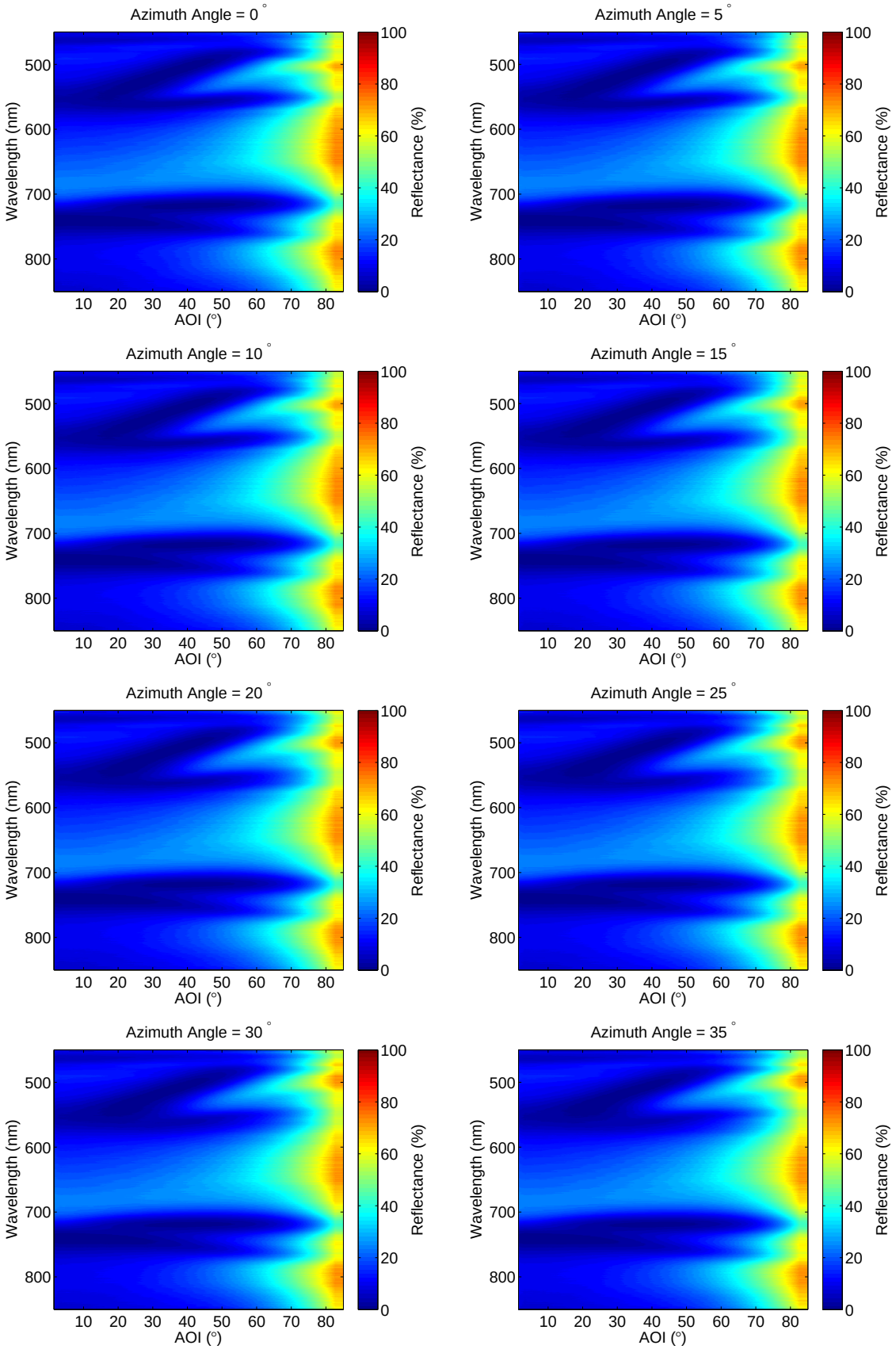

FIGURE B.1: Angular reflectance spectrum of silicon moth-eye, wafer 1, for AOI=2 − 83° and wavelength of 450 − 850nm, at *s* polarisations. The azimuth angle of the sample is rotated in each plot by 5°, from 0° to 35°.

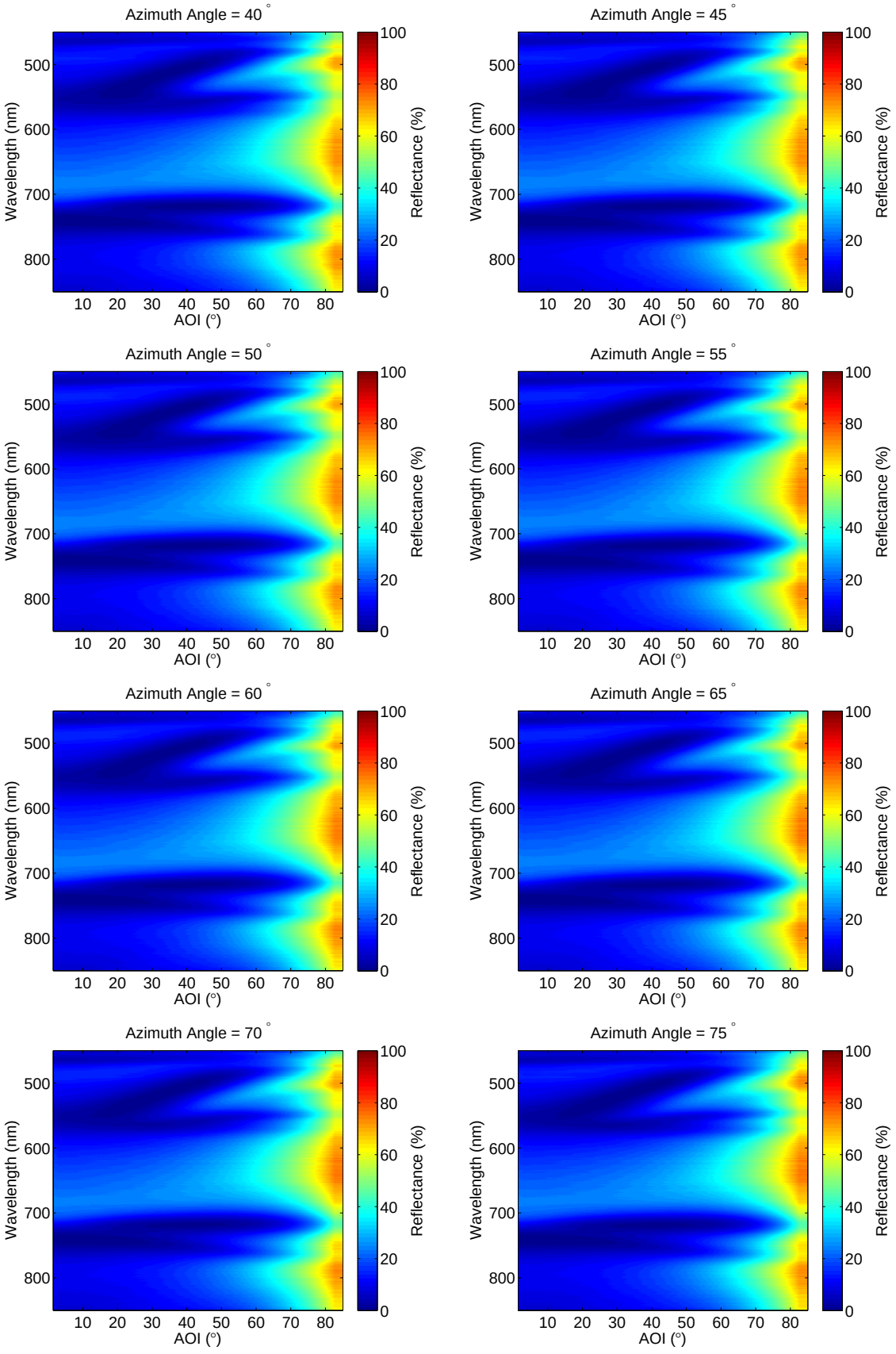

FIGURE B.2: Angular reflectance spectrum of silicon moth-eye, wafer 1, for AOI=2 – 83° and wavelength of 450 – 850nm, at *s* polarisations. The azimuth angle of the sample is rotated in each plot by 5°, from 40° to 75°.

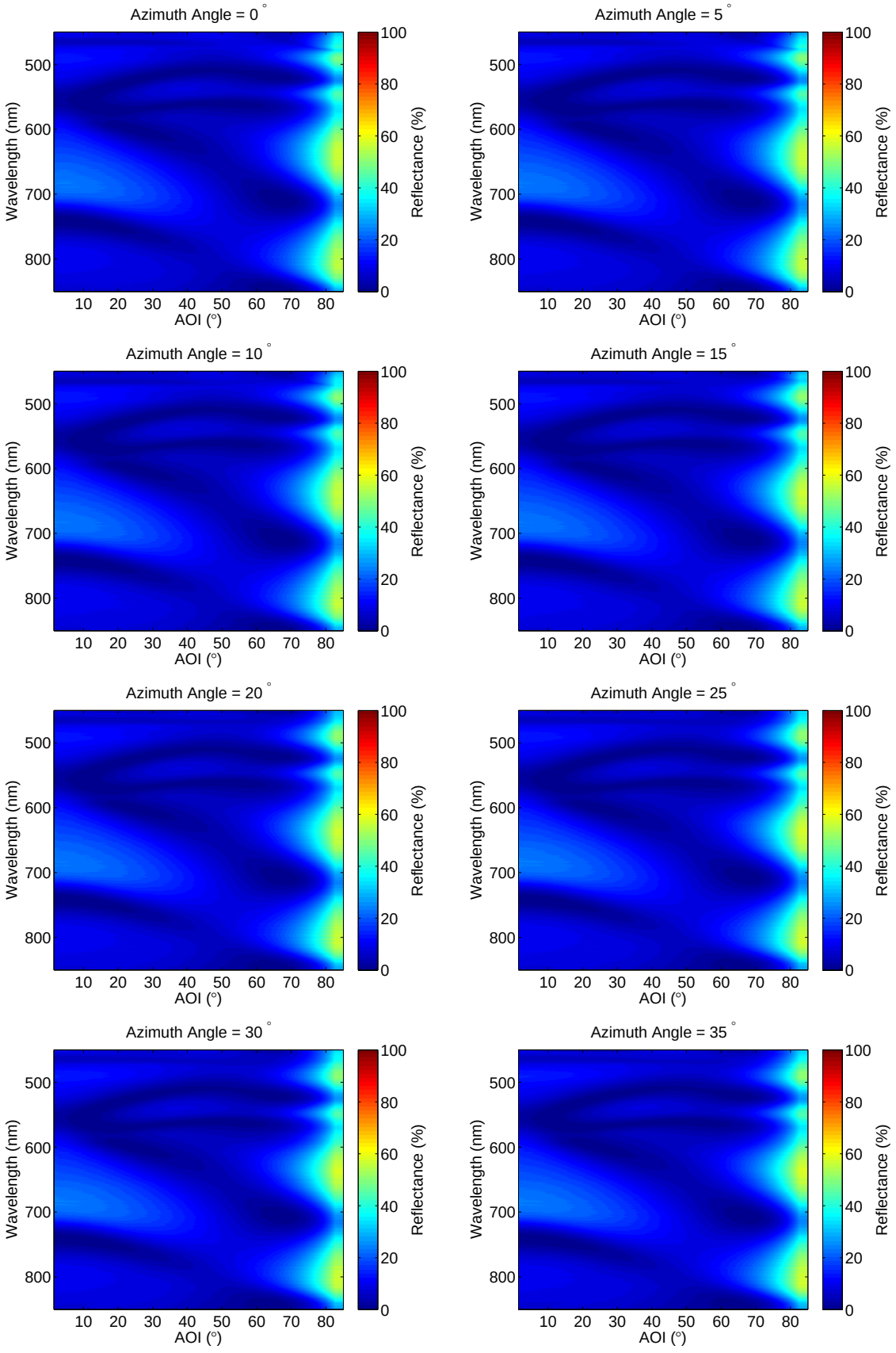

FIGURE B.3: Angular reflectance spectrum of silicon moth-eye, wafer 1, for AOI=2 − 83° and wavelength of 450 − 850nm, at p polarisations. The azimuth angle of the sample is rotated in each plot by 5°, from 0° to 35°.

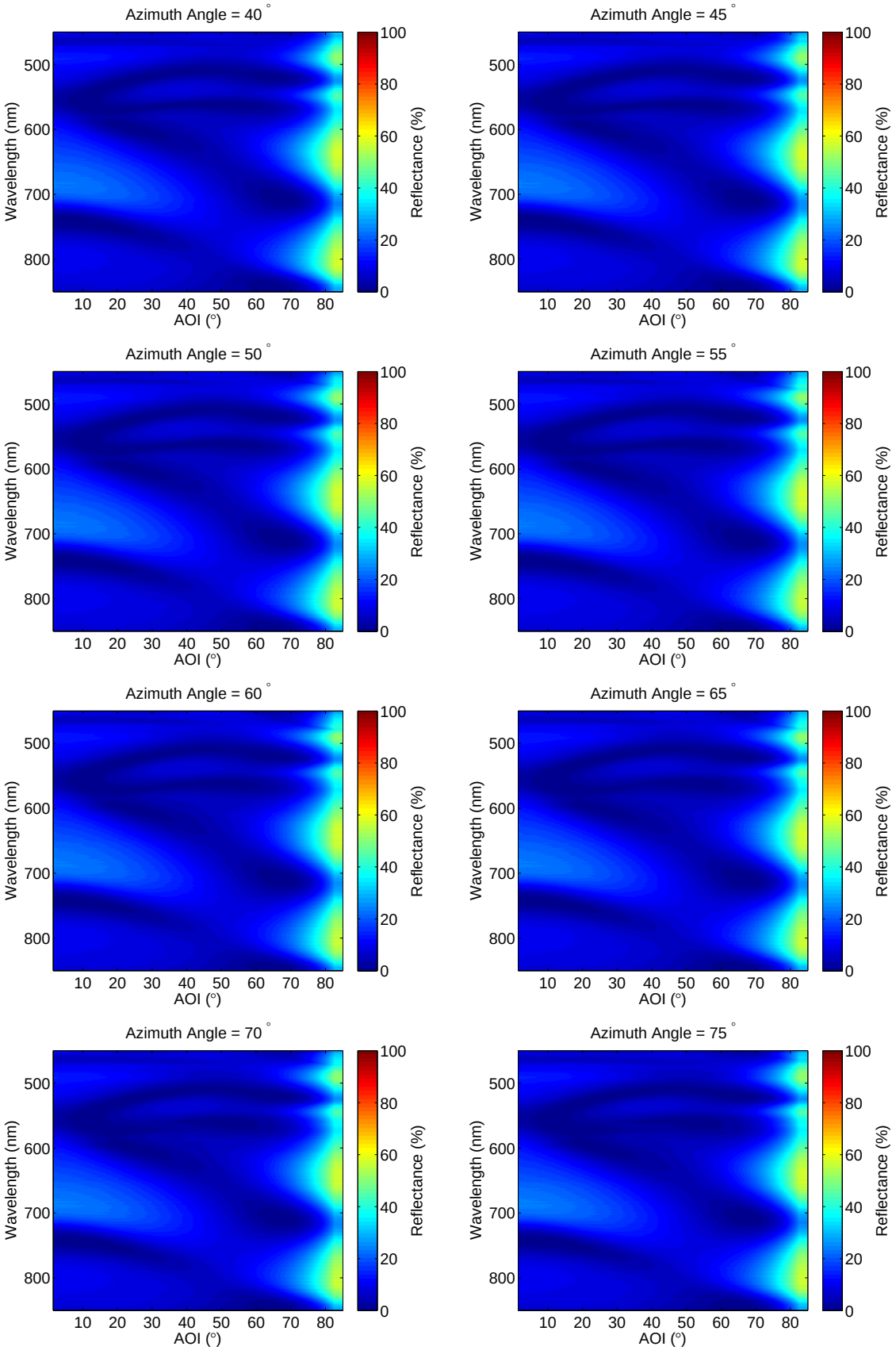

FIGURE B.4: Angular reflectance spectrum of silicon moth-eye, wafer 1, for AOI=2 – 83° and wavelength of 450−850nm, at p polarisations. The azimuth angle of the sample is rotated in each plot by 5°, from 40° to 75°.

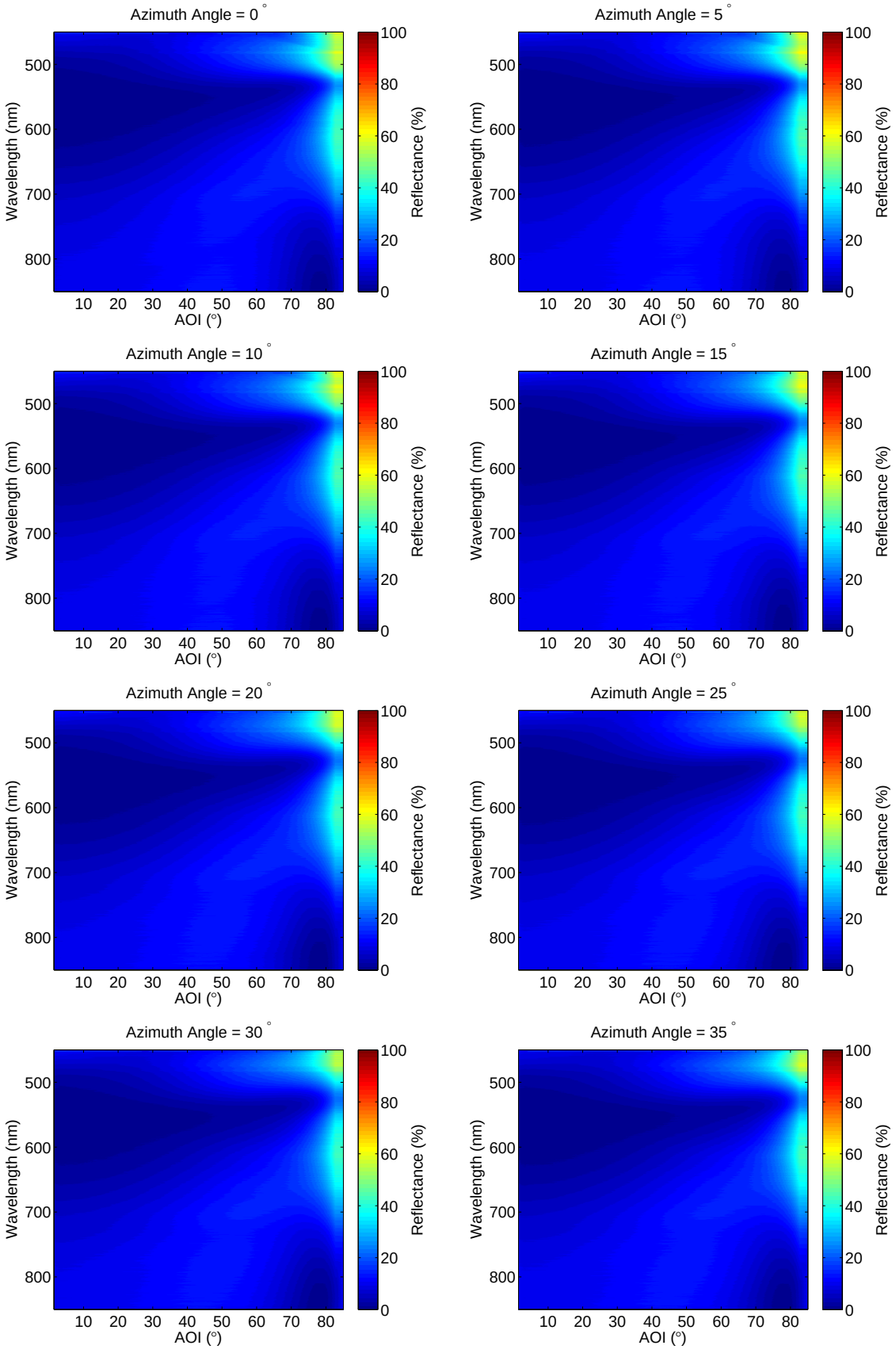

FIGURE B.5: Angular reflectance spectrum of silicon moth-eye, wafer 2, for AOI=2 − 83° and wavelength of 450 − 850nm, at *s* polarisations. The azimuth angle of the sample is rotated in each plot by 5°, from 0° to 35°.

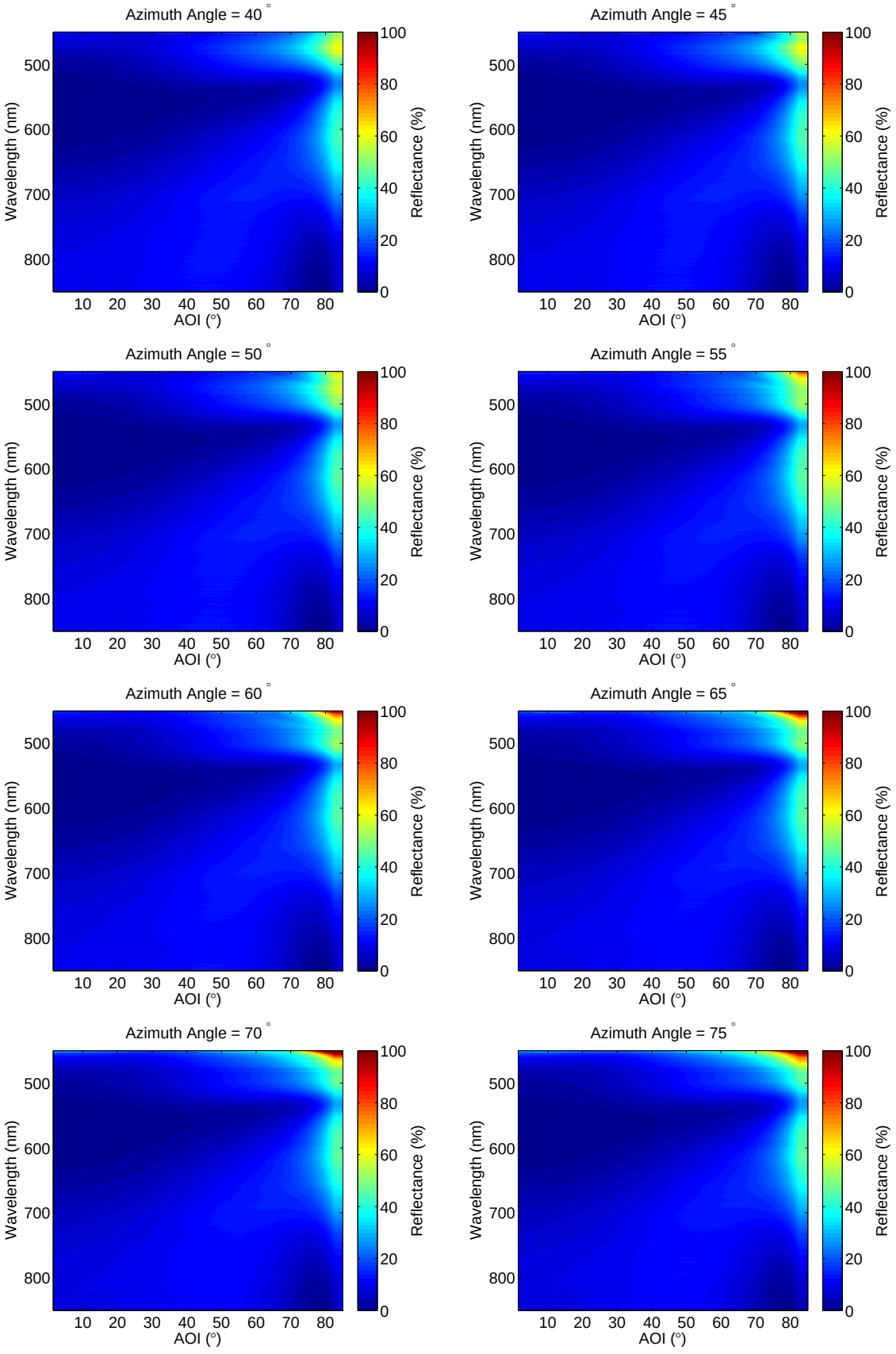

FIGURE B.6: Angular reflectance spectrum of silicon moth-eye, wafer 2, for AOI=2 – 83° and wavelength of 450 – 850nm, at *s* polarisations. The azimuth angle of the sample is rotated in each plot by 5°, from 40° to 75°.

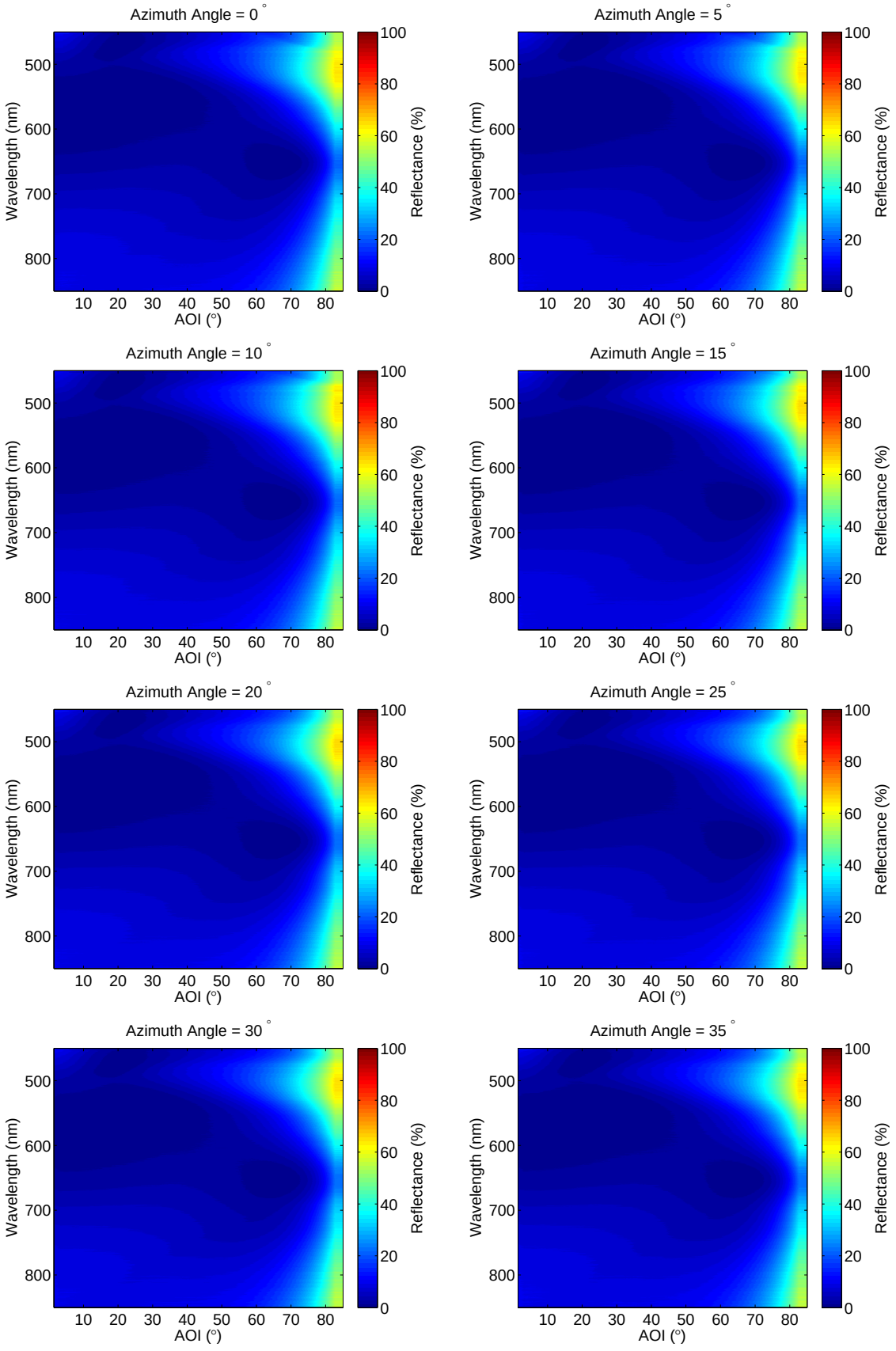

FIGURE B.7: Angular reflectance spectrum of silicon moth-eye, wafer 2, for AOI=2 − 83° and wavelength of 450 − 850nm, at p polarisations. The azimuth angle of the sample is rotated in each plot by 5°, from 0° to 35°.

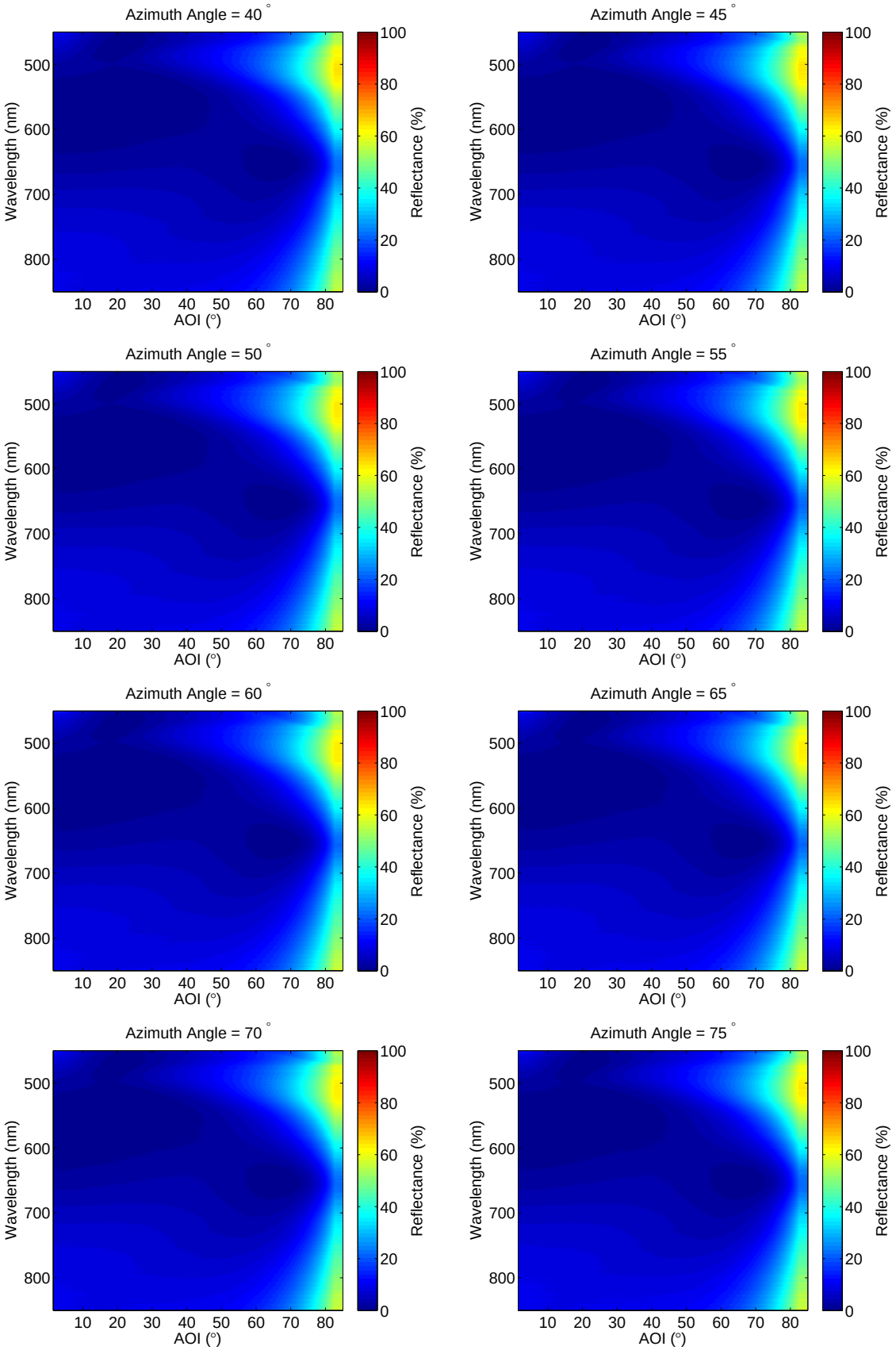

FIGURE B.8: Angular reflectance spectrum of silicon moth-eye, wafer 2, for AOI=2 – 83° and wavelength of 450−850nm, at p polarisations. The azimuth angle of the sample is rotated in each plot by 5°, from 40° to 75°.

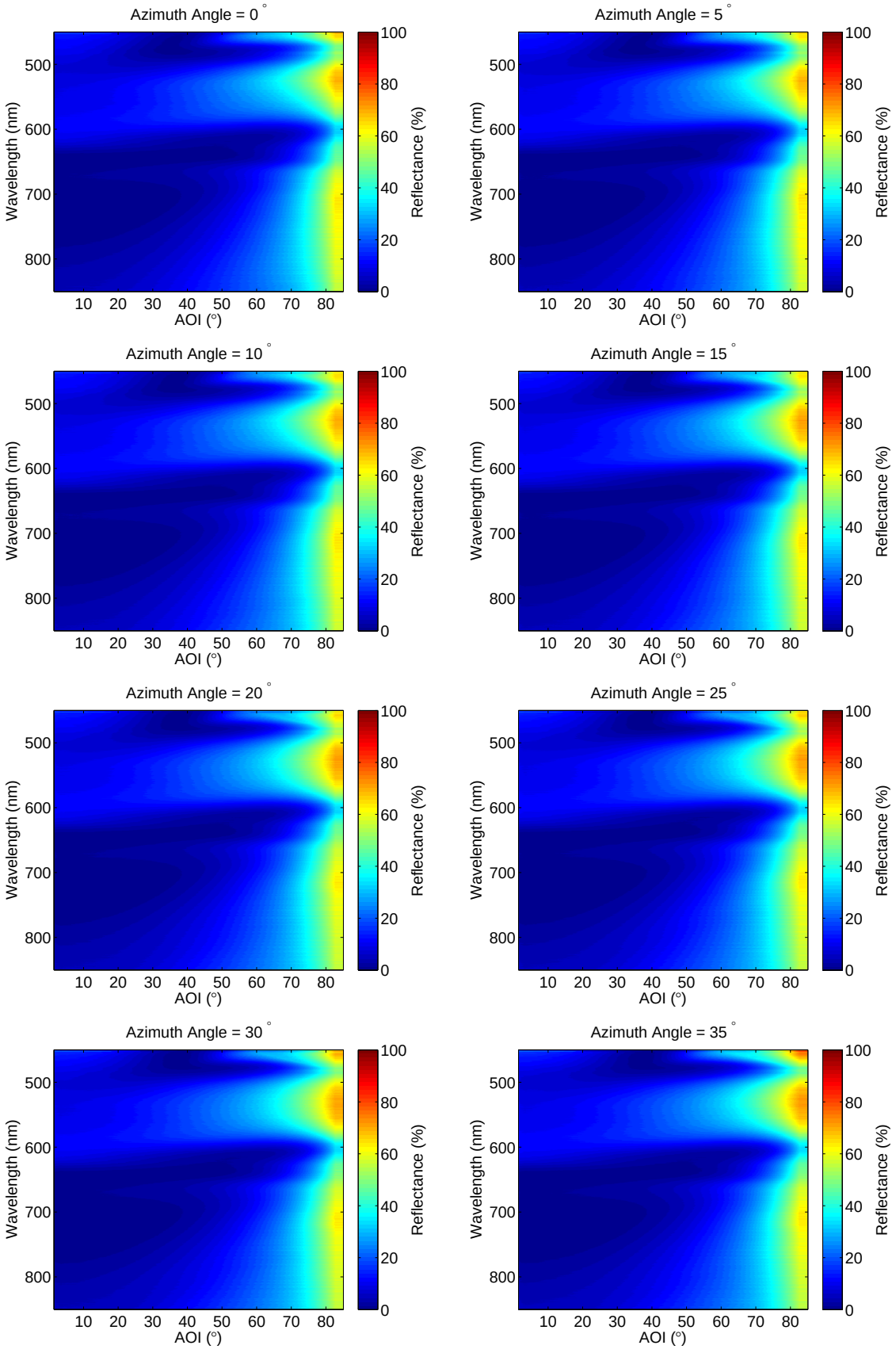

FIGURE B.9: Angular reflectance spectrum of silicon moth-eye, wafer 3, for AOI=2 − 83° and wavelength of 450 − 850nm, at *s* polarisations. The azimuth angle of the sample is rotated in each plot by 5°, from 0° to 35°.

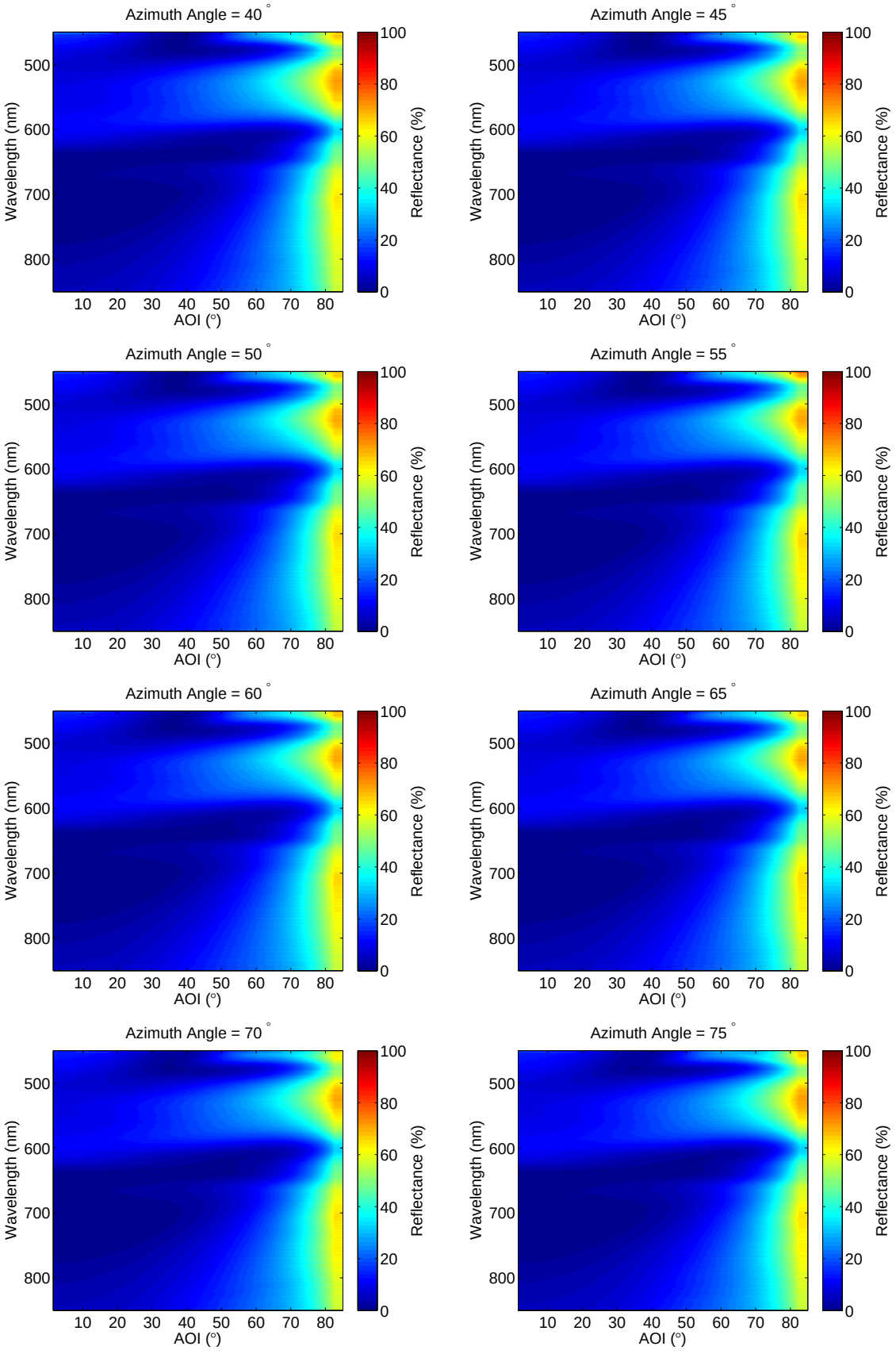

FIGURE B.10: Angular reflectance spectrum of silicon moth-eye, wafer 3, for AOI=2 – 83° and wavelength of 450 – 850nm, at *s* polarisations. The azimuth angle of the sample is rotated in each plot by 5°, from 40° to 75°.

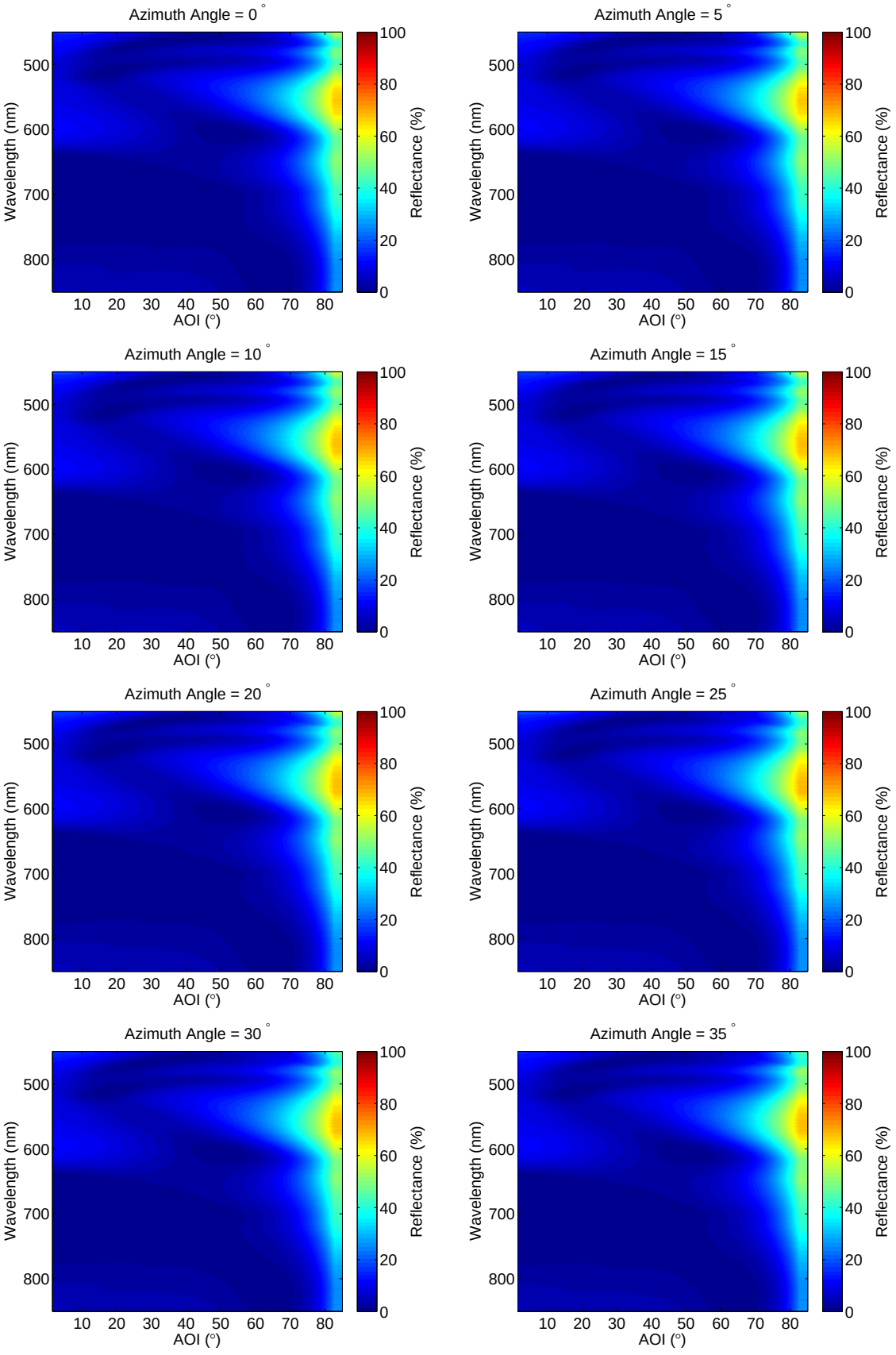

FIGURE B.11: Angular reflectance spectrum of silicon moth-eye, wafer 3, for AOI=2 − 83° and wavelength of 450 − 850nm, at p polarisations. The azimuth angle of the sample is rotated in each plot by 5°, from 0° to 35°.

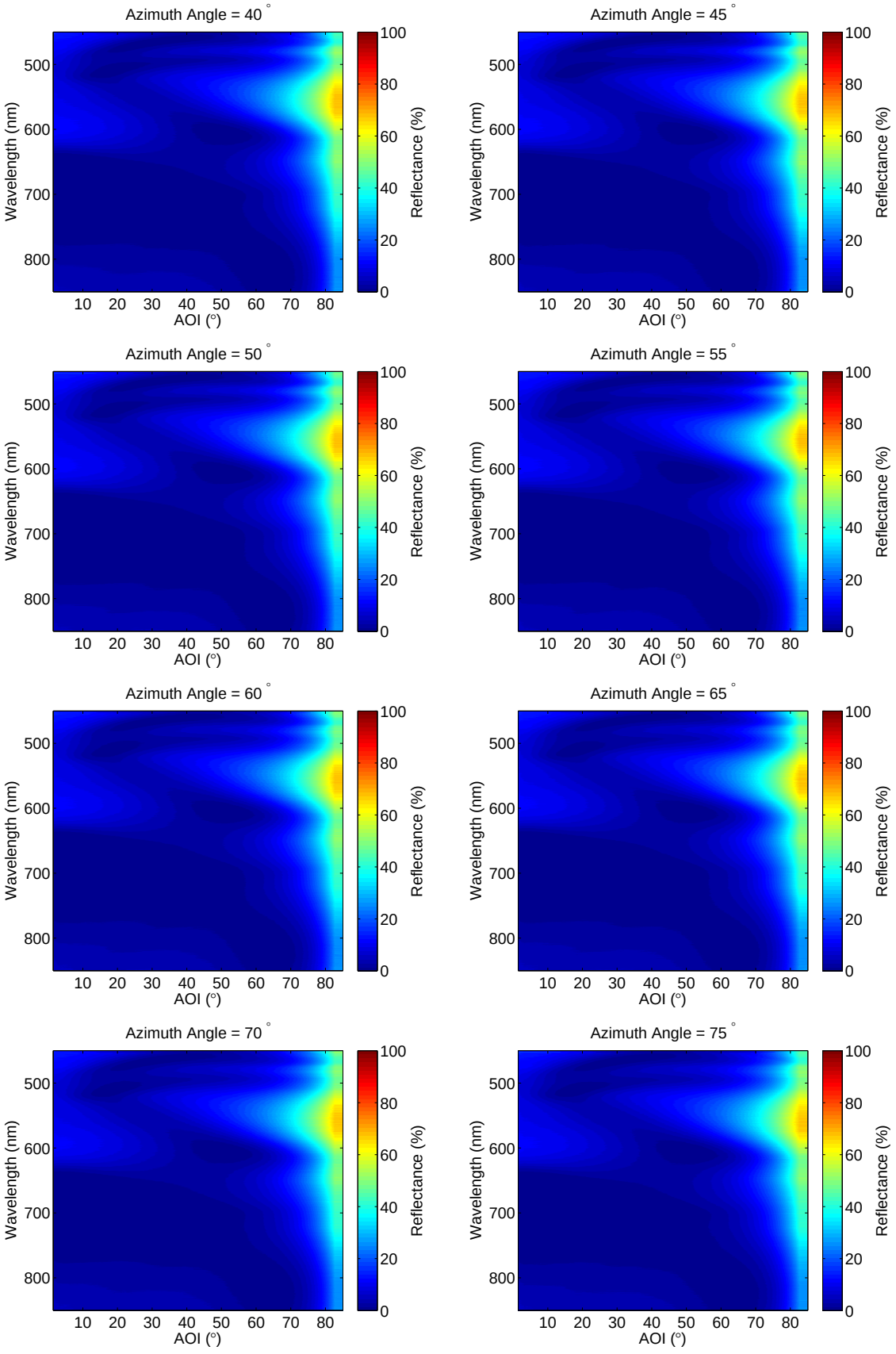

FIGURE B.12: Angular reflectance spectrum of silicon moth-eye, wafer 3, for AOI=2 − 83° and wavelength of 450 − 850nm, at p polarisations. The azimuth angle of the sample is rotated in each plot by 5°, from 40° to 75°.

Bibliography

[1] *http://polynet.dk/bionik/.*

[2] *http://www.asknature.org/product/b7fd4cfaf7380bb1f00e8759cfddc7e6.*

[3] *http://www.mirasoldisplays.com/how-it-works.*

[4] *http://www.rsoftdesign.com/products.php?sub=component+design&itm=diffractmod.*

[5] Reference solar spectral irradiance: Air mass 1.5. *http://rredc.nrel.gov/solar/spectra/am1.5/*, 2004.

[6] *Virginia Semiconductor Inc. "Optical properties of silicon", www.virginiasemi.com*, 2004.

[7] Malcolm Abbott and Jeffrey Cotter. Optical and electrical properties of laser texturing for high-efficiency solar cells. *Prog. Photovolt: Res. Appl.*, 14(3):225–235, 2006.

[8] Joanna Aizenberg, Alexei Tkachenko, Steve Weiner, Lia Addadi, and Gordon Hendler. Calcitic microlenses as part of the photoreceptor system in brittlestars. *Nature*, 412:819 – 822, 2001.

[9] Eric H. Anderson and Henry I. smith. Holographic lithography. Technical report, Massachusetts Institue of Technology, Cambridge, Mass., 1991.

[10] Byeong-Ju Bae, Sung-Hoon Hong, Eun-Ju Hong, Heon Lee, and Gun young Jung. Fabrication of moth-eye structure on glass by ultraviolet imprinting process with polymer template. *Japanese Journal of Applied Physics*, 48(1):010207–3, 2009.

[11] C. G. Bernhard. Structural and functional adaptation in a visual system. *Endeavour*, 26:79–84, 1967.

[12] C. G. Bernhard, W. H. Miller, and J. Sallstrom. Comparative ultrastructure of corneal surface topography in insects with aspects on phylogenesis and function. *Journal of Comparative Physiology A: Neuroethology, Sensory, Neural, and Behavioral Physiology*, 67:1–25, 1970.

[13] C.G. Bernhard, editor. *International Symposium on the Functional Organization of the Compound Eye*, International symposium series / Wenner-Gren Center ; no.7. Oxford : Pergamon, October 1965.

[14] R. E. Bird and C. Riordan. Simple solar spectral model for direct and diffuse irradiance on horizontal and tilted planes at the earth's surface for cloudless atmospheres. *Journal of Climate and Applied Meteorology*, 25:87–97, 1986.

[15] Stuart Boden. *Biomimetic Nanostructured Surfaces for Antireflection in Photovoltaics*. PhD thesis, University of Southampton, 2009.

[16] Stuart A. Boden and Darren M. Bagnall. Bio-mimetic subwavelength surface for near-zero reflection sunrise to sunset. In *4th World Conference on Photovoltaic Energy Conversion, Hawaii*, pages 1358–1361, 2006.

[17] Stuart A. Boden and Darren M. Bagnall. Tunable reflection minima of nanostructured antireflective surfaces. *Appl. Phys. Lett.*, 93(13):133108, 2008.

[18] Stuart A. Boden and Darren M. Bagnall. Nanostructured biomimetic moth-eye arrays in silicon by nanoimprint lithography. *Proc. SPIE*, 7401:74010J, 2009.

[19] Stuart A. Boden and Darren M. Bagnall. Optimization of moth-eye antireflection schemes for silicon solar cells. *Progress in Photovoltaics: Research and Applications*, 18:195–203, 2010.

[20] D. Bouhafs, A. Moussi, A. Chikouche, and J. M. Ruiz. Design and simulation of antireflection coating systems for optoelectronic devices: application to silicon solar cells. *Sol. Energ. Mat. Sol. Cells*, 52(1-2):79–93, 1998.

[21] Zhizhang Chen, Peyman Sana, Jalal Salami, , and Ajeet Rohatgi. A novel and effective pecvd sio2/sin antireflection coating for si solar cells. *IEEE TRANSACTIONS ON ELECTRON DEVICES*, 40:1993, 1993.

[22] Shang-Yu Chuang, Hsuen-Li Chen, Jiann Shieh, Chun-Hung Lin, Chao-Chia Cheng, Hao-Wei Liu, and Chen-Chieh Yu. Nanoscale of biomimetic moth eye structures exhibiting inverse polarization phenomena at the brewster angle. *The Royal Society of Chemistry*, Nanoscale, 2010.

[23] P. B. Clapham and M. C. Hutley. Reduction of lens reflexion by the "moth eye" principle. *Nature*, 244:281–282, 1973.

[24] Yoseph Bar Cohen. *Biomimetics: Biologically inspired Technologies*. CRC, 2006.

[25] Olivier Deparis, Nadia Khuzayim, Andrew Parker, and Jean Pol Vigneron. Assessment of the antireflection property of moth wings by three-dimensional transfer-matrix optical simulations. *Phys. Rev. E*, 79(4):041910, Apr 2009.

[26] A.B. Djurisic and E.H. Li. Modeling the index of refraction of insulating solids with a modified lorentz oscillator model. *Applied Optics*, 37:5291–5297, 1998.

[27] Micheal Gale. Diffraction, beuty and commerce. *Physics World*, 2:24–28, 1989.

[28] U. Gangopadhyay, K. Kim, D. Mangalaraj, and J. Yi. Low cost cbd zns antireflection coating on large area commercial mono-crystalline silicon solar cells. *Applied Surface Science*, 230:364–370, 2004.

[29] Gorachand Ghosh. Dispersion-equation coefficients for the refractive index and birefringence of calcite and quartz crystals. *Optics Communications*, 163:95–102, 1999.

[30] Martin A. Green, Keith Emery, Yoshihiro Hishikawa, Wilhelm Warta, and Ewan D. Dunlop. Solar cell efficiency tables (version 38). *PROGRESS IN PHOTOVOLTAICS: RESEARCH AND APPLICATIONS*, 19:565–572, 2011.

[31] Kang-Soo Han, Ju-Hyeon Shin, Kang-In Kim, and Heon Lee. Nanosized structural anti-reflection layer for thin film solar cells. *Japanese Journal of Applied Physics*, 50:020207–020207–3, 2011.

[32] Kang-Soo Han, Ju-Hyeon Shin, and Heon Lee. Enhanced transmittance of glass plates for solar cells using nano-imprint lithography. *Solar Energy Materials and Solar Cells*, 94(3):583 – 587, 2010.

[33] Kang-Soo Han, Ju-Hyeon Shin, Woo-Young Yoon, and Heon Lee. Enhanced performance of solar cells with anti-reflection layer fabricated by nano-imprint lithography. *Solar Energy Materials and Solar Cells*, 95(1):288 – 291, 2011. 19th International Photovoltaic Science and Engineering Conference and Exhibition (PVSEC-19) Jeju, Korea, 9-13 November 2009.

[34] Eugene Hecht. *Optics*. Addison Wesley, 2002.

[35] Yi-Fan Huang, Surojit Chattopadhyay, Yi-Jun Jen, Cheng-Yu Peng, Tze-An Liu, Yu-Kuei Hsu, Ci-Ling Pan, Hung-Chun Lo, Chih-Hsun Hsu, Yuan-Huei Chang, Chih-Shan Lee, Kuei-Hsien Chen, and Li-Chyong Chen. Improved broadband and quasi-omnidirectional anti-reflection properties with biomimetic silicon nanostructures. *Nature, Nanotechnology*, 2:770–774, 2007.

[36] Y. Inomata, K. Fukui, and K. Shirasawa. Surface texturing of large area multicrystalline silicon solar cells using reactive ion etching method. *Solar Energy Materials and Solar Cells*, 48(1-4):237 – 242, 1997.

[37] Akihiro Ishihara, Ryousuke Kawai, Thukasa Kitano, Atushi Suzuki, Toshiyuki Kondo, Motoaki Iwaya, Hiroshi Amano, Satoshi Kamiyama, and Isamu Akasaki. Growth and characterization of gan grown on moth-eye patterned sapphire substrates. *physica status solidi (c)*, 7(7-8):2056–2058, 2010.

[38] Y. Kanamori, M. Sasaki, and K. Hane. Broadband antireflection gratings fabricated upon silicon substrates. *Optics Letters*, 24:1422–1424, 1999.

[39] H. Kasugai, K. Nagamatsu, Y. Miyake, A. Honshio, T. Kawashima, K. Iida, M. Iwaya, S. Kamiyama, H. Amano, I. Akasaki, H. Kinoshita, and H. Shiomi. Light extraction process in moth-eye structure. *physica status solidi (c)*, 3(6):2165–2168, 2006.

[40] Ryosuke Kawai, Toshiyuki Kondo, Atushi Suzuki, Fumiharu Teramae, Thukasa Kitano, Kenta Tamura, Hisashi Sakurai, Motoaki Iwaya, Hiroshi Amano, Satoshi Kamiyama, Isamu Akasaki, Mark Chen, Alex Li, and Kidd Su. Realization of extreme light extraction efficiency for moth-eye leds on sic substrate using high-reflection electrode. *physica status solidi (c)*, 7(7-8):2180–2182, 2010.

[41] D.L. King and M. E Buck. Experimental optimization of an anisotropic etching process for random texturization of silicon solar cells. *In Proc. 22nd IEEE Photovolt. Spec. Conf. , Las Vegas, Nevada,*, 1991.

[42] Shuichi Kinoshita, Shinya Yoshioka, Yasuhiro Fujii, and Noako Okamoto. Photophysics of structural color in the morpho butterflies. *Forma*, 17:103–121, 2002.

[43] Shuichi Kinoshita, Shinya Yoshioka, and Kenji Kawagoe. Mechanisms of structural colour in the morpho butterfly: cooperation of regularity and irregularity in an iridescent scale. *Proceeding of the Royal Society , Biological Science*, 269:1417–1421, 2002.

[44] R. Kishore, S.N. Singh, and B.K. Das. Pecvd grown silicon nitride ar coatings on polycrystalline silicon solar cells. *Solar Energy Materials and Solar Cells*, 26(1-2):27 – 35, 1992.

[45] Svetoslav Koynov, Martin S. Brandt, and Martin Stutzmann. Black nonreflecting silicon surfaces for solar cells. *APPLIED PHYSICS LETTERS*, 88:203107–203110, 2006.

[46] Philippe Lalanne and Dominique Lemercier-lalanne. On the effective medium theory of subwavelength periodic structures. *Journal of Modern Optics*, 43:2063–2085, 1996.

[47] Philippe Lalanne and G Michael Morris. Antireflection behavior of silicon subwavelength periodic structures for visible light. *Nanotechnology*, 8:53–57, 1997.

[48] Yunfeng Li, Junhu Zhang, Shoujun Zhu, Heping Dong, Fei Jia, Zhanhua Wang, Zhiqiang Sun, Liang Zhang, Yang Li, Haibo Li, Weiqing Xu, and Bai Yang. Biomimetic surfaces for high-performance optics. *Advanced Materials*, 21(46):4731–4734, 2009.

[49] Shui-Yang Lien, Dong-Sing Wuu, Wen-Chang Yeh, and Jun-Chin Liu. Tri-layer antireflection coatings sio2 sio2 tio2 tio2 for silicon solar cells using a sol-gel technique. *Solar Energy Materials and Solar Cells*, 90(16):2710 – 2719, 2006.

[50] W. H. Lowdermilk and D. Milam. Graded-index antireflection surfaces for high-power laser applications. *Appl. Phys. Lett.*, 36(11):891–893, 1980.

[51] T. Machida, K. Nakajima, Y. Takeda, S. Tanaka, N. Shibuya, K. Okamoto, T. Nammori, T. Nunoi, and T. Tsuji. Efficiency improvement in polycrystalline silicon solar cell with grooved surface. pages 1033 –1034 vol.2, oct 1991.

[52] Bruce MacLeod and Greg Sonek. Thin films - motheye surfaces reflect little light. *LaserFocusWorld*, 35:85, 1999.

[53] D. Mailly. Nanofabrication techniques. *The European Physical Journal - Special Topics*, 172:333–342, 2009.

[54] C. Martinet, V. Paillard, A. Gagnaire, and J. Joseph. Deposition of sio2 and tio2 thin films by plasma enhanced chemical vapor deposition for antireflection coating. *Journal of Non-Crystalline Solids*, 216(0):77 – 82, 1997. ¡ce:title¿Structure and Defects in SiOin2, Fundamentals and Applications¡/ce:title¿.

[55] Jurgen R Meyer-Arendt. *Introduction to Classical and Modern Optics*. Prentice-Hall, 4 edition, 1995.

[56] W. H. Miller, A. R. Moller, and C. G. Bernhard. *The functional organization of the compound eye*. Pergamon Press, Oxford, 1966.

[57] Wei Lun Min, Amaury P. Betancourt, Peng Jiang, and Bin Jiang. Bioinspired broadband antireflection coatings on gasb. *Appl. Phys. Lett.*, 92(14):141109, 2008.

[58] Mark S. Mirotznik, Brandon Good, Paul Ransom, David Wikner, and Joseph N. Mait. Iterative design of moth-eye antireflective surfaces at millimeter wave frequencies. *Microwave and Optical Technology Letters*, 52:561–568, 2010.

[59] M. G. Moharam and T. K. Gaylord. Rigorous coupled-wave analysis of planar-grating diffraction. *J. Opt. Soc. Am.*, 71(7):811–818, 1981.

[60] H Nagel, A Metz, and R Hezel. Porous sio2 films prepared by remote plasma-enhanced chemical vapour deposition a novel antireflection coating technology for photovoltaic modules. *Solar Energy Materials and Solar Cells*, 65(1-4):71 – 77, 2001. ¡ce:title¿PVSEC 11 Part I¡/ce:title¿.

[61] Michel Neviere and Evgeny Popov. *Light Propagation in Periodic Media*. Univeristy of Rochester, 2003.

[62] Yuzo Ono, Yasuo Kimura, Yoshinori Ohta, and Nobuo Nishida. Antireflection effect in ultrahigh spatial-frequency holographic relief gratings. *Applied Optics*, 26(6):1142–1146, 1987.

[63] P. Papet, O. Nichiporuk, A. Kaminski, Y. Rozier, J. Kraiem, J.-F. Lelievre, A. Chaumartin, A. Fave, and M. Lemiti. Pyramidal texturing of silicon solar cell with tmah chemical anisotropic etching. *Solar Energy Materials and Solar Cells*, 90(15):2319 – 2328, 2006. ¡ce:title¿Selected Papers from the Solar Cells and Solar Energy Materials Symposium -IMRC 2005¡/ce:title¿ ¡xocs:full-name¿XIV International Materials Research Congress¡/xocs:full-name¿.

[64] A. R. Parker, D. R. Mckenzie, and MCJ. Large. Multilayer reflectors in animals using green and gold beetles as contrasting examples. *The Journal of Experimental Biology*, 201:1307–1313, 1998.

[65] Andrew Parker. Photonics applied: Biomimetics: Optical biomimetics emerge from a deep, dark past. *LaserFocusWorld*, 46, 2010.

[66] Andrew R. Parker. Natural photonic engineers. *Materials Today*, 5(9):26 – 31, 2002.

[67] Andrew R. Parker. A vision for natural photonic. *Philos Transact A Math Phys Eng Sci.*, 362:2709–2720, 2004.

[68] Andrew R Parker. Natural photonics for industrial inspiration. *Philosophical Transactions of the Royal Society A: Mathematical,Physical and Engineering Sciences*, 367(1894):1759–1782, 2009.

[69] Andrew R. Parker and Helen E. Townley. Biomimetics of photonic nanostructures. *Nature Nanotechnology*, 2:347–353, 2007.

[70] Andrew R. Parker, Victoria L. Welch, Dominique Driver, and Natalia Martini. Structural colour: Opal analogue discovered in a weevil. *Nature*, 426:786–787, 2003.

[71] A.R Parker, Z Hegedus, and R. A Watts. Solar-absorber antireflector on the eye of an eocene fly (45 ma). *Proceedings of the Royal Society B*, 265:811–815, 1998.

[72] Gregory J Parker. Biomimetically-inspired photonic nanomaterials. *Journal of Materials Science Materials in Electronics*, 21(10):965–979, 2010.

[73] I.O Parm, K Kim, D.G Lim, J.H Lee, J.H Heo, J Kim, D.S Kim, S.H Lee, and J Yi. High-density inductively coupled plasma chemical vapor deposition of silicon nitride for solar cell application. *Solar Energy Materials and Solar Cells*, 74(1-4):97 – 105, 2002. ¡ce:title¿PVSEC 12 Part I¡/ce:title¿.

[74] Antonio Parretta, Angelo Sarno, Pierpasquale Tortora, Haruna Yakubu, Pasqualino Maddalena, Jianhua Zhao, and Aihua Wang. Angle-dependent reflectance measurements on photovoltaic materials and solar cells. *Optics Communications*, 172(1-6):139 – 151, 1999.

[75] Richard Prum, Tim Quinn, and Rodolfo H. Torres. Anatomically diverse butterfly scales all produce structural colours by coherent scattering. *J Exp Biol*, 209(4):748–765, 2006.

[76] J. Rao, R. Winfield, and L. Keeney. Moth-eye-structured light-emitting diodes. *Optics Communications*, 283(11):2446 – 2450, 2010.

[77] Lord Rayleigh. On reflection of vibrations at the confines of two media between which the transition is gradual. *London Mathematical Society*, 11:51– 56, 1880.

[78] B. S. Richards. Comparison of tio2 and other dielectric coatings for buried contact solar cells: a review. *Prog. Photovolt: Res. Appl.*, 12:253–281, 2004.

[79] D. S. Ruby, S. H. Zaidi, B. M. Damiani, and A. Rohatgi. Rie-texturing of multicrystalline silicon solar cells. *PVSEC-12, Jeju. Korea*, pages 273–374, 2001.

[80] H. Sai, H. Fujii, Y. Kanamori, K. Arafune, Y. Ohshita, H. Yugami, and M. Yamaguchi. Numerical analysis and demonstration of submicron antire-flective textures for crystalline silicon solar cells. *In Proc. IEEE 4th World Conf. on Photovoltaic Energy Conversion, Hawaii*, pages 1191–1194, 2006.

[81] Martin Schnell, Ralf Ludemann, and Sebastian Schaefer. Plasma surface texturization for multicrystalline silison solar cells. *Proc. 28th IEEE Photovolt. Spec. Conf.,*, pages 367–370, 2000.

[82] Masatsugu Shimomura. The new trends in next generation biomimetics material technology: Learning from biodiversity. *Science and Technology Trends, Quarterly Reviews*, 37:53–75, 2010.

[83] William H. Southwell. Gradient-index antireflection coatings. *Opt. Lett.*, 8(11):584–586, Nov 1983.

[84] William H. Southwell. Pyramid-array surface-relief structures producing antireflection index matching on optical surfaces. *J. Opt. Soc. Am. A*, 8(3):549–553, Mar 1991.

[85] D.G Stavenga, S Foletti, G Palasantzas, and K Arikawa. Light on the moth-eye corneal nipple array of butterflies. *Proceeding of the Royal Society*, 273:661–667, 2006.

[86] Petros Stavroulakis. Unpublished.

[87] M. J. Stocks, A. J. Carr, and A. W. Blakers. Texturing of polycrystalline silicon. *In Proc. First World Conf. on Photovoltaic Energy Conversion, Waikoloa, Hawaii,*, page 15511554, 1994.

[88] Chih-Hung Sun, Peng Jiang, and Bin Jiang. Broadband moth-eye antireflection coatings on silicon. *Appl. Phys. Lett.*, 92(6):061112, 2008.

[89] Chih-Hung Sun, Wei-Lun Min, Nicholas C. Linn, Peng Jiang, and Bin Jiang. Templated fabrication of large area subwavelength antireflection gratings on silicon. *Applied Physics Letters*, 91(23):231105, 2007.

[90] C. M. Sotomayor Torres, S. Zankovych, J. Seekamp, A. P. Kam, C. Clavijo Cede, T. Hoffmann, J. Ahopelto, F. Reuther, K. Pfeiffer, G. Bleidiessel, G. Gruetzner, M. V. Maximov, and B. Heidari. Nanoimprint lithography an alternative nanofabrication approach. *Materials Science and Engineering C*, 23(1-2):23 – 31, 2003.

[91] Hiroshi Toyota, Koji Takahara, Masato Okano, Tsutom Yotsuya, and Hisao Kikuta. Fabrication of microcone array for antireflection structured surface using metal dotted pattern. *Japanese Journal of Appied Physics, Part 2*, 40:L747–L749, 2001.

[92] P. Vukusic, J. R. Sambles, C. R. Lawrence, and R. J. Wootton. Quantified interference and diffraction in single morpho butterfly scales. *Proceedings: Biological Sciences*, 266(1427):1403–1411, 1999.

[93] Pete Vukusic and J. Roy Sambles. Photonic structure in biology. *Nature*, 424:852–856, 2003.

[94] Neil White and Stephen Beeby, editors. *Energy Harvesting for Autonomous Systems*. Artech House, 2010.

[95] S. J Wilson and M. C Hutleyok. The optical properties of moth eye antireflection surfaces. *Journal of Modern Optics*, 29:993–1009, 1982.

[96] Hongbo Xu, Nan Lu, Dianpeng Qi, Juanyuan Hao, Liguo Gao, Bo Zhang, and Lifeng Chi. Biomimetic antireflective si nanopillar arrays. *Small*, 4(11):1972–1975, 2008.

[97] J S Yoo, I O Parm, U Gangopadhyay, Kyunghae Kim, S K Dhungel, D Mangalaraj, and Junsin Yi. Black silicon layer formation for application in solar cells. *Solar Energy Materials and Solar Cells*, 90(18-19):3085–3093, 2006.

[98] A. Yoshida, M. Motoyama, A. Kosaku, and K. Miyamoto. Nanoprotuberance array in the transparent wing of a hawkmoth, cephonodes hylas. *Zoological Science*, 13:525–526, 1996.

[99] Akihiro Yoshida, Mayumi Motoyama, Akinori Kosaku, and Kiyoshi Miyamoto. Antireflective nanoprotuberance array in the transparent wing of a hawkmoth, cephonodes hylas. *Zoological science*, 14:737–741, 1997.

[100] Zhaoning Yu, He Gao, Wei Wu, Haixiong Ge, and Stephen Y. Chou. Fabrication of large area subwavelength antireflection structures on si using trilayer resist nanoimprint lithography and liftoff. *Journal of Vacuum Science and Technology B*, 21:2874–2878, 2003.

[101] J. Zhao and M. A. Green. Optimized antireflection coatings for high-efficiency silicon solar cells. *IEEE Trans. Electron Dev.*, 38:1925–1934, 1991.

[102] J. Zhao, A. Wang, P. Altermatt, and M. A. Green. Twenty-four percent efficient silicon solar cells with double layer antireflection coatings and reduced resistance loss. *Applied Physics Letters*, 66:3636–3638, 1995.

[103] Jianhua Zhao, Aihua Wang, Martin A. Green, and Francesca Ferrazza. 19.8monocrystalline silicon solar cells. *Applied Physics Letters*, 73:1991–1993, 1998.